Development of novel synthesis routes and exploring application aspects of some transitional metal sulphide nanostructures

THESIS SUBMITTED FOR THE DEGREE OF

DOCTOR OF PHILOSOPHY (SCIENCE)

OF

JADAVPUR UNIVERSITY

by

RIMPA KHAN

Under the supervision of

Prof. (Dr.) K. K. Chattopadhyay

Department of Physics
Thin Film and Nanoscience Laboratory
Jadavpur University
Kolkata-700032, INDIA

October 2021

CERTIFICATE FROM THE SUPERVISOR

This is to certify that the thesis entitled "**Development of novel synthesis routes and exploring application aspects of some transitional metal sulphide nanostructures**" submitted by **Rimpa Khan**, who got her name registered on **17/08/2016** for the award of **Ph.D. (Science) degree** of **Jadavpur University**, is absolutely based upon her own work under the supervision of **Prof. K. K. Chattopadhyay** and that neither this thesis nor any part of it has been submitted for either any degree/diploma or any other academic award anywhere before.

1.10.2024

(Prof. Kalyan Kumar Chattopadhyay)
Signature of the Supervisor
Date with Office Seal

Dr. K. K. Chattopadhyay
Professor
Department of Physics
Jadavpur University, Kolkata-700 032

Dedicated to my family

My sincere gratitude
to Daaji

Acknowledgement

This thesis is based on synthesis of nanostructures of transition metal sulphides using novel routes, their characterizations and exploring their application aspects. Through this entire tenure of Ph.D. work, I have learned great things not only about academics but also about the truth of science and life. Though it was a difficult path but I have learnt, experienced and enjoyed every moment of my journey. All the success I have achieved in this period would have been impossible without all the people who supported me flawlessly and have given me valuable advice and motivation. It is a great pleasure to acknowledge and convey my gratitude to everyone who helped me out to complete my Ph.D.

First of all, I would like to express my sincere gratitude to my supervisor Prof. Kalyan Kumar Chattopadhyay for the continuous support and guidance throughout the time of research. He provided enough freedom to do work which helped me to complete my research work smoothly. His valuable suggestions allowed me to grow as a research scholar.

I would like to thank Dr. Sukhen Das, H.O.D. of Department of Physics and all faculty members of the Department of Physics, Jadavpur University for their constant cooperation. I pay my sincere thanks to the staffs of Research Section and Ph.D. Section, Jadavpur University for their official support.

I am grateful to Council of Scientific and Industrial Research (CSIR), India for providing me fellowship during the execution of my Ph.D. work.

I would like to express my deepest appreciation to Dr. Nirmalya Sankar Das (Nirmalya da) for his generous cooperation and motivation. He was like an elder brother to me rather than my senior lab colleague. He stood beside me in every step of research work as a continuous source of inspiration. His ideas and suggestions always made me feel confident to overcome all the difficulties during this entire journey.

I am indebted to all my former and present senior lab mates; Dr. Sourav Sarkar, Dr. Supratim Maity, Dr. Shreyasi Pal, Dr. Uttam Kumar Ghorai, Dr. Saswati Santra, Dr. Soumen Maiti, Dr. Swati Das, Dr. Subhajit Saha, Dr. Dipayan Sen, Dr. Rajarshi Roy, Dr. Nilesh Mazumder, Dr. Anuradha Mitra, Dr. Arunava Jha, Dr. Sayantani Das, Dr. Partha Bairi, Dr. Partha Hazra, Dr. Biplab Kr. Chatterjee, Dr. Biswajit Das, Dr. Samrat Sarkar, Prasanta Mandal and Dr. Moumita Mukherjee. Thank you to this entire team for their immense support and help.

I am extremely thankful to all my junior lab colleagues; Anibrata, Anirban, Ankita, Antika, Arnab, Bikram (Das), Bikram (Swar), Brahami, Dimitra, Dipanwita, Dipayan, Dr. Karamjyoti, Kausik (Chanda), Kausik (Sardar), Madhupriya, Dr. Mississippi, Nabanita, Nripen, Dr. Promita, Pulok, Ratna, Shrabani, Subhasish, Suvra and Tufan.

Most importantly, no word of thanks can sum up to the gratitude that I owe to my family members; especially my mother, father and my sweet sisters Sneha and Priya. Their encouragement, patience and unconditional love helped me to accomplish the journey. I am really grateful to my grandparents for their blessings which gave me the strength to complete this dissertation.

Finally, I would like to thank all my well-wishers, friends and teachers whom I will always keep in my mind throughout my life.

October 2021

Department of Physics, Jadavpur University

Kolkata –32, India.

_____

(Rimpa Khan)

Contents

ABSTRACT

Metal chalcogenides are mostly semiconductors with properties that are interesting for both fundamental and application points of view. There is tremendous renewed interest in this class of materials after the advent of nanotechnology because most of the properties exhibit enhanced behaviors at lower dimensions. However, the successful utilization of such properties of the metal chalcogenides depends on the controlled growth of nanocrystals. Also, properties of nanomaterials depend on the morphology, crystal quality, defect chemistry, structural parameters etc. This thesis is aimed to develop some metal chalcogenide nanostructures through some novel synthesis routes, understanding the growth process of the nanostructures and also to utilize the developed materials in various technological fields.

The first work is focused on mitigating the ever-increasing power requirement to keep the industrial and urban life running in its growing pace. In this view, application of metal chalcogenides in energy sectors was studied thoroughly. Hierarchical nano/micro Ni_3S_2 cactus like structures were fabricated using cost effective and eco-friendly hydrothermal technique. Both pure and Ni_3S_2:Co composite nanostructures were grown on nickel foam under different synthesis temperatures. The synthesized nanostructures showed a wide variation of hierarchical morphology with variation of synthesis temperatures. The obtained nanostructures were investigated for electrochemical water splitting performance. The morphologies of the samples were found to acquire higher aspect ratio with increment in synthesis temperature. This morphological tuning led to remarkable enhancement in hydrogen evolution performance with very low overpotential of 206 mV at 100 mA cm^{-2} current density in acidic medium. Owing to this superior morphology tuned water splitting performance, this low dimensional Ni_3S_2 system can be recognized as a potential leader in electrochemical energy harvesting sector.

Optical properties of such metal chalcogenides are also considered of utmost importance in view of fabrication of multipurpose materials systems involving them. To study this particular aspect, another important metal chalcogenide – ZnS was chosen. ZnS thin films have been synthesized by hydrothermal route on seeded glass and silicon substrates at various temperatures. The seeded substrates were prepared by RF magnetron sputtering technique. The good crystallinity and proper phase formation of the synthesized films was confirmed by X-ray diffraction and transmission electron microscopic studies. The crystallinity of the samples could be enhanced by varying the synthesis temperature. The morphological studies along with determination of particle dimensions were performed using field emission scanning electron microscopy. With increase of particle dimensions, the band gap of the ZnS thin films decreased from 3.48 eV to 3.23 eV as determined from UV-vis-NIR spectrophotometric measurement. The samples exhibited intense cathodoluminescence irradiated under electronic excitation thus indicating its effective application in display devices.

As mentioned in the above section, fabrication of multipurpose materials systems has been identified as a major goal of this work. In this direction, combination of two entirely different applications in a single system was attempted in my next work. Hierarchical nickel sulphide microtubes were prepared by cost effective sol-gel technique with tuning of morphology and it was applied for photo-induced hazardous dye segregation and cold electron emission. The synthesized samples were characterized for crystalline phase, morphology and composition via X-ray diffractometry, electron microscopy and energy dispersive X-ray studies respectively. The band gaps were estimated from UV–vis data. The samples were found to be effective as a dye degrading agent under UV irradiation. The pollutant removal efficiency of the nickel sulphide (NS) microstructures was found to be governed by dimension and compositional parameters jointly. The sample showing highest degradation efficiency was

found to degrade phenol effectively. Scavenger test was carried out to identify the active radicals involved in the catalysis process. To ensure long term action of the catalyst sample, recyclability of the same was investigated thoroughly. The NS microstructures also showed field emission behavior which is reported for the first time. The growth of different shapes and hierarchical units of NS structures was correlated with stoichiometric alteration which may also be extended for synthesis of other nickel chalcogenides.

After investigating the possibilities of novel technological applications using metal chalcogenides, a comparatively less studied property of cold cathode emission process by metal chalcogenides was emphasized in the next work. Molybdenum sulphide (MoS_2) nanoflakes were prepared by a facile room temperature wet chemical method which was further modified through RF magnetron plasma processing for morphological modification and generation of numerous edges. Proper phase formation was confirmed by X-ray diffraction study whereas the morphological feature was investigated using field emission scanning electron microscopy. In an attempt to explore the potential of the chalcogenide beyond conventional photovoltaic applications, the field emission performance of the nanostructure MoS_2 was investigated both through experiment and simulation. Finite-element based simulation was performed using ANSYS which was carried out to predict the feasibility of potential field emission behavior of the low dimensional MoS_2 flakes. Based on the results, the theoretical simulation was further extended to predict whether morphological modification can enhance the FE properties of the samples. Encouraged by the outcome of simulation-based results, the samples were further treated by inert ion bombardment via radio-frequency plasma processing technique. Both the pure and sputtered treated samples were subjected to FE studies. The turn-on field (electric field corresponding to 10 μA cm^{-2} current density) was obtained to be as low as 0.963 V $(\mu m)^{-1}$ with current density reaching up to 23.11 μA cm^{-2} for inter-electrode spacing of 2500 μm for the nanoflakes. The emission

current density enhanced remarkably after modification of sample morphology and reached up to 12 mA cm^{-2}. The significant improvement of the field emission properties of the plasma modified samples are explained primarily because of the generation of large number of emission sites in the plasma treated samples. The external macroscopic electric field gets enhanced at these emission sites thereby decreasing the local work function of the material leading to enhanced field emission properties.

List of Publications

1) Co incorporated Ni_3S_2 hierarchical nano/micro cactus for electrochemical water splitting.

Rimpa Khan, Madhupriya Samanta, Shrabani Ghosh, Nirmalya Sankar Das and Kalyan Kumar Chattopadhyay

Int. J. Hydrogen Energy 44 (2019) 21315-21323.

2) Cathodoluminescence and photoluminescence from ZnS thin films deposited by novel seeded hydrothermal route.

Rimpa Khan, Nirmalya Sankar Das and Kalyan Kumar Chattopadhyay

J. Mater. Sci: Mater. Electron. 30 (2019) 19189-19198.

3) Hierarchical nickel sulphide microstructures for controlled water disinfection and cold cathode emission.

Rimpa Khan, Nirmalya Sankar Das, Biswajit Das, Brahami Das and Kalyan Kumar Chattopadhyay

J. Photochem. Photobiol. A: Chem. 412 (2021) 113212.

4) Chalcogenide beyond photovoltaics: Field Emission from morphology tailored nanostructured molybdenum sulphide.

Rimpa Khan, Nirmalya Sankar Das, Brahami Das and Kalyan Kumar Chattopadhyay

(Communicated)

5) rGO-wrapped flowerlike Bi_2Se_3 nanocomposite: synthesis, experimental and simulation-based investigation on cold cathode applications.

Biswajit Das, Samrat Sarkar, **Rimpa Khan**, Saswati Santra, Nirmalya Sankar Das and Kalyan Kumar Chattopadhyay

RSC Advances 6 (2016) 25900-25912.

6) Enhanced field emission properties of rGO-wrapped Ga_2O_3 micro/nanobricks: Experimental investigation with theoretical validation.

Brahami Das, Biswajit Das, Nirmayla Sankar Das, Suvra Pal, Bikram Kumar Das, Ratna Sarkar, **Rimpa Khan**, Subrata Sarkar

(Communicated)

Papers presented in National and International Conferences

1) One day Seminar on Some Recent Trends in Research in Physics (SRTRP-2016).

Department of Physics, Jadavpur University, Kolkata, 21st March 2016, (Poster presentation)

Title: Dimensional tuning of sol-gel synthesized nickel sulphide nanoparticles: Future cold cathodes for smart devices.

Rimpa Khan, Nirmalya Sankar Das, Nripen Besra, Biswajit Das and Kalyan Kumar Chattopadhyay

2) UGC Sponsored National Level Seminar (2016)

Department of Industrial Chemistry, Ramakrishna Mission Vidyamandira, Belur Math, Howrah, 29th March 2016, (Participation)

3) International Conference on Energy, Functional Materials and Nanotechnology (ICEFN-2016).

Nanoscience and Nanotechnology Centre, Department of Chemistry, Kumaun University, Nainital, 27-29 March 2016 (Poster presentation)

Title: Synthesis of WS_2 nano-petals as smart potential flexible cold cathodes.

Rimpa Khan, Nirmalya Sankar Das, Uttam Kumar Ghorai, Anuradha Mitra and Kalyan Kumar Chattopadhyay.

4) National Conference on Nanotechnology: Materials and Applications (NCoN: M&A-2016).

School of Materials Science & Nanotechnology, Jadavpur University, Kolkata, 16-17 June 2016 (Poster presentation)

Title: Synthesis of MoS_2 nano-petals as potential smart flexible cold cathodes.

Rimpa Khan, Nirmalya Sankar Das, Uttam Kumar Ghorai, Biswajit Das and Kalyan Kumar Chattopadhyay.

5) Two days Seminar on Twists and Turns in Physics Research: Special Emphasis on Condensed Matter and Biophysics (TTPR-2017).

Department of Physics, Jadavpur University, Kolkata, 21-22 Feb 2017, (Poster presentation)

Title: WS_2 nano-flakes for flexible cold cathodes: Chemical synthesis for controlled screening effect.

Rimpa Khan, Nirmalya Sankar Das, Uttam Kumar Ghorai, Anuradha Mitra and Kalyan Kumar Chattopadhyay.

6) National Seminar titled Recent Advances in Materials Science (RAMS-2017).

Department of Industrial Chemistry and Applied Chemistry, Ramakrishna Mission Vidyamandira, Belur Math, Howrah, 12 April 2017 (Participation)

7) International Conference on Condensed Matter Physics (ICCMP-2017).

Indian Statistical Institute, Kolkata, 14-16 Nov 2017 (Oral presentation)

Title: MoS_2 cold cathodes on flexible substrates: Electrode separation for tuned performance.

Rimpa Khan, Nirmalya Sankar Das, Uttam Kumar Ghorai and Kalyan Kumar Chattopadhyay.

8) National Conference on Recent Developments in Nanoscience and Nanotechnology (NCRDNN-2019)

School of Materials Science & Nanotechnology, Jadavpur University, Kolkata, 29-31 Jan 2019 (Participation)

9) International Webinar on Recent Trends in Condensed Matter Physics and Applications (RTCMPA – 2020)

Department of Physics in collaboration with IQAC, Kulti College, Asansol, West Bengal, 22nd Aug 2020 (Participation)

10) National Webinar on Cosmology "Observing the origin and the evolution of our Universe"

Department of Physics, Bhairab Ganguly College, Belgharia, Kolkata, 23rd Sep 2020 (Participation)

11) National Webinar entitled Frontiers of Physics - 2021

Department of Physics in collaboration with IQAC, Acharya Prafulla Chandra College, New Barrackpore, Kolkata, 6th July 2021 (Participation)

Chapter 1

INTRODUCTION

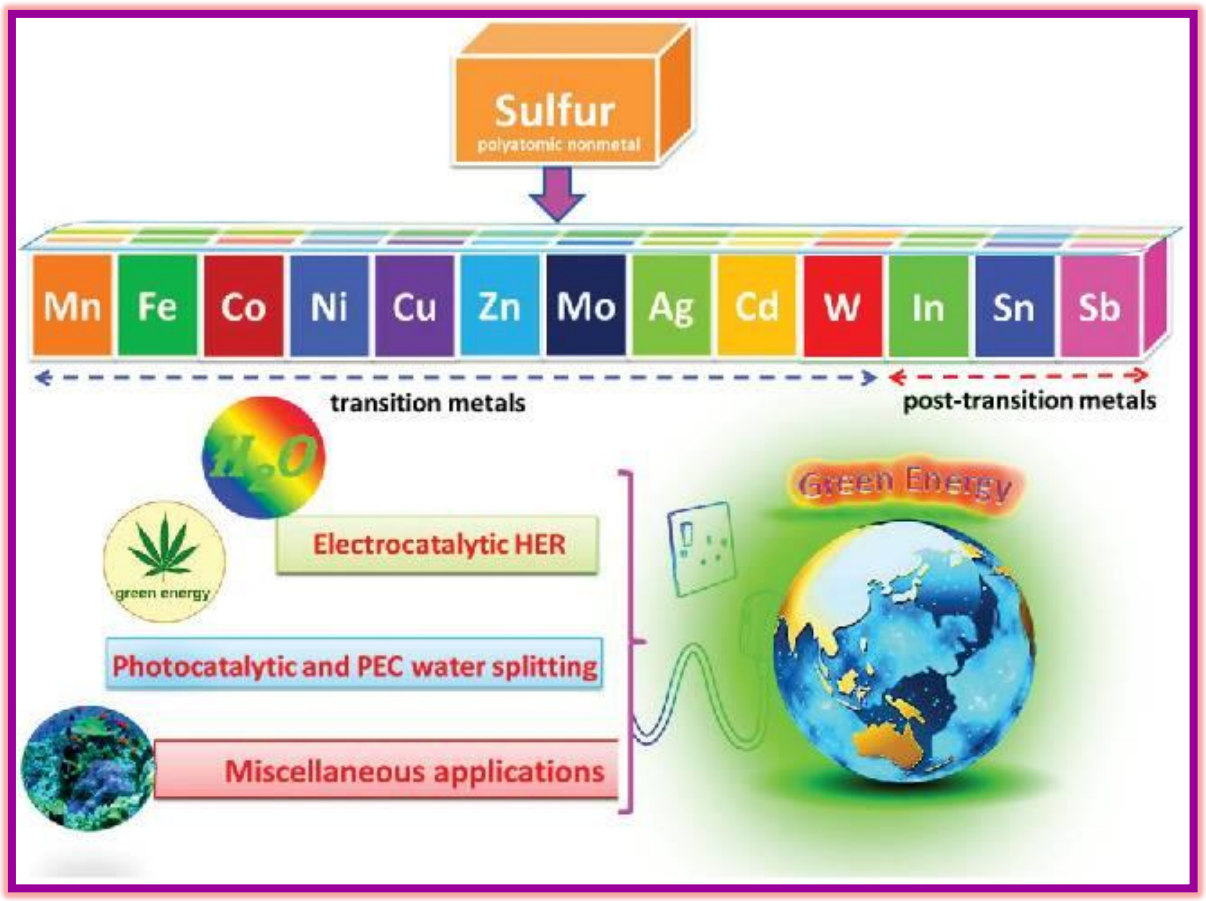

1.1. TRANSITION METALS:

According to IUPAC definition, transition metal is defined as an element whose atom has a partially occupied d-sub shell. These elements can also form stable cations with an incompletely filled d-sub shell. Between the two sides of the main group elements of the periodic table, the transition metals serve as a bridge. At the bottom of the table, the f-block elements comprising the lanthanides and the actinides are present which are sometimes known as the inner transition metals. It is because their atomic numbers fall between the first and second elements in the last two rows of the transition metals.

The transition elements are placed in periods 4 to 7 and groups 3 to 12. The electronic configuration of the transition elements is generally $(n\text{-}1)d^{1\text{-}10}ns^{0\text{-}2}$. To bond with other elements, most of the elements can only use electrons from their outer orbital whereas the transition elements can use two outermost shells or orbitals.

Generally, the transition metals are hard and dense; they are less reactive than alkali metals. Due to partially filled d-orbital, the transition elements show a number of properties that are absent in other elements. These elements can form coloured compounds whose colour is due to the d-d transition of electrons. As there is a relatively low energy gap between the possible oxidation states of these elements, they can form compounds in many oxidation states. Due to the participation of delocalized d-electrons in metallic bonding, the transition metals are good conductors of electricity and have high boiling and melting points. The presence of unpaired electrons in the d-orbital enables transition elements to form many paramagnetic compounds. The transition elements can also form a wide range of stable complexes because a large variety of ligands can bind themselves to these elements. The ratio of charge to the radius of these elements is large. However, the transition metals are similar to main group metals in some aspects - they are also malleable, ductile, can form positive ions, conduct heat and

electricity and look like metals. Unlike main group metals, the transition metals are more electronegative and are likely to form covalent compounds.

Due to the poor shielding offered by the small number of d-electrons, the atomic and ionic radii of the transition elements decreases from group 3 to 6. Elements placed in the groups 7 to 10 have somewhat similar atomic radii and that of groups 11 and 12 have larger radii. The reason behind this is that the nuclear charge is balanced out by the electron-electron repulsions. However, an increase in the atomic and ionic radii of the elements is observed while traversing down the group. The presence of a greater number of subshells explains the increase in radius of the elements. The atomic radius is also related to the ionization energy of an element. Atoms with smaller radii have greater ionization enthalpies as compared to that of elements with larger radii. While moving along the row, the ionization energies of the transition metals increase due to the increase in atomic number.

1.1.1. USES OF TRANSITION METALS:

Transitions metals have a wide range of uses. Titanium, iron, manganese, copper, nickel, cobalt, silver, gold and mercury are some of the well-known transitional metals. Among them, three elements namely iron, cobalt and nickel are most remarkable as they are the only one to produce a magnetic field. The uses of some of the main transition metals are listed below:

1. **Iron (Fe):** Usually, iron is too soft to be used as the metal alone. To make it harder and stronger, it is usually mixed with small amounts of other metals such as manganese and chromium to make steel. It is widely used in construction materials from vehicles to aircraft and as a catalyst in the chemical industry (manufacture of ammonia).
2. **Cobalt (Co):** After the discovery of cobalt element, its brilliant blue colour made it incredibly popular. It is also referred as a technology enabling element because of its

importance in rechargeable batteries, electronics, catalysts and healthcare. It is oxidation resistant, wear resistant, ferromagnetic and conducts electricity. It can also be alloyed with various metals to improve its magnetism and strength as well as reduces corrosion.

3. **Nickel (Ni):** For softer metals, nickel is commonly used as a protective outer coating. It is mainly used in stainless steel. In rechargeable batteries, nickel is used as a primary component. Nickel acts as an anti-corrosion coating for metals as it is naturally non-corrosive.
4. **Zinc (Zn):** One of the most important applications of zinc metal is that it is used for galvanizing iron and steel against corrosion. The oxide form of zinc is widely used in manufacture of paints, cosmetics, textiles, inks, soaps and the sulfide form is used in making fluorescent lights, luminous paints and X-ray screens.
5. **Molybdenum (Mo):** In environments of intense heat including aircraft parts, industrial motors, electrical contacts, military armor and supports for filaments in light bulbs; molybdenum is used as it can withstand extreme temperatures. For its high corrosion resistance and weldability, molybdenum is also used in steel alloys.
6. **Copper (Cu):** Copper is a soft, malleable and ductile metal i.e. it can be easily stretched, molded and shaped. It is a very good conductor of heat and electricity and often used in electricity cables. Copper wires are known to be used in power generation, distribution and transmission. As copper is resistant to corrosion, it is added with different metals to form alloys.

1.2. TRANSITION METAL SULPHIDES:

Transition metal sulphides have numerous applications in many fields i.e. mineralogy, geology, theoretical chemistry and catalysis. A marked anisotropy is observed in the physical properties of numerous transition metal sulphides such that there are two equivalent

directions and the third one is different. The chemical formula of the materials in this class is MX_2 where, M denotes transition metal atom (Mo, W etc.) and X (S, Se, Te) denotes a chalcogen. A prime example of these compounds is MoS_2 having layered structure comprising of a metal layer between two close-packed sulfur layers.

In chalcogenides, d-electrons participate in covalent bonding. So, the properties of transition metal chalcogenides are quite different from that of oxides. The formal charge on transition metals is reduced by this covalent bonding in chalcogenides. This helps in the formation of metal-metal bonds which plays an important role in determining the properties of transition metal chalcogenides. The layered compounds containing monoatomic anions and diatomic anions are formed by transition metal disulphides and diselenides. The six-coordinated cations occupy trigonal pyramidal or octahedral interstices in the layered compounds. The interstices share common edges in the close-packed layers formed by the cations and in between the layers, Van der Waals force exists.

Due to the unique properties and broad potential applications, the 2D layered nanomaterials have drawn great attention. The electrical properties of transition metal sulphides vary from semiconducting to metallic (in some cases, superconducting) and that of magnetic properties vary from weak diamagnetism to temperature independent Pauli paramagnetism.

1.3. WHY SYNTHESIS OF TRANSITION METAL SULPHIDES IS IMPORTANT?

Due to the electrical, optical, mechanical and magnetic properties of transition metal sulphides, their synthesis has attracted great interest. The transition metal sulphides (TMSs) have also shown great promise in high performance and abundant electrocatalysts for OER surpassing the OER activity and stability of noble metal-based materials (RuO_2, IrO_2) which

are considered as benchmark for OER catalysts. The limited amount of availability and high cost of noble metal-based materials has a major impact on its widespread commercial utilization [1]. Therefore, the need of low cost, Earth-abundant and high performance electrocatalysts arises extensively which is fulfilled by synthesizing TMSs containing elements like cobalt, nickel and also preparing hybrids of TMSs with rGO. TMSs have abundant active sites for adsorption or desorption processes and desirable electrical configuration for transfer of charge easily which makes them excellent electrocatalysts.

The well-aligned nanostructure arrays of TMSs are highly attractive for their excellent properties and novel applications in various fields. Energy conversion and storage are the main challenges in this 21st century for which TMSs nanostructures are potential materials as compared to other nanomaterials because they are cheap, light in weight, highly efficient, better flexibility and renewable sources of energy. The metal sulphides are usually available as minerals in nature abundantly such as heazlewoodite (Ni_3S_2), pyrite (FeS_2), chalcocite (Cu_2S) etc. In addition to this, low-dimensional nanostructures of TMSs have also drawn much attention because of their great potential applications in gas sensors, solar cells, nanothermometers, LEDs, fuel cells, lithium-ion batteries and piezoelectric nanogenerators [2, 3]. Their synthesis has also gain importance due to their fundamental roles in interpreting the quantum size effect. For device applications, one-dimensional nanostructures grown on substrates are highly demanding. Due to the fact that electrons of TMSs are in the partially filled d-subshells, their nanostructures are very interesting for studying the magnetic properties.

By different types of physical or chemical methods, TMS nanostructures have been synthesized like physical vapor deposition (PVD), solution-phase reactions, hydrothermal growth, chemical vapor deposition (CVD), high-pressure autoclave processes and arc discharge method. At lower temperature, high-pressure autoclave processes are used

commonly to synthesize TMS nanostructures without using any catalysts. It helps in overcoming the high interfacial energy between liquid, substrate and particle. Nowadays, biomolecule-assisted synthesis routes are also a promising method for producing metal sulphide nanomaterials as they have fascinating self-assembling functions and special structures [4].

1.4. NICKEL SULPHIDE:

Nickel sulphide is an inorganic compound. Its chemical formula is NiS and IUPAC name is sulfanylidenenickel. NiS is an interesting material as it shows metal-insulator transition either by doping or as a function of pressure and temperature. It is a black solid that is produced by treating nickel (II) salts with hydrogen sulphide. Nickel sulphide has been widely studied because of its boundless applications in lithium-ion batteries, dye-sensitized solar cells, ceramic toughenners and semiconductors. It also possesses interesting property in water splitting fields. This is due to its low cost, ease of fabrication, low toxicity and high electronic conduction. The synthesis technique of NiS is very simple and does not employ vigorous control of different parameters. The major advantage of NiS is that its most of the phases can be synthesized at low temperature easily. There are a large number of nickel rich and sulphur rich phases at low temperature. Its unique electromagnetic property which involves a first-order phase transition from anti-ferromagnetic semiconductor (low-temperature) to paramagnetic metal (high-temperature) has attracted considerable attention in many fields [5]. Its catalytic applications in hydrodenitrogenation and hydrodesulfurization processes give potential interest in the study of nickel sulphide. NiS also has considerable research attention in semiconductor application because it is an active energy storage material that can achieve high theoretical capacitance and multiple redox reactions. The physical properties of NiS are described in the table 1.1:

Table 1.1. *Physical properties of NiS.*

Property	Value	
Molecular weight	90.7584 g mol^{-1}	
Density	5.87 g cm^{-3}	
Melting point	797 ˚C	
Appearance	Black powder	
Odor	Odorless	
Solubility	Insoluble in water	Soluble in nitric acid
Band gap	1.92-2.41 eV	
Magnetic susceptibility	$+190.0\times10^{-6}$ cm^3 mol^{-1}	

Among the series of sulphides of nickel, Ni_3S_2 is the most nickel-rich member [6]. Ni_3S_2 is the heazlewoodite phase of nickel sulfide (NiS). Since, in nature, Ni_3S_2 exists as minerals such as heazlewoodite which is very cheap and available in large quantities. Its appearance is crystalline solid having density 5.8 g cm^{-3}. It is insoluble in water. Ni_3S_2 exhibits good metallic property [7]. Due to this metallic property, Ni_3S_2 materials are endowed with distinguishable electrical conductivity and electrochemical performance. Ni_3S_2 has many applications in the field of photocatalytic hydrogen evolution [8], non-enzymatic glucose detection [9], Li-ion batteries [10], dye-sensitized solar cells [11] etc. due to its abundant valence and metal-like fast electronic transfer. Ni_3S_2 also serve as good electrode materials for supercapacitor [12] as it has high specific capacitance. Because of its low cost, good catalytic activity and simple preparation method, nickel sulphides (NiS, NiS_2, Ni_3S_2 etc.) serve as an excellent electrocatalysts for hydrogen evolution reaction (HER) [13-16]. Due to existence of valence electrons in two shells, transition metals can easily supply or hold electrons during the HER by undergoing oxidation or reduction. Doping of transition

elements like Mo, Co etc. in these transition metal sulphides like Ni_3S_2 increases its electrochemical performance by creation of abundant Mo-S or Co-S interface sites [17, 18]. In the following sections, the crystal structure; optical, electrical and electrochemical properties of nickel sulphide are discussed.

1.4.1. Crystal Structure: Nickel sulfide adopts the nickel arsenide motif i.e. nickel is octahedral and the sulfide centers are in trigonal prismatic sites (Fig. 1.1). NiS has two phases- α and β. The crystal structure of NiS in α-phase is hexagonal and β-phase is rhombohedral. At temperatures above 379 °C, the α-phase is stable i.e. forms a hexagonal structure and at lower temperatures, it converts into the β-phase i.e. forms a rhombohedral structure called millerite. The lattice parameters of α-NiS are a = 3.4392 Å, c = 5.3484 Å and of β-NiS are a = 9.621 Å and b = 3.159 Å. The α-phase belongs to the space group $P6_3/mmc$ and β-phase belongs to the space group R3m [19]. At a temperature of about -8 °C, α-NiS undergoes a phase transition from an anti-ferromagnetic semiconductor to paramagnetic metal. β-NiS has highly conducting metallic properties; this is because in millerite NiS, the Ni-S bond length is 2.25 Å which is relatively shorter than that of α-NiS (2.39 Å).

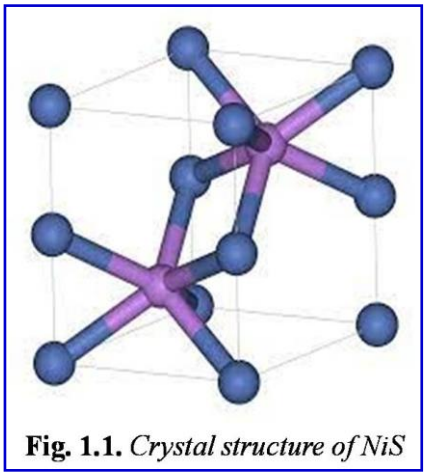

Fig. 1.1. *Crystal structure of NiS*

The crystal structure of Ni_3S_2 is rhombohedral (Fig. 1.2). It belongs to the space group R32 having lattice constants a_r = 4.071 Å, α_r = 89.459° and Z = 1 [20]. Heazlewoodite comprises of a series of triangular bipyramids with a Ni_3-triangle and S atoms situated at the apex.

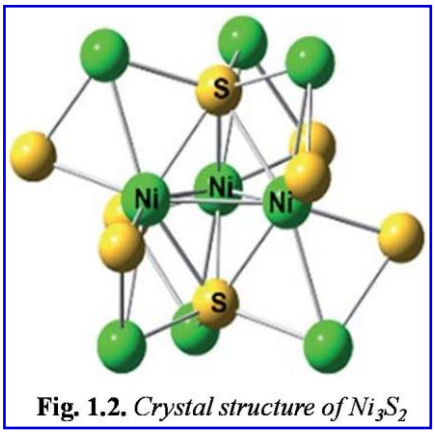

Fig. 1.2. *Crystal structure of Ni_3S_2*

In crystal structure, these Ni_3S_2 units are interrelated through short Ni-Ni and Ni-S bonds. The distance between these bonds within the Ni_3S_2 unit is greater than the distance between the bipyramids. Within Ni_3S_2 unit, the Ni-Ni and Ni-S distances are 2.5319 Å and 2.2914 Å whereas these distances between the bipyramids are 2.4966 Å and 2.2534 Å respectively [21].

Ni_3S_2 endows an intrinsic metallic property due to the short Ni-Ni and Ni-S bridge bonds in connecting crystal units which is further confirmed by its electronic band structure and electronic density of state crossing the Fermi level. In heazlewoodite, each nickel atom occupies a pseudo-tetrahedral site in the cubic sulphur lattice which is nearly body-centred. Also, four nickel atoms are co-ordinated to four sulphur atoms at a distance ~ 0.25 nm [22]. Ni_3S_2 changes into $Ni_{3+x}S$ with an fcc crystal structure at temperatures above 556 ˚C [23].

1.4.2. Electrical Properties: NiS exhibits p-type conductivity for which it receives increasing attention for scientific research [24]. β-phase of NiS delivers superior electrical conductivity due to its metallic character which enhances efficient electron or ion transport in the electrode. Due to high electrical conductivity of NiS, it shows preferable specific capacitance and cycling stability suggesting a potential application for supercapacitors. The electrical conductivity decreases with the temperature and it reflects the metallic behaviour of NiS. As reported by Boughalmi et. al. [25], the electrical conductivity of NiS thin film deposited on the glass substrate is 4.4×10^2 S cm^{-1} at 24 ˚C temperature and the electron mobility in layer is $\mu = 0.6$ cm^2 V^{-1} s^{-1}.

Ni_3S_2 has an excellent electrical conductivity which helps in facilitating electron transfer during electrochemical process. Ni_3S_2 has very high electrical conductivity i.e. 1.8×10^{-5} S cm^{-1} at ambient temperature [26] which is favourable for fast charge transfer. Yagi et. al. reported that with the increase of mole fraction of sulphur, the electrical conductivity

increased [27]. Also, due to this high conductivity property of Ni_3S_2, binary metal oxide grown on 1D Ni_3S_2 nanostructure could provide reliable electrical contact between the two and shows good cycling stability in supercapacitors [28]. So, it is a very useful support material for developing core-shell structure. Ni_3S_2 have tremendous potential for energy storage devices [29, 30] because of this better conductivity.

Ni_3S_2 exhibits n-type conductivity which endows it widespread applications in many fields because of its band gap 2.5 eV and high conductivity.

1.4.3. Optical Properties: The optical band gap of NiS generally varies between 1.92-2.41 eV [31]. Due to this optical band gap, the material becomes suitable to be used as a UV filter i.e. for making devices for good absorption of UV radiation. At λ = 800 nm, the refractive index of NiS film is found to be 1.82, this makes it suitable for use in optoelectronic devices.

In addition to the optical band gap, the photoluminescence (PL) property of NiS is also very much important for the experimenters in this field. Especially, the normal and defect induced behaviour of photoluminescence has always been an interesting topic for research. Excitation by different wavelengths affects different regions of the sample because the energy of the incident radiation strongly governs the adsorption behaviour. The synthesis parameters and several doping of other elements also affect the PL of NiS. The PL spectrum of pure NiS show peaks around 400 nm which is due to defect energy levels transitions. As reported by Linganiso et. al., NiS nanostructures decorated with Au enhances the emission of the NiS material in both UV and near IR regions with a slight blue shift in the positions of the peak [32]. Also, the excitation intensity of the PL spectrum of NiS nanoparticles embedded in the sol-gel silica xerogel increases as compared to that of undoped sample but the excitation spectrum of both the samples are same [33].

Ni_3S_2 have received much attention in various fields due to its excellent optical properties. The semiconducting nature of Ni_3S_2 film is confirmed by its energy band gap which is ~ 2.5 eV [34]. Ni_3S_2 is a promising material as a visible light photocatalyst as its band gap responds to the visible light [35]. To produce a large no. of excitons, a photocatalyst should ideally show strong light-harvesting ability in terms of its optical property. Substantial absorption occurs around 430 nm in case of simple Ni_3S_2 nanosheets [36].

The photoluminescence (PL) property of Ni_3S_2 films is also very crucial for their various applications. The separation of excitons and the electron-hole pair recombination is illustrated by the PL emission spectra. In the PL emission spectrum, the characteristic peaks of Ni_3S_2 occur at 667, 720 and 741 nm and the electron-hole pairs of Ni_3S_2 have exciton binding energy around 0.32 eV as reported by Shaohui Guo and his team [36]. The separation efficiency of electron-hole pairs is improved in the case of Ni_3S_2/MoS_2 heterostructures as the overall intensity of the PL emission spectra decreases. Also, when Ni_3S_2/CdS hybrid structures are synthesized, the photoluminescence peak intensity is reduced. This indicates that Ni_3S_2 functions as electron collector and transporter to quench the PL of CdS [37].

The scattering property of Ni_3S_2 is also studied using Raman spectroscopy. Li et. al. reported that the Raman peaks of Ni_3S_2 appears at 202, 304, 350 cm^{-1} which matches well with the literature [38].

1.4.4. Electrochemical Properties: Due to various valence states of NiS and being an inexpensive material, it has superior electrochemical properties. Among all the different phases and compositions of NiS, Ni_3S_2 is a promising electrode material for supercapacitors and good electrochemical performance due to its excellent intrinsic properties. Due to metallic property of Ni_3S_2, all the active sites easily facilitate transfer of electrons coming from the electrode.

Infact, 3D-Ni_3S_2 nanosheets array having porous structure shows excellent electrochemical performance as it has large surface area and enhanced kinetics. It also adequately facilitates the electrolyte accessible to the electroactive sites and the ion diffusion pathway is shortened [39]. But during charging-discharging process, the low rate and inferior capacity retention of Ni_3S_2 hinders practical application of supercapacitors in large scale. So, to overcome these limitations, the structural tuning and atomic substitution or doping was done such as Ni_3S_2 on CNT [40], vanadium-doped Ni_3S_2 nanowire [41], Cu-doped Ni_3S_2 nanosheet/rod nanoarray [42], Ni_3S_2 nanotube array [43] etc. Doping enhances intrinsic electronic conductivity and electrochemical performance by introducing defect energy levels near Fermi level. It contributes to an elevated charge transfer efficiency and rate capability. The doping of metal atom can change density of charge states and band gap. So, a feasible approach to obtain better performance supercapacitor is proper metal ion dopant with a pure phase that can be controlled multi-dimensionally.

The supercapacitive properties become superior when the hierarchical nanostructures of Ni_3S_2 are grown with graphene, carbon nanotubes and ZnO [44-46]. As reported by K. Krishnamoorthy [47], Ni_3S_2 acts as a binder free electrode material without any conductive additive for supercapacitor applications when hierarchical Ni_3S_2 is grown on Ni-foam. At a current density of 5 mA cm^{-2}, higher specific capacitance of 1293 F g^{-1} with energy density of 44.89 W h kg^{-1} is obtained. It also has an excellent cycling stability. Also, a specific capacity of 545.6 C g^{-1} at 1 A g^{-1} is obtained when cadmium sulphide (CdS) is incorporated with Ni_3S_2. This performance is attributed to superior improvements in ion and electron transfer mechanisms [48]. After 5000 charge-discharge cycles, a capacity retention of 103 % is attained i.e. it shows excellent cycle life.

Among the three nickel sulphides: NiS, NiS_2 and Ni_3S_2, the highest hydrogen evolution reaction (HER) catalytic performance is obtained for Ni_3S_2. The main three factors

responsible for the highest HER activity of Ni_3S_2 is high conductivity, large surface area which is electrochemically active and unique surface chemistry. The kinetic process of catalytic reaction is determined by Tafel slope. Ni_3S_2 produces largest amount of H_2 than NiS_2 and NiS [49]. The table 1.2 below shows a comparative data of HER of some identical catalysts.

Table 1.2. *Comparative data of HER of some identical Ni_3S_2 catalyst*

Catalyst	Electrolyte	Scan rate (mV s^{-1})	Current density (mA cm^{-2})	Over potential (mV)	Tafel slope (mV dec^{-1})	Reference
Ni_3S_2/Ni foam **Ni_3S_2/Ni foil** **Ni_3S_2/GCE**	Neutral	5	10	220 230 329	108 118 -	[50]
Ni_3S_2/Ni foam **Ni_3S_2/GCE**	Basic	5	10	123 204	110 -	[50]
Ni_3S_2/AT-Ni foam **Ni_3S_2 /Ni foam** **AT-Ni foam** **Ni-foam**	Basic	2	10	200 300 - -	107 141 144 148	[51]
Ni_3S_2 NWs	Basic	1	10	199.2	106.1	[38]
Ni_3S_2 nanorods **Sn-doped Ni_3S_2**	Acidic	2	10	254 201	114 51	[52]
Ni_3S_2 nanorods **Sn-doped Ni_3S_2**	Basic	2	10	164 137	225 148	[52]
p-Ni_3S_2 **V-Ni_3S_2-NW**	Basic	1	20	232 203	155 112	[41]
MoS_2–Ni_3S_2/NF **Ni_3S_2/NF** **MoS_2/NF** **NF**	Basic	-	10	98 183 235 308	61 108 121 149	[53]

1.5. MOLYBDENUM DISULPHIDE (MoS_2):

Molybdenum disulphide (MoS_2) has been a very attractive transition metal sulfide for its applications in many fields such as lithium ion batteries, photodetectors, solar cells, field-

effect transistors (FETs), memory devices and electrocatalysts for HER. MoS_2 is an inorganic compound that belongs to a class of materials known as transition metal dichalcogenides (TMDCs). The chemical formula of these materials is MX_2, where, M denotes a transition metal atom of groups 4-12 in the periodic table and X is a group 16 chalcogen. It occurs in nature in the form of mineral known as molybdenite which is the principal ore for molybdenum. It appears as a silvery black solid in bulk form and has very good chemical and thermal stability. MoS_2 is similar to graphite in appearance and feel. Also, because of its low friction and robustness, it is an excellent dry lubricant. It has higher intrinsic fast ionic conductivity (than oxides) and higher theoretical capacity (than graphite). For potential device applications, MoS_2 was the next two-dimensional material to be investigated after graphene [54]. MoS_2 has a great advantage over graphene in several fields due to its direct band gap. The physical properties of MoS_2 are described in the following table 1.3:

Table 1.3. *Physical properties of MoS_2*

Property	Value	Reference
Molar mass	160.07 g mol^{-1}	[55]
Density	5.06 g cm^{-3}	[55]
Melting point	1185 ˚C	[56]
Solubility in water	Insoluble	[57]
Band gap	1.2 eV (indirect, bulk MoS_2) 1.8-1.9 eV (direct, monolayer MoS_2)	[58]
Bulk conductivity	2.09×10^{-4} S m^{-1}	[59]
Dielectric constant	~ 3.3	[60]
Young's modulus	238 GPa (bulk MoS_2) 270 ± 100 GPa (monolayer MoS_2)	[61]

Hollow MoS_2 nanoparticles exhibiting ultra-low friction also exhibits very promising tribological applications and wear properties maintaining certain preparation conditions [62]. As the width of the energy band gap of MoS_2 can be controlled through the number of layers, it is considered to be a good candidate in the field of electronics and optoelectronics [63]. Moreover, low temperature synthesis routes [64] have explored for this material which enables low production cost and better opportunity of fabrication of MoS_2 based composites without hampering the intrinsic properties of the counterparts. For organic synthesis, MoS_2 finds use as a hydrogenation catalyst [65]. Also, in electrochemical supercapacitor, MoS_2 nanostructure is a promising electrode material [66, 67].

1.5.1. Crystal Structure: MoS_2 has a hexagonal crystal structure (Fig. 1.3). The co-ordination geometry of MoS_2 is trigonal prismatic. It belongs to the crystal system D^4_{6h} and space group P63 having lattice constants a = 0.315 nm, c = 1.230 nm and Z =2 [68]. In the crystal structure of MoS_2 monolayer, the hexagonal plane of "Mo" atom is sandwiched between the upper and lower layers of "S" atom.

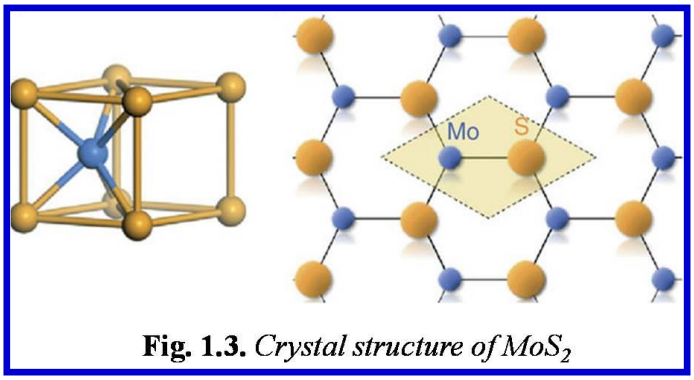

Fig. 1.3. *Crystal structure of MoS_2*

A strong covalent bond exists between molybdenum and sulphur atom and these triple layers are stacked on top of each other and form a monolayer of MoS_2. The stack of these monolayer forms bulk MoS_2 and are held together by weak Van der Waals interaction. Its sheet-like morphology provides large surface area for double layer charge storage.

The compounds of type MoX_2 (where, X = S, Se, Te) crystallize in the $2H_b$ structure whereas MoS_2 and $MoSe_2$ crystallizes in the 3R structure also [69]. Here, 'H' and 'R' indicates hexagonal and rhombohedral symmetry respectively. The common thing in both these structures is that each molybdenum atom exists at the centre of a trigonal prismatic coordination sphere and each Mo atom is bonded to six sulfide ions by covalent bond. Each sulphur atom is bonded to three molybdenum atoms and has a pyramidal coordination. Both the phases $2H_b$ and 3R are semiconducting. 2H is the thermodynamically stable phase of MoS_2. By intercalating 2H- MoS_2 with lithium metal, a third metastable crystalline phase of MoS_2 was found known as 1T-MoS_2 [70]. This phase is metallic showing higher electrical conductivity and catalytic activity and has tetragonal symmetry. Here, the coordination of Mo atoms becomes octahedral i.e. its polymorph is defined by a single S-Mo-S layer built from edge-sharing MoS_6 octahedra [71]. It is naturally found in monolayer. The space group of 1T-MoS_2 is $P\bar{3}m1$ with a unit cell having lattice constants a = b = 3.190(3) Å and c = 5.945(6) Å as indicated by the Rietveld-Refinement data [72].

In 2H MoS_2, the basal plane is inactive and the sulphur atoms located on the edge site are observed to be more conductive and hence, are responsible for catalytic activity. But in the metallic 1T phase, the whole basal plane is found to be catalytically active [73]. During room temperature aging or thermal annealing, the octahedral coordinated structure 1T gets transformed to trigonal prismatic coordinated structure 2H.

1.5.2. Electrical Properties: Among transition metal dichalcogenides, MoS_2 has excellent electrical characteristics because of its transparency in visible wavelength range, flexibility, mechanical stiffness and electrical carrier mobility. It exhibits n-type conductivity. Under S-rich growth conditions, the presence of hydrogen leads to the n-type conductivity in monolayer MoS_2 [74]. The conductivity of MoS_2 is about 2.09×10^{-4} S m^{-1}. Monolayer MoS_2

show high electrical performance when they are grown directly on insulating SiO_2 substrates. It shows electron mobility of 30 $cm^2 V^{-1} s^{-1}$ at room temperature and 114 $cm^2 V^{-1} s^{-1}$ at 90 K [75]. The undoped MoS_2 have n-type carriers as indicated by Hall measurement result. MoS_2 film deposited by CVD method using molybdenum trioxide and sulphur powder possesses excellent electrical characteristics [76]. Using semiconductor parameter analyzer, the transfer characteristics was studied and the n-type semiconductor behaviour is shown by MoS_2 with field-effect mobility (μ_{FE}) of 1.8 $cm^2 V^{-1} s^{-1}$ and at V_{DS} of 1 V, on/off ratio of over 10^4 is obtained. Radisavljevic et. al. [77] reported that top-gated transistors based on mechanically exfoliated single layer MoS_2 flakes exhibits mobility of ~ 200 $cm^2 V^{-1} s^{-1}$ and room-temperature current on/off ratio greater than 10^8. Such MoS_2 transistors that could be fabricated on insulating boron nitride substrates could form the backbone of future electronics.

1T-MoS_2 nanosheets show p-type conductivity and its electrical conductivity is 10^3 times higher than that of the 2H-MoS_2 single crystal [78]. The electrical conductive behaviour of the composite film of 2H-MoS_2 nanosheet/ 1T-MoS_2 nanosheet follows the classical behaviour observed for percolation in a random metal-dielectric composite. Also, the overall conductivity of the composite film and the concentration of the metallic 1T-phase MoS2 nanosheets are related non-linearly.

1.5.3. Optical Properties: As the width of the energy band gap of MoS_2 can be controlled through the number of layers, it is considered to be a promising candidate in the field of optics. The bulk form of MoS_2 is an indirect band gap semiconductor having band gap ~ 1.2 eV whereas monolayer MoS_2 is a direct band gap semiconductor having band gap ~ 1.8-1.9 eV [58, 76]. So, with increasing no. of layers of single-layer MoS_2, a direct band gap semiconductor is transformed into an indirect band gap. Due to direct band gap of single

layer MoS_2, it is being suitable acting as switching nanodevices. Zongyou Yin's group in 2012 fabricated the single-layer MoS_2-based phototransistor and the switching behaviour of this device was studied for the first time which is outstanding [79]. The photocurrent generation and annihilation behaviour is so instantaneous that it takes place only within 50 ms and it also has good stability. Under illumination with a low optical power of 80 μW and gate voltage of 50 V, the photoresponsivity is obtained as high as 7.5 mA W^{-1}. This is much higher than that obtained from graphene-based devices which explore its application in the field of optoelectronic device.

Another convenient optical characterization technique known as Raman spectroscopy is also popularly used for determining the number of layers of MoS_2. This is reflected by two typical Raman peaks E_{2g}^1 and A_{1g} which are indicators of in-plane and out-of-plane vibration modes of sulphur atoms respectively. Firstly, if E_{2g}^1 is located at ~ 384 cm^{-1} and A_{1g} at 405 cm^{-1}, it indicates that a single layer MoS_2 is formed. Secondly, the bulk and monolayer MoS_2 is determined by the peak frequency difference between E_{2g}^1 and A_{1g} i.e. if the frequency spacing is 25 cm^{-1}, it is bulk MoS_2 and if it is 19 cm^{-1}, it is monolayer MoS_2. Thirdly, up to four layers with increasing thickness of layer, the intensities of two peaks almost increase while for thicker MoS_2, it decreases [54]. In bulk MoS_2, due to local field effect, Raman signal is weak. Also, the number of layers in MoS_2 has a co-relation with PL spectra. With decreasing thickness of layers, photoluminescence (PL) of MoS_2 increases. In bulk form, luminescence behaviour is absent because at energies much larger than the indirect band gap, it has strong direct excitonic absorption. But in MoS_2 monolayer, these excitonic states remain at the same transition energies as in bulk but they become strongly luminescent. So, the monolayer of MoS_2 shows strongest luminescence behaviour [80]. In the spectrum of 1L MoS_2, two evident absorption peaks can be observed at 670 nm and 627 nm identified as A1 and B1 excitons. The Raman and photoluminescence intensities show opposite layer

dependence for ultrathin MoS_2 layers where local field effects are relatively small. Due to reduced amount of material, MoS_2 Raman signal is weakest in the monolayer MoS_2. But instead of this reduced amount of material, PL is strongest in monolayer MoS_2. So, compared to that in multilayer and bulk, the luminescence quantum efficiency is much higher in MoS_2 monolayer as indicated by this PL behaviour.

1.5.4. Field-emission properties: MoS_2 is an excellent field emitter due to availability of numerous thin free edges and atomically sharp edges in its nanostructure. A suitable combination of electronic and mechanical properties of MoS_2 makes it a good field emitter. At low onset voltage, its atomically sharp edges help in enhancing the electric field and it ultimately increases the tunnelling probability of electrons. Since the physical geometry provides a field enhancement near the emitting surface, electrons can be easily extracted from the cathode surface by applying a considerably lower electric field if it has sharp edges or protrusions. For the field emission intensity, the tip morphology and the pinnacle density are very crucial factors. The small radius of curvature of tips enable enhancement of the local electric field. The surface roughness of the MoS_2 nanostructure also plays an important role in enhancing the number of electron emission centres. The non-linear nature of F-N plot gives a direct consequence of the semiconducting nature of field emitter. It is due to the presence of surface states and inherently, in the conduction band, there is limited number of charge carriers. As reported by Li et. al. [81], elegant three-dimensional MoS_2 nanoflowers synthesized by heating a MoO_2 thin film in sulphur vapor atmosphere appeared to be excellent field emitters. Due to very thin open edges of petals and the quasi-aligned assembly of as-obtained nanostructure, a turn-on field (electric field required to produce a current of 10 $\mu A\ cm^{-2}$) of 4.5-5.5 V $(\mu m)^{-1}$ and threshold field (electric field required to produce a current of 10 $mA\ cm^{-2}$) of 7.6-8.6 V $(\mu m)^{-1}$ is obtained. Also, its good emission stability against a high current emission indicates its promising application as field emitters and in practical

flat-panel displays. A field emission study was reported for the first time on layered MoS_2 sheets by Kashid et. al. [82]. Here, the turn-on field for drawing a current density of 10 μA cm^{-2} is found to be 3.5 V $(\mu m)^{-1}$. Due to the presence of sharp protruding edges of MoS_2, high field enhancement factor (~1138) is attained which results in low turn-on field. Also, MoS_2@ZnO nano-heterojunctions [83], pulsed-laser deposited MoS_2 thin films grown on W-tip and Si-substrates [84], MoS_2 nanoflowers on copper foil [85] possesses enhanced field emission properties because of presence of more emission sites and decrease in potential barrier of energy.

1.6. ZINC SULPHIDE (ZnS):

Zinc Sulphide (ZnS) is an inorganic compound and the most important II-VI semiconductors. Its chemical formula is ZnS. Pure ZnS is transparent and white crystalline powder. It mainly occurs in the form of minerals sphalerite and wurtzite. They are wide band gap semiconductors. It is non-toxic and available in abundance in nature. ZnS is considered as a favourable host material because it is chemically much stable than its alternative chalcogenides. ZnS nanostructures have various applications in photonics, nanoelectronics, electro-luminescent devices, optoelectronics, solar cells and as tools in biomedical due to its electronic, optical, luminescent and mechanical properties. ZnS nanoparticles also include use in UV-light sensors, gas sensors, biosensors and Field Emitting Diodes. For the direct conversion of ethanol in fuel cells, ZnS nanoparticles can also been used as an electrocatalysts [86]. In environmental protection, they can be used as an important catalyst for removing organic and toxic water pollutants. Under visible irradiation, ZnS can be doped with Cu or Ni to modify the photocatalytic activity. In the following table 1.4, the physical properties of ZnS are mentioned.

Table 1.4. *Physical properties of ZnS*

Property	Value
Molecular weight	97.474 g mol^{-1}
Density	4.090 g cm^{-3}
Lattice Constant	5.4093 Å
Melting point	1850 ˚C
Appearance	White powder
Odor	Sulphurous odor
Solubility in water	Negligible
Dielectric constant	8.9
Band gap	(3.54 – 3.75) eV
Refractive index	2.3677
Poisson's ratio	0.27

1.6.1. Crystal Structure: ZnS is a polymorphous material and exists in two main crystalline forms, cubic and hexagonal. The cubic form is also known as Zinc blende or sphalerite and hexagonal form is known as Wurtzite. Among them, the cubic form is most stable. The co-ordination geometry at Zn and S is tetrahedral in both the forms. Zinc blende/sphalerite is based on face-centered cubic (fcc) crystal structure and wurtzite is based on hexagonal close packed (hcp) crystal structure. The no. of asymmetric units in the unit cell of sphalerite is four and wurtzite is two [87].

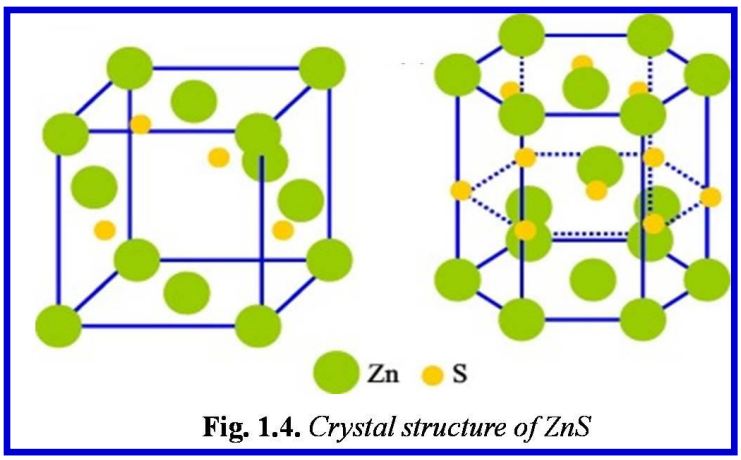

Fig. 1.4. *Crystal structure of ZnS*

At around 1020 ˚C, the transition from the sphalerite to the wurtzite form occurs. Depending upon the synthesis techniques and parameters, the crystal phase of ZnS may be cubic or hexagonal or a combination of both. β-ZnS i.e. sphalerite can be grown at relatively low temperature whereas α-ZnS i.e. wurtzite corresponds to a high temperature phase. Zinc blende and wurtzite belongs to the space group $F\bar{4}3m$ and $P6_3mc$ respectively [88, 89]. The lattice constant of Zinc blende is 5.420 Å and wurtzite are a = 3.82 Å, c = 6.26 Å. The degree of crystallinity of ZnS is also determined by several factors and the most important among them is the deposition temperature which on increasing gives better crystalline films. In case of obtaining better crystallinity of the thin films deposited physically, the ambient pressure should be optimized efficiently.

1.6.2. Electrical Properties: At room temperature, pure ZnS is generally highly resistive in nature. ZnS has n-type conductivity [90, 91]. However, Ni-doped ZnS thin films also shows n-type conductivity with lower doping levels but on increasing the doping concentration, it becomes p-type semiconductor [91]. The electrical conductivity of ZnS films is of the order of 10^{-9} S cm^{-1} [92]. ZnS nanoparticles have smaller electrical conductivity by one order of magnitude as compared to ZnS films; it may be because of size and dimension of the confinement. In low temperature region, the conductivity increases slowly and in high temperature region, it increases abruptly. ZnS also exhibits effective photoconductivity characteristics.

1.6.3. Optical Properties: ZnS due to its wide direct band gap exhibits a large optical transparency from UV (ultraviolet) to IR (infrared) region. The band gap of zinc blende and wurtzite structures are approximately 3.54 eV and 3.91 eV respectively [87]. ZnS is one of the most widely used materials in heterojunction photovoltaic solar cells as a window layer when the optical transparency property is combined with chemical and thermal stability. The

band gap of ZnS film decreases with increasing temperature because of the increased particle size which in turn decreases the quantum confinement [90]. ZnS is also well-known for its normal and defect induced photoluminescence behavior. Different excitation wavelengths produces different PL spectrum of the sample. Under same UV excitation, ZnS exhibits blue emission and on doping, the emission changes. As reported, ZnS nanoparticles show blue emission peaked at 465 nm and Mn^{2+} doped ZnS sample shows peak at 574 nm indicating efficient emission of yellow colour light [93]. This happens because in between the conduction band and valence band, energy levels are produced by doping of Mn^{2+} in ZnS. Also, undoped ZnS quantum particles excited by wavelength of 326 nm shows blue emission at ~ 424 nm and due to copper induced levels, the emission changes to green at ~ 480 nm [94]. This change in emission colour occurs due to the transition from conduction band of ZnS to the level t_2 of excited Cu^{2+} (d^9) in the ZnS band gap. So, doping of different elements in ZnS sample effects its optical properties which make it a highly efficient luminescent material.

1.6.4. Cathodoluminescence Properties: ZnS being a direct wide band gap semiconductor, is one of the most important nanostructure being explored in the optoelectronic field with prominent applications in sensors, flat-panel displays and lasers. The size, shape and local dielectric environment of a material determines its optoelectronic properties. ZnS nanostructures show strong cathodoluminescence (CL) spectroscopy in the near-UV to green region of the electromagnetic spectrum. In the following table 1.5, a comparative data of CL spectroscopy of ZnS and its composite nanostructures is given.

Table 1.5. *Comparative data of cathodoluminescence property of some identical ZnS nanostructures*

ZnS sample	Wavelength	Emission type	Reference
ZnS single crystals	465 nm	Blue and green emission	[95]
Mn-doped ZnS nanoparticles	582 nm	Yellow emission	[96]
ZnS tetrapod tree-like heterostructures	Peak I - 336 nm for ZB phase Peak II- 323 nm for WZ phase	Strong intrinsic emission	[97]
ZnS hexagonal pyramids	337 nm for ZB phase	Strong intrinsic emission	[98]
ZnS nanowires on Si-substrate	~ 449 nm and 581 nm	Blue emission	[99]
ZnS nanostructures (particle size 2-3 nm)	~ 450 nm	Blue emission	[100]
$(ZnS).(Ag_2S)_{0.025}$ (heteronanostructures)	~ 600 nm	-	[100]

1.7. OBJECTIVES OF THE THESIS:

The major objectives of the thesis are as follows:

- Development of some novel synthesis routes for the technologically important metal chalcogenide nanostructures with greater control for generating tailored nanostructures of such materials.
- To carry out detailed structural, morphological, optical and other relevant characterizations of the developed nanomaterials.
- To study the potential of applications of the developed nanomaterials in different exotic fields; such as application of Ni_3S_2 nanostructures for water splitting.
- To develop a novel and more effective seeded hydrothermal growth route for ZnS nanostructures. ZnS is a material which is used for display application. Hence, we

wanted to study the cathodoluminescence performance of the developed ZnS nanostructures also.

- To study the effect of morphological variation of MoS_2 nanostructures on the electron field emission performance. Both experimental and simulation investigations are to be carried out.

- To correlate the different results to develop meaningful information about the properties of such nanomaterials and their technological applications.

Organization of the thesis:

The thesis contains 8 self-sufficient chapters. A very brief sketch of the different chapters is presented below:

➢ Chapter 1: Introduction

At first, a brief introduction about transition metals and transition metal sulphides is mentioned. Then, a detailed study of structural, optical, electrical and related properties of the as-synthesized transition metal sulphides (NiS, Ni_3S_2, MoS_2, ZnS) is given. Lastly, the objectives of the thesis are clearly mentioned.

➢ Chapter 2: Review of Past Work

The summary of previous works on synthesis methods and applications of transition metal sulphides are described in the different sections of this chapter. An exhaustive literature review on the photocatalytic activity of NiS, electrochemical properties of Ni_3S_2, cathodoluminescence of ZnS, and field emission property of MoS_2 are addressed in this chapter.

- **Chapter 3: Instruments and Apparatus**

This chapter covers the details of the characterization tools used for studying the crystal structure, morphology and applications of transition metal sulphides. A brief description of synthesis procedures of nanomaterials and major synthesis apparatus is discussed. The instrumentations that were used during the execution of the work i.e. X-Ray Diffractometer, Field Emission Scanning Electron Microscope (FESEM), Transmission Electron Microscope (TEM), X-Ray Photoelectron Spectroscopy (XPS), Autolab PGSTAT for electrochemical measurement etc. are summarized in this chapter. Also, finite element based simulation (ANSYS) carried out in order to identify the potential field emission behaviour of MoS_2 is described in the last section.

- **Chapter 4: Work 1**

In this chapter, work on "Co incorporated Ni_3S_2 hierarchical nano/micro cactus for electrochemical water splitting" is illustrated.

- **Chapter 5: Work 2**

This chapter demonstrates the "Cathodoluminescence from ZnS thin films deposited by novel seeded hydrothermal route".

- **Chapter 6: Work 3**

Chapter 6 describes work on "Hierarchical nickel sulphide microstructures for controlled water disinfection and cold cathode emission".

- **Chapter 7: Work 4**

Chalcogenide beyond photovoltaics: Field emission from morphology tailored nanostructured molybdenum sulphide.

- **Chapter 8: Grand Conclusion and Scope for future work**

Finally, at the end, this chapter addresses a brief summary of the thesis in nutshell and scopes of future work.

1.8. References:

[1] N.T. Suen, S.F. Hung, Q. Quan, N. Zhang, Y.J. Xu, H.M. Chen, *Chem. Soc. Rev.* 46 (2017) 337– 365.

[2] H.K. Mulmudi, S.K. Batabyal, M. Rao, R.R. Prabhakar, N. Mathews, Y.M. Lam, S.G. Mhaisalkar, *Phys. Chem. Chem. Phys.* 13 (2011) 19307-19309.

[3] N. Higashitarumizu, H. Kawamoto, K. Ueno, K. Nagashio, *MRS Adv.* 3 (2018) 2809-2814.

[4] B. Zhang, X. Ye, W. Dai, W. Hou, Y. Xie, *Chem. Eur. J.* 12 (2006) 2337-2342.

[5] Q. Pan, K. Huang, S. Ni, F. Yang, D. He, *Mater. Res. Bull.* 43 (2008) 1440-1447.

[6] J. Dong, F.Q. Zhang, Y. Yang, Y.B. Zhang, H. He, X. Huang, X. Fan, X.M. Zhang, *Appl. Catal. B: Environ.* 243 (2019) 693-702.

[7] X. Zheng, X. Han, Y. Zhang, J. Wang, C. Zhong, Y. Deng, W. Hu, *Nanoscale* 11 (2019) 5646-5654.

[8] M. Tong, L. Wang, P. Yu, C. Tian, X. Liu, W. Zhou, H. Fu, *ACS Sustainable Chem. Eng.* 6 (2018) 2474-2481.

[9] F. Luan, S. Zhang, D. Chen, F. Wei, X. Zhuang, *Microchem. Journal* 143 (2018) 450-456.

[10] W. Duan, W. Yan, X. Yan, H. Munakata, Y. Jin, K. Kanamura, *J. Pow. Sour.* 293 (2015) 706-711.

[11] W. Maiaugree, A. Tangtrakarn, S. Lowpa, N. Ratchapolthavisin, V. Amornkitbamrung, *Electrochimica Acta* 174 (2015) 955-962.

[12] J.S. Chen, C. Guan, Y. Gui, D.J. Blackwood, *ACS Appl. Mater. Interfaces* 9 (2017) 496-504.

[13] W. Zhu, X. Yue, W. Zhang, S. Yu, Y. Zhang, J. Wang, J. Wang, *Chem. Comm.* 52 (2016) 1486-1489.

[14] Y. Liang, Y. Yang, K. Xu, T. Yu, S. Yao, Q. Peng, C. Yuan, *Journal of Catal.* 381 (2020) 63-69.

[15] P. Liu, J. Li, Y. Lu, B. Xiang, *Int. J. Hydrogen Energy* 43 (2018) 72-77.

[16] S. Hao, J. Liu, Q. Cao, Y. Zhao, X. Zhao, K. Pei, J. Zhang, G. Chen, R. Che, *Journal of Colloid and Interface Sci.* 559 (2020) 282-290.

[17] Z. Cui, Y. Ge, H. Chu, R. Baines, P. Dong, J. Tang, Y. Yang, P.M. Ajayan, M. Ye, J. Shen, *J. Mater. Chem. A* 5 (2017) 1595-1602.

[18] R. Khan, M. Samanta, S. Ghosh, N.S. Das, K.K. Chattopadhyay, *Int. J. Hydrogen Energy* 44 (2019) 21315-21323.

[19] C. Buchmaier, M. Glänzer, A. Torvisco, P. Poelt, K. Wewerka, B. Kunert, K. Gatterer, G. Trimmel, T. Rath, *J. Mater. Sci.* 52 (2017) 10898-10914.

[20] P.A. Metcalf, P. Fanwick, Z. Kakol, J.M. Honig, *J. Solid State Chem.* 104 (1993) 81-87.

[21] J.B. Parise, *Acta Crystallographica Section B: Structural Crystallography and Cryst. Chem.* 36 (1980) 1179-1180.

[22] A.N. Buckley, R. Woods, *J. Appl. Electrochemistry* 21 (1991) 575-582.

[23] C. Gervas, S. Mlowe, M.P. Akerman, I. Ezekiel, T. Moyo, N. Revaprasadu, *Polyhedron* 122 (2017) 16-24.

[24] C.V.V.M. Gopi, S.S. Rao, S.K. Kim, D. Punnoose, H.J. Kim, *J. Power Sources* 275 (2015) 547-556.

[25] R. Boughalmi, R. Rahmani, A. Boukhachem, B. Amrani, K.D. Khodja, M. Amlouk, *Mater. Chem. Phys.* 163 (2015) 99-106.

[26] J.J. Li, Y.X. Hu, M.C. Liu, L.B. Kong, Y.M. Hu, W. Han, Y.C. Luo, L. Kang, *J. Alloys Comp.* 656 (2016) 138-145.

[27] H. Yagi, J.B. Wagner, *Oxidation of Metals* 18 (1982) 41-54.

[28] F. Chen, S. Ji, Q. Liu, H. Wang, H. Liu, D.J.L. Brett, G. Wang, R. Wang, *Small* 14 (2018) 1800791.

[29] M.C. Liu, J. Li, Q.Q. Yang, Y. Xu, L.B. Kong, R.J. Bai, W.W. Liu, W.J. Niu, Y.L. Chueh, *ACS Appl. Nano Mater.* 2 (2019) 2634-2641.

[30] K. Cui, J. Fan, S. Li, M.F. Khadidja, J. Wu, M. Wang, J. Lai, H. Jin, W. Luo, Z. Chao, *Nanoscale Adv.* 2 (2020) 478-488.

[31] A. Molla, M. Sahu, S. Hussain, *Scientific Rep.* 6 (2016) 1-11.

[32] E.C. Linganiso, B.W. Mwakikunga, S.D. Mhlanga, N.J. Coville, *J. Lumin.* 155 (2014) 305-310.

[33] P. Yang, M. Lü, C.F. Song, G. Zhou, D. Xu, D.R. Yuan, *J. Phys. Chem. Solids* 63 (2002) 2047-2051.

[34] H. He, A. Chen, H. Lv, H. Dong, M . Chang, C. Li, *J. Alloys Comp.* 574 (2013) 217-220.

[35] P. Hu, X. Liu, B. Liu, L. Li, W. Qin, H. Yu, S. Zhong, Y. Li, Z. Ren, M. Wang, *J. Colloid Interface Sci.* 496 (2017) 254-260.

[36] S. Guo, L. Yang, Y. Zhang, Z. Huang, X. Ren, W.E.I. Sha, X. Li, *J. Alloys Comp.* 749 (2018) 473-480.

[37] Z. Li, X. Chen, W. Shangguan, Y. Su, Y. Liu, X. Dong, P. Sharma, Y. Zhang, *Int. J. Hydrogen Energy* 42 (2017) 6618-6626.

[38] J. Li, P.K. Shen, Z. Tian, *Int. J. Hydrogen Energy* 42 (2017) 7136-7142.

[39] Y.L. Wang, X.Q. Wei, M.B. Li, P.Y. Hou, X.J. Xu, *Appl. Surface Sci.* 436 (2018) 42-49.

[40] T. Zhu, H.B. Wu, Y. Wang, R. Xu, X.W. (David) Lou, *Adv. Energy Mater.* 2 (2012) 1497-1502.

[41] Y. Qu, M. Yang, J. Chai, Z. Tang, M. Shao, C.T. Kwok, M. Yang, Z. Wang, D. Chua, S. Wang, Z. Lu, H. Pan, *ACS Appl. Mater. Interfaces* 9 (2017) 5959-5967.

[42] G. Li, X. Cui, B. Song, H. Ouyang, K. Wang, Y. Sun, Y. Wang, *Chem. Engineering Journal* 388 (2020) 124319.

[43] D. Li, X. Li, X. Hou, X. Sun, B. Liu, D. He, *Chem. Commun.* 50 (2014) 9361-9364.

[44] W. Zhou, X. Cao, Z. Zeng, W. Shi, Y. Zhu, Q. Yan, H. Liu, J. Wang, H. Zhang, *Energy Environ. Sci.* 6 (2013) 2216–2221.

[45] C.S. Dai, P.Y. Chien, J.Y. Lin, S.W. Chou, W.K. Wu, P.H. Li, K.Y. Wu, T.W. Lin, *ACS Appl. Mater. Interf.* 5 (2013) 12168–12174.

[46] Z. Xing, Q. Chu, X. Ren, C. Ge, A.H. Qusti, A.M. Asiri, A.O. Al-Youbi, X. Sun, *J. Power Sources* 245 (2014) 463–467.

[47] K. Krishnamoorthy, G.K. Veerasubramani, S. Radhakrishnan, S.J. Kim, *Chem. Engineering Journal* 251 (2014) 116-122.

[48] B. Safdar, J.A. Rajesh, S.H. Kang, H. Kim, K.S. Ahn, *J. Alloys Comp.* 826 (2020) 154211.

[49] N. Jiang, Q. Tang, M. Sheng, B. You, De-en Jiang, Y. Sun, *Catal. Sci. Technol.* 6 (2016) 1077-1084.

[50] C. Tang, Z. Pu, Q. Liu, A.M. Asiri, Y. Luo, X. Sun, *Int. J. Hydrogen Energy* 40 (2015) 4727-4732.

[51] C. Ouyang, X. Wang, C. Wang, X. Zhang, J. Wu, Z. Ma, S. Dou, S. Wang, *Electrochimica Acta* 174 (2015) 297-301.

[52] J. Yu, F.X. Ma, Y. Du, P.P. Wang, C.Y. Xu, L. Zhen, *ChemElectroChem* 4 (2017) 594-600.

[53] Y. Yang, K. Zhang, H. Lin, X. Li, H.C. Chan, L. Yang, Q. Gao, *ACS Catal.* 7 (2017) 2357-2366.

[54] X. Li, H. Zhu, *Journal of Materiomics* 1 (2015) 33-44.

[55] C.P. Koshy, P.K. Rajendrakumar, M.V. Thottackkad, *Wear* 330 (2015) 288-308.

[56] X. Li, L. Chen, H. Liu, C. Shi, D. Wang, Z. Mi, L. Qiao, *Nanomaterials* 9 (2019) 382.

[57] Z. Wang, A. von dem Bussche, Y. Qiu, T.M. Valentin, K. Gion, A.B. Kane, R.H. Hurt, *Environmental Sci. & Technol.* 50 (2016) 7208-7217.

[58] F. Urban, M. Passacantando, F. Giubileo, L. Iemmo, A.D. Bartolomeo, *Nanomaterials* 8 (2018) 151.

[59] L.M. Wang, *J. Appl. Electrochem.* 38 (2008) 245-249.

[60] H. Liu, M. Si, Y. Deng, A.T. Neal, Y. Du, S. Najmaei, P.M. Ajayan, J. Lou, P.D. Ye, *ACS Nano* 8 (2014) 1031-1038.

[61] S. Bertolazzi, J. Brivio, A. Kis, *ACS Nano* 5 (2011) 9703-9709.

[62] M. Chhowalla, G.A.J. Amaratunga, *Nature* 407 (2000) 164-167.

[63] K.F. Mak, C. Lee, J. Hone, J. Shan, T.F. Heinz, *Phys. Rev. Lett.* 105 (2010) 136805.

[64] D. Wang, Z. Pan, Z. Wu, Z. Wang, Z. Liu, *J. Power Sources* 264 (2014) 229-234.

[65] B.K. Miremadi, S.R. Morrison, *J. Catal.* 103 (1987) 334-345.

[66] X. Zhou, B. Xu, Z. Lin, D. Shu, L. Ma, *J. Nanosci. Nanotechnol.* 14 (2014) 7250-7254.

[67] M. Acerce, D. Voiry, M. Chhowalla, *Nature Nanotechnol.* 10 (2015) 313-318.

[68] D. Liu, X. Chen, D. Li, F. Wang, X. Luo, B. Yang, *J. Mol. Struc.* 980 (2010) 66-71.

[69] Th. Böker, R. Severin, A. Müller, C. Janowitz, R. Manzke, D. Voß, P. Krüger, A. Mazur, J. Pollmann, *Phys. Rev. B* 64 (2001) 235305.

[70] G. Eda, H. Yamaguchi, D. Voiry, T. Fujita, M. Chen, M. Chhowalla, *Nano Lett.* 11 (2011) 5111-5116.

[71] M.A. Lukowski, A.S. Daniel, F. Meng, A. Forticaux, L. Li, S. Jin, *J. Am. Chem. Soc.* 135 (2013) 10274-10277.

[72] W. Zhao, J. Pan, Y. Fang, X. Che, D. Wang, K. Bu, F. Huang, *Chemistry–A European Journal* 24 (2018) 15942-15954.

[73] Y. Guo, D. Sun, B. Ouyang, A. Raja, J. Song, T.F. Heinz, and L.E. Brus, *Nano Lett.* 15 (2015) 5081-5088.

[74] A. Singh, A.K. Singh, *Phys. Rev. B* 99 (2019) 121201.

[75] K. Kang, S. Xie, L. Huang, Y. Han, P.Y. Huang, K.F. Mak, C.J. Kim, D. Muller, J. Park, *Nature* 520 (2015) 656-660.

[76] T.Y. Kim, M. Amani, G.H. Ahn, Y. Song, A. Javey, S. Chung, T. Lee, *ACS Nano* 10 (2016) 2819-2826.

[77] B. Radisavljevic, A. Radenovic, J. Brivio, V. Giacometti, A. Kis, *Nature Nanotechnol.* 6 (2011) 147-150.

[78] H. Huang, Y. Cui, Q. Li, C. Dun, W. Zhou, W. Huang, L. Chen, C.A. Hewitt, D.L. Carroll, *Nano Energy* 26 (2016) 172-179.

[79] Z. Yin, H. Li, H. Li, L. Jiang, Y. Shi, Y. Sun, G. Lu, Q. Zhang, X. Chen, H. Zhang, *ACS Nano* 6 (2012) 74-80.

[80] A. Splendiani, L. Sun, Y. Zhang, T. Li, J. Kim, C.Y. Chim, G. Galli, F. Wang, *Nano Lett.* 10 (2010) 1271-1275.

[81] Y.B. Li, Y. Bando, and D. Golberg, *Appl. Phys. Lett.* 82 (2003) 1962-1964.

[82] R.V. Kashid, D.J. Late, S.S. Chou, Y.K. Huang, M. De, D.S. Joag, M.A. More, V.P. Dravid, *Small* 9 (2013) 2730-2734.

[83] Y.H. Tan, K. Yu, J.Z. Li, H. Fu, Z.Q. Zhu, *J. Appl. Phys.* 116 (2014) 064305.

[84] D.J. Late, P.A. Shaikh, R. Khare, R.V. Kashid, M. Chaudhary, M.A. More, S.B. Ogale, *ACS Appl. Mater. Interfaces* 6 (2014) 15881-15888.

[85] F. Giubileo, A. Grillo, M. Passacantando, F. Urban, L. Iemmo, G. Luongo, A. Pelella, M. Loveridge, L. Lozzi, A.D. Bartolomeo, *Nanomaterials* 9 (2019) 717.

[86] M. Bredol, M. Kaczmarek, H.D. Wiemhöfer, *J. Power Sources* 255 (2014) 260-265.

[87] N. Kaur, S. Kaur, J. Singh, M. Rawat, *J Bioelectron Nanotechnol* 1 (2016) 1-5.

[88] M. Dong, J. Zhang, J. Yu, *APL Materials* 3 (2015) 104404.

[89] E. Omurzak, T. Mashimo, S. Sulaimankulova, S. Takebe, L. Chen, Z. Abdullaeva, C. Iwamoto, Y. Oishi, H. Ihara, H. Okudera, A. Yoshiasa, *Nanotechnol.* 22 (2011) 365602.

[90] H.M.M.N. Hennayaka, H.S. Lee, *Thin Solid Films* 548 (2013) 86-90.

[91] C.M. Huang, L.C. Chen, G.T. Pan, T.C.K. Yang, W.S. Chang, K.W. Cheng, *Mater. Chem. Phys.* 117 (2009) 156-162.

[92] F. Göde, *Physica B: Condensed Matter* 406 (2011) 1653-1659.

[93] C.S. Pathak, M.K. Mandal, *Chalcogenide Lett.* 8 (2011) 147-153.

[94] A.A. Khosravi, M. Kundu, L. Jatwa, S.K. Deshpande, U.A. Bhagwat, *Appl. Phys. Lett.* 67 (1995) 2702-2704.

[95] S. Oda, K. Akagi, H. Kukimoto, T. Nakayama, *J. Lumin.* 16 (1978) 323-330.

[96] A.D. Dinsmore, D.S. Hsu, H.F. Gray, S.B. Qadri, Y. Tian, B.R. Ratna, *Appl. Phys. Lett.* 75 (1999) 802-804.

[97] Z.G. Chen, J. Zou, G. Liu, X. Yao, F. Li, X.L. Yuan, T. Sekiguchi, G.Q. Lu, H.M. Cheng, *Adv. Funct. Mater.* 18 (2008) 3063-3069.

[98] Z.G. Chen, J. Zou, D.W. Wang, L.C. Yin, G. Liu, Q. Liu, C.H. Sun, X. Yao, F. Li, X.L. Yuan, T. Sekiguchi, G.Q. Lu, H.M. Cheng, *Adv. Funct. Mater.* 19 (2009) 484-490.

[99] M.W. Huang, Y.W. Cheng, K.Y. Pan, C.C. Chang, F.S. Shieu, H.C. Shih, *Appl. Surf. Sci.* 261 (2012) 665-670.

[100] S.I. Sadovnikov, A.V. Ishchenko, I.A. Weinstein, *J. Alloys Comp.* 831 (2020) 154846.

Chapter 2

REVIEW OF PAST WORK

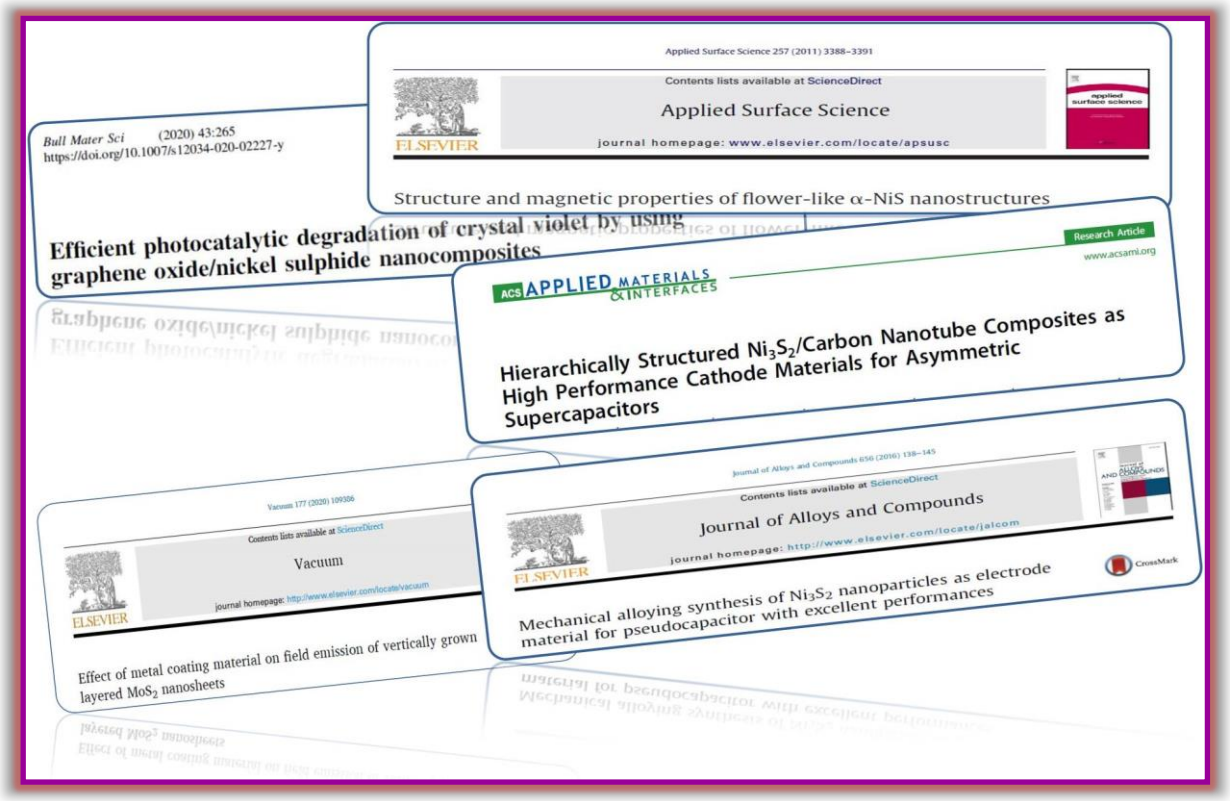

2.1. Review of past works on transition metal sulphides:

The transition metal sulphide nanostructures are very important in the field of supercapacitor, hydrogen evolution reaction, fabrication of lithium-ion batteries, sodium-ion batteries etc. because of its unique properties which is already discussed in the introduction chapter. Due to their high specific power and long stability, transition metal sulphides have attained great attention in electrochemical supercapacitors. These chalcogenides have short path lengths for electron transport, flexibility, improved life cycle and can provide additional reactive sites which explore its applications in the field of solar cells, fuel cells, light-emitting diodes, electrocatalysts etc. For establishing the relative importance of transition metal sulphides, a literature survey on these chalcogenides nanostructure (NiS, ZnS, MoS_2 etc.) by other researchers is also important.

2.2. Review of past works on Nickel Sulphide:

2.2.1. Why Nickel Sulphide?

NiS is an inorganic compound which is very easy to synthesize and does not employ vigorous control of different parameters. Due to its boundless applications in lithium-ion batteries, dye-sensitized solar cells, ceramic toughеners and semiconductors, nickel sulphide has been widely studied. NiS has low charge transfer resistance property, superior corrosion resistance and exhibits good stability. The major advantage of NiS is that its most of the phases can be synthesized at low temperature easily. There are a large number of nickel rich and sulphur rich phases at low temperature. As NiS has efficient ionic conductivity due to oxygen vacancies, NiS has been extensively studied as a photocatalyst [1].

Ni_3S_2 exhibits much better performance than other phases of NiS. In nature, Ni_3S_2 exists as minerals in the form of heazlewoodite which is very cheap and available in large quantities. Due to its different types of morphology and simple synthesis route, it serves as an excellent electrode material for supercapacitor (SC) applications, hydrogen evolution reaction etc. The flaky Ni_3S_2 nanostructure on Ni-foam was first synthesized by Chou et. al. [2] and employed it for SC in 1M KOH solution achieving a remarkable capacitance retention of 91%. By simply adjusting the extent of sulfidation, Ou et. al. [3] synthesized Ni_3S_2/graphene composites to achieve the highest specific capacitance. Ni_3S_2 can also be easily doped with transition metals like Mo, Co etc. to attain better electrochemical performance [4,5]. Ni_3S_2 has low conductivity which can be easily overcomed by incorporating highly conductive electrode materials.

2.2.2. Past works on synthesis of Nickel Sulphide nanostructures:

The synthesis of different phases of transition metal sulphide, nickel sulphide i.e. NiS, NiS_2, Ni_3S_2 etc. have been carried out by various research groups. Here, we have mainly discussed the past works on synthesis of two phases of nickel sulphide i.e. NiS and Ni_3S_2.

2.2.2.1. NiS nanostructures:

In past years, many methods have been used to prepare NiS nanostructures like molecular precursor method [6], thermal decomposition of compounds having an M-S bond such as thiocyanate complex [7,8] and dithiolato complex [9]; homogenous precipitation reactions between sulphiding agent and metal salts [10]. But the products obtained by these methods exhibit small surface areas, large grain sizes and irregular morphology which was a barrier for their applications in many fields. Then, Chen et. al. [11] used solvo (hydro-) thermal method to prepare millerite NiS nanocrystals. The rod-like nanocrystalline NiS was formed

when ethylenediamine and hydrazine hydrate were used as solvent whereas spherical nanoparticles were formed when aqueous ammonia was used as solvent. The obtained products have relatively large surface area but the solvents used were organic. Phase controlled synthesis of NiS nanorods was done by Shen et. al. [12] by a simple solvothermal route and CO_2 gas was used as the phase controlled additive. Ghezelbash et. al. [13] synthesized NiS nanorods and triangular nanoprisms by solventless thermolytic degradation of nickel thiolate precursors in the presence of octanoate. Here, the growth of NiS nanorods is controlled by the capping ligand octanoate as revealed by FTIR spectra. The rod-to-triangle shape transition primarily depends on the Ni/dodecanethiol/octanoate ratio. Novel sea-urchin-like nanocrystallines of both α- and β-phases of NiS were prepared by Liu et. al. [14] by hydrothermal process under mild conditions. These led to important applications in electrode materials, magnetic devices and hydrogenation catalysts but the reaction time for doing the synthesis was a disadvantage. With the assistance of polymer, Xie and his group [15] synthesized 3D-NiS with flower-like architectures. Most of these synthesis methods [11-14] used highly reactive chemicals which is may cause environmental and biological risks. To get rid of this, Pan et. al. [16] synthesized flower- and rod-like NiS nanostructures by hydrothermal process which was organic free by using the precursors nickel acetate and thiourea and water as solvent. Tang et. al. [17] prepared flower-like α-NiS nanostructures by a facile one-step hydrothermal method and studied the coexistence of anti-ferromagnetism and ferromagnetism at 5 K.

As hydrothermal route is one of the most commonly used hybrid technique in which nanophase materials and inorganic compounds with different sizes, shapes and morphologies can be synthesized; so it is used by many research groups. But as inhomogeneous heating takes place which makes the conventional hydrothermal process slow and time taking. So, for increasing its reaction rate and phase purity, microwave heating was incorporated along with

this hydrothermal process by Nandhini's group [18] to synthesize NiS nanostructures. Microwave-assisted hydrothermal method is an energy-saving, more efficient and convenient route to synthesize stable nanostructures with facile morphologies. Recently, Bhardwaj et. al. [19] successfully synthesized two different phases of NiS via facile hydrothermal route using de-ionised water as solvent. Without adding any carbonaceous agent, cabbage and caterpillar-like nanostructures were obtained having enlarged surface area, reduced band gap and enhanced electrocatalytic performance. The immense pore size reduced the diffusion pathways and unique morphology was obtained. Beyond all these protocols, there are very rare reports in which the importance on aspect ratio is given such as a rational method to synthesize morphology-controlled NiS micro/nano-structure was reported by Dong et.al. [20] using hydrothermal process. Triggered by this idea, in our work, we synthesized nickel sulphide microstructure by simply varying its compositional stoichiometry using sol-gel method which is very reliable and low-cost method. Appropriate modulation of input precursor ratios caused effective variation in the structure of the building blocks which served as the unit of hierarchical NiS microtubes.

2.2.2.2. Ni_3S_2 nanostructures:

Among different phases of nickel sulphide such as α-NiS, β-NiS, NiS_2, Ni_3S_2, Ni_3S_4, Ni_7S_6, Ni_9S_8 etc.; Ni_3S_2 exhibits better performance as electrode materials for supercapacitors, batteries and electrochemical performances. For these numerous applications, many research groups have synthesized Ni_3S_2 nanostructures by various methods. Zhang et. al. [21] synthesized nanothread-based porous sponge-like Ni_3S_2 nanostructures directly on Ni-foil by using biomolecule-assisted method at very low temperature. The mass of cysteine and the reaction temperature were optimized to control the morphology of nanostructures. Then, Chou et. al. [2] used a facile potentiodynamic deposition method for the first time to

synthesize Ni_3S_2 nanoflakes on a Ni-foam substrate. The intercrossing nanoflakes formed the nanostructure and facilitated the penetration of electrolyte. In the past few years, some research works have also been reported on growth of hierarchical Ni_3S_2 nanostructures with carbon nanotubes, graphene and ZnO [22-24] which exhibited superior supercapacitive properties. Then, Krishnamoorthy et. al. [25] synthesized hierarchical Ni_3S_2 nanostructures directly on Ni-foam by one pot hydrothermal method using thiourea to increase the supercapacitive behaviour. The Ni-foam acts as a binder free electrode material for high performance of supercapacitors. To further make Ni_3S_2 as an active material for electrochemical performance, Zhang et. al. [26] prepared novel Ni_3S_2 3D hierarchical dendrites on Ni-foam by using one-step hydrothermal reaction. Various morphologies of nanostructures were obtained by varying both reaction temperature and time. The electrode materials made by all these methods showed excellent electrochemical behaviour but the methods used to prepare them needed a long preparation time and expensive cost. So, J.J. Li and his team [27] used mechanical alloying method under inert (Argon) atmosphere combined with a post heat treatment to synthesize Ni_3S_2 nanoparticles. This simple procedure and low cost method facilitated the development of high energy storage performance electrodes. Chen et. al. [28] reported a rationally designed two-step integrated approach to fabricate self-supported Ni_3S_2 nanosheet array on the Ni-foam substrate and they have applied the technologies of both nanostructural engineering and modification of material chemistry. It greatly enhanced capacitive properties with a high value of reversible capacitance. Further investigations led Wang et. al. [29] to prepare novel 3D-Ni_3S_2 nanosheets array on Ni-foam by adjusting the reaction temperature using facile and efficient solvothermal method. The porous structure with silkworm egg-like morphology produced best cycle stability and rate capability. Li et. al. [30] extended the use of Ni_3S_2 nanostructures for using them as rechargeable aluminum batteries by successfully synthesizing mountain-

like 3D-Ni_3S_2 nanostructure on Ni-foam using hydrothermal method. By employing powder vapor transport technique (PVT), Khan et. al. [31] synthesized nanostructured polycrystalline Ni_3S_2 on Ni-foil. The obtained flower-like nanostructures made them as a promising electrode material for Li^+ batteries. Recently, for improving sodium storage performance, Zhou and his team [32] prepared 3D carbon nanotubes-interwoven Ni_3S_2 micro-nanostructures through vulcanization with sulphur in the Ar-H_2 atmosphere at 550℃ with NiO/Ni/CNTs precursor.

For the excellent behaviour of Ni_3S_2 nanostructures as electrocatalysts, it became high demand for developing environment friendly electrocatalysts for both HER and OER. Lin et. al. prepared a Ni_3S_2 and multi-walled CNT nanocomposite with high catalytic activity towards HER [33]. Zhou et. al. reported Ni_3S_2 nanorods as an efficient electrocatalyst for OER [34]. So, these studies concluded that the performance of Ni_3S_2 is sensitive to the structure and morphology. Therefore, Ouyang et. al. [35] used simple hydrothermal process to design hierarchically porous Ni_3S_2 nanorod arrays on Ni foam for HER and OER by tailoring the structure of Ni_3S_2. Finally, to extend the utilization aspect of the Ni_3S_2 nanostructures, modification with doping was done by Cui et. al. [4]. They fabricated Mo-doped Ni_3S_2 nanorods on 3D Ni-foam as efficient and stable bi-functional electrocatalysts for water splitting by using simple hydrothermal method. Triggered by this idea, in our work, we synthesized Co incorporated Ni_3S_2 hierarchical nano/micro-cactus on Ni-foam substrate using hydrothermal process. The superior morphological features with high aspect ratio were identified as the key factor for such efficient HER catalytic performance.

2.2.3. Past works on applications of Nickel Sulphide nanostructure:

Nickel sulphide, a transition metal chalcogenide with variety of phases such as NiS, NiS_2, Ni_3S_2, Ni_3S_4, Ni_6S_5, Ni_7S_6, Ni_9S_8 and wide range of nano-morphologies have attracted much

attention in diverse directions. So, nickel sulphide has many important applications such as in solar cells, batteries, supercapacitors, ceramic toughners, electrode materials, hydrogenation catalysts etc. Nickel sulphide can also be used sensors, memory devices, thermoelectric devices and fluorescence devices. As my thesis is mainly focused on photocatalytic activity of NiS and hydrogen evolution reaction of Ni_3S_2; I have discussed on the past work of these two works of nickel sulphide in the next section.

2.2.3.1. Photocatalytic activity of NiS:

Different research groups have worked on nickel sulphide (NiS) to develop it as a photocatalyst in recent years. Chao et. al. [36] synthesized NiS nanoflowers by using facile polyol refluxing process in open-air condition for the first time and photocatalytic degradation of organic dyes methylene blue (MB) and Rhodamine B (RhB) was studied under visible light irradiation. The formation of 3D flower-like nanostructures can be clearly seen from the FESEM image (Fig. 2.1(a)) having diameter of about 150-200 nm. The overlapping of the adjacent nanoflakes causes the formation of porous NiS nanoflowers. The absorption spectra of MB solution and an aqueous solution of RhB in the presence of NiS nanoflowers and NiS nanoarchitectures respectively irradiated by visible light for a time period of 3 h are shown in Fig. 2.1 (b,c).

In case of dye MB, it can be clearly seen that the absorption intensity of the peaks decreased in intensity after 2 h of adsorption equilibrium and 3 h of irradiation under visible light and it degraded about 98% (Fig. 2.1(d)). This enhanced photocatalytic performance of NiS may be used for the development of visible-light-driven semiconductors.

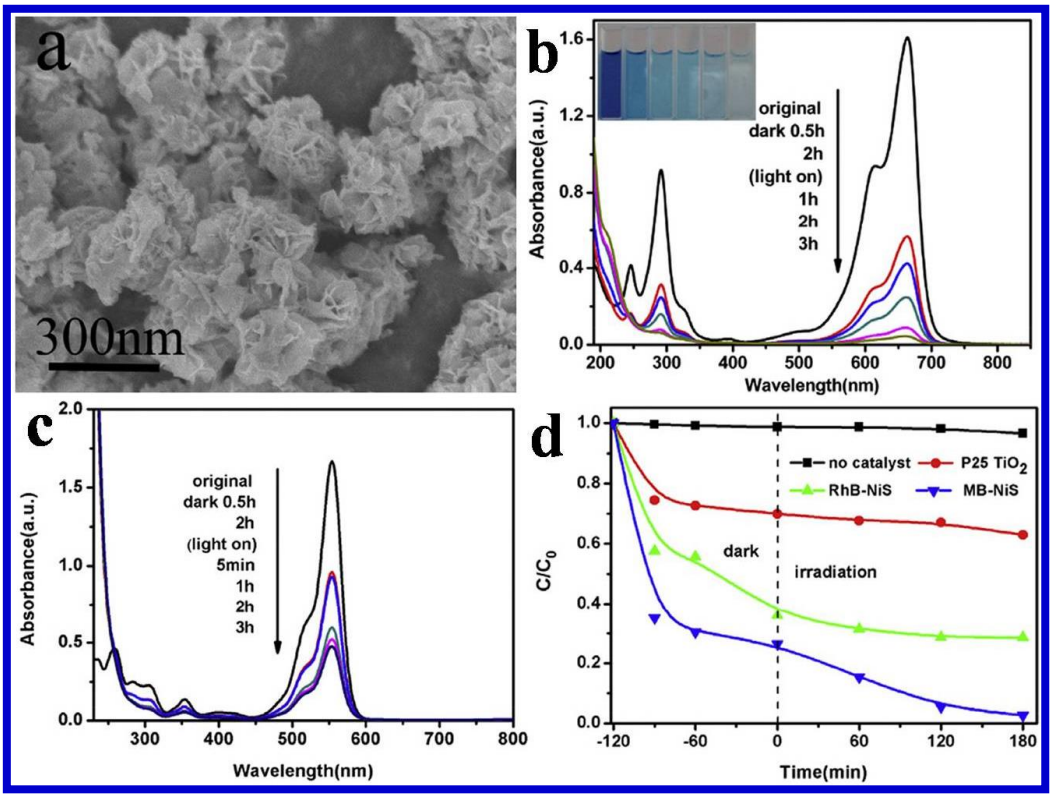

Fig. 2.1. ***(a)*** *SEM image of the as-synthesized NiS nanoflowers,* ***(b) and (c)*** *Absorption spectra of MB solution and RhB aqueous solution in presence of NiS nanostructures under visible light irradiation respectively,* ***(d)*** *Degradation profile against irradiation time.* [36]

Another study of photocatalytic activity of NiS nanoparticles was reported by Fazli et. al. and his team [37]. The synthesis was done by chemical precipitation in aqueous media followed by hydrothermal method; the obtained product was washed with absolute ethanol and dried for 4 h at 80˚C. The as-synthesized nickel sulphide nanoparticle was used to study the photocatalytic degradation of methylene blue (MB) under UV-irradiation. The UV-vis absorption spectra of MB solution and photocatalytic performance of NiS nanoparticles are shown in Fig. 2.2 (a) and (b) respectively. After 160 min, about 98.5 % i.e. maximum degradation of MB was achieved. So, for removal of organic pollutants (MB) from water, it can also be used as an efficient photocatalyst.

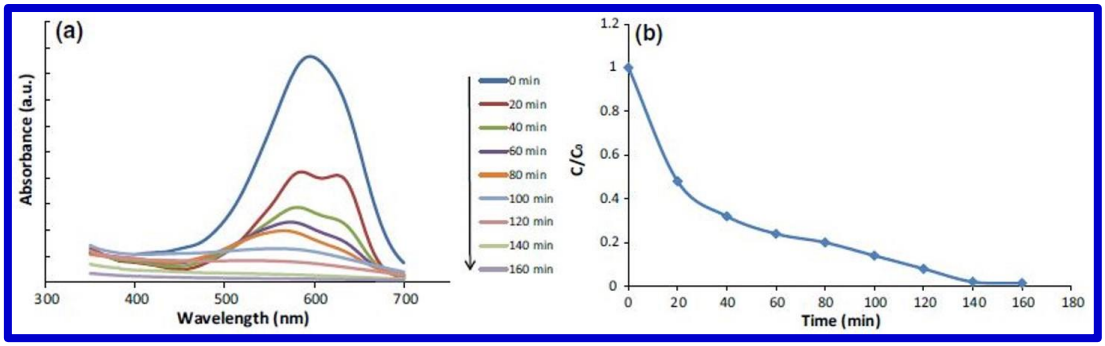

Fig. 2.2. ***(a)*** *Absorption spectra of MB solution in presence of NiS nanoparticles irradiated by UV light,* ***(b)*** *C/C_0 plot against irradiation time.* [37]

In a research work by Aniruddha Molla, the photocatalytic activity of nickel sulphide nanoparticles in various highly toxic dyes i.e. crystal violet (CV), Rhodamine B (RhB), methylene blue (MB), nile blue (NB) and eriochrome black T (EBT) was studied in both light and dark [38]. The reactive oxygen species (ROS) generated by the catalyst is responsible for the degradation of dyes both in presence and absence of light. 12 different variants of NiS (Ni1-Ni12) nanoparticles were synthesized using different capping agents. Within few minutes to hour, all the catalysts degraded the various dyes effectively both in light (visible light) and dark.

2.2.3.2. Hydrogen evolution reaction (HER) of Ni_3S_2:

The production of hydrogen through the process of water electrolysis is called hydrogen evolution reaction. Electrolysis of water combines of two half-cell reactions i.e. hydrogen evolution reaction and oxygen evolution reaction. Reduction of H^+ ions takes place at the cathode. HER consists of three steps- Volmer, Heyrovsky and Tafel.

$A + H^+ + e^- \longrightarrow AH_{ads}$ (Volmer reaction)

$AH_{ads} + H^+ + e^- \longrightarrow H_2 + A$ (Heyrovsky reaction)

$AH_{ads} + AH_{ads} \longrightarrow H_2 + 2A$ (Tafel reaction)

There are several reports on hydrogen evolution reaction of Ni_3S_2. The HER activity of Ni_3S_2/Ni foam in both neutral and basic solutions was first reported by Tang et. al. [39]. The three dimensional macroporous structure of Ni foam enables fast electron conduction and due to its high electrical conductivity, it is chosen as an electrode substrate. To produce current density of 10 mA cm^{-2}, Ni_3S_2 nanosheets array needs overpotential of 220 mV in neutral media and 123 mV in basic solutions as shown in Fig. 2.3.

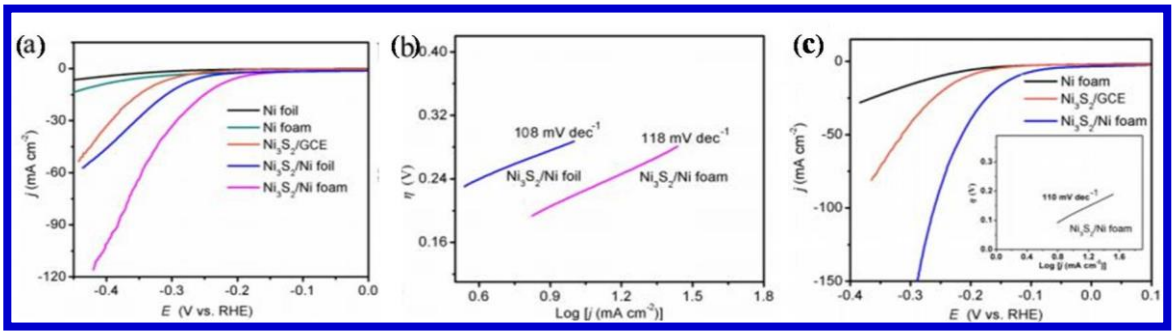

Fig. 2.3. *Polarization curves and their corresponding Tafel plots* ***(a, b)*** *in neutral media (1M PbS) and* ***(c)*** *basic media (1M KOH).* [39]

So, in both media, this electrode shows high catalytic activity and durability which is very useful in technological devices.

Canbin Ouyang and his group [35] reported the catalytic activity and stability of hierarchically porous Ni_3S_2 nanostructures towards HER with low overpotential of 200 mV at current density of 10 mA cm^{-2} in 1 M KOH solution. The reason for this best HER activity is because of the prior treatment of Ni-foam with HCl as it increases the roughness of Ni-foam. This also helps in achieving high density of Ni_3S_2 nanorod arrays. An enhanced electron transport and stability over the long term operation is obtained when porous Ni_3S_2 nanorods are grown on AT-Ni foam as it provides a strong combination between both of them. The linear sweep voltammetry (LSV) curves and their corresponding Tafel plots of the obtained

Ni_3S_2 nanostructures on acid treated (AT) Ni-foam compared with bare Ni-foam, AT-Ni foam and Ni_3S_2 on Ni-foam is shown in Fig. 2.4 (a) and (b) respectively. It can be seen from Fig. 2.4 (b) that Ni_3S_2 grown on AT Ni-foam has smaller Tafel slope which indicates its best HER response. A sample giving small Tafel slope means that at low overpotential, it attains high current density.

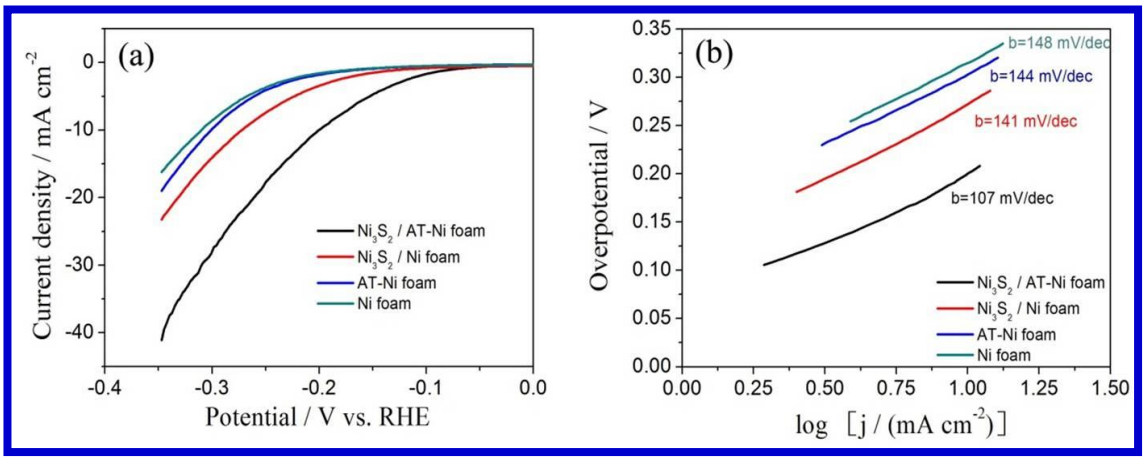

Fig. 2.4. *HER performance* ***(a)*** *LSV curves of Ni foam, AT-Ni foam, Ni_3S_2/Ni foam and Ni_3S_2/AT-Ni foam (scan rate = 2 mV sec^{-1}),* ***(b)*** *corresponding Tafel plots.* [35]

Junjie Li and co-authors reported the synthesis of Ni_3S_2 nanowires (NW) at low temperature by a facile one-step method using resin containing sulphur source [40]. On the surface of Ni-foam, Ni_3S_2 NW is fabricated using sulphur containing gas from the resin. From Fig. 2.5, it can be clearly seen from the SEM images that Ni_3S_2 nanowires are formed in high density on Ni foam in the nanometre range.

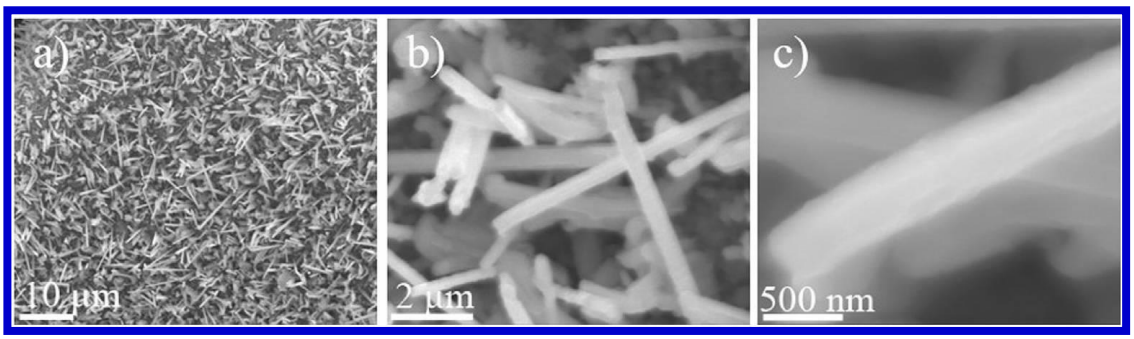

Fig. 2.5. ***(a-c)*** *SEM images of Ni_3S_2 nanowires.* [40]

In a three-electrode configuration, the HER activity of Ni_3S_2 NW arrays was studied in 1M KOH solution at scan rate of 1 mV s^{-1}. To afford current density of 10 mA cm^{-2}, the nanowires need overpotential of 199.2 mV which is much better than pristine Ni-foam as shown in Fig. 2.6 (a). From Tafel plot (Fig. 2.6 (b)), it can be concluded that Ni_3S_2 NW has lower slope rather than pure Ni-foam. The accelerated durability test was also conducted at scan rate of 50 mV s^{-1} as shown in Fig. 2.6 (c) and after completion of this test over 3000continuous cycles, a minor change was observed in the polarization curve. The stability curve in the inset of the same figure shows its outstanding durability for 30 h at 20 mA cm^{-2}. So, this Ni_3S_2 NW synthesized by a cost effective method is an excellent HER catalyst.

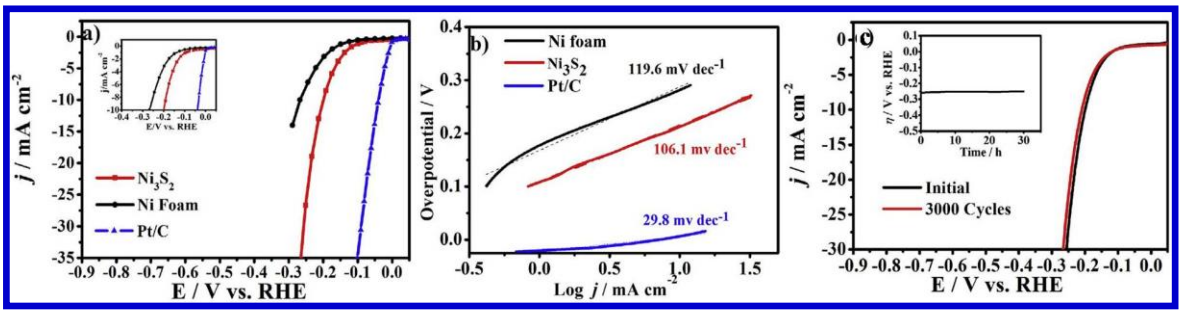

Fig. 2.6. ***(a)*** *Polarization curves and* ***(b)*** *Tafel plots of Pt/C, Ni-foam and Ni_3S_2 NWs,* ***(c)*** *Durability test of Ni_3S_2 after 3000 continuous cycles.* [40]

Yuanju Qu and his co-workers [41] reported the HER activity of vanadium-doped Ni_3S_2 nanowire (NW) arrays on Ni-foam. Vanadium doping improves the electrocatalytic activity by increasing the amount of free carriers around Fermi level which leads to reduced onset potential. From SEM image, it can be clearly seen that pure Ni_3S_2 nanostructures grown on Ni-foam (Fig. 2.7(a)) are simply triangular spikes and no nanowire growth is observed. But the V-doped Ni_3S_2 growth on Ni-foam is nanowire (Fig. 2.7 (b, c)) due to the presence of sodium orthovanadate which enhances the hydrogen evolution reaction.

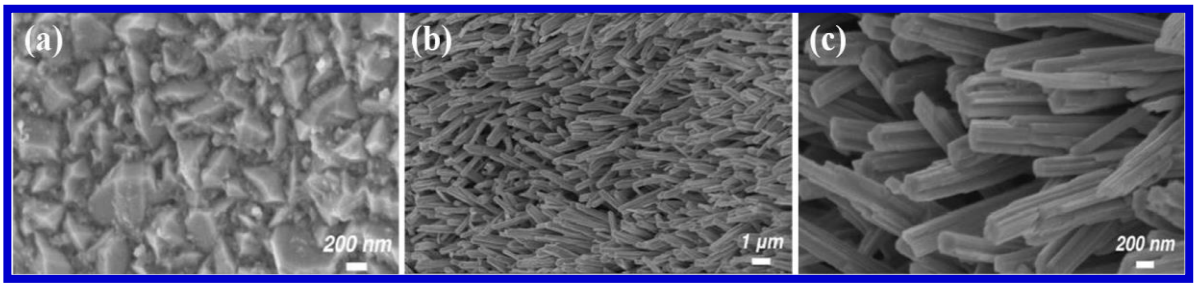

Fig. 2.7. *SEM images of* ***(a)*** *undoped Ni_3S_2 nanostructures and* ***(b,c)*** *V-doped Ni_3S_2 nanowire.* [41]

The HER measurement was conducted in 1M KOH to study the electrolysis of water of Ni_3S_2 nanowires. The overpotential of pure-Ni_3S_2 nanostructures is 232 mV and that of V-doped-Ni_3S_2 NW is 203 mV at 20 mA cm^{-2} as shown in Fig. 2.8(a).

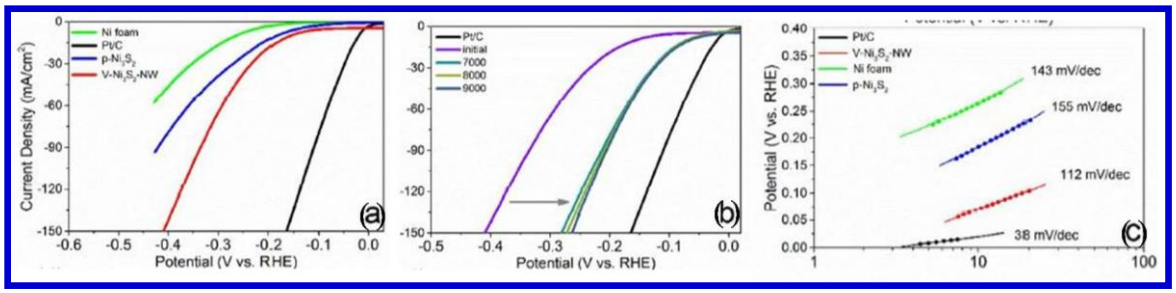

Fig. 2.8. ***(a)*** *Comparative polarization curves of p-Ni_3S_2, V-Ni_3S_2, Ni-foam and Pt/C,* ***(b)*** *performance after thousands of cycles,* ***(c)*** *Tafel plots after stabilization.* [41]

After 7000 cycles, the performance of V-Ni_3S_2-NW is enhanced to a great extent and pure Ni_3S_2 has negligible improvement. At a current density of 10 mA cm^{-2}, the overpotential of V-Ni_3S_2 is reduced to 68 mV from 157 mV and gets stabilized after thousands of cycles as we can see from Fig. 2.8(b). The value of Tafel slope (112 mV dec^{-1}) is also obtained less than that of undoped sample (155 mV dec^{-1}) represented in Fig. 2.8(c). So, the application of Ni_3S_2 as electrocatalysts in hydrogen production can be improved by doping vanadium.

Another work of Sn-doped Ni_3S_2 nanostructures was reported by Yu et. al. by solvothermal method on Ni-foam in both acidic and alkaline medium [42]. Sn-doping increases the active sites of the nanostructure, ability to absorb atomic hydrogen steadily and shortens the transmission path of electron as these nanosheets posses unique 3D network (Fig. 2.9). The electrocatalysis is also promoted by the transformation of morphology.

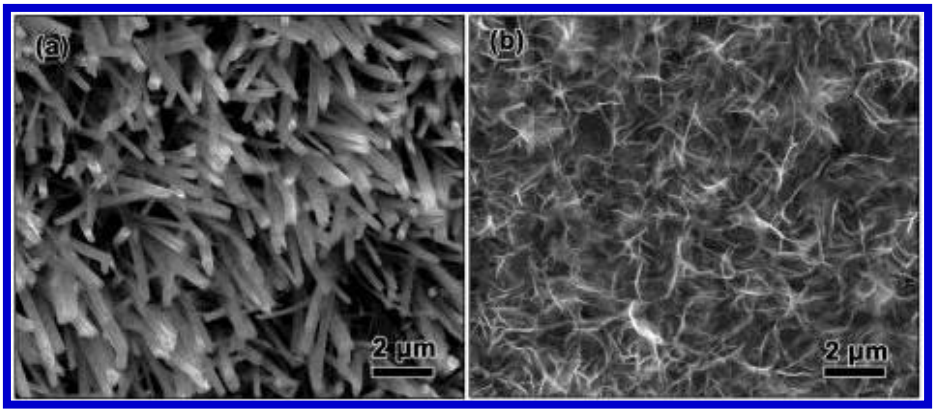

Fig. 2.9. *SEM image of* ***(a)*** *as-synthesized of* Ni_3S_2 *nanorods,* ***(b)*** *Sn-doped* Ni_3S_2 *nanosheets.* [42]

To study the electrochemical property of the nanosheets, a three-electrode set-up was designed firstly in acidic medium (0.5 M H_2SO_4) and secondly in alkaline medium (1 M KOH). In acidic medium, from Fig. 2.10(a), it can be seen that Sn-doped Ni_3S_2 nanosheets exhibits a lower overpotential of 201 mV rather than Ni_3S_2 nanorods (254 mV) and Ni-foam at 10 mA cm^{-2}. The doping gives a Tafel slope of 51 mV dec^{-1} which is far better than undoped sample and Ni-foam (Fig. 2.10(b)). It means that adsorption reaction takes place at a faster rate following electrochemical desorption process. The most important criteria for a best HER catalyst is its durability for long time which can be clearly seen from Fig. 2.10(c).

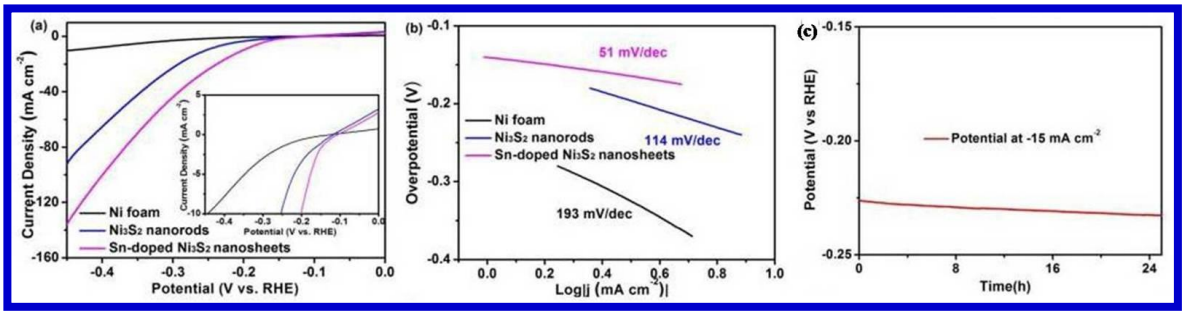

Fig. 2.10. *In 0.5 M H_2SO_4* ***(a)*** *Comparative polarization curves of Ni-foam, Ni_3S_2 nanorods and Sn-doped Ni_3S_2 nanosheets,* ***(b)*** *corresponding Tafel plots,* ***(c)*** *Catalyst retention test of Sn-doped sample.* [42]

In alkaline medium (1M KOH), both Ni_3S_2 nanorods (164 mV) and Sn-doped Ni_3S_2 nanosheets (137 mV) gives a lower overpotential compared to that of acidic medium at same current density (10 mA cm^{-2}) as shown in Fig. 2.11(a). The Tafel slope of undoped Ni_3S_2 also decreases after Sn-doping from 225 to 148 mV dec^{-1} (Fig. 2.11(b)) and the long-term chronoamperometric stability test was also carried out for 10 h to achieve 20 mA cm^{-2} current density indicating excellent performance (Fig. 2.11(c)).

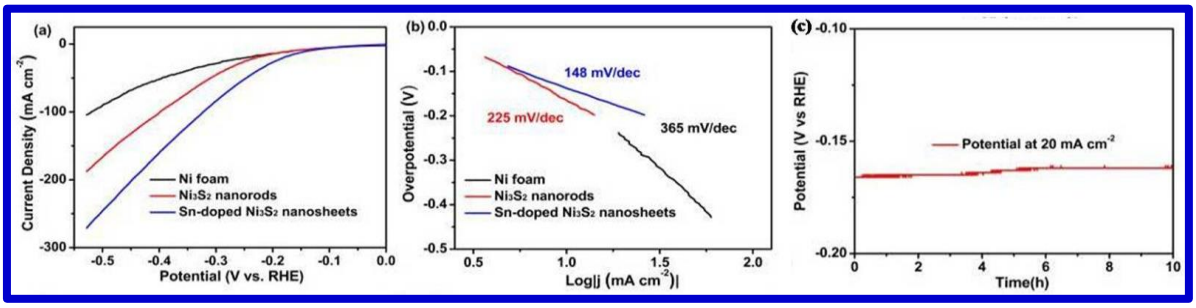

Fig. 2.11. *In 1 M KOH* ***(a)*** *Comparative polarization curves of Ni-foam, Ni_3S_2 nanorods and Sn-doped Ni_3S_2 nanosheets,* ***(b)*** *corresponding Tafel plots,* ***(c)****Stability test of Sn-doped sample.* [42]

So, doping Sn enhances the morphology of Ni_3S_2 nanostructures which provides more active edges for the electrocatalytic process and it becomes a promising HER catalyst.

2.3. Review of past works on Zinc Sulphide:

2.3.1. Why Zinc Sulphide (ZnS)?

ZnS is an inorganic semiconductor material which has always been the interesting material of research due to its tunable properties. ZnS is a polymorphous material and exists in two main crystalline forms, cubic and hexagonal which widens its application in various fields such as in photonics, nanoelectronics, electro-luminescent devices, optoelectronics, solar cells and as tools in biomedical. It is very easy to synthesize ZnS nanostructures both by physical and chemical routes [43] and by doping external impurity or doing other modifications [44], their properties can be varied. ZnS due to its wide direct band gap exhibits a large optical transparency from UV (ultraviolet) to IR (infrared) region which explored its application further. So, the study of ZnS nanostructures is of considerable importance.

2.3.2. Past works on synthesis of Zinc Sulphide nanostructures:

Due to the wide range of potential applications of zinc sulphide, synthesis of ZnS nanomaterials have attracted considerable attention. Using different synthesis methods such as thermal evaporation of ZnS powder [45-47], solvothermal process [48,49], liquid crystal template method [50], chemical vapour deposition (CVD) [51] etc., one-dimensional ZnS nanostructures have been prepared. Among these, solvothermal process is such a technique in which both one-dimensional nanostructures and nanoparticles could be synthesized in powder form in bulk quantities. Biswas et. al. [52] synthesized ZnS nanoparticles and nanorods using solvothermal process. By using different types of solvent and varying the temperature, size and morphology of nanostructures of ZnS were controlled. Feng Gu and his co-authors [53] synthesized hollow and solid ZnS nanospheres by a facile solution-phase method in which no templates were used. In addition to this, they encapsulated these ZnS nanospheres within a

uniform silica layer without making any modification of surface and this enhances their use in biochemistry and biodiagnostics. To study whether any relation exists between the desirable morphology and structure in ZnS nanomaterial, Li et. al. [43] studied the controllable synthesis of ZnS nanocrystals using solvothermal method with different structures and morphologies. Also, by changing the molar ratio of reactants, the phase transformation between the two structures of ZnS i.e. zinc-blende and wurtzite can be easily induced. 1D-ZnS nanostructures such as nanorods, nanobelts, tetrapods and nanoslices were synthesized by Peng et. al. [54] using a simple and rapid method i.e. RF thermal plasma method. For controlling the morphology of the synthesized products, the critical experimental parameters such as the feeding rate and the cooling flow rate were varied. ZnS thin films were also produced using several techniques such as spray pyrolysis, thermal evaporation, chemical bath deposition, molecular beam epitaxy etc. [55-58]. For the first time, Hankare et. al. [59] deposited ZnS thin films by a new technique using dip method and succinic acid was used as a complexing agent. Sol-gel technique was also used to produce ZnS thin films on quartz slide in four different annealing temperatures as reported by Maheran et. al. [60]. Polycrystalline ZnS thin film on quartz substrate was synthesized by Mukherjee et. al. [61] using spin coating technique and hexagonal wurtzite structure was obtained. A.N. Singh and his co-workers [62] fabricated polyvinyl alcohol (PVA) capped nanocrystalline ZnS thin films on glass substrates by using the method chemical bath deposition. Another method for obtaining nanocrystalline ZnS thin films on glass substrates was reported by Offor et. al. [63] using the technique chemical spray pyrolysis in which zinc chloride was used as cationic source and thiourea as anionic source with EDTA complex. For potential applications in modern technology, synthesis of ZnS nanostructure from single source precursor has been employed. Abdullah et. al. [64] prepared ZnS nanoparticles from precursor zinc N-ethyl cyclohexyl dithiocarbamate complex by thermal decomposition method. A very simple and

cost-effective, solid state reaction method was used for the first time by Jothibas et. al. [65] to synthesize ZnS nanoparticles at different temperatures to modify the photocatalytic applications. ZnS nanopowder was synthesized by Sadovnikov et. al. [66] using chemical deposition method from aqueous solutions of zinc nitrate and sodium sulfide. The complexing and stabilizing agents used were aqueous solutions of trisodium citrate and Trilon B. Further, this group prepared Ag_2S/ZnS heteronanostructures for the first time by a facile two-stage hydrochemical co-deposition of zinc and silver sulfides. A green synthesis method i.e. bio-molecule assisted synthetic method was employed by Samanta et. al. [67] for the first time to prepare ZnS nanomaterials (nanospheres, nanoflowers and nanotubes) using the extract of Citrus limetta, as a capping agent and it improved the photocatalytic activity of ZnS. An inexpensive, facile and versatile chromatography sprayer (CS) technique was reported for the first time to synthesize ZnS thin films by V.H. Choudapur and his team [68] in which the ZnS nanoparticles were synthesized by hydrothermal method and then, the thin films were prepared by this colloidal spray coating method.

Several research groups reported doping of Fe and Ni; Co, Cr, Al within ZnS [69-72]. But Goudarzi et al. first reported the successful doping of Mn in ZnS [73]. Also, Ramasamy et. al. synthesized transition metal (Mn, Co, Ni, Cu, Ag and Cd) doped ZnS nanoparticles in an air atmosphere using chemical precipitation method in the absence of capping agent [74].

2.3.3. Past works on applications of Zinc Sulphide nanostructure:

ZnS, a semiconductor metal chalcogenide has been a very interesting material of study. Due to its wide band-gap energy of 3.6 eV - 3.7 eV at 300 K [53,60,75], ZnS has potential application as a luminescent material well-known for its electroluminescence [76,77], photoluminescence [54,57,78-80], thermal luminescence [55], acoustoluminescence [81] and mechanoluminescence [82]. Also, by considering the band-to-band emission and defect

related emission of ZnS thin films, the luminescence property of ZnS thin films was explained. ZnS also has broad applications in various fields such as sensors, lasers [78,81], displays [83] and photocatalysis [67,84]. ZnS has been used in photoconductor [85] and photovoltaic cells [86] and in fabrication of optoelectronic devices such as blue light-emitting diodes and green light-emitting diodes [87]. Due to high transmittance of ZnS in visible range and also high refractive index, it can be used as reflectors and dielectric filter [88,89] in the area of optics. Doping of the transition metal in ZnS extends its extensive attention as 'dilute magnetic semiconductor' (DMS) for spintronics applications [90,91]. ZnS thin films also exhibit field emission properties [92,93].

Other than photoluminescence property, zinc sulphide nanostructures show strong cathodoluminescence (CL) spectroscopy in the near-UV to green region of the electromagnetic spectrum. As my thesis is focused on the CL property of ZnS, the following section gives a detail of previous works done on this application by various research groups.

Oda et. al. [94] first observed cathodoluminescence from ZnS single crystals. For measurement of low-voltage CL of the sample, they used an experimental device whose structure was same as that of a simple vacuum tube with an anode and a hot-cathode. The CL measurements were carried out at room temperature under d.c. operation. Under the excitation of low-energy electron beams of several tens of volts, bright blue and green CL spectra were observed from low resistivity ZnS crystals. Dinsmore et. al. [95] synthesized Mn-doped ZnS nanoparticles of 100-nm diameter and studied low-voltage CL of these nanoparticles by keeping the range of electron-beam energy between 500 and 3500 eV. The obtained emission from the as-synthesized nanoparticles was compared with similar-sized powder patch of a ZnS:Mn phosphor manufactured by the Sarnoff Corporation which was comparatively similar. The wavelength of the CL peak of ZnS:Mn nanoparticles appeared at 582 nm as compared to that of the commercial phosphor at 580 nm and the luminescence

appeared yellow to the eye of all the samples. These Mn-doped ZnS cathodoluminescent phosphors exhibited less current saturation as compared to that of large-sized phosphors which explores its use in field emission displays. Further improvement in the CL property of nanophosphors can be obtained by optimizing the concentration of Mn-doping. To synthesize undoped and doped ZnS thin films for luminescence study, Hichou et. al. [96] used spray pyrolysis technique and chloride precursors. In the visible range, ZnS film exhibited highest transmittance which decreased on doping with Al and Sn. The CL emission spectra was studied at room temperature maintaining electron beam energy E = 5 keV. It was found that undoped ZnS and Al-doped ZnS thin films as shown in Fig. 2.12 (a) and (b) respectively, presented same experimental CL characteristics i.e. a blue emission peak at 405 nm (E = 3.56 eV) which corresponds to the band edge and blue-green emission peak at 524 nm (E = 2.37 eV) due to presence of chloride precursor.

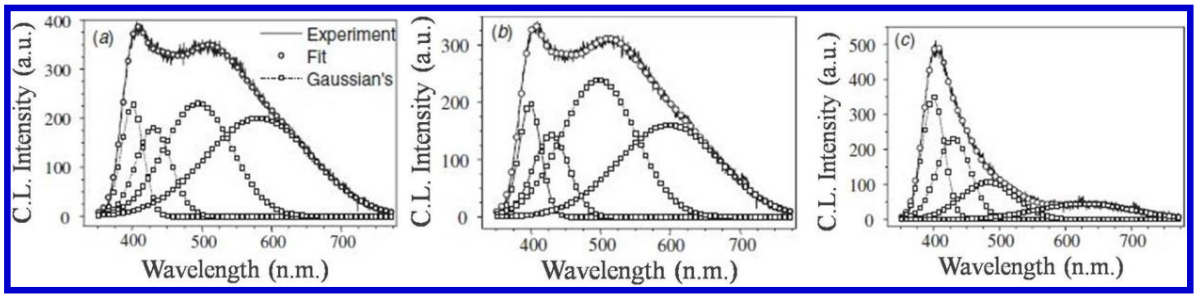

Fig. 2.12. *CL spectra of* ***(a)*** *undoped ZnS,* ***(b)*** *Al-doped ZnS and* ***(c)*** *Sn-doped ZnS thin films obtained with electron beam energy of 5 keV.* [96]

It can be seen from Fig. 2.12(c) that the emission peak of Sn-doped ZnS thin films appeared only at about 405 nm. The insertion of 4 at% of Sn in ZnS material led to the elimination of blue-green emission that appeared in both undoped and Al-doped ZnS thin films. It happened by the reaction of Sn^{2+} ions and a large part of Cl^{-} ions which led to the formation of $SnCl_2$ compound. So, for obtaining blue light emitting ZnS films, Sn doping is favourable as it reacts with chloride precursors and eliminates the emission band at 524 nm.

Lee et. al. [97] synthesized ZnS films by single-source chemical vapor deposition (CVD) of zinc dimethyldithiocarbamate under a variety of precursor fluxes and studied its cathodoluminescent property. They found that the light emitting properties of the films were strongly dependent on the deposition conditions of film.

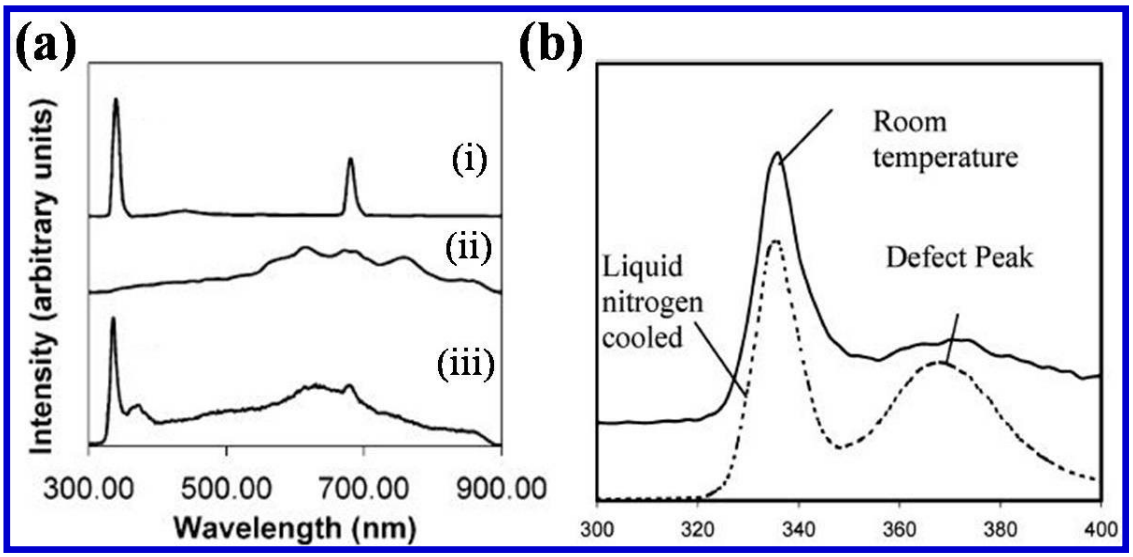

Fig. 2.13. ***(a)*** *CL spectra of i) ZnS single crystal, ii) a ZnS film having no band-gap emission, iii) a ZnS film having a strong band-gap emission.* ***(b)*** *High resolution scan of ZnS film having a strong band-gap emission.* [97]

The CL spectra of ZnS single crystal as shown in Fig. 2.13(a) (i) shows that the band edge emission occurs at ~340 nm and the secondary harmonic at ~680 nm. For a ZnS film grown at maximum precursor flux for 2h (Fig. 2.13(a) (ii)), only a broad and continuous background occurs but no distinct band gap emission is observed. For ZnS film grown at minimum precursor flux for 8 h, no significant peak broadening of the band gap emission was observed for the film as shown in Fig. 2.13(a) (iii). It confirms the high quality nature of the film. In Fig. 2.13(b), high resolution scan of the region of band gap of ZnS film at room temperature and also after cooling the sample with liquid nitrogen. So, synthesizing ZnS films using CVD technique produces strong band gap emissions.

Z.G. Chen and his team [98] synthesized ZnS dual-phase tetrapod tree-like heterostructures consisting of two phases zinc blende for the trunk and hexagonal wurtzite for the branch as shown in Fig. 2.14.

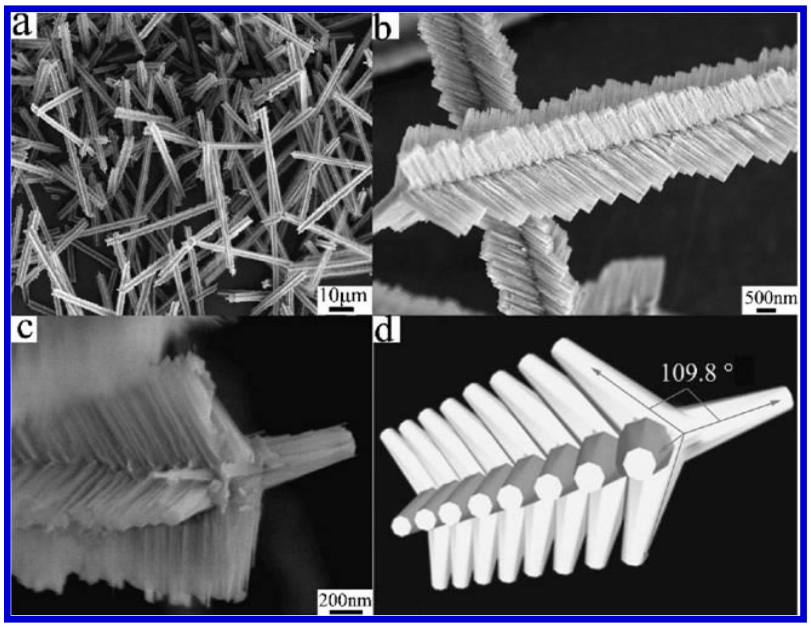

Fig. 2.14. *SEM images of the as-synthesized ZnS tetrapod tree-like heterostructures.* [98]

At room temperature, two strong intrinsic emissions centered at 3.68 eV (peak I, 336 nm) and 3.83 eV (peak II, 323 nm) have been observed with a shoulder centered around 3.42 eV (peak III, 362 nm) in the CL spectra (Fig. 2.15). Peak I is attributed to band gap emission from zinc blende phase and peak II is for hexagonal wurtzite. Peak III is a new near-band emission which may be attributed from the native interface between both phases of the dual

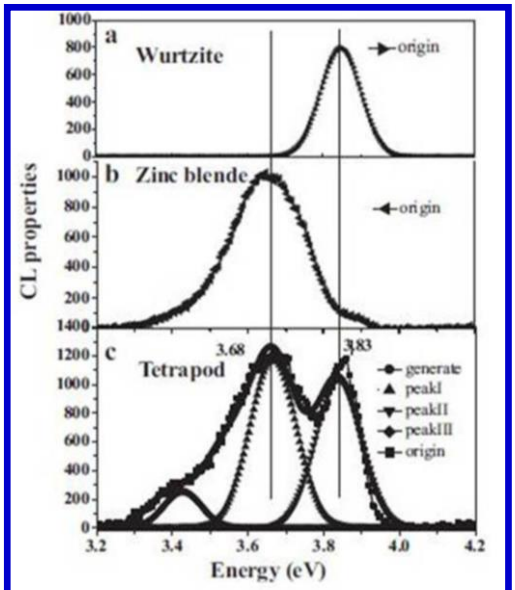

Fig. 2.15. *CL spectra of a single nanostructure* ***(a)*** *Wurtzite phase,* ***(b)*** *Zinc blende phase and* ***(c)*** *Dual-phase tetrapod heterostructure.* [98]

phase tetrapod tree-like heterostructures. These structures can be used in various fields such as light emitting display devices, medical diagnostics, electromechanical and optoelectronic components.

Zinc blende hexagonal ZnS pyramid was fabricated by Chen et. al. [99] using a facile thermal evaporation process in ammonia atmosphere at 1150℃. At room temperature, the CL property of the hexagonal pyramid was studied. A strong intrinsic emission centered at 337 nm (3.68 eV) was observed which indicates high crystallinity of the product. Fig. 2.16 depicts the CL spectra of a single ZnS hexagonal pyramid and the SEM-CL image taken at 337 nm wavelength shown in inset indicates a uniform CL emission across the entire pyramid. This strong emission of CL shows potential applications of ZnS as optic and optoelectronic devices in surgery and spectroscopy.

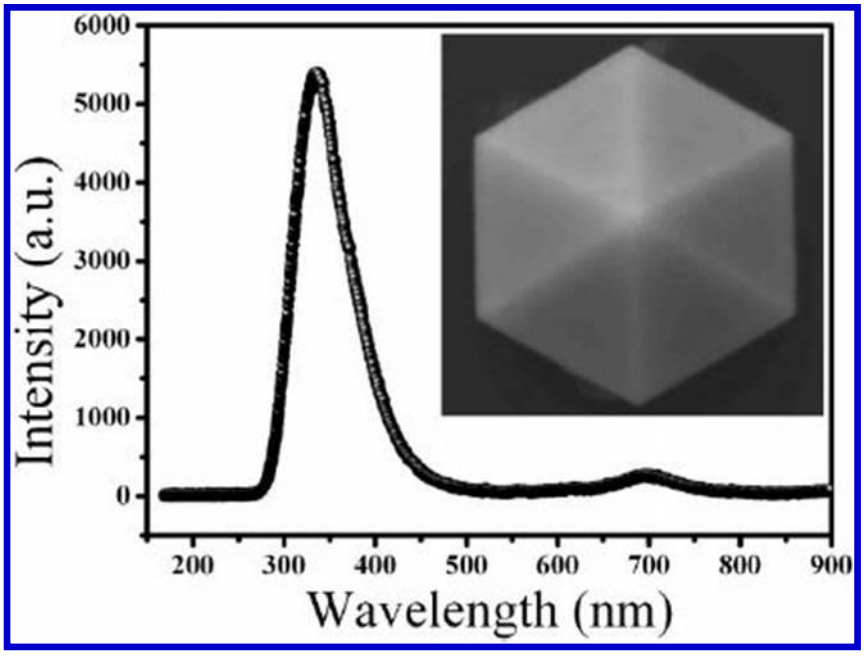

Fig. 2.16. *CL spectrum of a single ZnS hexagonal pyramid and the SEM-CL image is shown in inset.* [99]

Huang et. al. [100] synthesized single crystal ZnS nanowires on Si substrate by using thermal chemical vapor deposition (CVD) method without using any catalyst. A series of experiments

further confirmed that both the phases of ZnS i.e. wurtzite (hexagonal) and sphalerite (face-centered cubic) co-existed in the product obtained a shown in the XRD pattern in Fig. 2.17(a). FESEM image (Fig. 2.17(b)) shows that the nanowires were uniform with a one-dimensional morphology having diameter of 20-50 nm and several tens of micrometers in length.

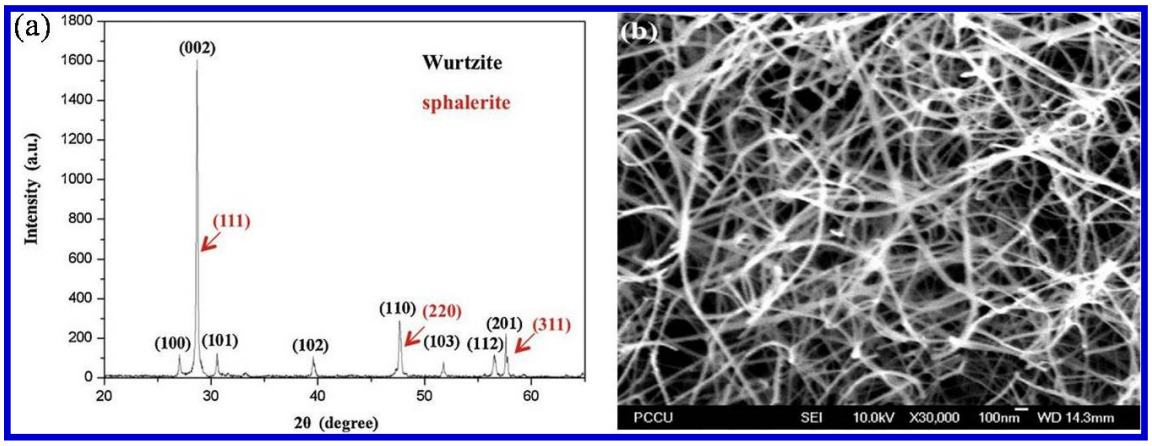

Fig. 2.17. (*a*) *XRD pattern of ZnS nanowires showing both phases wurtzite and sphalerite,* ***(b)*** *High magnification FESEM image of ZnS nanowires.* [100]

At room temperature, the CL property of ZnS nanowires was studied and broad, strong emission was obtained. The characteristic peaks appeared at 357 nm (3.47 eV), 449 nm (2.76 eV) and 581 nm (2.13 eV) which were attributed to the direct band-to-band emission, blue-emission peak of maximum intensity and peak due to impurity-related defects in the nanowires, respectively. So, the main emission peak was located at 449 nm in the blue region as shown in Fig. 2.18. This property explores the applications of these ZnS nanowires to be used as UV/blue LED phosphor materials.

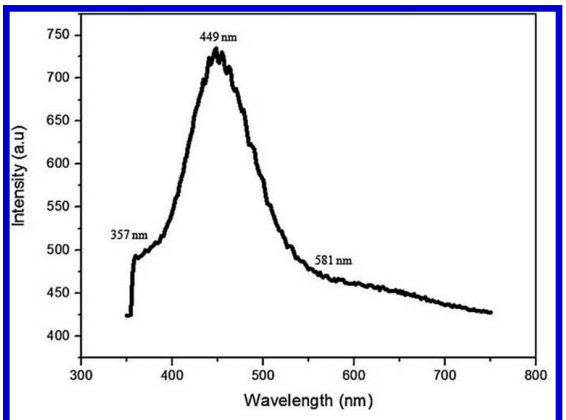

Fig. 2.18. *CL spectra of the as-synthesized ZnS nanowires.* [100]

ZnS nanopowder was synthesized by Sadovnikov et. al. [66] using the chemical deposition method from aqueous solutions of zinc nitrate and sodium sulfide in the presence of sodium citrate. Ag_2S/ZnS heteronanostructures were also prepared by a facile two-stage hydrochemical co-deposition of zinc and silver sulfides. The CL spectra of ZnS nanostructures and $(ZnS).(Ag_2S)_{0.025}$ heteronanostructure was studied and is represented in Fig. 2.19. The maxima of CL spectra are located at ~ 450 nm and ~ 600 nm for ZnS nanopowder and $(ZnS).(Ag_2S)_{0.025}$ heteronanostructure respectively. ZnS nanopowders possess strongest emission in the blue region and can be used as materials for potential application in light-emitting diodes and lasers.

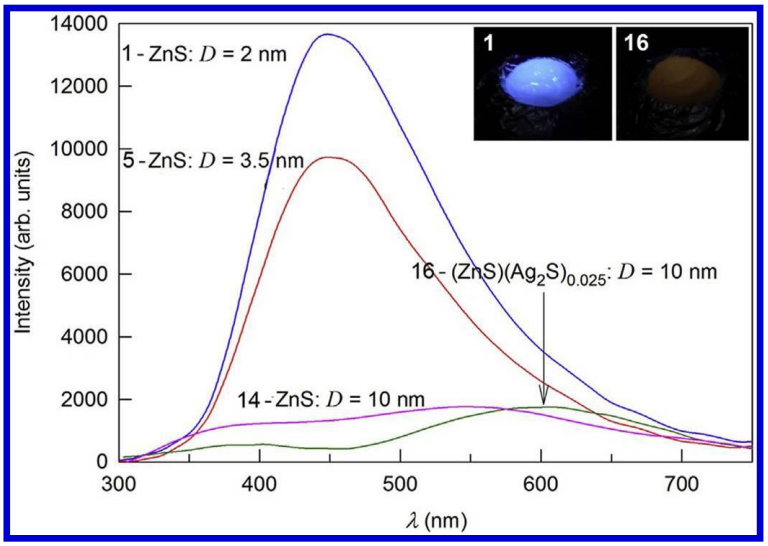

Fig. 2.19. *Pulsed CL spectra of ZnS nanopowder with particles of different size and* $(ZnS).(Ag_2S)_{0.025}$ *heteronanostructure and inset showing the colour of the emission.* [66]

2.4. Review of past works on Molybdenum Disulphide:

2.4.1. Why Molybdenum Disulphide (MoS_2)?

MoS_2 is a two-dimensional material which has unique chemical, optical, mechanical and electronic properties. Due to these properties, it can be employed for novel optoelectronics and nanoelectronics devices. Its low temperature synthesis reduces its production cost. MoS_2,

being useful in its polycrystalline form finds applications in energy storage, catalysis, gas sensing and water treatment. It has higher theoretical capacity (than graphite) and higher intrinsic fast ionic conductivity (than oxides). The sheet-like morphology of MoS_2 provides large surface area for double layer charge storage for which they are extensively used in supercapacitors [101,102]. Due to its layered structure, easy-functionalization and large surface area, MoS_2 is considered analogous to graphene-like nanomaterial. Also, its band gap transformation from indirect to direct when exfoliation of bulk MoS_2 is done to a single-layer MoS_2 nanosheet, plays a significant role in exploring its applications in various fields [103]. MoS_2-based nanocomposites have attracted more attention in environmental monitoring, food safety, disease diagnosis, biochemical analysis etc. because of their extra-ordinary properties.

2.4.2. Past works on synthesis of Molybdenum Disulphide nanostructures:

Among transition metal sulphides, MoS_2 exhibits so many intriguing applications and therefore, the synthesis of MoS_2 nanomaterials have been focused by many researchers. Tenne's group [104] firstly synthesized MoS_2 nanotubes by the gas-phase reaction between MoO_{3-x} and H_2S in a reducing atmosphere and the reaction temperature was maintained between 800℃ to 950℃. A pure nested inorganic fullerene (IF) phase of MoS_2 with a relatively narrow size distribution was obtained. Zelenski et. al. [105] prepared hollow tubules of MoS_2 of uniform size and shape in large quantities by thermal decomposition of two different ammonium thiomolybdate molecular precursors. They also used a porous aluminum oxide template to get control over the size and size distribution of the nanostructures of MoS_2. The obtained tubules were ~ 30 μm long with diameters of 50 nm. Li et. al. [106] synthesized MoS_2 nanowires by hydrothermal method using MoO_3 and Na_2S as precursors in HCl solution. The nanowires obtained were of diameter 4 nm and length 50 nm. Triangular-shaped MoS_2 nanoclusters were synthesized by Lauritsen et. al. [107] on a weakly

interacting gold substrate in an ultra-high vacuum chamber under sulphiding conditions. Almost all of these synthesis method required toxic gas which were harmful for the environment. So, an environment-friendly biomolecule-assisted hydrothermal synthesis method was employed by Chen. et. al. [108] to prepare MoS_2 microspheres consisting of nanorods with length of about 100 nm and L-cysteine was used as the sulphur source. Further, to grow highly crystalline and large-area MoS_2 thin sheets on insulating substrates, a two-step thermolysis process was used by Liu et. al. [109]. The thermally decomposed ammonium thiomolybdate layer was annealed at high temperature in the presence of sulphur. Najmaei and his group [110] also synthesized highly crystalline MoS_2 atomic layers on insulating SiO_2/Si substrates by a CVD-based procedure. They used MoO_3 as precursor and pure sulphur as reactant material to grow MoS_2 atomic layers in a vapour phase deposition process at reaction temperature of 850℃. Tontini et. al. [111] synthesized nanostructured flower-like MoS_2 particles of mean diameter 250 nm by hydrothermal method without using any surfactant maintaining a temperature of 160℃. A facile aqueous hydrothermal method to synthesize few layer MoS_2 nanosheets was reported by Veeramalai et. al. [112] in which MoO_3 and L-cysteine were used as the molybdenum and the sulphur source respectively for the first time. Due to Van der Waals interaction between the adjacent layers of MoS_2 with atomic edges, the as-synthesized MoS_2 nanosheets appeared as free-standing layers aggregated together. Shao Su and his group [103] synthesized noble metal nanostructure-decorated molybdenum disulfide nanocomposites by different types of methods such as the chemical reduction method, self-assembly method, laser beam and microwave-assisted synthesis, electrochemical method and hydrothermal method. Due to synergetic effects, MoS_2-based nanocomposites possess charming properties for which they are used in sensors, catalysts, batteries, antibacterial agents etc. Kanade et. al. [113] synthesized flower-like MoS_2 nanostructures and for the first time, they also prepared nitrogen-doped MoS_2 nanosheets as

electrode materials using varying concentrations of urea by hydrothermal method. They used ammonium heptamolybdenate as molybdenum precursor and thiourea as sulphur precursor. The doping of nitrogen in MoS_2 enhanced the electrochemical performance of pristine nano-shaped MoS_2 by four times. Abraham and his team [114] synthesized MoS_2-wrapped graphene nanohybrids for energy-oriented and hydrogen evolution reaction applications in which graphene acts as a substrate or supporting material to grow MoS_2-based nanostructures. They used a simple and facile two-step sonication method (bath and probe). Chothe et. al. [115] also synthesized MoS_2 and MoS_2-graphene hybrids by a single-step facile, low-cost, scalable and high-yield approach i.e. the in situ solid state method. These layered MoS_2 nanosheets anchored on graphene sheets improved the electrochemical performance by accelerating the ion and electron transport.

To increase the conductivity of MoS_2 which further increases the efficiency of electrocatalysis, MoS_2 nanostructures were developed directly on a highly conductive substrate i.e. on a carbon cloth. Carbon cloth possesses a large surface area, high electrical conductivity, excellent chemical stability, more electrochemical active sites which makes it an ideal substrate. Zhang et. al. [116] used a highly reproducible physical vapour deposition (PVD) approach to prepare MoS_2 nanosheet arrays supported on carbon cloth via a magnetron sputtering system. This explored its applications in water splitting and energy conversions. Mao et. al. [117] reported a one-step simple hydrothermal method to obtain 3D-hierarchical MoS_2 nanoflower arrays directly on carbon cloth as an efficient cathode electrode for hydrogen evolution reaction over a wide range of pH. Zhou et. al. [118] synthesized vertical MoS_2 nanosheet arrays on carbon cloth as a flexible electrode without any binder using a facile hydrothermal method to explore the application of supercapacitors. Lee et. al. [119] synthesized free-standing MoS_2 nanofilm on porous carbon cloth via facile electric-wire-explosion, dip-coating and thermal sulfidation processes. These MoS_2 nanofilms

were used as an anode in Li-ion batteries. Due to this outstanding performance of MoS_2 nanostructures grown on carbon cloth, we also synthesized MoS_2 nanoflakes on carbon cloth (discussed in Chapter 7).

2.4.3. Past works on applications of Molybdenum Disulphide nanostructure:

Molybdenum disulfide has been the subject of significant research due to its wide applications ranging from nanoelectronics to heterogeneous catalysis. MoS_2 nanostructures are used as sensors [120], anti-bacterial [121], catalysts [122] and as electrode materials in supercapacitors and batteries [123,124]. MoS_2 has also emerged as a promising candidate for HER electrocatalysts [125,126]. MoS_2 nanostructures exhibit excellent field emission property on which a detailed discussion is given below.

The characterization of field emission of MoS_2 nanoflower was done by Y.B. Li and his team in 2003 [127]. The three-dimensional flower-like MoS_2 nanoflowers were prepared in sulphur vapor atmosphere by reducing MoO_2 thin film on surface of Mo foil. Fig. 2.20 shows the SEM images of MoS_2 nanoflowers in both low and high magnifications which are of approximately 2 μm in size.

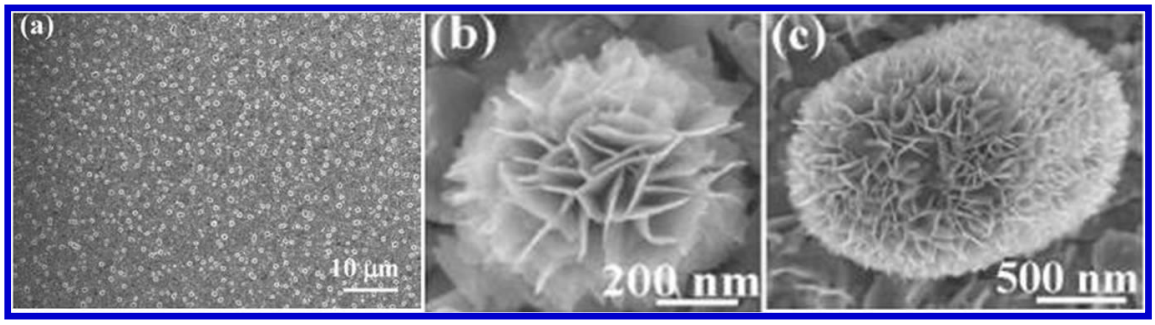

Fig. 2.20. *SEM images of MoS_2 nanostructures in **(a)** low and **(b,c)** high magnifications.* [127]

To study the field emission property of the MoS_2 nanoflowers, the nanoflower film was taken as cathode and aluminum probe of rod-like shape of cross-sectional area 1 mm^2 was placed as anode. This was carried out in a vacuum chamber and the pressure was maintained nearly

equal to 2.0×10^{-7} Torr. At different inter-electrode distances from 100 to 150 µm, the field emission curve J vs. V was recorded as shown in Fig. 2.21. As the inter-electrode distance increases, the current density decreases. To draw a current of 10 µA cm^{-2}, the electric field needed is 4.5- 5.5 V $(\mu m)^{-1}$ which is defined as the turn-on field and to draw a current of 10 mA cm^{-2}, the electric field needed is 7.6- 8.6 V $(\mu m)^{-1}$ which is defined as the threshold field. The extremely thin open edges of the petals of nanoflower result in low turn-on and threshold fields. The inset of Fig. 2.21 shows the Fowler-Nordheim (F-N) plot following linear relationship. These MoS_2 nanostructures can be used for making practical flat-panel displays.

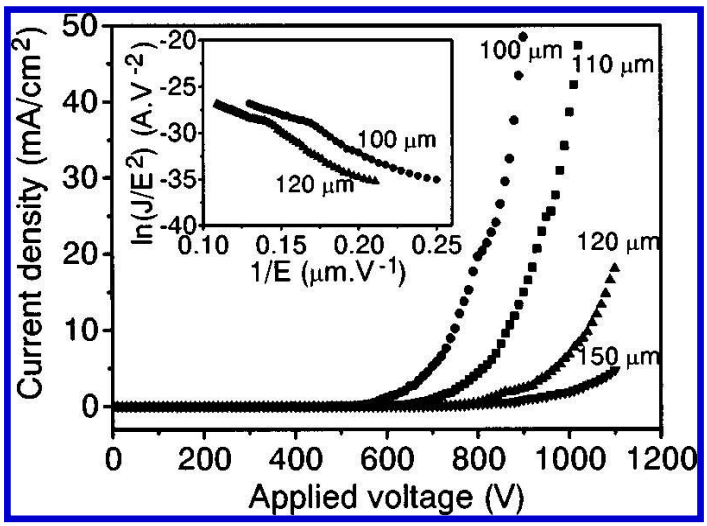

Fig. 2.21. *J vs. V curves and corresponding F-N plots.* [127]

On layered MoS_2 sheets, the first report of field emission was reported by Ranjit V. Kashid and his co-workers in 2013 [128]. The sample was synthesized in an inert atmosphere by solution method. The FESEM images in Fig. 2.22 shows the layered sheets of MoS_2 deposited on silicon substrate and the dimension of the layered MoS_2 sheets is ~ 1-2 µm.

At base pressure of ~ 1×10^{-8} mbar, the field emission study of the layered MoS_2 sheets was studied in ultra-high vacuum chamber.

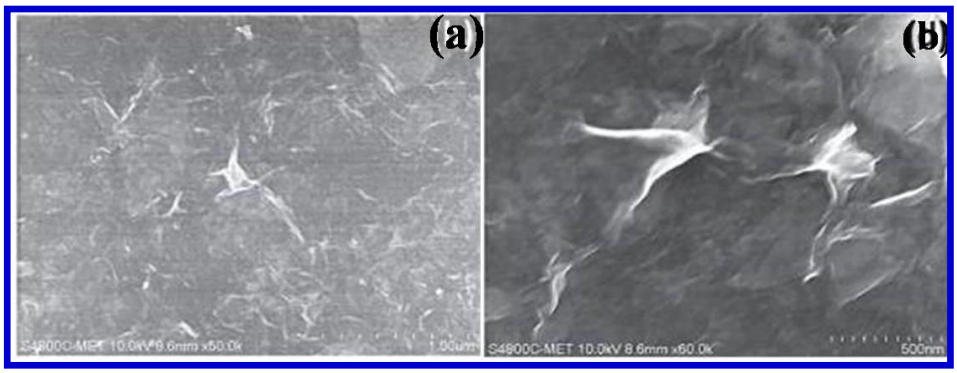

Fig. 2.22. *FESEM images of MoS_2 sheets deposited on Si-substrate.* [128]

For attaining a current density of 10 µA cm^{-2}, the turn-on field obtained is 3.5 V $(\mu m)^{-1}$ as can be seen from field emission current density (J) vs. applied electric field (E) plot shown in Fig. 2.23(a). The non-linear nature of F-N plot in Fig. 2.23(b) shows that the field emitter is of semiconducting nature. From F-N equation, the calculated enhancement factor (β) is ~ 1138. Due to this high value of β, a low turn-on field is obtained. The field emission current was also found to be stable for 3 h at 1 µA for time interval of 10 s and only ±15 % variation takes place in field emission current as shown in Fig. 2.23(c). These MoS_2 nanostructures show future applications in flat panel display and micro/nano-electronics.

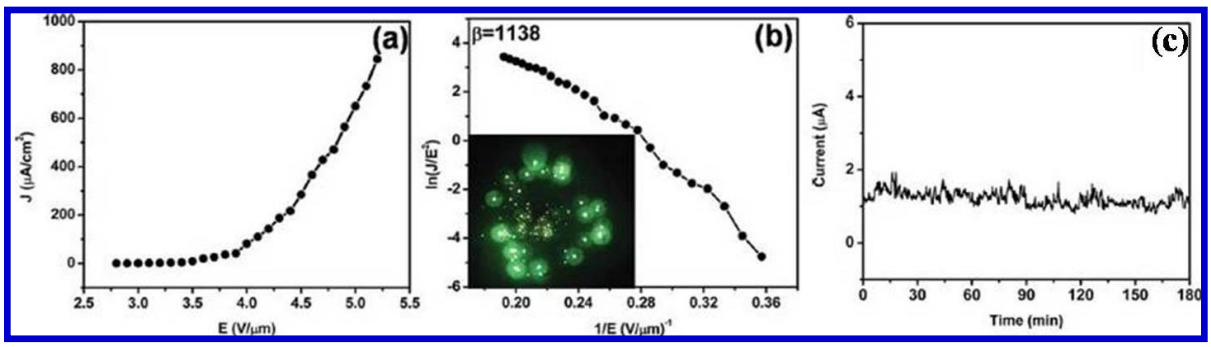

Fig. 2.23. ***(a)*** *J vs E curve,* ***(b)*** *F-N plot,* ***(c)*** *Field emission current stability for 3 h of few layers of MoS_2.* [128]

Ying-Hua Tan and his co-workers synthesized MoS_2@ZnO nano-heterojunctions and studied its field emission property [129]. At first, both MoS_2 and ZnO were synthesized separately by hydrothermal method and then, in presence of PEI solution, MoS_2-PEI hybrid was formed in

which ZnO nanoparticles were further added to form MoS_2-PEI-ZnO heterostructures. Argon annealing removes PEI and MoS_2@ZnO heterojunctions were formed. From SEM images as shown in Fig. 2.24, it can be clearly observed that both MoS_2 nanoflowers and ZnO nanoparticles are present in the nano-heterojunctions.

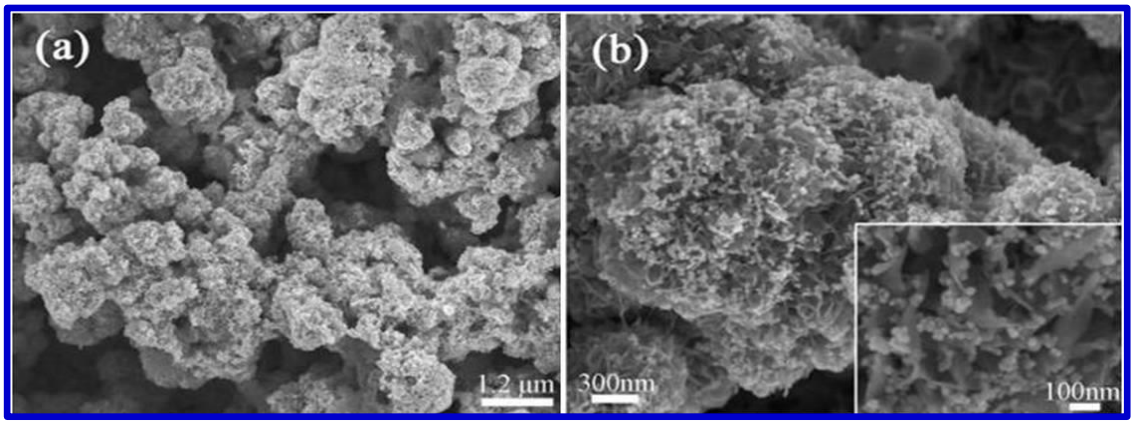

Fig. 2.24. *SEM images of MoS_2@ZnO nano-heterojunctions in **(a)** low and **(b)** medium magnification.* [129]

After incorporating MoS_2 on ZnO, it can be seen that the value of turn-on field and threshold field decreases which indicates that they have better field emission properties as compared to pure MoS_2 nanoflowers as shown in Fig. 2.25(a). To draw a current density of 10 μA cm^{-2}, the electric field required is defined as the turn-on field which is 3.65 and 3.08 V $(\mu m)^{-1}$ for MoS_2 nanoflowers and MoS_2@ZnO heterojunctions respectively. The threshold field which is defined as the electric field required to draw a current density of 1 mA cm^{-2} is 9.03 and 6.9 V $(\mu m)^{-1}$ for MoS_2 nanoflowers and MoS_2@ZnO heterojunctions respectively. The corresponding F-N plot is shown in Fig. 2.25(b). So, after incorporating ZnO nanoparticles, the field emission property of pure MoS_2 is enhanced due to decrease in potential energy barrier and presence of more emission sites on the composite surface. These materials can be used as field emission devices in future.

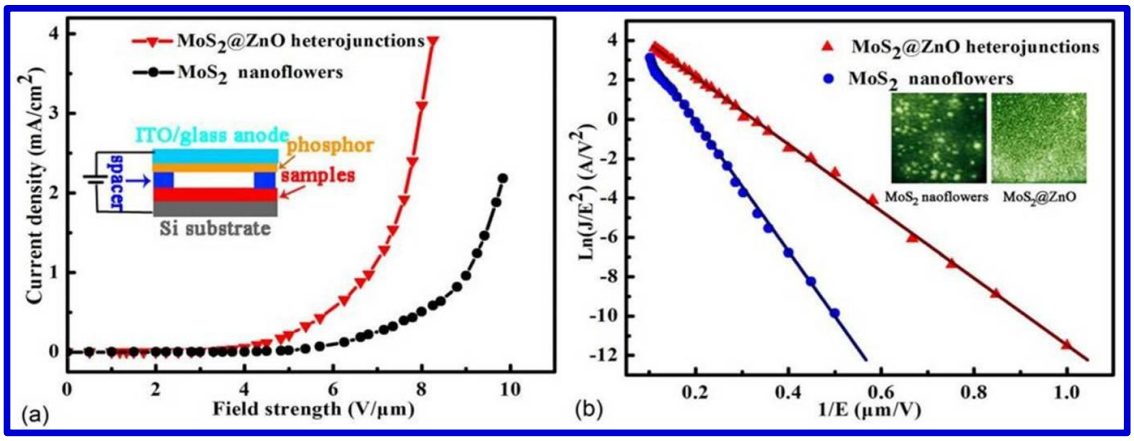

Fig. 2.25. ***(a)*** *J vs E curves and* ***(b)*** *corresponding F-N plots of MoS_2 nanoflowers and MoS_2@ZnO heterojunctions.* [129]

Dattatray J. Late and his co-workers studied the field emission property of MoS_2 thin films on W and Si-substrates by pulsed laser deposition method [130]. The FESEM images clearly show that on W-tip, nanocrystals of MoS_2 are overgrown which makes it an electron emitter because this type of growth is advantageous for film-substrate combination (Fig. 2.26(a,b)). MoS_2 grown on Si-substrate shows nanometric protrusions and the entire surface of Si-substrate is covered by them uniformly as depicted in Fig. 2.26(c).

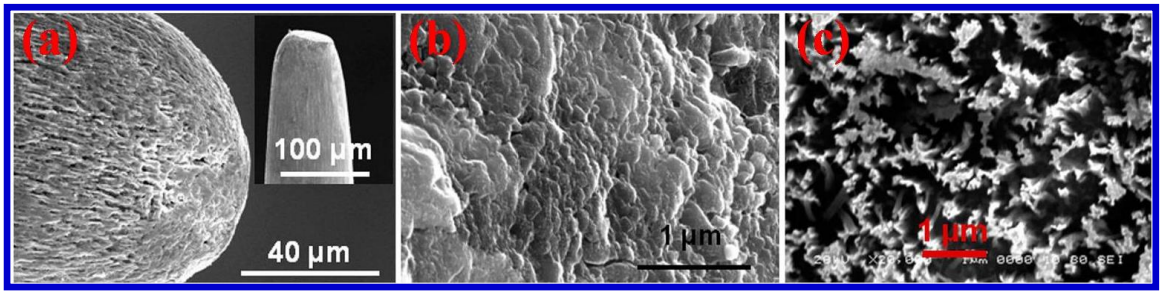

Fig. 2.26. *FESEM images of MoS_2 thin film on substrates W-tip* ***(a,b)*** *and Si* ***(c)***. [130]

At first, on W-tip, the field emission of PLD MoS_2 films was studied as shown in Fig. 2.27. From current density (J) vs. applied voltage (V) curve, it can be seen that at voltage 3.8 kV, the current density of about 30 mA cm^{-2} can be drawn. Also, the semiconducting nature of

MoS_2 is confirmed by the non-linear nature of its corresponding F-N plot. From Fig. 2.27(c), it can be seen that at preset value of 1 μA, the emission current exhibits good stability over a period of 3 h.

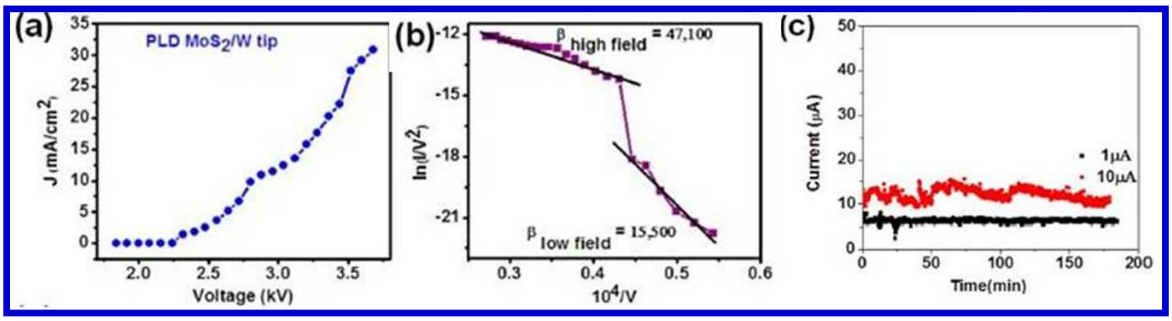

Fig. 2.27. ***(a)*** *J vs. V curve and* ***(b)*** *F-N plot of PLD MoS_2 films on W-tip,* ***(c)*** *Stability plot of field emission current.* [130]

Further, the field emission characterization was studied on Si-substrate (Fig. 2.28), the electric field required to draw a current density of 10 μA cm^{-2} obtained is 2.8 V $(\mu m)^{-1}$ which is less than a previous report of MoS_2 nanosheet on Si-substrate (~3.5 V $(\mu m)^{-1}$) [128]. The presence of nanometric protrusions may be the reason for this low value of turn-on field. The quantum mechanical tunneling process is followed by PLD MoS_2 grown on Si-substrate which can be depicted from the linear nature of F-N plot.

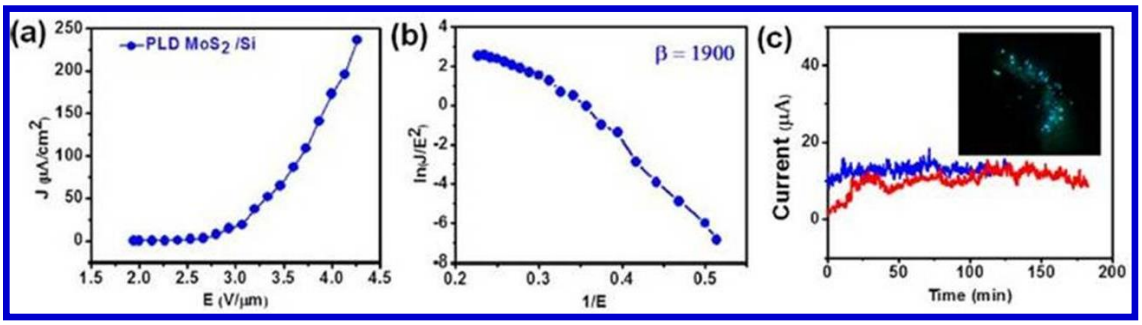

Fig. 2.28. ***(a)*** *J vs. E curve and* ***(b)*** *F-N plot of PLD MoS_2 thin film on Si-substrate,* ***(c)*** *Stability plot of field emission current.* [130]

At preset values of current 1 μA and 10 μA, the emission current-time plot shows fluctuations within ±10 % of average value (Fig. 2.28(c)). These PLD MoS_2 nanostructures grown on W and Si-substrates have future applications in field emission display and fundamental research.

Wang et. al. studied the field emission of layered MoS_2 nanosheets on different metal coated substrates by using the technique vacuum electron beam vapor deposition (EBVD) [131]. By modifying growth conditions and time of deposition, the thickness of nanosheets and metal coating are well-controlled. From FESEM images in Fig. 2.29, it can be seen that on both metal coated (Al or Mo) glass and ceramic substrates, the prepared MoS_2 film have large number of nanosheets stacked vertically. But in case of glass substrate, the surface of MoS_2 film is flat whereas in ceramic surface, it is irregular due to the pre-treatment of ceramic.

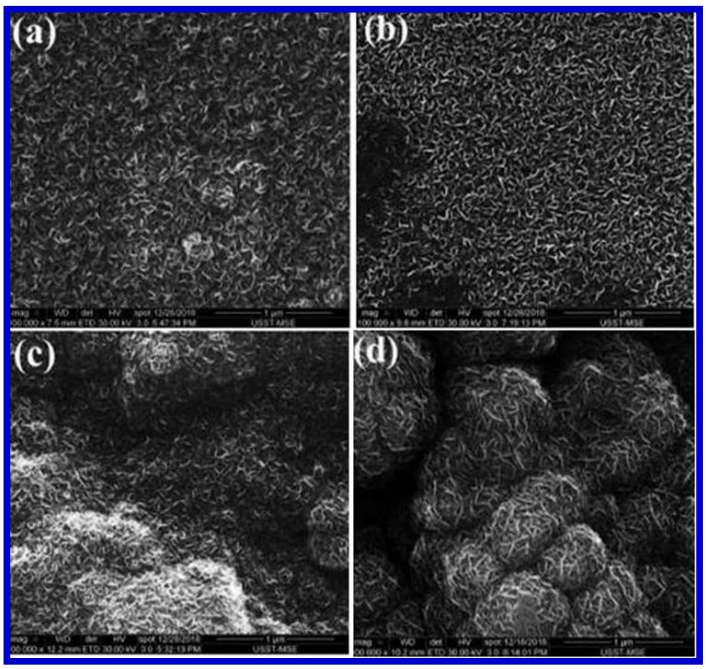

Fig. 2.29. *FESEM images of MoS_2 thin film on different substrates **(a)** glass-Al/MoS_2, **(b)** glass-Mo/MoS_2, **(c)** ceramic-Al/MoS_2, **(d)** ceramic-Mo/MoS_2.* [131]

The effect of different substrates on field emission properties of MoS_2 nanosheets was studied which is represented in Fig. 2.30 (a). It was observed that the glass-Al/MSNS sample (J_{max}=103.0 μA cm^{-2}) shows better field emission behavior as compared to that of glass-Mo/MSNS sample (J_{max}=28.1 μA cm^{-2}) whereas the E_{th} (for attaining a current density of 10 μA cm^{-2}) of glass-Al/MSNS sample (3.6 V/μm) is less than glass-Mo/MSNS sample (6.0 V/μm). Besides these values of J_{max} and E_{th}, FE performance of glass-Al/MSNS sample is better because Al is more convenient than Mo for MoS_2 in terms of work function and metal resistivity. It allows Al to make ohmic contact with MoS_2 very easily which further allows electrons in Al to enter the FE layer of MSNS. Also, the field enhancement factor of glass-Al/MSNS sample is greater than glass-Mo/MSNS sample which permits electron to enter vacuum very smoothly through the tunneling effect.

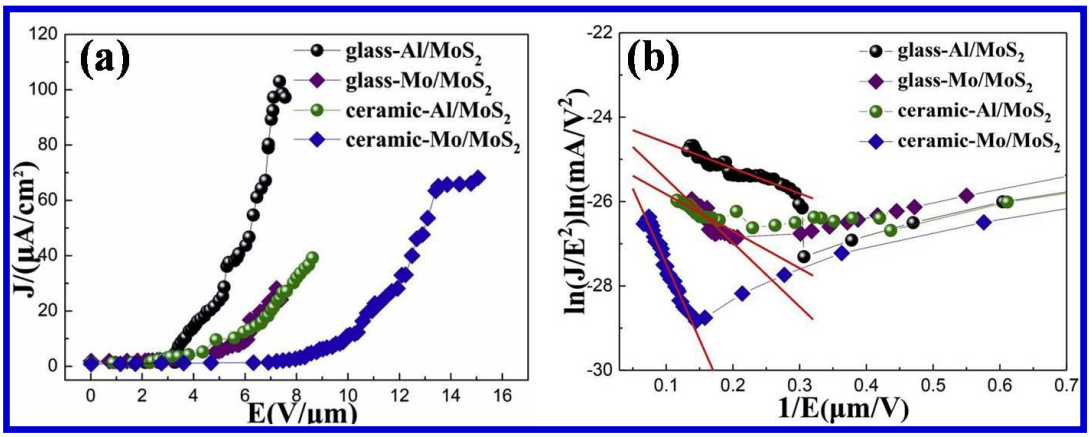

Fig. 2.30. ***(a)*** *Emission current density (J) vs. electric field (E) curves and* ***(b)*** *corresponding F-N plots of various MoS_2 samples on different substrates.* [131]

On the other hand, in case of sample grown on ceramic substrate, the E_{th} (9.9 V/μm) and J_{max} (68.1 μA cm^{-2}) of ceramic-Mo/MSNS sample is greater than E_{th} (5.5 V/μm) and J_{max} (39.2 μA cm^{-2}) of ceramic-Al/MSNS sample. But ceramic-Al/MSNS sample gives better FE performance when the device is working properly and the electric field applied externally is same. The corresponding F-N plots of all MoS_2 samples synthesized are shown in Fig. 2.30(b) indicating linear relationship of negative slope in the high electric field region only.

So, the FE performance of MoS_2 can be increased by using different types of substrate in such a way that the difference between the work function of MoS_2 sample and substrate is small.

2.5. References:

[1] V. Manikandan, R. Elancheran, P. Revathi, P. Suganya, K. Krishnasamy, *Bull. Mater. Sci.* 43 (2020) 1-10.

[2] S.W. Chou, J.Y. Lin, *J. Electrochem. Soc.* 160 (2013) D178-D182.

[3] X. Ou, L. Gan, Z. Luo, *J. Mater. Chem. A* 2 (2014) 19214-19220.

[4] Z. Cui, Y. Ge, H. Chu, R. Baines, P. Dong, J. Tang, Y. Yang, P.M. Ajayan, M. Ye, J. Shen, *J. Mater. Chem. A* 5 (2017) 1595-1602.

[5] R. Khan, M. Samanta, S. Ghosh, N.S. Das, K.K. Chattopadhyay, *Int. J. Hydrogen Energy* 44 (2019) 21315-21323.

[6] D.M. Wilhelmy, E. Matijevie, *J. Chem. Soc., Faraday Trans.* (1984) 563.

[7] T. Krogulec, Z. Galus, *J. Electroanal. Chem.* 117 (1981) 109-118.

[8] H. Tomesz, J.K. Jan, C. Ewe, K. Tadeusz, *J. Electroanal. Chem.* 367 (1994) 212.

[9] M. Abboudi, A. Mosset, *J. Solid State Chem.* 109 (1994) 70-73.

[10] A. Olivas, J. Cruz-Reyes, V. Petranovskii, M. Avalos, S. Fuentes, *J. Vac. Sci. Technol. A* 16 (1998) 3515-3520.

[11] N. Chen, W. Zhang, W. Yu, Y. Qian, *Mater. Lett.* 55 (2002) 230-233.

[12] G. Shen, D. Chen, K. Tang, C. An, Q. Yang, Y. Qian, *J. Solid State Chem.* 173 (2003) 227-231.

[13] A. Ghezelbash, M.B. Sigman, B.A. Korgel, *Nano Lett.* 4 (2004) 537-542.

[14] X. Liu, *Mater. Sci. and Eng. B* 119 (2005) 19-24.

[15] F. Xu, Y. Xie,* X. Zhang, C. Wu, W. Xi, J. Hong, X. Tian, *New J. Chemistry* 27 (2003) 1331-1335.

[16] Q. Pan, K. Huang, S. Ni, F. Yang, D. He, *Mater. Res. Bull.* 43 (2008) 1440-1447.

[17] C. Tang, C. Zang, J. Su, D. Zhang, G. Li, Y. Zhang, K. Yu, *Appl. Surf. Sci.* 257 (2011) 3388-3391.

[18] S. Nandhini, A.J.C. Mary, G. Muralidharan, *Appl. Surf. Sci.* 449 (2018) 485-491.

[19] R. Bhardwaj, R. Jha, M. Bhushan, *Appl. Nanosci.* 10 (2020) 3757-3772.

[20] W. Dong, L. An, X. Wang, B. Li, B. Chen, W. Tang, C. Li, G. Wang, *J. Alloys and Comp.* 509 (2011) 2170-2175.

[21] B. Zhang, X. Ye, W. Dai, W. Hou, Y. Xie, *Chem. Eur. J.* 12 (2006) 2337-2342.

[22] C.S. Dai, P.Y. Chien, J.Y. Lin, S.W. Chou, W.K. Wu, P.H. Li, K.Y. Wu, T.W. Lin, *ACS Appl. Mater. Interfaces* 5 (2013) 12168-12174.

[23] W. Zhou, X. Cao, Z. Zeng, W. Shi, Y. Zhu, Q. Yan, H. Liu, J. Wang, H. Zhang, *Energy Environ. Sci.* 6 (2013) 2216-2221.

[24] Z. Xing, Q. Chu, X. Ren, C. Ge, A.H. Qusti, A.M. Asiri, A.O. Al-Youbi, X. Sun, *J. Pow. Sour.* 245 (2014) 463-467.

[25] K. Krishnamoorthy, G.K. Veerasubramani, S. Radhakrishnan, S.J. Kim, *Chemical Eng. J.* 251 (2014) 116-122.

[26] Z. Zhang, Z. Huang, L. Ren, Y. Shen, X. Qi, J. Zhong, *Electrochimica Acta* 149 (2014) 316-323.

[27] J.J. Li, Y.X. Hu, M.C. Liu, L.B. Kong , Y.M. Hu, W. Han, Y.C. Luo, L. Kang, *J. Alloys Comp.* 656 (2016) 138-145.

[28] J.S. Chen, C. Guan, Y. Gui, D.J. Blackwood, *ACS Appl. Mater. Interfaces* 9 (2017) 496-504.

[29] Y.L. Wang, X.Q. Wei, M.B. Li, P.Y. Hou, X.J. Xu, *Appl. Surf. Sci.* 436 (2018) 42-49.

[30] Z. Li, C. Gao, J. Zhang, A. Meng, H. Zhang, L. Yang, *J. Alloys Comp.* 798 (2019) 500-506.

[31] I.A. Khan, R. Medwal, S. Fareed, A. Farid, J.V. Vas, M.V. Reddy, R.S. Rawat, *Mater. Res. Exp.* 7 (2020) 015517.

[32] S. Zhou, A. Hu, D. Liu, X. Chen, Q. Tang, T. Tao, H. Chen, *Electrochimica Acta* 339 (2020) 135938.

[33] T.W. Lin, C.J. Liu, C.S. Dai, *Appl. Catal. B: Environmental* 154 (2014) 213-220.

[34] W. Zhou, X.J. Wu, X. Cao, X. Huang, C. Tan, J. Tian, H. Liu, J. Wang, H. Zhang, *Energy & Environmental Science* 6 (2013) 2921-2924.

[35] C. Ouyang, X. Wang, C. Wang, X. Zhang, J. Wu, Z. Ma, S. Dou, S. Wang, *Electrochimica Acta* 174 (2015) 297-301.

[36] J. Chao, D. Duan, S. Xing, Y. Zhao, X. Zhang, S. Gao, X. Li, Q. Fan, J. Yang, *Solid State Sciences* 43 (2015) 59-62.

[37] Y. Fazli, S.M. Pourmortazavi, I. Kohsari, M.S. Karimi, M. Tajdari, *J Mater. Sci.: Mater. Electron.* 27 (2016) 7192-7199.

[38] A. Molla, M. Sahu, S. Hussain, *Scientific Reports* 6 (2016) 1-11.

[39] C. Tang, Z. Pu, Q. Liu, A.M. Asiri, Y. Luo, X. Sun, *Int. J. Hydrogen Energy* 40 (2015) 4727-4732.

[40] J. Li, P.K. Shen, Z. Tian, *Int. J. Hydrogen Energy* 42 (2017) 7136-7142.

[41] Y. Qu, M. Yang, J. Chai, Z. Tang, M. Shao, C.T. Kwok, M. Yang, Z. Wang, D.H.C. Chua, S. Wang, Z. Lu, H. Pan, *ACS Appl. Mater. Interfaces* 9 (2017) 5959-5967.

[42] J. Yu, F.X. Ma, Y. Du, P.P. Wang, C.Y. Xu, L. Zhen, *ChemElectroChem* 4 (2017) 594-600.

[43] Z. Li, B. Liu, X. Li, S. Yu, L. Wang, Y. Hou, Y. Zou, M. Yao, Q. Li, B. Zou, T. Cui, G. Zou, G. Wang, Y. Liu, *Nanotechnol.* 18 (2007) 255602.

[44] B. Bhattacharjee, D. Ganguli, K. Iakoubovskii, A. Stesmans, S. Chaudhuri, *Bull. Mater. Sci.* 25 (2002) 175.

[45] Y. Wang, L. Zhang, C. Liang, G. Wang, X. Peng, *Chem. Phys. Lett.* 357 (2002) 314-318.

[46] X.M. Meng, J. Liu, Y. Jiang, W.W. Chen, C.S. Lee, I. Bello, S.T. Lee, *Chem. Phys. Lett.* 382 (2003) 434–438.

[47] Y.C. Zhu, Y. Bando, D.F. Xue, *Appl. Phys. Lett.* 82 (2003) 1769–1771.

[48] Q. Zhao, L. Hou, R. Huang, *Inorganic Chem. Comm.* 6 (2003) 971-973.

[49] Z. Qi-Tao, H. Li-Song, H. Rui-An, G. Si-Peng, *Chin. Phys. Lett.* 20 (2003) 1496.

[50] X. Jiang, Y. Xie, J. Lu, L. Zhu, W. He, Y. Qian, *Chem. Mater.* 13 (2001) 1213-1218.

[51] Q.J. Feng, D.Z. Shen, J.Y. Zhang, H.W. Liang, D.X. Zhao, Y.M. Lu, X.W. Fan, *J. Cryst. Growth* 285 (2005) 561-565.

[52] S. Biswas, S. Kar, S. Chaudhuri, *Synthesis and Reactivity in Inorganic, Metal-Organic and Nano-Metal Chemistry*, 36 (2006) 33-36.

[53] F. Gu, C.Z. Li, S.F. Wang, M.K. Lü, *Langmuir* 22 (2006) 1329-1332.

[54] H. Peng, B. Liuyang, Y. Lingjie, L. Jinlin, Y. Fangli, C. Yunfa, *Nanoscale Res. Lett.* 4 (2009) 1047-1053.

[55] A.N. Yazici, M. Öztaş, M. Bedir, *J. Lumin.* 104 (2003) 115-122.

[56] V. Dimitrova, J. Tate, *Thin Solid Films* 365 (2000) 134-138.

[57] P. Roy, J.R. Ota, S.K. Srivastava, *Thin Solid Films* 515 (2006) 1912-1917.

[58] M. Yoneta, M. Ohishi, H. Saito, T. Hamasaki, *J. Cryst. Growth* 127 (1993) 314-317.

[59] P.P. Hankare, P.A. Chate, D.J. Sathe, A.A. Patil, *Appl. Surf. Sci.* 256 (2009) 81-84.

[60] A.H. Afifah Maheran, H. Abdullah, M. Said, M. N. Zul Atfyi Fauzan, N.Z. Haron, *2011 IEEE Regional Symposium on Micro and Nano Electronics.*

[61] A. Mukherjee, P. Mitra, *J. Physical Sci.* 16 (2012) 171-175.

[62] A.N. Singh, L.R. Singh, S.N. Singh, S.B. Singh, *Int. J. Luminescence and Applications* 3 (2013) 64-67.

[63] P.O. Offor, B.A. Okorie, F.I. Ezema, V.S. Aigbodion, C.C. Daniel-Mkpume, A.D. Omah, *J. Alloys Comp.* 650 (2015) 381-385.

[64] N.H. Abdullah, Z. Zainal, S. Silong, M.I.M. Tahir, K.B. Tan, S.K. Chang, *Mater. Chem. Phys.* 173 (2016) 33-41.

[65] M. Jothibas, S.J. Jeyakumar, C. Manoharan, I.K. Punithavathy, P. Praveen, J.P. Richard, *J. Mater. Sci: Mater. Electron.* 28 (2017) 1889-1894.

[66] S.I. Sadovnikov, A.V. Ishchenko, I.A. Weinstein, *J. Alloys Comp.* 831 (2020) 154846.

[67] D. Samanta, P. Basnet, T.I. Chanu, S. Chatterjee, *J. Alloys Comp.* 844 (2020) 155810.

[68] V.H. Choudapur, S.B. Kapatkar, A.B. Raju, K.G. Kodancha, *AIP Conference Proceedings* 2265 (2020) 030270.

[69] P.H. Borse, N. Deshmukh, R.F. Shinde, S.K. Date, S.K. Kulkarni, *J. Mater. Sci.* 34 (1999) 6087-6093.

[70] S. Sambasivam, D.P. Joseph, J.G. Lin, C. Venkateswaran, *J. Solid State Chem.* 182 (2009) 2598-2601.

[71] D.A. Reddy, G. Murali, R.P. Vijayalakshmi, B.K. Reddy, B. Sreedhar, *Cryst. Res. Technol.* 46 (2011) 731-736.

[72] D.A. Reddy, C. Liu, R.P. Vijayalakshmi, B.K. Reddy, *J. Alloys Comp.* 582 (2014) 257-264.

[73] A. Goudarzi, G.M. Aval, S.S. Park, M.C. Choi, R. Sahraei, M.H. Ullah, A. Avane, C.S. Ha, *Chem. Mater.* 21 (2009) 2375-2385.

[74] V. Ramasamy, K. Praba, G. Murugadoss, *Spectrochimica Acta Part A: Molecular and Biomolecular Spectroscopy* 96 (2012) 963-971.

[75] X.S. Fang, C.H. Ye, X.S. Peng, Y.H. Wang, Y. C. Wu, L.D. Zhang, *J. Cryst. Growth* 263 (2004) 263-268.

[76] W. Tang, D.C. Cameron, *Thin Solid Films* 280 (1996) 221-226.

[77] D. Adachi, T. Hama, T. Toyama, H. Okamoto, J. Mater. Sci: Mater. Electron. 20 (2009) 130-133.

[78] C. Falcony, M. Garcia, A. Ortiz, J.C. Alonso, *J. Appl. Phys.* 72 (1992) 1525-1527.

[79] C.S. Pathak, D.D. Mishra, V. Agarawala, M.K. Mandal, *Indian J. Phys.* 86 (2012) 777-781.

[80] Y. Lu, Y. Yang, L. Guan, D. Wang, J. Zhao, J. Yang, Z. Wei, F. Wang, Z. Yang, X. Li, *J. Lumin.* 226 (2020) 117332.

[81] T.V. Prevenslik, *J. Lumin.* 87 (2000) 1210-1212.

[82] C.N. Xu, T. Watanabe, M. Akiyama, X.G. Zheng, *Mater. Res. Bull.* 34 (1999) 1491-1500.

[83] M. Bredol, J. Merikhi, *J. Mater. Sci.* 33 (1998) 471-476.

[84] Y. Wada, H. Yin, T. Kitamura, S. Yanagida, *Chem. Commun.* 24 (1998) 2683-2684.

[85] A. Kumar, M. Kumar, V. Bhatt, D. Kim, S. Mukherjee, J.H. Yun, R.K. Choubey, *Chem. Phys. Lett.* 763 (2021) 138162.

[86] S.S. Kawar, B.H. Pawar, *Micro and Nano Lett.* 5 (2010) 100-104.

[87] M. Lădar, E.J. Popovici, I. Baldea, R. Grecu, E. Indrea, *J. Alloys Comp.* 434 (2007) 697-700.

[88] V. Kumar, M.K. Sharma, J. Gaur, T.P. Sharma, *Chalcogenide Lett.* 5 (2008) 289-295.

[89] K. Giribabu, R. Suresh, R. Manigandan, L. Vijayalakshmi, A. Stephen, V. Narayanan, *AIP Conf. Proc.* 1576 (2014) 148-151.

[90] I. Sarkar, M.K. Sanyal, S. Kar, S. Biswas, S. Banerjee, S. Chaudhuri, S. Takeyama, H. Mino, F. Komori, *Physical Review B* 75 (2007) 224409.

[91] T. Kang, J. Sung, W. Shim, H. Moon, J. Cho, Y. Jo, W. Lee, B. Kim, *J. Phys. Chem. C* 113 (2009) 5352-5357.

[92] F. Lu, W. Cai, Y. Zhang, Y. Li, F. Sun, S.H. Heo, S.O. Cho, *Appl. Phys. Lett.* 89 (2006) 231928.

[93] X. Fang, U.K. Gautam, Y. Bando, B. Dierre, T. Sekiguchi, D. Golberg, *J. Phys. Chem. C* 112 (2008) 4735-4742.

[94] S. Oda, K. Akagi, H. Kukimoto, T. Nakayama, *J. Lumin.* 16 (1978) 323-330.

[95] A.D. Dinsmore, D.S. Hsu, H.F. Gray, S.B. Qadri, Y. Tian, B.R. Ratna, *Appl. Phys. Lett.* 75 (1999) 802-804.

[96] A.E. Hichou, M. Addou, J.L. Bubendorff, J. Ebothé, B.E. Idrissi, M. Troyon, *Semicond. Sci. Technol.* 19 (2003) 230-235.

[97] E.Y.M. Lee, N.H. Tran, J.J. Russell, R.N. Lamb, *J. Phys. Chem. B* 108 (2004) 8355-8358.

[98] Z.G. Chen, J. Zou, G. Liu, X. Yao, F. Li, X.L. Yuan, T. Sekiguchi, G.Q. Lu, H.M. Cheng, *Adv. Funct. Mater.* 18 (2008) 3063-3069.

[99] Z.G. Chen, J. Zou, D.W. Wang, L.C. Yin, G. Liu, Q. Liu, C.H. Sun, X. Yao, F. Li, X.L. Yuan, T. Sekiguchi, G.Q. Lu, H.M. Cheng, *Adv. Funct. Mater.* 19 (2009) 484-490.

[100] M.W. Huang, Y.W. Cheng, K.Y. Pan, C.C. Chang, F.S. Shieu, H.C. Shih, *Appl. Surf. Sci.* 261 (2012) 665-670.

[101] M.S. Javed, S. Dai, M. Wang, D. Guo, L. Chen, X. Wang, C. Hu, Y. Xi, *J. Pow. Sour.* 285 (2015) 63-69.

[102] L.Q. Fan, G.J. Liu, C.Y. Zhang, J.H. Wu, Y.L. Wei, *Int. J. Hydrogen Energy* 40 (2015) 10150-10157.

[103] S. Su, Y. Xu, Q. Sun, X. Gu, L. Weng, L. Wang, *J. Mater. Chem. B* 6 (2018) 5323-5334.

[104] Y. Feldman, E. Wasserman, D.J. Srolovitz, R. Tenne, *Science* 267 (1995) 222-225.

[105] C.M. Zelenski, P.K. Dorhout, *J. Am. Chem. Soc.* 120 (1998) 734-742.

[106] W.J. Li, E.W. Shi, J.M. Ko, Z.Z. Chen, H. Ogino, T. Fukuda, *J. Cryst. Growth* 250 (2003) 418-422.

[107] J.V. Lauritsen, J. Kibsgaard, S. Helveg, H. Topsøe, B.S. Clausen, E. Lægsgaard, F. Besenbacher, *Nature Nanotechnol.* 2 (2007) 53-58.

[108] X. Chen, H. Li, S. Wang, M. Yang, Y. Qi, *Mater. Lett.* 66 (2012) 22-24.

[109] K.K. Liu, W. Zhang, Y.H. Lee, Y.C. Lin, M.T. Chang, C.Y. Su, C.S. Chang, H. Li, Y. Shi, H. Zhang, C.S. Lai, L.J. Li, *Nano Lett.* 12 (2012) 1538-1544.

[110] S. Najmaei, Z. Liu, W. Zhou, X. Zou, G. Shi, S. Lei, B.I. Yakobson, J.C. Idrobo, P.M. Ajayan, J. Lou, *Nature Mater.* 12 (2013) 754-759.

[111] G. Tontini, G.D.L. Semione, C. Bernardi, R. Binder, J.D.B. de Mello, V. Drago, *Industrial Lubrication and Tribology* 68 (2016) 658-664.

[112] C.P. Veeramalai, F. Li, Y. Liu, Z. Xu, T. Guo, T.W. Kim, *Appl. Surf. Sci.* 389 (2016) 1017-1022.

[113] C. Kanade, S. Arbuj, K. Kanade, K.S. Kim, G.Y. Yeom, T. Kim, B. Kale, *RSC Adv.* 8 (2018) 39749-39755.

[114] A.M. Abraham, G. Bharath, A. Hai, F. Banat, *J. Phys. D: Appl. Phys.* 53 (2019) 065501.

[115] U. Chothe, C. Ugale, M. Kulkarni, B. Kale, *Crystals* 11 (2021) 660.

[116] X. Zhang, Y. Zhang, B.B. Yu, X.L. Yin, W.J. Jiang, Y. Jiang, J.S. Hu, L.J. Wan, *J. Mater. Chem. A* 3 (2015) 19277-19281.

[117] B. Mao, B. Wang, F. Yu, K. Zhang, Z. Zhang, J. Hao, J. Zhong, Y. Liu, W. Shi, *Int. J. Hydrogen Energy* 43 (2018) 11038-11046.

[118] C. Zhou, J. Wang, X. Yan, X. Yuan, D. Wang, Y. Zhu, X. Cheng, *Ceramics Int.* 45 (2019) 21534-21543.

[119] D.Y. Lee, S.D. Seo, H.J. Song, D.W. Kim, *Int. J. Energy Research* 45 (2021) 11329-11337.

[120] D. Burman, A. Sharma, P.K. Guha, *IEEE Sensors Lett.* 2 (2018) 1-4.

[121] P. Basu, K. Mukherjee, S. Khamrui, S. Mukherjee, M. Ahmed, K. Acharya, D. Banerjee, P.M.G. Nambissan, K. Chatterjee, *Mater. Adv.* 1 (2020) 1726-1738.

[122] T. Feduschak, A. Akimov, M. Morozov, M. Uymin, V. Zaikovskii, I. Prosvirin, A. Vosmerikov, S. Zhuravkov, V. Vlasov, V. Kogan, *Comptes Rendus Chimie* 19 (2016) 1315-1325.

[123] F. Wang, G. Li, J. Zheng, J. Ma, C. Yang, Q. Wang, *RSC Adv.* 8 (2018) 38945-38954.

[124] D.K. Nandi, U.K. Sen, D. Choudhury, S. Mitra, S.K. Sarkar, *Electrochimica Acta* 146 (2014) 706-713.

[125] J. Benson, M. Li, S. Wang, P. Wang, P. Papakonstantinou, *ACS Appl. Mater. Interfaces* 7 (2015) 14113-14122.

[126] X. Geng, W. Sun, W. Wu, B. Chen, A. Al-Hilo, M. Benamara, H. Zhu, F. Watanabe, J. Cui, T.P. Chen, *Nature Comm.* 7 (2016) 1-7.

[127] Y.B. Li, Y. Bando, D. Golberg, *Appl. Phys. Lett.* 82 (2003) 1962-1964.

[128] R.V. Kashid, D.J. Late, S.S. Chou, Y.K. Huang, M. De, D.S. Joag, M.A. More, V.P. Dravid *Small* 9 (2013) 2730-2734.

[129] Y.H. Tan, K. Yu, J.Z. Li, H. Fu, Z.Q. Zhu, *J. Appl. Phys.* 116 (2014) 064305.

[130] D.J. Late, P.A. Shaikh, R. Khare, R.V. Kashid, M. Chaudhary, M.A. More, S.B. Ogale, *ACS Appl. Mater. Interfaces* 6 (2014) 15881-15888.

[131] X.P. Wang, M.H. Li, M.M. Guo, L.J. Wang, X.W. Yang, Y. Yang, M.J. Deng, G.R. Yang, Y.T. Qian, *Vacuum* 177 (2020) 109386.

Chapter 3

INSTRUMENTS AND APPARATUS

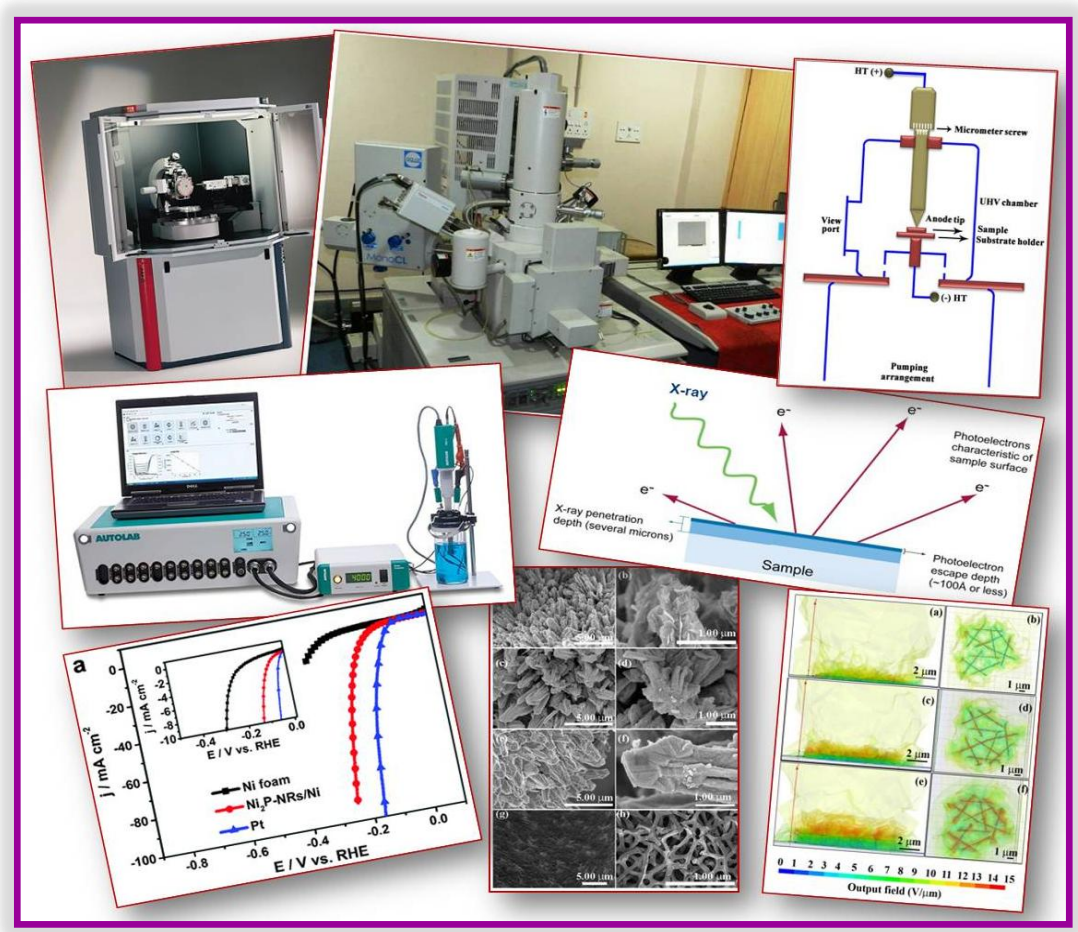

3.1. General description of synthesis methods of nanomaterials:

In the recent times, the synthesis of nanostructured materials has received significant attention which can be achieved by suitable physical and chemical techniques. The shape, size as well as the functionality of basic structural units of the nanomaterials to be synthesized can be controlled efficiently. Although, the synthesis of nanostructured materials can be done in several ways but generally, they can be classified into two main approaches: the top-down and the bottom-up. In top-down approach, the size of bulk material is reduced to nano-sized particle or structure with the help of physical processes like grinding, crushing, milling, electron-beam lithography etc. The greatest disadvantage of this method is the imperfection of crystallographic and surface structure. On the other hand, bottom-up approach involves gradual building of a nanomaterial from the bottom by assembling atom-by-atom or molecule-by-molecule. This method is very much economical as well as the shape and size distribution of the units of nanomaterials can be controlled easily. It includes chemical methods such as hydrothermal method, sol-gel synthesis, colloidal precipitation, electrodeposition etc. The methods we have used for the synthesis of nanostructured materials (Co-incorporated Ni_3S_2 hierarchical nanostructures, ZnS thin films, NiS microtubes, MoS_2 nanoflakes) are described below:

3.1.1. Hydrothermal set-up:

Hydrothermal method is a technique for synthesizing nano-hybrid and nano-composite materials. It is a non-conventional method of growing nanoparticles in an aqueous solution at high temperature (> room temperature) and pressure (> 1-2 atm) in an autoclave. Hydrothermal process has various advantages beginning from high product purity to

homogeneity. In 21st century, this method has become a frontline technology in the developing field of advanced material processing.

For material processing, hydrothermal technique requires a robust, non-reactive vessel known as autoclave as shown in Fig. 3.1. An autoclave is a pressurized device which is Teflon-lined from inner side and outer side is made from stainless steel. In this device, the heating of aqueous solution or organic solvents take place above their boiling point at a pressure higher than normal atmospheric pressure. Basically, an autoclave is a cylindrical iron chamber which is fitted with an iron screw cap. To withstand very high pressure during the reaction, the iron screw cap may be fitted very tightly with the iron chamber. Inside the iron chamber, a cylindrical Teflon tube with a Teflon cap is fitted which serves as the inert reaction chamber.

Fig. 3.1. ***(a)*** *Autoclave arrangement and* ***(b)*** *Teflon tube inside the autoclave used here*

3.1.2. Sol-gel set-up:

Sol-gel process is a wet-chemical method used for the synthesis of nanostructures. It is an economical and low-temperature technique that allows fine control on the product's chemical

composition. The primary advantage of chemical method is that at the molecular level, it has good chemical homogeneity.

At first, a 'sol' i.e. a colloidal solution is formed which gradually advances toward the formation of a gel-like substance. This gel is a diphasic system containing both liquid and solid phases. For phase separation, the simplest method is sedimentation and then, the remaining liquid is poured off but it is a time-taking process. Centrifugation is the best method to separate both solid and liquid phases; and the remaining liquid i.e. the solvent is removed by drying in vacuum oven. The distribution of porosity in the gel determines the rate at which the solvent can be removed.

3.2. General description of major synthesis apparatus:

3.2.1. Oven:

For performing hydrothermal reaction, a simple low temperature oven was used. Here, the reaction temperature was not more than 220 $^{\circ}$C. By the help of an electronic temperature controller with an accuracy of ± 0.5 $^{\circ}$C, the heating rate of the oven can be controlled. Apart from carrying out synthesis process, the ovens were also used for drying the sample. Fig. 3.2. shows the image of oven used.

Fig. 3.2. *Photograph of an oven*

3.2.2. Autoclavable Pyrex glass bottle:

Here, in our work, before carrying out the synthesis of MoS_2 nanoflakes on carbon cloth, the carbon cloth was activated with potassium permanganate ($KMnO_4$). This process was done within Pyrex glass bottle (Schott Duran, Germany) fitted with an autoclavable polyprelene screw cap. The maximum temperature these bottles can withstand is 140 $^{\circ}$C. But generally, the reaction in this system is carried below the boiling temperature of water i.e. 100 $^{\circ}$C. The diagram of the Pyrex bottle is shown in Fig. 3.3.

Fig. 3.3. *Autoclavable Pyrex glass bottle*

For finer tuning of aspect ratio of synthesized nanomaterials, a combination of physical and chemical techniques may be effective. For this purpose, RF magnetron sputtering technique was further introduced to sharpen or modify the initially synthesized nanomaterials.

3.2.3. Radio Frequency (RF) magnetron sputtering unit:

In sputtering, when the target is bombarded by high energy particles, the atoms are ejected (due to collision between surface atoms and the energetic particles) from a target or source material that is to be deposited on a substrate like silicon wafer. The process of sputtering starts when a substrate to be coated is placed in a vacuum chamber containing an inert gas (generally Argon) and a negative charge is applied to a target source material that will be deposited on to the substrate which causes the plasma to glow. By magnetron sputtering, a large quantity of thin films can be prepared at relatively high purity and low cost, so it's a dominant technique to grow thin films. Magnetron sputtering greatly increases the growth rate of the material because when a magnetic field is applied on the surface of the target cathode, it increases the plasma density. The sputtering yield is also increased by utilizing the constraints of the magnetic field on the charged particles. Magnetron sputtering is generally categorized into two parts, direct current (DC) magnetron sputtering and radio frequency (RF) magnetron sputtering. RF magnetron sputtering does not require the target as an electrode to be electrically conductive that's why it is more advantageous than DC magnetron sputtering.

To avoid building up of charge on certain types of sputtering target materials, RF sputtering technique alternates the electric potential of the current in the vacuum environment at radio frequencies. Otherwise, it can lead to complete termination of the sputtering of atoms and thus, ending the process.

In this present work, the sputtering system used for coating the required samples, is 12 inches vacuum coating unit which is being manufactured by HindHivac, Bangalore, India (Model: 12" MSPT). Fig. 3.4 shows the diagram of the RF-magnetron sputtering unit. The lower electrode is electrically grounded while the upper electrode is connected to a 13.56 MHz RF

generator in the standard parallel plate electrode configuration. For maximizing forward power and minimizing reverse power (which can damage the power supply), a set of variable capacitors and an inductor is provided to the RF source before being connected to the chamber.

Fig. 3.4. *Photograph of the RF-magnetron sputtering unit used here (HindHivac, Bangalore, India (Model: 12" MSPT))*

The sputtering unit consists of a vacuum system, deposition chamber and RF-generator. The vacuum system consists of an oil diffusion pump (Model: 114 D) of 114 mm backed by a rotary pump (Model: ED-12). The chamber can be evacuated using rotary and oil diffusion pump by closing it. The required vacuum could be attained up to the order of 10^{-6} mbar which can be measured by two gauges- Pirani (range: 0.5 mbar – 10^{-3} mbar, Model A6 STM) and Penning (range: 10^{-2} mbar – 10^{-6} mbar, Model STP 4M-1). A stainless steel circular base plate is present inside the sputtering chamber whose diameter is 33 cm and thickness is ~ 1.3 cm. There is a shutter which separates the target and the substrate which could be regulated

from the outside of the chamber. The RF electrode is properly linked with the target. The substrate temperature can be controlled from both outside the chamber and inside the chamber by liquid nitrogen and heater respectively. The RF-generator (Model: HindHivac RFG-500) is solid state, highly reliable for continuous operation and secured against reflected power. The analog panel meters is used for matching the RF power for forward and reflected powers.

3.3. Characterization Tools:

3.3.1. X-ray Diffractometer (XRD):

X-ray diffractometer is based on the principle of scattering of X-rays by the atomic planes of a crystal. The phenomenon by which an incident beam of X-rays interfere with one another due to the atomic planes of a crystal as the X-rays leave the crystal is called X-ray diffraction. X-rays was discovered in 1895 by Roentgen. X-ray scattering techniques are non-destructive analytical techniques. X-ray diffraction pattern is like a signature of the substance. They depict the information about the structure of the crystal, their chemical composition and physical properties of materials. XRD is used to identify crystalline phases and orientation of the substance. The average spacing's between layers or rows of atoms can also be measured in XRD.

Under what conditions the diffraction will take place depends on Bragg's law of diffraction. When a beam of X-ray falls on the crystal at glancing angle θ then, some of these rays will be reflected from the upper plate at same angle θ (Fig. 3.5). If the incident plane wave hits the crystal at an arbitrary angle, the interference of the reflected waves can be either destructive or constructive. If the waves that are combining are out of phase then, the destructive interference occurs. But Bragg's diffraction occurs when the wavelengths of the scattered X-rays interfere constructively. So, the constructive interference which occurs when the path

difference of travelling waves matches with the integral multiplication of the wavelength. After this constructive interference, a diffracted beam of X-rays escapes back out of the crystal at an angle equal to that of the incident beam. Bragg's law of diffraction is written as

$$2d\ sin\theta = n\lambda$$

where, d is the interplanar distance, θ is the glancing angle i.e. the angle formed by the incident ray (or reflected ray) and the plane surface of the crystal, n is the order of diffraction (n = 1,2,3,…) and λ is the wavelength of the incident beam.

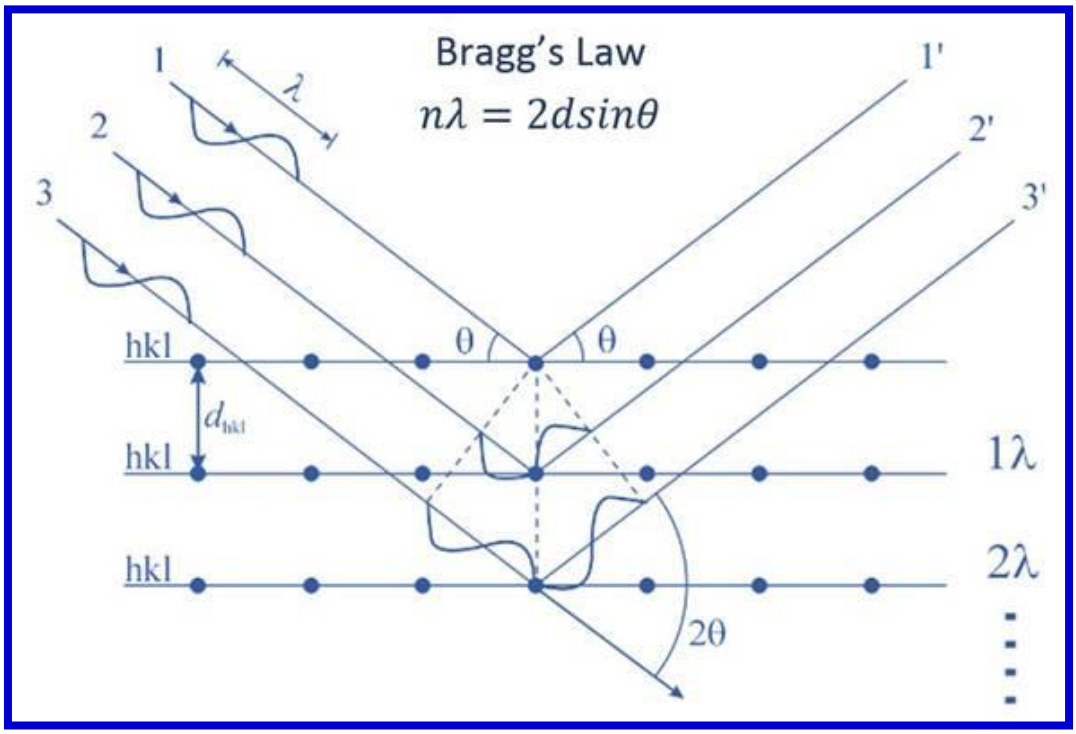

Fig. 3.5. *Basic diagram of Bragg's law of diffraction*

From XRD diffraction peaks, using Scherrer's formula the average crystallite size can be determined.

$$D = K\lambda/\beta \cos\theta$$

where, D is the average crystallite size, K is a constant whose value is approximately equal to unity, λ is the wavelength of the X-ray, β is full width at half maximum and θ is the angle of diffraction.

The components of a typical X-ray diffractometer are a source of radiation, slits which adjusts the shape of the beam, a monochromator to choose the wavelength, a sample and a detector. In a sophisticated apparatus, for fine adjustment of the sample and the positions of the detector, a goniometer can also be used. When the diffracted radiation is monitored by an area detector, the intense primary beam that has not been diffracted by the sample is usually stopped by a beamstop; otherwise the detector might be damaged. Usually, the beamstop may be semitransparent or it can be completely impenetrable to the X-rays. To figure out how much amount of radiation is absorbed by the sample is determined by the use of a semitransparent beamstop using the intensity observed through the beamstop.

The design of Bruker D8 X-ray diffractometers is done in such a way so that they can easily accommodate all applications of X-ray diffraction in material research, powder diffraction and high resolution diffraction. To ensure extremely precise angular values, all new D8 goniometer are equipped with stepper motors with optical encoder. Here, the XRD instrument used was Bruker D8 Advanced with Cu-Kα radiation of 1.54 Å as shown in Fig. 3.6(b).

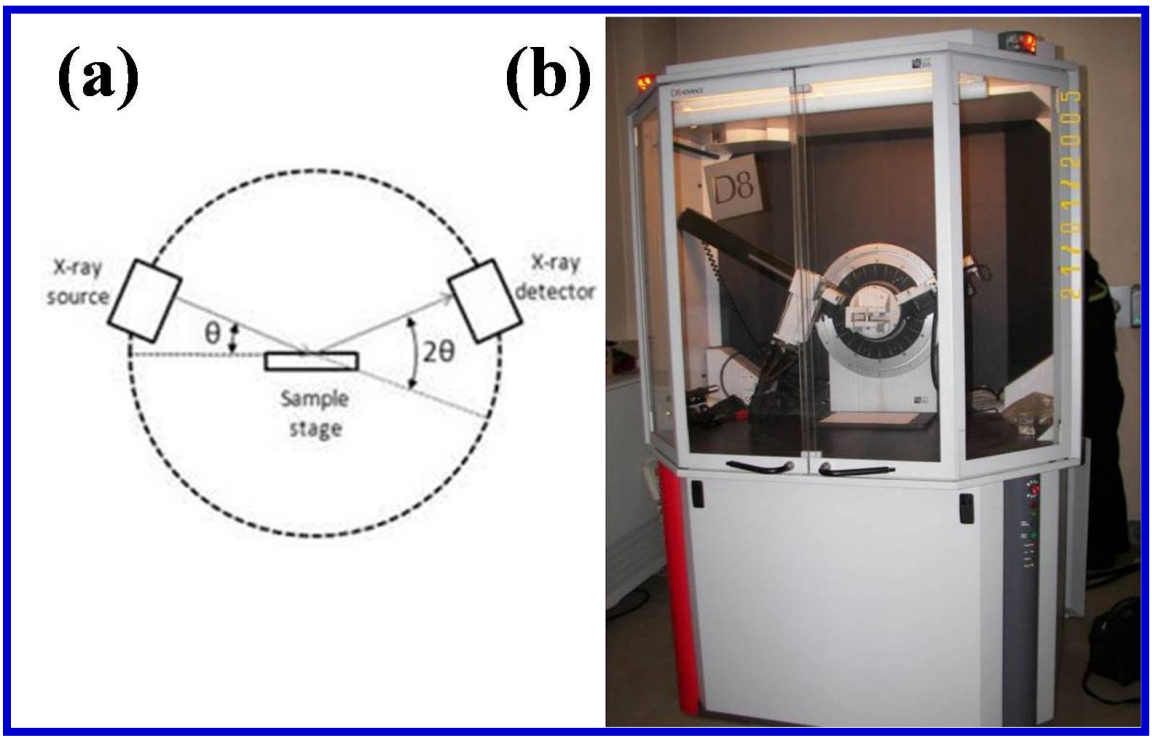

Fig. 3.6. ***(a)*** *Basic components of XRD diffractometer and* ***(b)*** *photograph of XRD instrument used here*

3.3.2. Electron Microscope:

An electron microscope enables to observe things at small scales. Instead of visible light, an electron microscope uses an electron beam to focus the object of study. As electrons have lower mass than those of protons and neutrons and hence, longer de Broglie wavelength for a given energy that's why wave properties of electrons are suitable for using in electron microscope. The wavelength of electron is much smaller than that of visible light which helps to distinguish features even less than fraction of a nanometer. The electron microscope has many advantages over ordinary microscope. In an ordinary microscope, the lenses which are used to magnify the specimen are replaced by a series of coil-shaped electromagnets which bends the electron beams when it travels through it. An electron micrograph is formed as an

image in electron microscope as compared to that of magnified image of the sample in ordinary microscope. Most familiar types of electron microscope are scanning electron microscope (SEM), transmission electron microscope (TEM) and scanning transmission electron microscope (STEM).

3.3.2.1. Field Emission Scanning Electron Microscope (FESEM):

FESEM is a type of electron microscope that uses a focused beam of electrons to produce images of a sample by scanning the surface. These electrons are released from a field emission source and accelerated in a gradient of high electrical field. The electron beam typically has an energy ranging from few hundred to 40 K eV. When the electrons interact with the atoms present in the sample, they produce various signals which enables to know information about the topography of the surface and composition of the specimen. When the interaction of electrons takes place with the material, it triggers the emission of secondary electrons. A detector captures these secondary electrons and an image of the surface of the sample is formed. The direction of the emission of the secondary electrons depends on the orientation of the features of the surface. The characteristic feature of the region of the surface which was exposed to the electron beam is reflected by the image formed. The size of SEM samples should be small enough so that it can easily fit on the specimen stage, and to increase their electrical conductivity, they may need special preparation. To withstand the high vacuum conditions and the high energy beam of electrons, they are to be stabilized. The mounting of samples are generally done on a specimen holder or stub using a conductive adhesive. Also, for defect analysis of semiconductor wafers, SEM is used. The instruments are manufactured in such a way that can examine any part of a 300 mm semiconductor wafer.

Here, to obtain resolution, the wave properties of electrons ($\lambda = \frac{h}{p}$, λ associated with a beam of electrons of momentum p) are used. If the electrons are accelerated through a potential difference V, the energy acquired by them is

$$eV = \frac{p^2}{2m}$$

$$\lambda = \sqrt{\frac{1}{(2meV)h}}$$

So, the wavelength obtained is $\lambda = 3.9 \times 10^{-12}$ m at V = 100,000 Volt, which is about a hundredth of the separation of the atoms in molecules (~0.25 nm) or crystals.

The digital image of FESEM instrument used here is shown in Fig. 3.7(b).

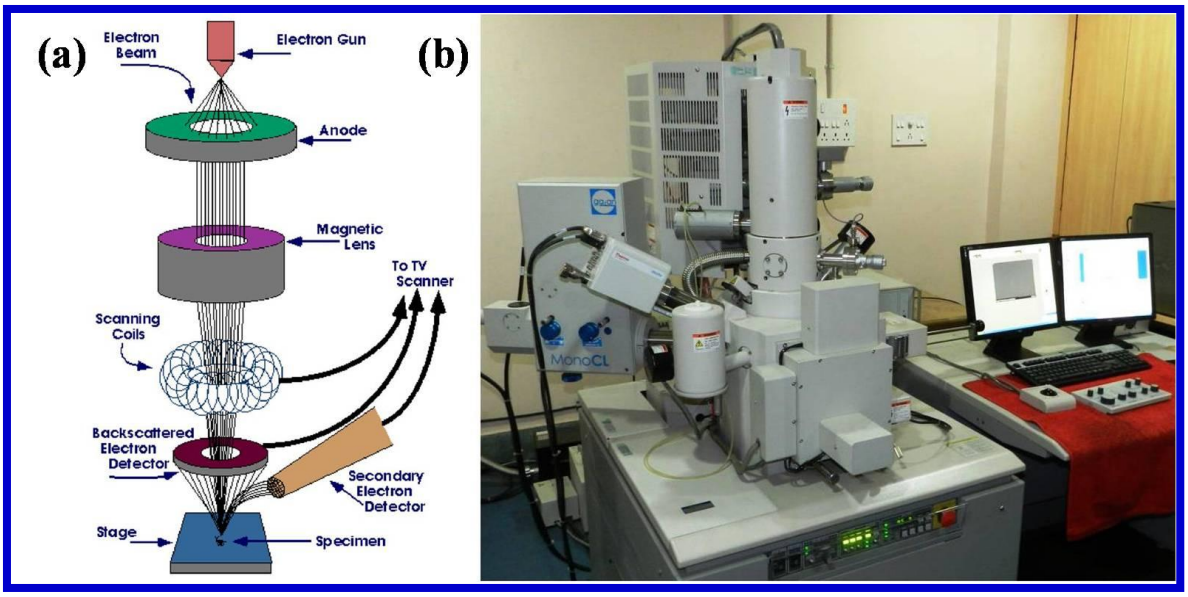

Fig. 3.7. ***(a)*** *Schematic representation of working principle of a scanning electron microscope and* ***(b)*** *digital photograph of FESEM instrument (Hitachi, S-4800) with EDX attachment*

3.3.2.2. Energy Dispersive X-ray Spectroscopy (EDS):

Energy Dispersive X-ray Spectroscopy, sometimes also referred to as EDX or EDAX, is an analytical technique used for the analysis of elemental composition of the specimen. During bombardment by an electron beam to analyze the composition, the EDS technique interacts with the X-rays produced from the sample. The characterization process of this technique follows the fundamental principle that each element has a specific atomic structure due to which a unique set of peaks appear on its electromagnetic emission spectrum. When SEM's electron beam bombards the sample, electrons are ejected from the atoms present in the surface of the sample. This results in electron vacancies which are filled by higher state electrons and then, to balance the energy difference between these two states of electrons, an X-ray is emitted. This X-ray energy is indication of the element from which it is radiated.

The EDS X-ray detector is lithium-drifted silicon, solid state device. It measures the relative abundance of the X-rays emitted versus their energy. When the detector is strike by the incident X-ray, a charge pulse is created which is proportional to X-ray's energy. Then, by a charge-sensitive pre-amplifier, the charge pulse is transformed to a voltage pulse (still remains proportional to X-ray's energy). A multi-channel analyzer then receives the signal where the pulses are sorted by voltage. For each incident X-ray, the energy obtained from voltage measurement is sent for display and data evaluation to a computer. Now, to determine the composition of elements of the sampled volume, the spectrum of X-ray energy versus counts is evaluated. EDX is an attachment of FESEM instrument and the digital image is shown in Fig. 3.7.

3.3.2.3. High Resolution Transmission Electron Microscope (HRTEM):

In 1931, the first prototype of electron microscope was demonstrated by Max Knoll and Ernst Ruska and in 1938; the first practical electron microscope was built by Eli Franklin Burton. The first commercial TEM was constructed by Siemens in 1939. The transmission electron microscope (TEM) is a very powerful tool for material science to observe the features of very small specimens. High Resolution Transmission Electron Microscope (HRTEM) is a specialized imaging mode of transmission electron microscope (TEM) which provides direct images of the specimen's crystallographic structure at an atomic scale more precisely.

TEM is a microscopy technique which uses high energy beam of electrons to illuminate the specimen to form an image. The specimen used is generally an ultra-thin section of thickness less than 100 nm or it is a suspension on a grid. As the electron beam is transmitted through the specimen, an image is formed when the electrons interact with the sample. Then, the image is magnified and focused on an imaging device like a layer of photographic film, a fluorescent screen or a sensor. This microscopy provides details about structure, morphology, crystallization and stress of a substance as compared to scanning electron microscope that tell us only about morphology of a specimen.

TEM has three main components: an electron gun, the image producing system and the image recording screen. An electron gun which is the source of electrons acts as a cathode is a heated V-shaped tungsten filament or it is a sharply pointed rod made up of lanthanum hexaboride (LaB_6) single crystal source. This electron gun is connected to a source of high voltage (~ 100-300 kV) and the gun can emit electrons by field electron or thermionic emission in vacuum when sufficient amount of current is given to it. The electron source is typically mounted in a Wehnelt cylinder when the source is thermionic to provide

preliminary focus of the emitted electrons into a beam. Some electrostatic electrodes with different voltages on each of them are used by field emission source to control the electric field shape and intensity. So, the electron gun is a combination of these electrostatic lens elements and the cathode. After it leaves the gun, a series of electrostatic plates accelerate the beam until it reaches its final voltage and then, it enters the condenser lens system. Further, the electron beam is focused by these upper lenses of the TEM to desired size and location on the specimen. Among these lenses, a diffraction pattern is generated by the objective lens in the back focal plane which can be described as the Fourier transform $F\Psi(r)$ of the wave function at the object exit plane $\Psi(r).n$. After this, the image is focused on a fluorescent screen when the collimated beam is passed through the sample. Finally, the image is recorded by direct exposure of a photographic emulsion or by a CCD camera and via other methods.

Generally, in TEM, there are two types of imaging technique named bright field imaging and dark field imaging. In bright field imaging, the scattered electrons are blocked and the unscattered i.e. transmitted electron beam is selected with the aperture. On the other hand, in dark field imaging, the scattered electrons are selected and the unscattered electron beam is excluded from the aperture.

Here, the high resolution transmission electron microscope used for the characterization of morphologies of the as synthesized nanomaterials is JEOL JEM 2100 (shown in Fig. 3.8).

Fig. 3.8. *Digital photograph of HRTEM instrument having phosphor screen and sample holders in left and right insets*

There are three independent condenser lenses present in this model and for any given probe size, produces the high probe current which strengthens the analytical and diffraction capabilities. There are numerous pumping options in this model including turbo-pumped/dry-pumped versions for lab environments and it do not allow for rotary or oil-based pumps. The instrument has a resolution of 0.1 nm and during routine measurements; the attained resolution is 8–10 Å. In this model, magnification could be varied from 50 X to 1,500,000 X with accelerating voltage 80-200 kV. The samples for TEM were prepared by dropping the suspension of the desired sample (to be characterized) onto a copper grid which is carbon coated and allowing the solvent to evaporate.

3.3.3. X-ray Photoelectron Spectrometer (XPS):

To measure the elemental composition, chemical state and electronic states of the elements that exist within composite nanostructures, X-ray photoelectron spectroscopy (SPECS, HSA 3500) is used. The excitation of photoelectron was achieved by the monochromatic Al Kα X-ray (1486.6 eV) source operated at 10 kV and 17 mA anode current. The residual pressure of the system was better than ~10^{-9} mbar. XPS also allows to find whether the metal is in a +1 or +2 state of a metal oxide and to know that ratio. The main working principle of X-ray photoelectron spectroscopy is that the XPS spectra is obtained when the sample is illuminated with an X-ray beam which results in emission of photoelectron from the sample simultaneously measuring the kinetic energy of the emitted electrons. This mechanism is schematically represented in Fig. 3.9.

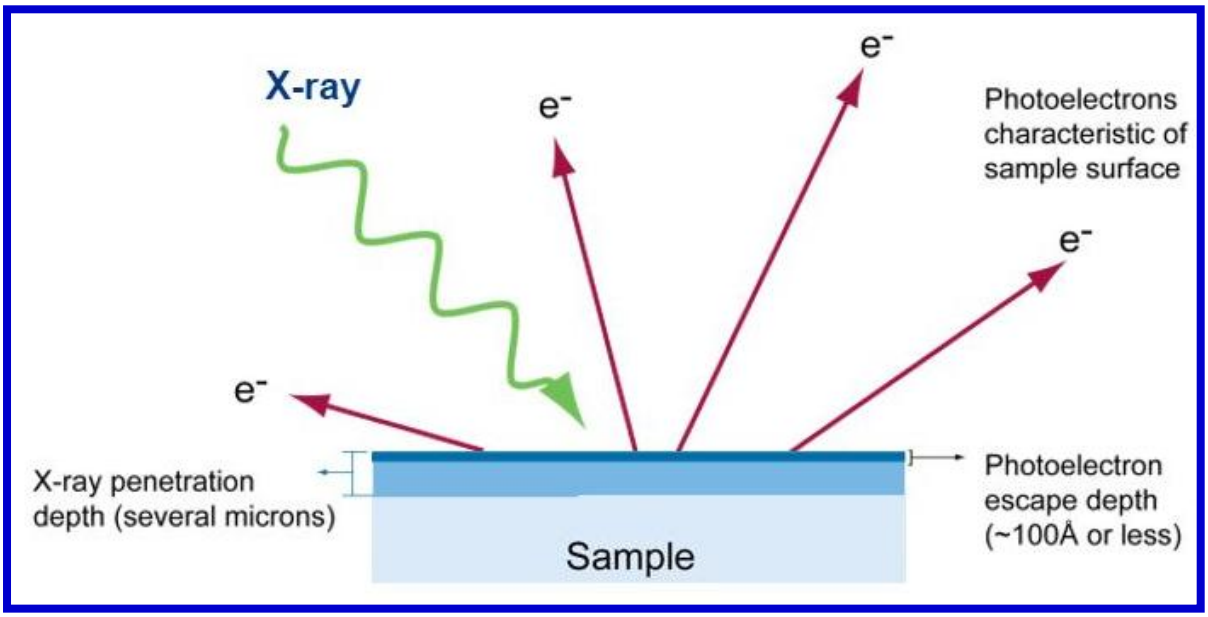

Fig. 3.9. *Pictorial representation of emission of photo-excited electron in XPS instrument*

The equation which relates the kinetic energy of the emitted electron (E_k) and the binding energy (E_B) is

$$E_B = h\nu - E_k$$

where, hν is the X-ray energy which is measured as a function of number of electrons.

In XPS, the sample requires ultra-high vacuum environment. When X-rays are incident on the sample from a low-energy monochromatic X-ray source, it causes ejection of electrons from the core-level. The energy of a photo emitted core electron is a characteristic of the element from which it was emitted and function of its binding energy. The primary data used for XPS is the energy analysis of the emitted photoelectrons. When the incident X-ray ejects the core electron, a core hole is created which is filled by an outer electron. Then, the emission of an Auger electron balances the energy of this transition. In addition to emitted photoelectrons, analysis of Auger electrons can be used in XPS.

Now, an electron energy analyzer detects the photoelectrons and Auger electrons emitted from the sample. The energy of these electrons is measured as a function of their velocity entering the detector. A spectrum representing the surface composition is obtained by counting the number of photoelectrons and Auger electrons as a function of their energy. An element present in the sampled volume is characterized by the energy corresponding to each peak and the area below a peak in the spectrum measures the relative amount of the element represented by that peak. The chemical state for the element is indicated by the peak shape and precise position.

As only those electrons generated near the surface escape and detected, XPS is also called a surface sensitive technique. The kinetic energy of the photoelectrons of interest is relatively low. Within the sample's atomic structure, inelastic collision occurs and that's why the photoelectrons originating more than 20 to 50 Å below the surface cannot escape with sufficient energy to be detected. The digital image of XPS instrument used here is shown in Fig. 3.10.

Fig. 3.10. *Photograph of XPS instrument (SPECS, HSA 3500)*

3.4. Electrochemical Measurement:

3.4.1. Basic principle of a potentiostat/galvanostat (Autolab PGSTAT):

Potentiostat/galvanostat is designed to perform electrochemical measurements. There are two modes of operation of a PGSTAT i.e. potentiostatic mode and galvanostatic mode. In potentiostatic mode, the potential of the counter electrode against the working electrode is

controlled accurately by a potentiostat/galvanostat so that the potential difference between the working electrode and the reference electrode is well-defined and also, corresponds to the value specified by the user. On the other hand, in galvanostatic mode, the current flow between the working electrode and the counter electrode is controlled and continuously monitored. So, a PGSTAT enables to control the value of applied potential or current specified by the user very accurately, anytime during the measurement by using a negative feedback mechanism.

In Fig. 3.11, a schematic diagram of the working principle of a PGSTAT is presented. As shown, the counter electrode (CE) is connected to the output of an electronic block named as Control Amplifier (CA) which forces current to flow through the cell. The low value of current is measured using a Current Follower (Low CF) and high values of current by a Shunt (High CR). With a Differential Amplifier (Diffamp), the potential difference is measured always between the reference electrode (RE) and connector S. The PSTAT/GSTAT switch is set accordingly depending on the mode the instrument is used (potentiostatic or galvanostatic). Then, the signal is fed into the summation point (Σ) which, together with the waveform set by the digital-to-analog converter (E_{in}) will serve as an input for the control amplifier.

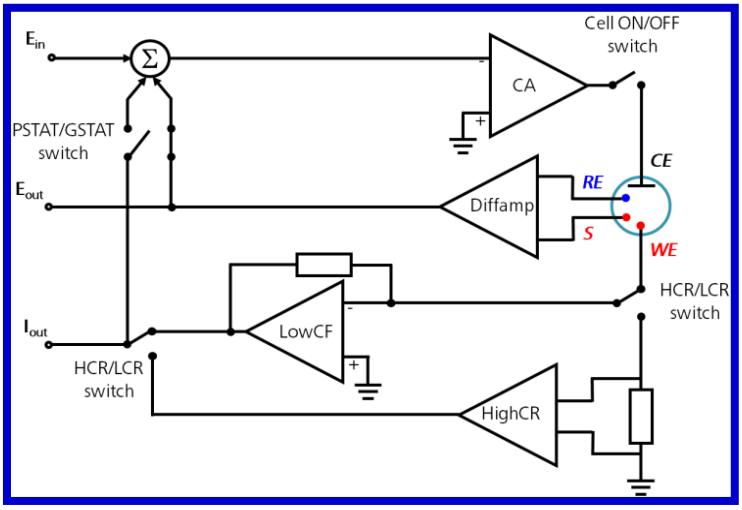

Fig. 3.11. *Basic schematic diagram of a potentiostat/galvanostat (PGSTAT)*

Here, the electrochemical measurements were conducted in Autolab PGSTAT (M-204) potentiostat/galvanostat connected to a computer using Nova 1.1 software. The digital image is shown in Fig. 3.12.

Fig. 3.12. *Digital image of Autolab PGSTAT*

3.4.2. Electrodes used in electrochemical set up:

(a) Counter electrode (CE) – The counter electrode, also known as auxiliary electrode is usually made of an inert material such as Pt, Au, glassy carbon, graphite. As the current flows between the working electrode (WE) and the counter electrode (CE), the surface area of CE must be higher than that of the WE so that the half-reaction occurring at the CE could be fast enough which will not limit the electrochemical process at the WE. The counter electrode acts as a source or sink for electrons so that current can be passed from the external circuit through the cell.

(b) Reference electrode (RE) – This electrode is used as a point of reference in the electrochemical cell for the potential control and measurement. It has a stable and well-known electrode potential which is generally obtained by employing a redox system with

constant concentrations of each reactants of the redox reaction. Also, the current flow through the reference electrode is kept close to zero.

(c) Working electrode (WE) – In an electrochemical system, the reaction of interest occurs on the working electrode. The materials of which the working electrode consist of ranges from inert metals (Au, Ag, Pt) to inert carbon (glassy carbon), and mercury drop and film electrodes. In a three-electrode system, the working electrode is often used in conjunction with the counter electrode and reference electrode.

3.4.3. Three-electrode configuration in Autolab:

Three-electrode configuration is the most commonly used electrochemical set-up used in electrochemistry. This system consists of a working electrode, counter electrode and reference electrode. In this set-up, the current is measured between the CE and the WE. The potential difference is controlled between the WE and the CE whereas it is measured between the RE and the WE. The function of reference electrode is to act as a reference in controlling and measuring the potential of working electrode, without passing any current. At low current density, the reference electrode should have a constant electrochemical potential. Also, the iR drop between the RE and WE is often very small since; the reference electrode passes negligible current. To reduce the uncompensated resistance and also, the ohmic losses arising from this resistance, the reference electrode should be placed as close as possible to the working electrode which can be achieved by using a Luggin-Haber capillary. A schematic view of three-electrode configuration is represented in Fig. 3.13(a).

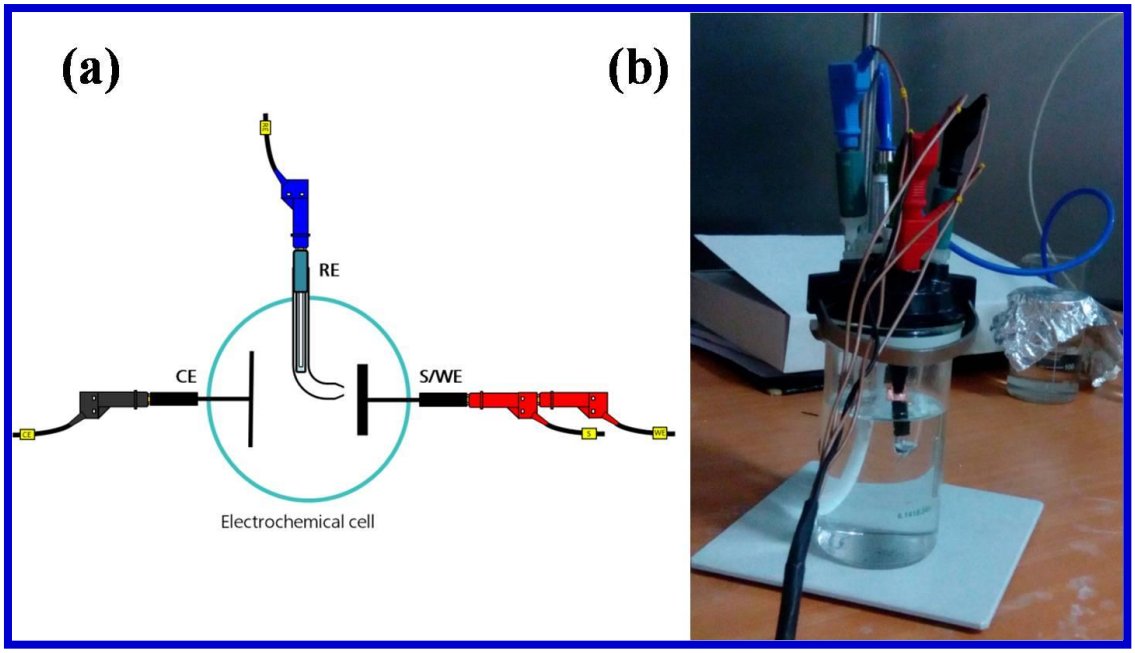

Fig. 3.13. ***(a)*** *Schematic view of the three-electrode configuration and* ***(b)*** *three-electrode cell attached in Autolab PGSTAT*

In our work, to assess the electrochemical activity for HER, the three-electrode configuration used is described here and is shown in Fig. 3.13(b). In this configuration, the as-prepared samples were directly taken as the working electrode, platinum wire as counter electrode and Ag/AgCl (saturated in 3 M KCl) as reference electrode. All the measurements were performed using the acidic electrolyte (0.5 M H_2SO_4). The linear sweep voltammetry (LSV) was conducted in the acidic solution at a scan rate of 10 mV s^{-1}. Reversible hydrogen electrode (RHE) was taken into account for all measurements by adding 0.27 V with Ag/AgCl reference electrode:

$$E\ (RHE) = E\ (Ag/AgCl) + 0.27\ V.$$

3.5. Optical Spectroscopy

3.5.1. Ultraviolet-Visible-Near Infrared Spectroscopy (UV-vis-NIR):

UV-vis-NIR spectroscopy is an instrument which is used to measure the reflection, absorbance or transmission characteristics i.e. optical properties of a sample. In this spectroscopy, light of ultraviolet region (200-400 nm) is absorbed by the molecule. The absorbance of light by a compound is measured as a function of wavelength in the UV-vis range. When a photon of UV-vis light is absorbed by a molecule, the molecule is excited from its ground state to an electronic excited state. It can also be said that an electron is promoted from the highest energy occupied molecular orbital (HOMO) of the molecule to the lowest energy unoccupied molecular orbital (LUMO) of the molecule. The energy of the ultra-violet radiation that is absorbed is equal to the energy difference between HOMO and LUMO. This is the basic principle of this spectroscopy.

The parameters like ionization energy, electron affinity and band gap (i.e. absorption energy) can be calculated from the absorption measurements. The experiment provides the accurate measure of the material's band gap since the photon with energies greater than band gap are absorbed while photon with energy less than band gap is transmitted.

According to Bardeen, the relation between the absorption co-efficient (α) and the band gap of the material, for the parabolic band structure is given by

$$\alpha h\nu = A\,(\hbar\omega - Eg)^{\gamma}$$

where, γ tells the electronic nature of the band gap. γ = 1/2 for direct allowed transition, γ = 2 for indirect allowed transition, γ = 3 for indirect forbidden transition and γ = 3/2 for direct forbidden transition.

A is measured by

$$A = \log(\frac{I}{I_0})$$

where, I_0 and I are the intensity of the incident and transmitted beams respectively.

E_g is the energy difference between the valence band and the conduction band called optical gap of the material and hν is the incident photon energy. $(\alpha h\nu)^2$ will show a linear dependence on the photon energy hν in case of direct transition. If $(\alpha h\nu)^2$ vs. hν is plotted, a straight line is obtained and the intercepts on the energy axis at $(\alpha h\nu)^2 = 0$ gives the optical gap of the sample.

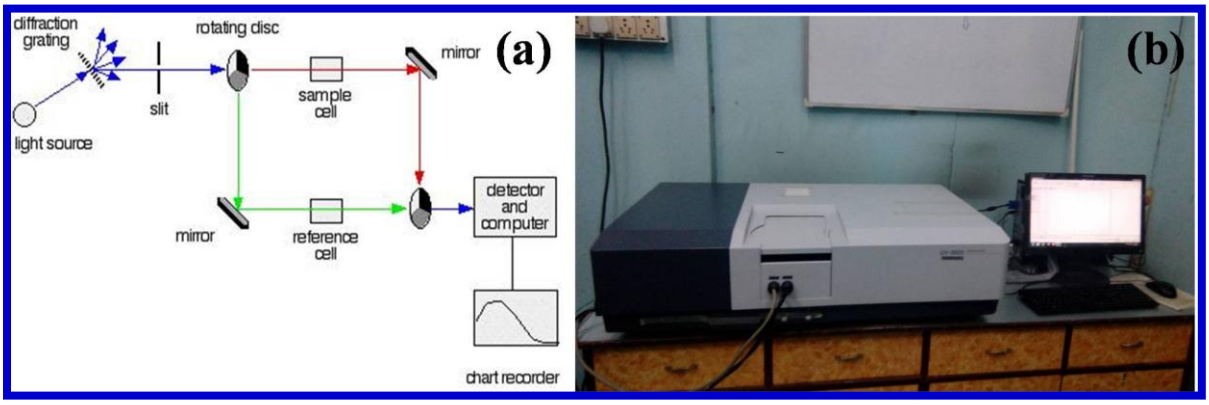

Fig. 3.14 shows the digital image and working principle of the UV-vis-NIR Spectrophotometer (Shimadzu, UV-3600).

Fig. 3.14. ***(a)*** *Schematic representation of working principle of UV-vis-NIR Spectrophotometer and* ***(b)*** *Photograph of the instrument used (Shimadzu, UV-3600)*

3.5.2. Fourier Transform Infrared Spectroscopy (FTIR):

Infrared radiation is that region of the electromagnetic spectrum which starts from the nominal red edge of the visible light to the microwave range. This radiation is invisible to the eye and it can be detected as a sensation of warmth on the skin. The infrared radiation (IR) can be further divided into three regions: near IR (14000 – 4000 cm^{-1}), mid IR (4000 – 400 cm^{-1}) and far IR (400 – 20 cm^{-1}). Most of the molecules change their fundamental vibration

levels in the mid IR region and for this reason; an infrared spectrometer which works in mid region of IR uses a method of obtaining infrared spectra by collecting an interferogram of a sample signal using an interferometer. Then, to obtain the spectrum, a Fourier transform is performed on the interferogram.

Fourier transform infrared spectroscopy (FTIR) is an analytical technique which measures the absorption of infrared radiation by the specimen versus wavelength. The molecular components and structures are identified by the infrared absorption bands. It is also used to identify chemical composition of organic materials, semiconductor materials, polymers and also inorganic materials in some cases. The samples used for analysis in FTIR can be in the form of solid, liquid, gas, powders, pastes, fibers etc. FTIR can be used to analyze samples having diameter up to ~ 12 millimeters and either measure in bulk or the top ~1.5 micrometer layer.

When a material is illuminated with infrared radiation, usually absorbed IR radiation excites molecules into a higher vibrational state. The energy difference between the at-rest and excited vibrational states determines the wavelength of light absorbed by a particular molecule. The molecular structure of the sample is characterized by the wavelengths that are absorbed by the sample.

An interferometer present in the FTIR spectrometer is used to modulate the wavelength from a broadband infrared source. The intensity of reflected or transmitted light is measured as a function of its wavelength by a detector. The signal that is attained from the detector is an interferogram then, to obtain a single-beam infrared spectrum it must be analyzed with a computer using Fourier transform. Generally, the FTIR spectra are plotted as intensity versus wavenumber (in cm^{-1}) where, the intensity can be plotted as the percentage of light absorbance or transmittance at each wavenumber (reciprocal of wavelength).

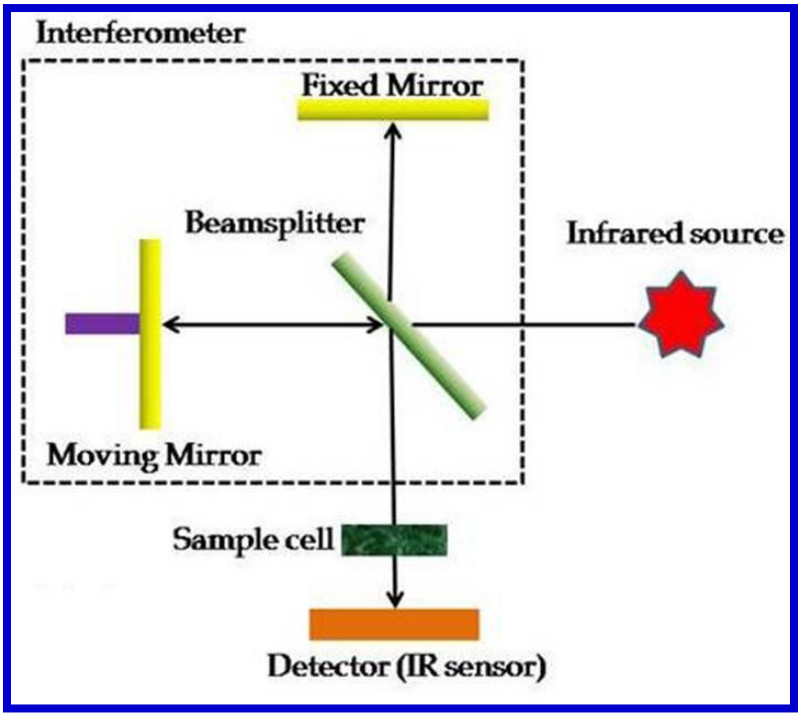

Fig. 3.15. *Schematic representation of the working principle of FTIR spectrometer*

The above figure 3.15. represents the schematic diagram of working principle of FTIR. The light from the infrared source after passing through the aperture of Michelson interferometer is collimated and enters the beam splitter. It splits the single beam into two parts, half of the light is reflected towards the fixed mirror and the other half is transmitted to the movable mirror. The light is reflected back to the beam splitter from both the mirrors and some fraction of this original light is then focused on the sample by entering sample compartment. Then, the light is refocused on to the detector after leaving the sample compartment. The difference in optical path length between the two arms to the interferometer is called optical path difference or retardation. By varying the retardation and recording the signal from the detector for different values of retardation, an interferogram is obtained. Then, the measured interferogram digitizes, the FT function is performed, and the required spectrum is obtained, i.e., a plot of the intensity at each individual frequency. The FTIR spectrometer used here is shown in Fig. 3.16.

Fig. 3.16. *Digital image of the FTIR spectrometer (Here, Shimadzu FTIR-8400S spectrometers were used for IR spectroscopic analysis)*

3.5.3. Photoluminescence (PL) Spectroscopy:

Photoluminescence spectroscopy often referred to as PL is a non-contact, non-destructive technique used for the characterization impurity levels and excitonic structure of semiconductors. PL is a process in which light emission takes place after the absorption of photons. It is one of the forms of luminescence i.e. light emission. In PL, when monochromatic light of certain wavelength is directed onto a sample, it absorbs the light and a process called photo-excitation occurs. This photo-excitation describes a situation which causes the material to jump to a higher electronic state, and equivalent photons are released very rapidly and come back to a lower energy level.

In terms of conduction and valence band, the PL process can be explained as follows. By optical excitation, the electron-hole pairs are produced when the absorbed photons bring electrons to the conduction band by creating holes in the valence band. Now, the excess

energy of the electron-hole pair after photon absorption is given to the crystal by the creation of phonons. This relaxation process is known as thermalization and takes typically around 10^{-12} seconds to bring electron and hole to their lowermost energy levels in the CB and VB, respectively. After that, the electron-hole pairs recombine.

Generally, PL instruments consist of an excitation source, a monochromator, a photo-detector, an amplifier and a cryostat with temperature controller.

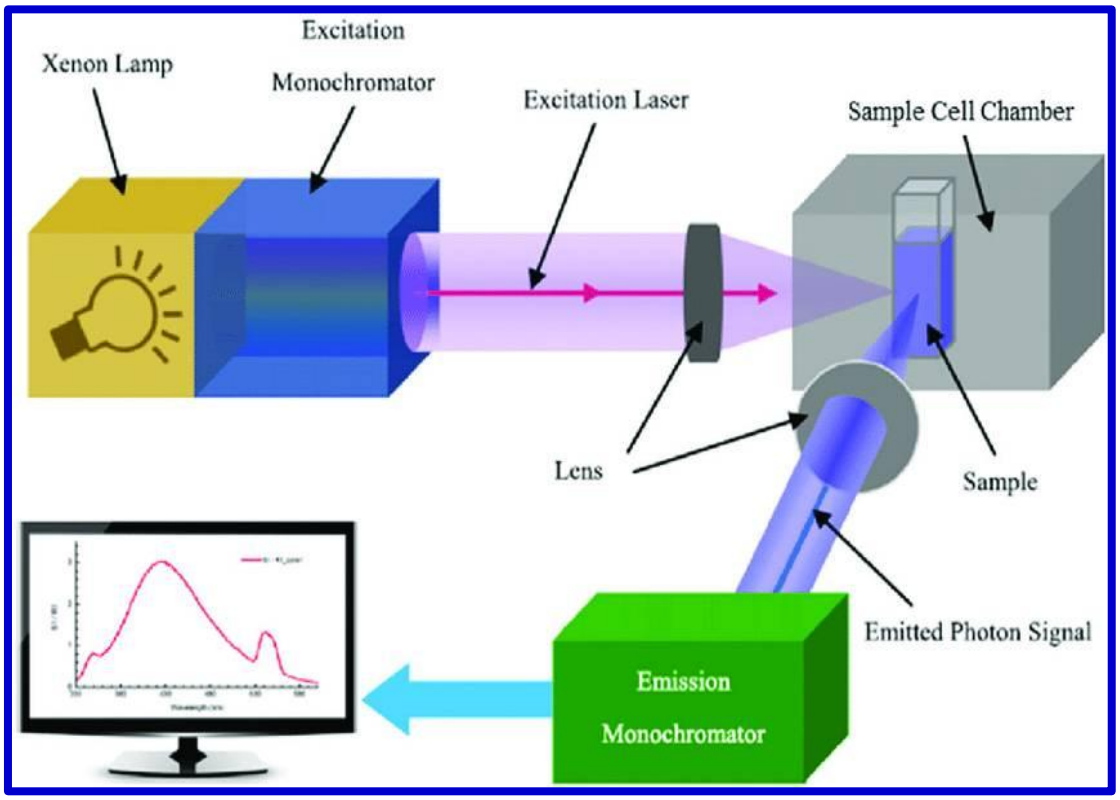

Fig. 3.17. *Schematic diagram of spectrofluorometer instrument*

Here, the PL spectrofluorometer used is Edinburgh FLS-980 (Fig. 3.18) to study the steady state PL spectra.

Fig. 3.18. *Photograph of PL instrument used here (Edinburgh FLS-980).*

3.5.4. Cathodoluminescence (CL) Spectroscopy:

Cathodoluminescence (CL) spectroscopy is an optical and electromagnetic phenomenon to investigate and characterize inorganic compounds such as ceramics, minerals and semiconductors. Cathodoluminescence is light or electromagnetic radiation which ranges from ultraviolet to infrared region of the electromagnetic spectrum. In CL, when a material is bombarded with a beam of high energy electrons, emissions of light or photons take place. The excitation process results in the transfer of electrons from the valence band into the conduction band leaving behind a hole. Subsequently, these electrons recombine with the holes created in the valence band and as a result of energy difference, a photon is emitted.

When a high energy electron beam is incident on the material, these primary electrons carry far too much energy to excite electrons directly. Then, the emission of secondary electrons, Auger electrons and X-rays take place by the inelastic scattering of the primary electrons in the crystal, which in turn can also scatter. For every incident electron, these cascades of scattering events lead up to 10^3 secondary electrons. Now, when these secondary electrons

have kinetic energy about three times the band gap energy of the material ($E_k \approx 3E_g$), they can excite valence electrons into the conduction band. From there, a photon is created when the electron recombines with a hole in the valence band.

As compared to photoluminescence, one of the advantages of excitation with an electron beam in cathodoluminescence is that the band gap energy of materials that are investigated is not limited by the energy of the incident light. Therefore, in cathodoluminescence, the "semiconductor" examined can almost be any non-metallic material.

Here, the CL spectra of the samples were recorded by using the CL equipment (Gatan Mono CL) attached with FESEM using a beam accelerating voltage of 5 kV as shown in Fig. 3.19.

Fig. 3.19. *Photograph of CL equipment attached with the FESEM*

3.6. Photocatalytic Measurements

3.6.1. Experimental set-up:

A standard set up for investigation of photocatalytic activity was used which includes two 40W UV (Philips) tubes capable of 254.6 nm (UVC) emission and a photocatalysis media placed at 15cm distance. The catalysis media was composed of 40 mL 10^{-5} M RhB test solution and 0.03g sample. The photocatalysis experiment was carried out under constant stirring for different time durations. After a pre-defined time interval, a certain portion of the degraded solution was collected. Those collected solutions were later subjected to absorption studies.

3.6.2. Photocatalytic Activity Study:

Here, in our work, Rhodamine B (RhB) has been used as organic dye for photocatalytic measurement of as-synthesized samples. In 40 mL quartz beaker, dye solution was made and the sample was dispersed within it. Prior to exposure in UV light, the mixture was then kept under dark stirring for one hour to achieve the adsorption-desorption between the catalyst sample and the dye molecules. Then, the solutions exposed to UV light were collected at interval of 1 hr. The dye degradation rate in different time has been monitored by UV–vis-NIR Spectrophotometer.

Also, the degradation efficiency (η) of the as-synthesized samples can be calculated from C_t/C_0 *vs.* t plot using the equation,

$$\eta = \frac{C_0 - C_t}{C_0} \times 100\%$$

where, C_0 and C_t are the concentrations of RhB at time t = 0 (initial RHB concentration) and t = t (final RhB concentration).

3.7. Field emission measurement apparatus:

Field emission also known as cold cathode emission is a quantum mechanical phenomenon in which on the application of a strong electric field on a solid, the electrons tunnel through a potential barrier at the surface of that solid. So, field emission is the emission of electrons from the surface of a material after applying a strong electric field.

The field emission measurements were carried out in our laboratory made high vacuum emission set up. This conventional parallel plate configuration includes two electrodes consisting of a stainless steel platform on which the sample to be investigated is mounted, acts as the cathode and a stainless steel conical tip of diameter 1 mm serves as anode. This entire diode system was placed in liquid nitrogen trapped rotary-diffusion vacuum chamber with required baking arrangements of the chamber. Furthermore, this chamber was evacuated up to 10^{-7} mbar base pressure. The transparency of the chamber enabled us to ensure that no discharge from the surface of the sample took place while applying high electric field. Generally, the powder sample is directly pasted on the conducting adhesive tape on the stage whereas the thin film samples are mounted on the conducting substrate with the help of two small micrometer screws attached with the base. To make the substrate glass conducting, the negative terminal of the high voltage dc power supply was connected with the films by using silver paint which is placed at least at a distance of 6 μm from the position of the anode tip. Before the field emission experiment, the ohmic nature of the contact was checked. With the help of spherometric arrangement having screw pitch of 10 μm, the distance between the cathode and anode was continuously adjustable from few μm to mm. The samples were placed at different inter-electrode distances by a micrometer screw attached to the system. An Agilent multimeter (model 3440-1A) was used to measure the current-voltage of field

emission. A last, the emission characteristics were registered and analyzed by using software. Fig. 3.20 shows the schematic diagram of the field emission apparatus.

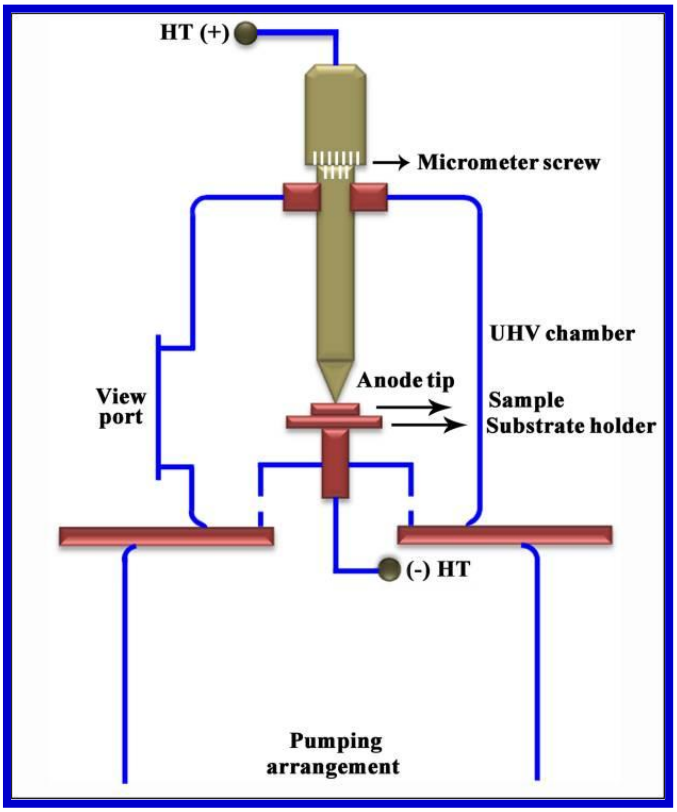

Fig. 3.20. *Schematic diagram of the field-emission apparatus*

Theoretically, the emission current density 'J' and the applied electric field 'E' are related by the well-known Fowler-Nordheim (F-N) equation

$$J = (a\beta^2 E^2/\phi)\exp[-b\phi^{3/2}/(\beta E)]$$

where, ϕ is the work function of the material and β is the field enhancement factor.

'a' = 1.54 × 10^{-6} A eV V^{-2} and b = 6.83 × 10^3 $eV^{-3/2}$ V $(\mu m)^{-1}$ are Fowler-Nordheim (F-N) constants. J was calculated by dividing the emission current I by the emission area A (= area of the anode tip = $(\pi/4)*(1.5\ mm)^2$ and E was calculated by dividing the externally applied input voltage V (in Volt) by the inter-electrode distance x (in μm).

The above equation can be re-written as

$$\ln(J/E^2) = \ln(a\,\beta^2/\phi) - b\phi^{3/2}/(\beta E)$$

By plotting ln (J/E^2) vs. 1/E i.e. F-N plot, a straight line is obtained having slope (say m) = $-b\phi^{3/2}/\beta$ and intercept = ln ($a\beta^2/\phi$). So, by knowing the value of this slope, the field enhancement factor β can be figured out using

$$\beta = -b\phi^{3/2}/m$$

The negative slopes of the F-N plots ensure the cold emission nature of the material.

The major supporting accessories used for the field emission measurement are discussed below:

(a) High voltage D.C. power supply:

D.C. voltage is applied between the cathode (i.e. the sample under investigation) and the anode for field emission measurement. A 3 kV- 500 mA DC regulated power supply unit (Model NTPL/91/03-04), designed by Neo Tele-Tronix Pvt. Ltd., Calcutta was used for this purpose. The input to the unit is 230 V, 50 Hz, 1 Phase AC and output can continuously vary from 100 V to 3 kV DC. The power supply was housed within a powder coated steel enclosure movable with wheels.

(b) Electrometer, Multimeter: Model 671 and 6517A of Keithley electrometer was used to record current voltage characteristics and resistance of the samples. The current and voltage ranges are ± 1 pA to ± 20 mA and ± 1000 V respectively. Another model 6514 of Keithley electrometer was used to measure the field emission current having a current range of ± 100 nA to ± 21 mA. Also, other multimeters such as RISH MULTI 15 S, Agilent (Model 3440-1A) were used during the experiment.

3.8. Finite element based simulation (ANSYS):

Finite element method (FEM) is a particular numerical approach that is widely used for solving partial differential equations in two or three space variables i.e. for boundary value problems. In FEM, for solving a problem, a large system is sub-divided into smaller and simpler parts which are called finite elements.

In such type of simulation based analysis, FESEM generated micrographs of real samples are referred to as the primary hint for modeling. The dimension, shape and dispersion densities are maintained up to maximum possible extent to mimic the actual experimental set up. A simple duplication of the models can actually replicate the sample under investigation.

During this modeling, a huge number of possible variations of morphological parameters can be simulated. Models can be prepared via varying dimension, shapes, attachment of foreign boosting candidates and variation of dispersion density can be simulated. Consequences of those entire factors can be predicted prior to actual experimental attempts to achieve them. This is very much helpful in view of optimum use of resources.

After modeling is complete, actual excitation – mostly electrical, can be virtually applied in the appropriate section of the models. During this, a wide range of electrical field can be virtually applied and the resulting output field can be easily simulated. The density of output field lines in the proximity of the sample model can also be plotted. This also includes appropriate information about the non uniformity of the output field around the sample model/emitter. These results are normally used for pre-determination of nanostructure density in view of screening effect etc. This information is largely used to plan synthesis conditions in order to obtain appropriate results.

The ANSYS Maxwell simulation can also be used to explain obtained experimental results and correlating the same with different morphological parameters. A number of intermediate nanostructures can be virtually formed and their field emission studies can be predicted which often contributes in supporting appropriate explanation for experimental findings.

In this thesis, experimental output of field emission related investigations of some chalcogenides were supported using ANSYS Maxwell simulation.

Chapter 4

Co incorporated Ni_3S_2 hierarchical nano/micro cactus for electrochemical water splitting

- Synthesis of Co doped Ni_3S_2 hierarchical nanostructures by hydrothermal method were done for the first time.
- Morphological tuning was successfully correlated with synthesis temperature.
- High aspect ratio was identified as key factor for better electrochemical property.
- Highly efficient hydrogen evolution with very low overpotential of 206 mV.

Abstract

Hierarchical nano/micro Ni_3S_2 cactus like structures were fabricated using cost effective and eco-friendly hydrothermal technique. Both pure and Co:Ni_3S_2 composite nanostructures were grown on nickel foam under different synthesis temperatures. The synthesized nanostructures showed a wide variation of hierarchical morphology with variation of synthesis temperatures. The obtained nanostructures were investigated for electrochemical water splitting performance. The morphologies of the samples were found to acquire higher aspect ratio with increment in synthesis temperature. This morphological tuning led to remarkable enhancement in hydrogen evolution performance with very low overpotential 206 mV at 100 mA cm^{-2} in acidic medium. Owing to this superior morphology tuned water splitting performance, this low dimensional Ni_3S_2 system can be recognized as potential leader in electrochemical energy harvesting sector.

4.1. Introduction

Although, fossil fuels are continuously being formed via natural processes, they are generally considered to be non-renewable resources because they take millions of years to form. Several attempts are made to find out alternative sources of consumable fuel by extensive focused research. Energy harvesting through electrochemical water splitting has been emerged as one of the effective ways combining oxygen and hydrogen evolution reactions taking place at the anode and cathode sites respectively [1,2]. Hydrogen is the most ideal and promising fuel source with an abundance of more than 99.98%. There are some traditional ways of hydrogen production like using $NaBH_4$ [3] which though cost effective, offers poor control on amount and rate of production leaving the purpose partially unfulfilled. The most promising method to produce hydrogen gas is by electrolysis of water i.e. decomposition of water into oxygen and hydrogen gas due to an electric current passed through the water. The

reaction has a standard potential of -1.23 V i.e. it ideally requires a potential difference of 1.23 V to split water. Electrocatalysts decrease the overpotential. However, the most efficient electrocatalysts for HER are Pt-based materials [4] but their limited availability and high cost has a major impact on its wide use. Therefore, it is needed to develop Earth-abundant catalysts which are cheaper and highly efficient by economical method.

Recently, transition metal chalcogenides have been reported as most important materials for water electrolysis. Nickel sulphides (NiS, NiS_2, Ni_3S_2 etc.) serve as an excellent electrocatalysts for HER [5-8] because of its low cost, good catalytic activity and simple preparation method. For its high specific capacitance, Ni_3S_2 also serve as good electrode materials for supercapacitor [9]. Also, Ni_3S_2 has many applications in the field of Li-ion batteries [10], dye-sensitized solar cells [11], photocatalytic hydrogen evolution [12], non-enzymatic glucose detection [13] etc. Tang et al. [14] reported that in both basic and neutral solutions, nickel sulphide nanostructures supported on Ni foam can be used as an efficient electrocatalyst for hydrogen evolution reaction.

As there is large number of protons available in acidic conditions, HER is reliable in this medium. The experimentally obtained value of Tafel slope depicts the mechanism by which HER proceeds. At first, Volmer reaction takes place in which adsorbed hydrogen is formed by discharging protons on the electrode surface. It is then, succeeded either by Heyrovsky reaction i.e. electrochemical desorption of hydrogen or Tafel reaction i.e. chemical desorption of hydrogen depending on the scope of H_2 adsorbed. It is well explained that the materials/ composites play the role of catalysts in HER. Due to existence of valence electrons in two shells, transition metals can easily supply or hold electrons during the HER by undergoing oxidation/reduction. Systems involving transition metals are therefore often used as popular catalysts in HER/ORR. In some earlier reports, electrodeposition technique combined with thermal treatment [15,16] has been employed to synthesize novel electrocatalysts. Earlier,

Cui et al. [17] reported the electrochemical water splitting by Mo doped Ni_3S_2 nanostructures. Co is another very important and major transition element with wide range of natural availability and additional magnetic properties. Ni and Co based catalysts are already popular to result in low cost OER electrocatalysis [15].

Herein, we report for first time the HER performance of Co:Ni_3S_2 composite nanostructures in acidic medium. Like many other popular applications, HER also depends on several factors like morphology, temperature etc. However, tuning those parameters in single reaction set up is also challenging. But sophisticated experimental set ups may serve the purpose but is likely to add newer barrier like production cost. Keeping this in mind, in this work, we have employed simple eco-friendly and cost effective hydrothermal route to fabricate Co:Ni_3S_2 composite nanocatalysts. The synthesized samples were characterized for phase information, morphology and compositional information thoroughly. Finally, their ability to generate hydrogen by water splitting was characterized in acidic medium. It was observed that the sample synthesized in optimized temperature of 220℃ is morphologically most favoured and shows a remarkable water splitting performance by registering overpotential as low as 206 mV at current density 100 mA cm^{-2}.

4.2. Experimental details

4.2.1. Synthesis of Co:Ni_3S_2 composite

0.4 g of cobalt sulphate heptahydrate $CoSO_4{\cdot}(H_2O)_7$ was mixed with 80 mL of DI water and stirred for 5 min. Thiourea was used as sulphur source, 0.4 g of thiourea was added into the solution and stirred for 15 min so that all materials were mixed properly. Prior to synthesis, commercially available Ni foams were cut into 1 cm × 5 cm pieces and cleaned with HCl, acetone and DI water subsequently. Then, the cleaned Ni-foams were put in the solution and kept 5 min for sonication. This entire solution was shifted into a Teflon-lined stainless-steel 120 mL autoclave and heated in oven for 16 h at 180℃. After the completion of reaction, the

system was cooled down to room temperature and the samples grown on Ni foam substrates were taken out from the solution. To remove the impurities on its surface, it was washed consequently with DI water and ethanol 3 times and dried in a vacuum oven for 6 h at 80℃. The same procedure was repeated varying the synthesis temperature to 200℃ and 220℃, and samples synthesized at 180℃, 200℃ and 220℃ were labeled as CoNS180, CoNS200 and CoNS220 respectively. A pristine nickel sulphide sample without Co precursor was also synthesized at 220℃ and labeled as NS220.

4.2.2. Characterization

Routine characterizations with XRD ((Bruker D8 Advanced) with Cu-Kα radiation (λ = 1.54 Å) in a 2θ range from 20°-80°), FESEM and EDX (Hitachi S-4800), HRTEM (JEOL JEM 2010) and XPS (SPECS, HSA 3500 (monochromatic Al source 1486.6 eV)) were carried out to investigate the crystalline, morphological and compositional properties of the samples.

4.2.3. Electrochemical measurements

The electrochemical measurements were conducted in Autolab PGSTAT (M-204) potentiostat/galvanostat through Nova 1.1 software and in a three-electrode configuration. Co:Ni_3S_2 composite nanostructures grown on nickel foam was directly taken as the working electrode and Pt wire and Ag/AgCl (saturated in 3 M KCl) as counter and reference electrode respectively. Reversible hydrogen electrode (RHE) was taken into account for all measurements by adding 0.27 V with Ag/AgCl reference electrode.

$$\text{In 0.5 M } H_2SO_4\text{, E (RHE) = E (Ag/AgCl) + 0.27 V.}$$

The linear sweep voltammetry (LSV) was conducted in acidic solution at a scan rate of 10 mV s^{-1}. Stability test of the sample CoNS220 was also done as it gave best HER activity at the same scan rate.

4.3. Results and Discussion

4.3.1. XRD Analysis

The XRD patterns of the as-synthesized samples are presented in Fig. 4.1(a). It can be clearly seen that all the samples show different diffraction peaks of NiS and Ni_3S_2 appearing at appropriate positions as matched with JCPDS card nos. (75-0613, 44-1418, 43-1477) as expected, strong peaks corresponding to Ni from the substrates also appeared (03-1051). The XRD results eliminate the possibility of existence of any phase of cobalt chalcogenide or unreacted precursors. The intense peaks corresponding to every material ensures the proper crystalline phases of the components and this can be attributed to sufficient ambient temperature maintained during the synthesis of the samples. The pristine sample without Co incorporation did not show the diffraction peak correspond to $NiCo_2S_4$ lattice which is quite expected. However, on careful analysis of the XRD pattern, a minor peak corresponding to $NiCo_2S_4$ [JCPDS 43-1477] near 47.8° can be observed. This indicates the presence of very small amount of $NiCo_2S_4$ phase as represented by diffraction peak of very low relative intensity.

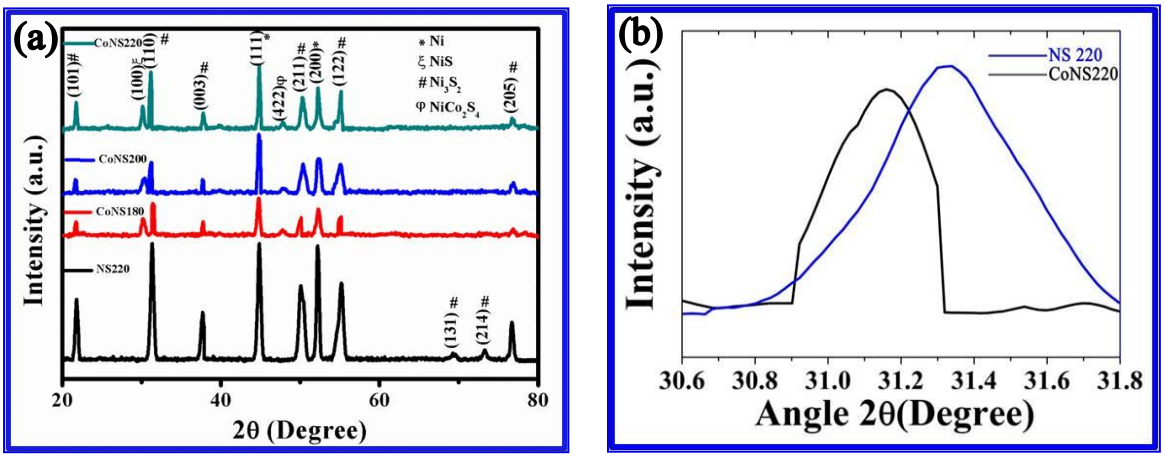

Fig. 4.1. (a) *XRD spectra of Co:Ni_3S_2 composite nanostructures and* **(b)** *XRD Peak shift of Ni_3S_2 due to Co doping*

In order to achieve better clarity on the type of Co incorporation in to the lattice of Ni_3S_2, the peak positions of pristine sample and CoNS220 was compared. It was observed that the (110)

peak of Ni_3S_2 was shifted to a lower diffraction angle after Co incorporation (Fig. 4.1(b)). This type of minor shift of XRD peak is expected when a larger dopant atom (here Co, ionic radii ~2 Å) replaces a smaller host atom (here Ni, ionic radii ~1.63 Å). Successful doping of Co, contributed by major portion of initial cobalt precursor was predicted from XRD spectra which was further confirmed from XPS study (discussed later).

4.3.2. Morphological studies

All the samples were initially characterized with FESEM to find out the basic morphology. The obtained micrographs are depicted in Fig. 4.2. All the samples show uniform rod like morphology grown over large area. Fig. 4.2(a and b) shows that the CoNS180 rods are grown in closed packed fashion with 3 μm length. A closer look on the surfaces of the CoNS180 nanorods shows that they are covered with flake like structure. Those flakes were found to be 20 nm thick. Samples synthesized at 200℃ showed slightly changed morphology. The length of the rods has been increased appreciably up to 5 μm. The surfaces of these CoNS200 nanorods were also found to be different. The earlier flake like wrapping in CoNS180 changed to very small nanoparticle surface features in CoNS200 Fig. 4.2(c and d). In Fig. 4.2(e and f), sample CoNS220 nanorods were found to be even longer than CoNS200 rods. They were found to be 7-10 μm long. The surfaces of the rods were found to have very thin and small flaky wrapping. Additionally, the tips of the rods in each sample were found to be attached together i.e. those nanorods are actually formed by attachment of thinner rods. The constituent nanorods are not distinct in case of CoNS180 but became separately identifiable as the synthesis temperature increased. The thinner rods were found to be of 300 nm and 200 nm in diameter in case of CoNS200 and CoNS220 respectively. The growth of such special morphology can possibly arise due to minor tuning by temperature. In case of CoNS200, the rise in temperature compared to that of CoNS180 caused further growth of surface flakes which finally disintegrated to result in very small nanoparticles. Further increment in

synthesis temperature caused the surface particle to grow further and form small flakes. However, the increment of rod length was directly associated with increment of synthesis temperature.

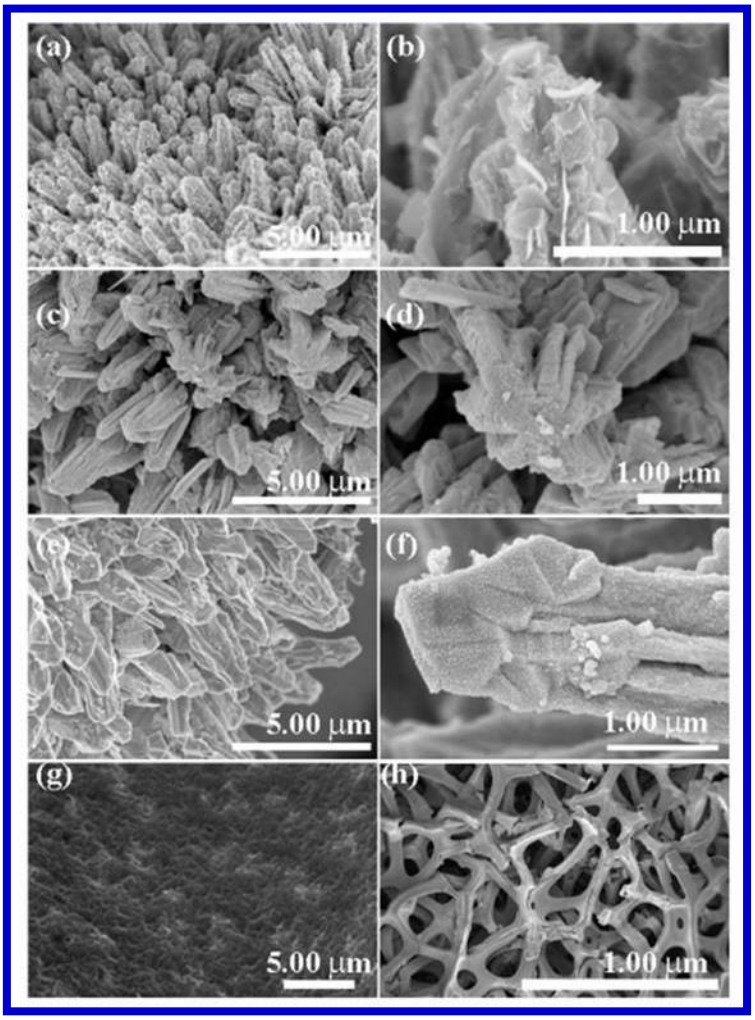

Fig. 4.2. *FESEM images of sample (a-b) CoNS180, (c-d) CoNS200, (e-f) CoNS220, (g-h) NS220*

A completely different morphology was found for NS220 Fig. 4.2(g and h) where no well-defined morphology was visible, only some particulate elongations, though uniformly grown, was found in large area. The particle size was around 30 nm and no morphology with enhanced aspect ratio was found. The absence of Co atoms as growth centres was identified as the major reason behind this general blunt morphology.

Finer investigation of morphology was carried out with high resolution transmission electron microscopy for CoNS220 and the result is presented in Fig. 4.3. The rod diameter ~500 nm was reconfirmed. The attached flake like structures on the surface of the rods is also clearly visible from TEM micrographs. It was found that the visible lattice planes have d-spacing of about 2.9 Å which corresponds to (110) plane of Ni_3S_2 lattice as shown in Fig. 4.3(b). This confirms the presence of Ni_3S_2 in the sample.

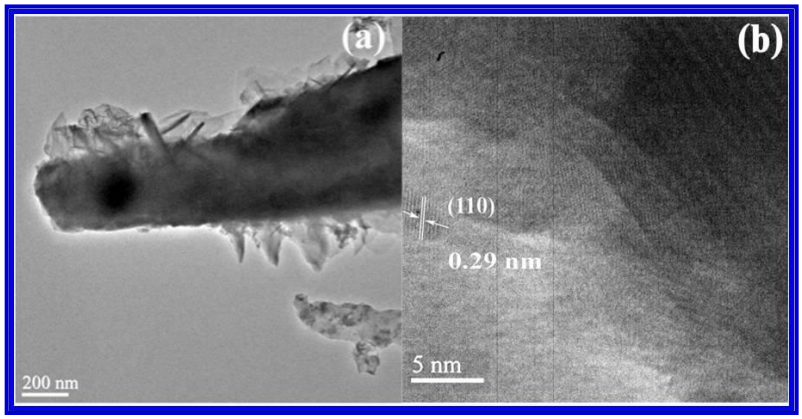

Fig. 4.3. *TEM micrograph of (a-b) Co:Ni_3S_2 composite nanostructures*

4.3.3. Compositional analysis

4.3.3.1. EDX study

The composition of the samples was investigated via energy dispersive X-ray studies.

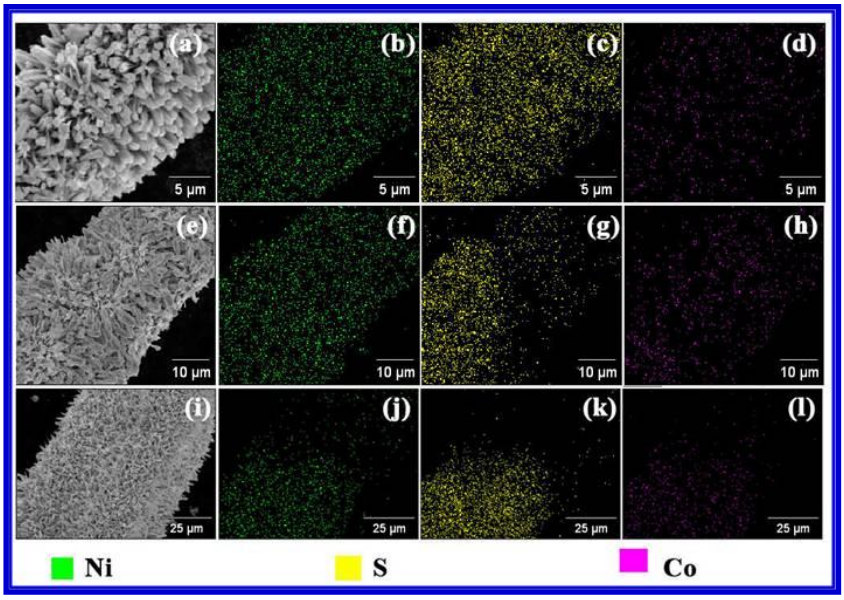

Fig. 4.4. *EDX spectra of sample (a-d) CoNS180, (e-h) CoNS200, (i-l) CoNS220*

All samples showed (Fig. 4.4) the presence of constituent elements (Ni, O, S and Co) in proper stoichiometric ratio. The samples also showed appreciable uniformity of the constituent elements.

To have a clearer idea on the coverage of sulfurized portion of Ni foam during the reaction, a single strand of the Ni foam was subjected to EDX elemental mapping. The results (Fig. 4.5.) showed that the exposed surface area of the Ni foam strands was properly sulfurized and the deep inner core remained unaffected. The existence of the unreacted inner core of the Ni foam strand was reflected in the strong XRD peak of Ni (111) plane.

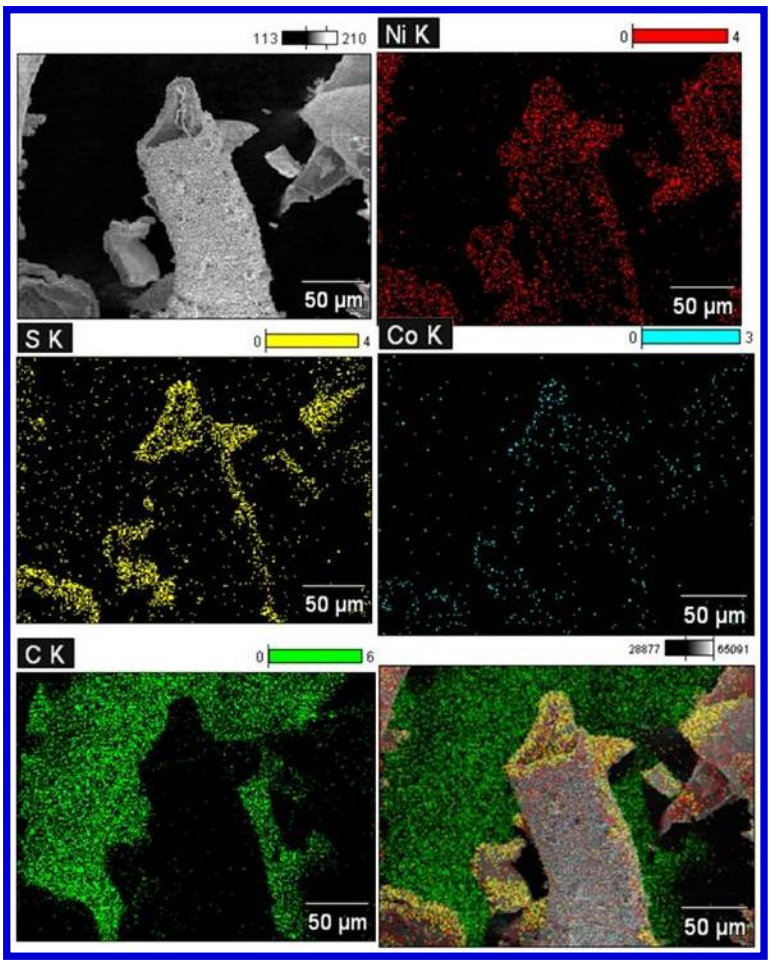

Fig. 4.5. *EDX elemental mapping for a single strand of Ni foam*

4.3.3.2. XPS study

To measure the elemental composition, chemical state and electronic state of the elements that exist within Co:Ni_3S_2 composite nanostructures, X-ray photoelectron spectroscopy (XPS)

was also done. As CoNS220 exhibits best HER activity, it was selected for XPS analysis. Fig. 4.6. shows the outcomes of XPS measurement. The survey scan presented in Fig. 4.6(a) shows the existence of constituent pristine and dopant elements. The peaks appeared around 164.27 eV and 162.69 eV was assigned to S $2p_{1/2}$ and S $2p_{3/2}$ state. Strong peaks appearing around 871.95 eV and 854.42 eV were assigned to Ni $2p_{1/2}$ and Ni $2p_{3/2}$ states respectively. Further, Co $2p_{1/2}$ and two Co $2p_{3/2}$ appeared around 794.43 eV and 778.57 eV and 770.58 eV which proves the existence of Co within Ni_3S_2 system.

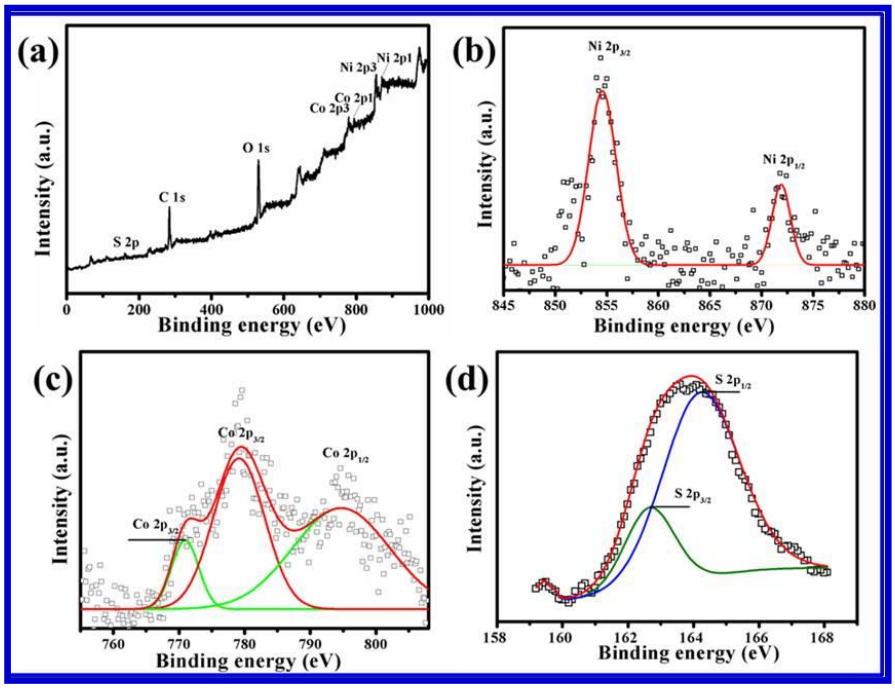

Fig. 4.6. *XPS spectra of (a) the survey spectrum of CoNS220, (b) Ni 2p spectrum, (c) Co 2p spectrum and (d) S 2p spectrum*

Along with general analysis of elemental composition, the XPS study was also used to find out possible amount of cobalt present in the sample. For this, the comparative peak areas under the XPS peaks for Ni 2p, S 2p and Co 2p, the elements were analyzed. The results showed (Fig. 4.7.) that amount of Co present in the sample (CoNS220) is about 20.41%.

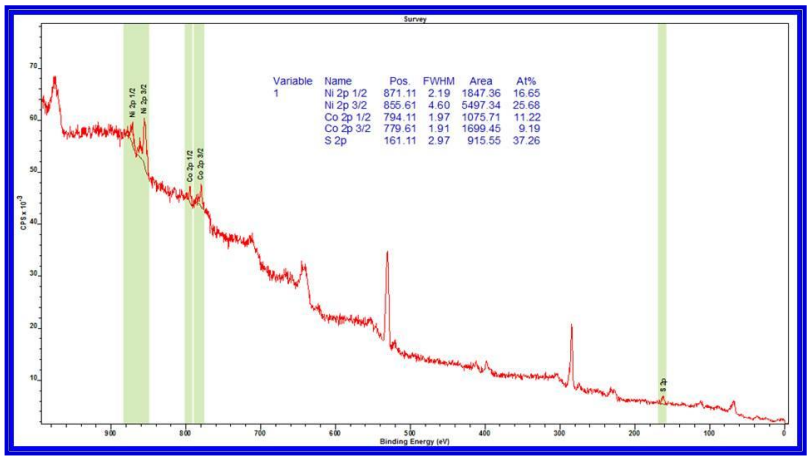

Fig. 4.7. *Area under curve for different XPS peaks*

4.3.4. Electrochemical Analysis

To assess the electrochemical activity for HER, a three-electrode configuration was set up. The linear sweep voltammetry curves at scan rate 10 mVs^{-1} of Co:Ni_3S_2 composite at different temperatures (180℃, 200℃ and 220℃) were investigated in acidic medium (0.5 M H_2SO_4) using the sample deposited nickel foams. The prepared samples were of 2 cm × 0.5 cm dimension from which, geometrical area of 1 cm × 0.5 cm was immersed in the electrolyte for carrying out HER activity. To compare their performances, the LSV curves of bare NF, NS180 and commercial Pt tip electrode were also evaluated at same scan rate and electrolyte. Fig. 4.8 depicts the iR corrected LSV curves of Co:Ni_3S_2 composite on NF at different synthesis temperatures and in Fig. 4.9, comparative LSV curves of bare Ni-foam, NS220, CoNS220 and commercial Pt-tip are shown. We can see from Fig. 4.8, CoNS220 shows lower overpotential of 206 mV at 100 mA cm^{-2} with respect to CoNS180 and CoNS200 with overpotentials of 238 mV and 219 mV respectively. So, the best sample was compared with bare Ni foam, NS220 and commercial Pt tip electrode.

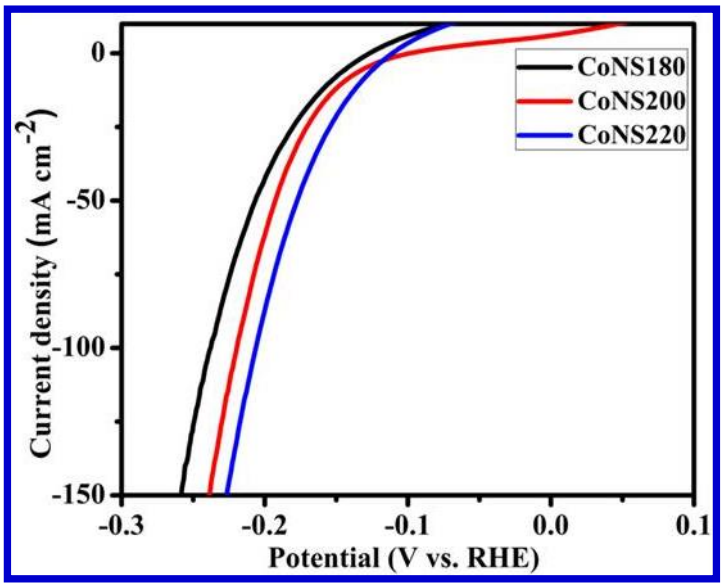

Fig. 4.8. *Polarization curves (iR corrected) of CoNS180, CoNS200 and CoNS220 in 0.5 M H_2SO_4 with scan rate of 10 mV s^{-1}*

In Fig. 4.9, we can observe that bare Ni foam shows moderate HER response with overpotential of 318 mV at same current density.

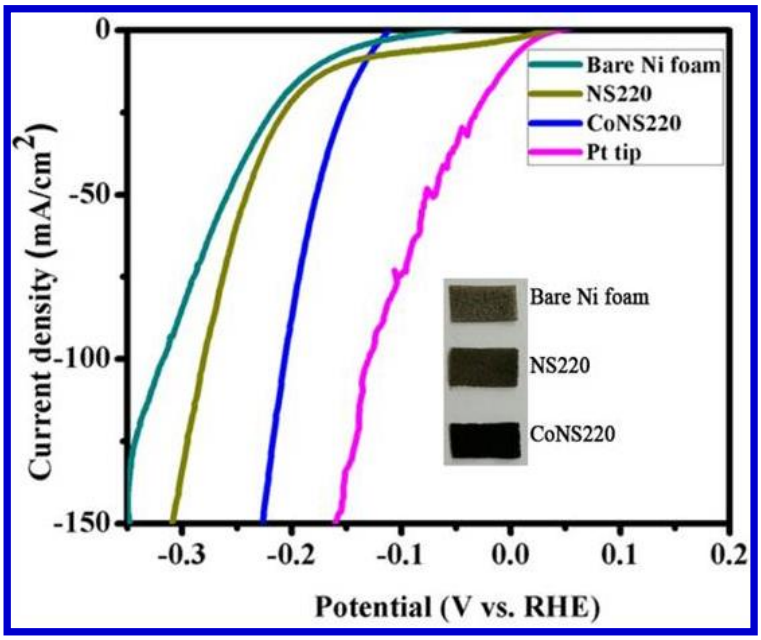

Fig. 4.9. *Comparative polarization curves (iR corrected) of bare Ni foam, NS220, CoNS220 and commercial Pt tip, Inset showing the digital image of Ni foam with and without samples*

In electrochemical kinetics, Tafel equation relates overpotential to the current density (log scale).

$$\eta = a + b\ log|J|$$

where, η is the overpotential (RHE), J is the measured current density, b is the Tafel slope, and a is the constant. Rate determining step of HER mechanism is obtained from the Tafel slope (b). Theoretically, there are three types of HER mechanisms: Volmer, Heyrovsky and Tafel which are derived from Tafel slopes of 118 mV dec^{-1}, 39 mV dec^{-1} and 29 mV dec^{-1} respectively [18]. The reactions are given below [19].

$A + H^+ + e^- \longrightarrow AH_{ads}$ (Volmer reaction)

$AH_{ads} + H^+ + e^- \longrightarrow H_2 + A$ (Heyrovsky reaction)

$AH_{ads} + AH_{ads} \longrightarrow H_2 + 2A$ (Tafel reaction)

In this work, the obtained Tafel slope of CoNS220 is 40 mV dec^{-1} whereas NS220 and bare Ni foam give Tafel slope of 46.5 mV dec^{-1} and 64 mV dec^{-1} respectively as in Fig. 4.10. The commercial Pt tip exhibits the Tafel slope of 30 mV dec^{-1} as shown in Fig. 4.10.

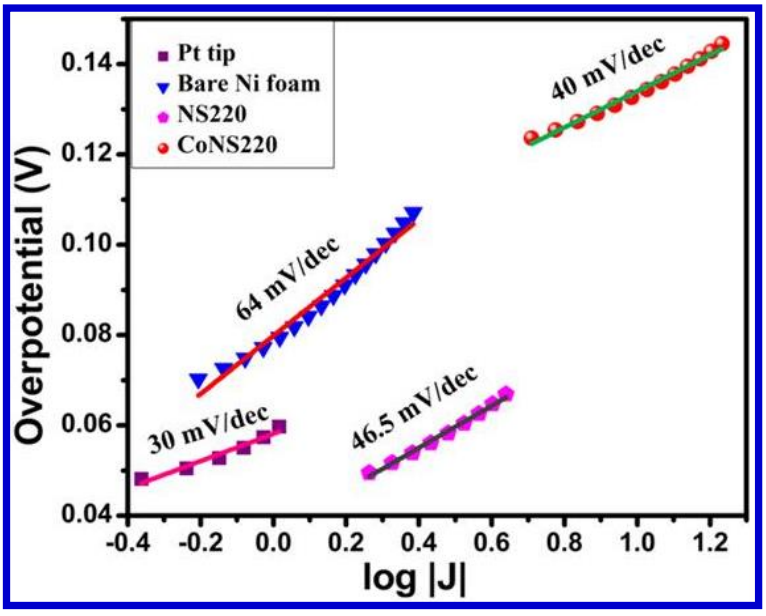

Fig. 4.10. *Tafel plots of Pt tip, bare Ni foam, NS220 and CoNS220*

Generally, in HER, electrochemical desorption process (Heyrovsky reaction) occurs followed by electrochemical adsorption process (Volmer reaction). As derived from Tafel slope, Heyrovsky reaction mechanism is rate determining step for CoNS220 sample.

The results show that sample CoNS220 shows best performance in view of electrochemical efficiency. HER performance of any catalyst is usually governed by several parameters like effective surface area, nanostructural superiority, porosity etc. The aspect ratio of the samples, signifying their comparative nanostructural feature was identified as the key factor here. Transition metal incorporation is itself a very smart technique which has been applied here with Co for the first time. This metal itself offer easy hold or release of electrons during oxidation/reduction reaction. Additionally, further tuning of morphology in turn controls the aspect ratio and enhances hydrogen adsorption on increased effective surface area. From the morphological studies; it was clearly observed that the samples exhibited higher aspect ratio with the increment in synthesis temperature. The highest aspect ratio obtained in CoNS220 effectively enhances the chance of higher amount of hydrogen adsorption leading to higher possibility of oxidation/reduction reaction for electrons hold/released by the guest metal ion. Thus, the Co incorporated Ni_3S_2 nanostructure with a particular growth condition has been established as the most promising candidate for future energy solutions with hydrogen storage.

The Nyquist plot of the samples for -450 mV is presented in Fig. 4.11. The diameter of the semicircle region indirectly estimates the charge transfer resistance which is an important factor for HER related catalysts. It can be clearly seen that the charge transfer resistance significantly decreased after increment of synthesis temperature leading to better electrochemical performances for sample CoNS200 and CoNS220. This superiority can also be accounted for enhanced aspect ratio obtained in higher temperature samples.

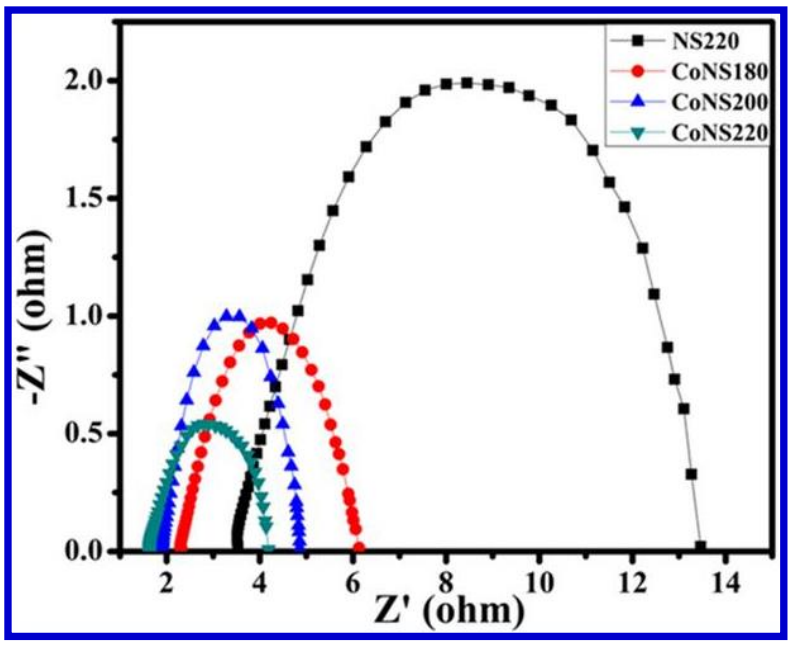

Fig. 4.11. *Nyquist plots of NS220, CoNS180, CoNS200 and CoNS220 at -450 mV potential*

The uncompensated resistance of the solution (R_s) and the charge transfer resistance (R_{ct}) of the four samples are outlined in Table 4.1. The values of R_s of NS220, CoNS180, CoNS200, CoNS220 are 3.50, 2.29, 1.90 and 1.63 respectively. It can be observed that there is very slight difference in R_s values of Co-doped samples as compared to undoped sample (NS220). Different values of R_s are observed due to the variation of synthesis temperature [20]. Compared to others, CoNS220 exhibits low R_s as well as low R_{ct} which correspond to good electrical conductivity and efficient charge transfer mechanism. This can also be due to morphological modification as already discussed in FESEM characterization.

Table 4.1: *Comparative table of solution resistance (R_s) and charge transfer resistance (R_{ct}) of the samples.*

Sample	$R_s(\Omega)$	$R_{ct}(\Omega)$
NS220	3.50	9.94
CoNS180	2.29	3.79
CoNS200	1.90	2.94
CoNS220	1.63	2.55

Another criteria for determining whether the HER catalyst is an efficient one is its stability test. The long-term chronoamperometric stability test was also carried out for 11 h in case of CoNS220 at -200 mV vs. RHE applied potential to achieve ~100 mA cm^{-2} current density as shown in Fig. 4.12.

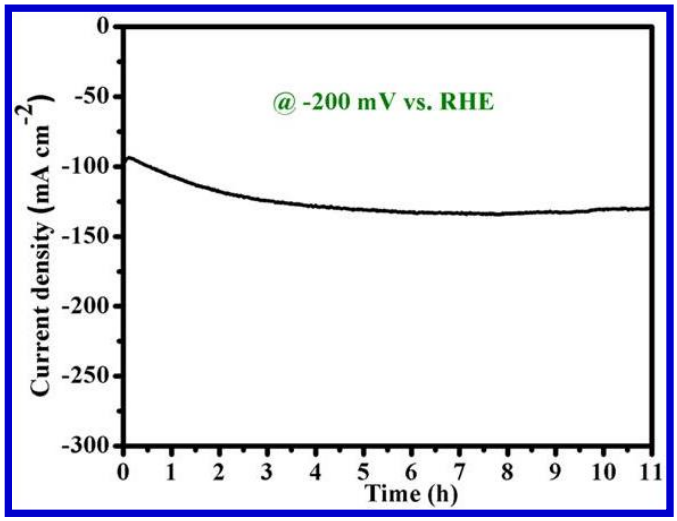

Fig. 4.12. *Stability test of CoNS220 at -200 mV vs. RHE applied potential to achieve ~100 mA cm^{-2} current density*

As depicted in Fig. 4.12, it can be seen that the current density slightly decreased from the starting value for initial 1-2 h but then achieved appreciable stability and did not vary much for more than 10 h. This established higher capability of the samples for future sophisticated electrochemical devices.

A comparative study of some identical systems is presented in Table 4.2 which shows that the samples synthesized here in this work, especially CoNS220 works better or with almost equal efficiency.

Table 4.2: *Comparative study of some identical catalyst*

Catalyst	Current density (mA cm^{-2})	Over-potential (mV)	Electrolyte	Scan rate (mV s^{-1})	Tafel slope	Reference
Ni_3S_2/AT-Ni foam	10	200	1M KOH	2	107	[8]
Ni_3S_2 /Ni foam		300			141	
AT-Ni foam					144	
Ni-foam					148	
MoS_2-Ni_3S_2 HNRs/NF	10	98	1M KOH		61	[21]
NF		308			149	
MoS_2/NF		235			121	
Ni_3S_2/NF		183			108	
Ni-foam	10	350	1M PBS	5		[14]
Ni_3S_2/NF		220			108	
Ni_3S_2/NF		123	1M KOH		110	
NiS		474	1M KOH	2	124	[22]
NiS_2		454			128	
Ni_3S_2		335			97	
CoNS220	100	206	0.5 M H_2SO_4	10	40	This work

4.4. Conclusion

Co incorporated Ni_3S_2 nanostructured composites were synthesized using low cost hydrothermal method on Ni foam substrates. In addition to regular structural, morphological and compositional studies, the efficiency of the samples for HER was tested in acidic medium. It was observed that the samples synthesized with higher temperature shows most efficient catalysis performance for HER with overpotential 206 mV. The superior morphological features with high aspect ratio were identified as the key factor for such efficient HER catalytic performance.

4.5. References

[1] Li X, Li S, Yoshida A, Sirisomboonchai S, Tang K, Zuo Z, Hao X, Abudula A, Guan G. Mn doped CoP nanoparticle clusters: an efficient electrocatalyst for hydrogen evolution reaction. Catal Sci Technol 2018;8(17):4407-12.

[2] Li X, Su X, Pei Y, Liu J, Zheng X, Tang K, Guan G, Hao X. Generation of edge dislocation defects in Co_3O_4 catalysts: an efficient tactic to improve catalytic activity for oxygen evolution. J Mater Chem 2019;7(17):10745-50.

[3] Xu D, Dai P, Guo Q, Yue X. Improved hydrogen generation from alkaline $NaBH_4$ solution using cobalt catalysts supported on modified activated carbon. Int J Hydrogen Energy 2008;33(24):7371-7.

[4] Xu Y, Zhang B. Recent advances in porous Pt-based nanostructures: synthesis and electrochemical applications. Chem Soc Rev 2014;43(8):2439-50.

[5] Zhu W, Yue X, Zhang W, Yu S, Zhang Y, Wang J, Wang J. Nickel sulfide microsphere film on Ni foam as an efficient bifunctional electrocatalyst for overall water splitting. Chem Comm 2016;52(7):1486-9.

[6] Wu X, Yang B, Li Z, Lei L, Zhang X. Synthesis of supported vertical NiS_2 nanosheets for hydrogen evolution reaction in acidic and alkaline solution. RSC Adv 2015;5(42):32976-82.

[7] Liu P, Li J, Lu Y, Xiang B. Facile synthesis of NiS_2 nanowires and its efficient electrocatalytic performance for hydrogen evolution reaction. Int J Hydrogen Energy 2018;43(1):72-7.

[8] Ouyang C, Wang X, Wang C, Zhang X, Wu J, Ma Z, Dou S, Wang S. Hierarchically porous Ni_3S_2 nanorod array foam as highly efficient electrocatalyst for hydrogen evolution reaction and oxygen evolution reaction. Electrochim Acta 2015;174:297-301.

[9] Chen JS, Guan C, Gui Y, Blackwood DJ. Rational design of self-supported Ni_3S_2 nanosheets array for advanced asymmetric supercapacitor with a superior energy density. ACS Appl Mater Interfaces 2016;9(1):496-504.

[10] Duan W, Yan W, Yan X, Munakata H, Jin Y, Kanamura K. Synthesis of nanostructured Ni_3S_2 with different morphologies as negative electrode materials for lithium ion batteries. J Power Sources 2015;293:706-11.

[11] Maiaugree W, Tangtrakarn A, Lowpa S, Ratchapolthavisin N, Amornkitbamrung V. Facile synthesis of bilayer carbon/Ni_3S_2 nanowalls for a counter electrode of dye-sensitized solar cell. Electrochim Acta 2015;174:955-62.

[12] Tong M, Wang L, Yu P, Tian C, Liu X, Zhou W, Fu H. Ni_3S_2 nanosheets in situ epitaxially grown on nanorods as high active and stable homojunction electrocatalyst for hydrogen evolution reaction. ACS Sustainable Chem Eng 2018;6(2):2474-81.

[13] Luan F, Zhang S, Chen D, Wei F, Zhuang X. Ni_3S_2/ionic liquid-functionalized graphene as an enhanced material for the non-enzymatic detection of glucose. Microchem J 2018;143:450-6.

[14] Tang C, Pu Z, Liu Q, Asiri AM, Luo Y, Sun X. Ni_3S_2 nanosheets array supported on Ni foam: a novel efficient three-dimensional hydrogen-evolving electrocatalyst in both neutral and basic solutions. Int J Hydrogen Energy 2015;40(14):4727-32.

[15] Li X, Li C, Yoshida A, Hao X, Zuo Z, Wang Z, Abudula A, Guan G. Facile fabrication of CuO microcube@ Fe-Co_3O_4 nanosheet array as a high-performance electrocatalyst for oxygen evolution reaction. J Mater Chem 2017;5(41):21740-9.

[16] Li X, Du X, Ma X, Wang Z, Hao X, Abudula A, Yoshida A, Guan G. CuO nanowire@Co_3O_4 ultrathin nanosheet core-shell arrays: an effective catalyst for oxygen evolution reaction. Electrochim Acta 2017;250:77-83.

[17] Cui Z, Ge Y, Chu H, Baines R, Dong P, Tang J, Yang Y, Ajayan PM, Ye M, Shen J. Controlled synthesis of Mo-doped Ni_3S_2 nano-rods: an efficient and stable electro-catalyst for water splitting. J Mater Chem 2017;5(4):1595-602.

[18] Anantharaj S, Ede SR, Sakthikumar K, Karthick K, Mishra S, Kundu S. Recent trends and perspectives in electrochemical water splitting with an emphasis on sulfide, selenide, and phosphide catalysts of Fe, Co, and Ni: a review. ACS Catal 2016;6(12):8069-97.

[19] Li X, Hao X, Abudula A, Guan G. Nanostructured catalysts for electrochemical water splitting: current state and prospects. J Mater Chem 2016;4(31):11973-2000.

[20] Chen K, Wang M, Li G, He Q, Liu J, Li F. Spherical α-MnO_2 supported on N-KB as efficient electrocatalyst for oxygen reduction in Al-Air battery. Materials 2018;11(4):601.

[21] Yang Y, Zhang K, Lin H, Li X, Chan HC, Yang L, Gao Q. MoS_2-Ni_3S_2 heteronanorods as efficient and stable bifunctional electrocatalysts for overall water splitting. ACS Catal 2017;7(4):2357-66.

[22] Jiang N, Tang Q, Sheng M, You B, Jiang DE, Sun Y. Nickel sulfides for electrocatalytic hydrogen evolution under alkaline conditions: a case study of crystalline NiS, NiS_2, and Ni_3S_2 nanoparticles. Catal Sci Technol 2016;6(4):1077-84.

Chapter 5

Cathodoluminescence from ZnS thin films deposited by novel seeded hydrothermal route

- ZnS thin films were deposited via unique combination of sputtering and hydrothermal techniques.
- Particle sizes within the as prepared thin films were varied in a wide range (micrometer to nanometer).
- Effect of pH value and particle size on cathodoluminescence property was studied thoroughly.

Abstract

ZnS thin films have been synthesized by hydrothermal route on seeded glass and silicon substrates at various temperatures. The seeded substrates were prepared by RF magnetron sputtering technique. The good crystallinity and proper phase formation of the synthesized films was confirmed by X-ray diffraction and transmission electron microscopic studies. The crystallinity of the samples could be enhanced by varying the synthesis temperature. The morphological studies along with determination of particle dimensions were performed using field emission scanning electron microscopy. With increase of particle dimensions, the band gap of the ZnS thin films decreased from 3.48 eV to 3.23 eV as determined from UV-vis-NIR spectrophotometric measurement. The samples exhibited intense cathodoluminescence irradiated under electronic excitation thus indicating its effective application in display devices.

5.1. Introduction

II–VI semiconductor thin films have emerged as the key materials for optoelectronic device technologies due to their extraordinary tunable optical and electronic [1–3] properties. In photovoltaic technology [4], photoelectrochemistry [5], display technology and water disinfection technology [6], the major materials used are II–VI semiconductors. Unlike the organic and bio-ingredient based materials, the wide range of tuning of their properties of II–VI semiconductors are successfully correlated with the underlying physics or chemistry and therefore, the behavior of such materials can be predicted upon application of any external excitation. It is therefore technically advantageous to fabricate different devices using these materials. For example, ZnO thin films have been used as UV sensors and its mechanism is well understood [7]. Other binary transparent conducting oxides have also been effectively

used for sensing [8], field emission based displays [9] and junction based applications [10] depending upon their transparency and electrical conductivity. Similarly, II–VI chalcogenides thin films are well-known candidates for luminescence based applications [11]. Among this group, ZnS is a well-known chalcogenide material investigated widely for various optoelectronic properties and smart application. Especially, luminescence properties of this particular material have been under focus since several decades [12]. Moreover, the properties of these materials changes significantly when they are in the nanoregime. With the proven advantages of low dimensional materials, ZnS was also studied in large extent to fabricate nanobelts [13], nanorods [14] and nanoparticles [15] and their optical properties were also widely reported. But most of these reported nanostructured materials are in powdered form. However, it is of utmost importance to achieve nanostructured thin films of this smart material to fully utilize the same in actual device fabrication for applications. Most of the wet chemical routes reported so far for the synthesis of ZnS nanostructures resulted in production of nanostructures in powder form [16]. On the other hand, ZnS thin film fabrication through physical routes often involve techniques like atomic layer deposition (ALD) [17], pulsed laser deposition (PLD) [18], spray pyrolysis [19] etc. The mentioned processes are not cost effective as they require difficult experimental set up for successful operation. Sputtering technique is much useful in this aspect as mentioned in several reports [20]. But morphology controlled synthesis of nanostructured thin films are difficult through sputtering method. It must be mentioned that luminescence property of ZnS can be tuned [21] over its bulk values. Pure ZnS can be used for emitting blue to green visible emission upon UV excitation just by variation of particle dimension. But this requires an appreciable range of variation of particle diameters ranging from nano to micro. This is an important aspect as bluish green or cyan emission from ZnS thin films opens up possibility for fabrication of white phosphor thin film if only a thin coating of red light emitting material like CuI [22] is

deposited on the ZnS layers. RF sputtering technique, although comparatively cheaper among the popular physical routes of thin film fabrication, unfortunately cannot meet this purpose. Variation of the deposition parameters in sputtering technique may be effective to fabricate thin films having particle dimensions varying by few tens of nanometers [23]. But achieving cyan and green emission in the same composition of ZnS thin film is not possible using RF sputtering technique. Moreover, sputtered thin films are generally composed of particles although reports on other morphologies are not rare [23, 24]. But nanostructure morphology is also important for any multipurpose advance material. Hydrothermal technique is a proven route to synthesize various sulfide nanostructures [25]. It includes synthesis in closed atmosphere and hence, minimizes the possibility of oxidation of the product chalcogenide. Moreover requiring very simple experimental set up, hydrothermal synthesis technique is also useful in financial aspect and thus indicate stronger claim for industrial usage. However, thin film synthesis employing solely this route is rarely reported [26]. Photo-assisted growth of ZnS film on seeded glass substrate was studied [27] where a very thin film of ZnS was grown initially by SILAR method. In some reports, intermediate complexes are considered as nucleation sites and hence these are suggested to serve the function of seed [28]. Deposition of CdS layer on ZnS seeds [29] is also reported in the literature. In this technological scope, we presented in this work, a combination of the two routes to fabricate nanostructured pure ZnS thin films capable of multi-colored emission. The same is achieved by simply varying the deposition condition resulting in variation of constituent particle size in wide range from few nanometers to several hundred nanometers. Moreover, the synthesized thin films were observed to consist of perfect spherical particles of different dimensions with large effective surface area favoring many possible applications. The synthesized films also showed extraordinary cathodoluminescence indicating their favorable application in modern display technology.

5.2. Experimental details

At first, using rf sputtering technique, ZnS seeds were deposited in glass and silicon substrates. For fabricating targets, commercially available ZnS powder (99.99%) was taken and by applying proper hydrostatic pressure, the powder was pressed in a grooved aluminium holder of diameter 5 cm. Then, the glass substrates and silicon wafers (1 cm × 1 cm pieces) were cleaned in dilute HCl and 2 % dilute HF for 20 min respectively and further, they were cleaned with 5% NH_4Cl solution for another 20 min. Thereafter, the substrates were rinsed with deionized water and finally, cleaned ultrasonically in acetone for 20 min. In the sputtering chamber which was evacuated up to 10^{-6} mbar, thin seed layers were deposited on the cleaned Si and glass substrates for 5 min in Ar atmosphere with 100 W RF power. The distance between the target and the substrate was kept at 4 cm whereas the bias voltage was maintained at 250 V.

Now, for film deposition in hydrothermal route, these seeded substrates were taken. The source of Zn i.e. $Zn(O_2CCH_3)_2$ (99.99%) was dissolved in DI water to prepare 0.4 M solution of zinc acetate and thiourea (99.99%) powder taken as sulphur source was dissolved in DI water to prepare 0.8 M thiourea solution. These solutions of molar ratio 1:2 were mixed and stirred for some time. Using the same procedure, two more solutions with $Zn(O_2CCH_3)_2$ and thiourea molar ratio 1:1 and 1:4 were prepared separately. The Teflon-lined autoclave was filled with 80% of the mixture solution (pH maintained at 12) and the seeded substrates were kept vertically in it; the set-up was kept within a chamber made of stainless steel and tightened to maintain high pressure. After completion of the hydrothermal treatment at 110 °C temperature for 12 h, the set up was cooled gradually at room temperature and thin films were collected. To wash away the residual impurity, the films were washed with DI water for several times and then, dried in open air.

To study the effect of temperature on the crystallinity and other properties, the same synthesis procedure was repeated at 130 °C, 150 °C and 180 °C for both glass and silicon substrates by taking the solutions in molar ratio 1:2 as it showed best crystallinity (discussed later).

5.3. Results and Discussion

5.3.1. Basic Characterization of ZnS thin films

The as-prepared ZnS thin films deposited in various molar ratios (1:1, 1:2, 1:4) of $Zn(O_2CCH_3)_2$ and thiourea were characterized by studying X-ray diffraction (XRD, Bruker, D-8 Advance) with the Cu-K_α radiation of wavelength λ = 1.5406 Å. The film obtained for molar ratio 1:2 showed best crystallinity and almost amorphous phase was obtained for the other two molar ratios. Further, the thin films of this particular ratio deposited in various synthesis temperatures (110℃, 130℃, 150℃ and 180℃) on glass and Si substrates also indicated proper phase formation. The crystallinity of the ZnS thin films are directly related with the synthesis temperature. Using Field effect scanning electron microscope (FESEM, Hitachi S-4800) and High resolution transmission electron microscope (HRTEM JEOL JEM 2100), the particle size and surface morphology were studied. ZnS films grown on both glass and Si substrates showed well-defined spherical shape at high temperature which confirmed the good crystallinity of the films. The obtained particles were ~ 2 μm, 1.5 μm, 1.0 μm and 250 nm at temperatures 180℃, 150℃, 130℃, 110℃ respectively. So, with increment in synthesis temperature, the particles become smaller with a variation of nano to micro range. HRTEM studies confirmed the nanocrystalline nature of the film synthesized at lower temperatures. The average particle dimension of the sample synthesized at 110℃ was found to be ~ 16 nm. Also, the (110) plane of ZnS was confirmed by obtaining 0.336 nm as the interplanar d-spacing. By UV-vis-NIR spectrophotometric (Shimadzu UV-3101PC) study,

the band gaps of the ZnS films on glass substrates were determined. To study compositional purity, EDX study was carried out. It was observed that the samples exhibit nearly stoichiometric composition of Zn and S (Fig. 5.1 and Table 5.1).

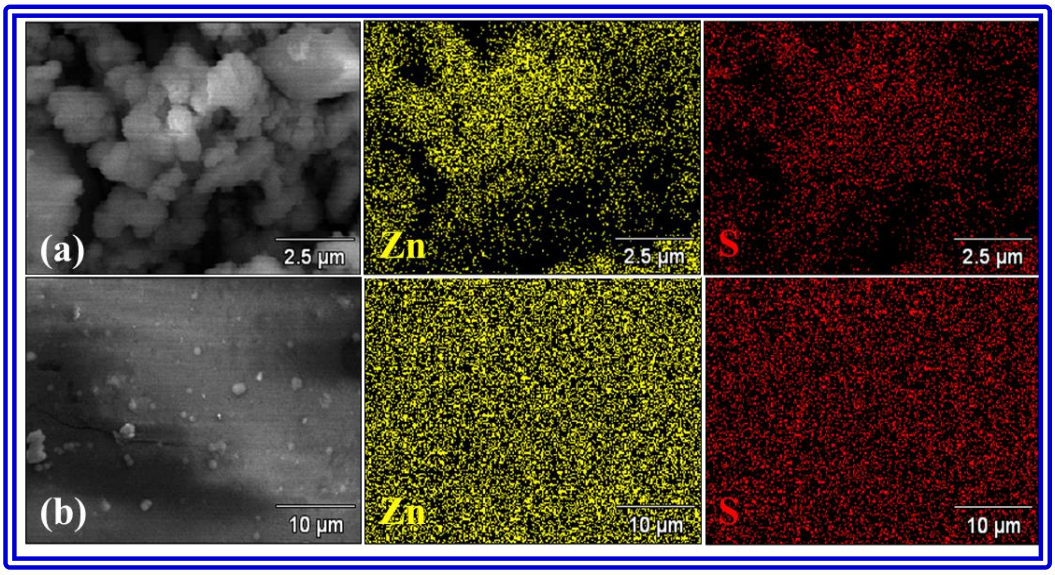

Fig. 5.1. *EDX elemental mapping of ZnS film on* ***(a)*** *glass substrate,* ***(b)*** *Si substrate*

Table 5.1. *Table for stoichiometric ratio of Zn and S on glass slide and silicon wafer*

Type of film	Atomic % of Zn	Atomic % of S
Glass slide	49.20	50.80
Silicon wafer	52.90	47.10

5.3.2. Optical studies

5.3.2.1. UV-visible spectroscopic studies

For the films deposited on glass substrates, the transmission spectra of the films were recorded in the wavelength range 300-700 nm. From Fig. 5.2(a, c); it was observed that in the visible range, the films showed 30-50% transparency. The value of optical band gaps were calculated from the relation between the absorption coefficients α and the incident photon energy hν which can be written as

$$(\alpha h\nu)^{1/n} = A(h\nu - E_g)$$

where, A is a constant, E_g is the band gap and the exponent n depends on type of transition. n= 1/2 for allowed direct, 2 for allowed indirect, 3/2 and 3 for forbidden direct and forbidden indirect transition respectively. Here, $(\alpha h\nu)^{1/n}$ vs hν was plotted by taking n = 1/2 and the direct band gap was determined from the intercept by extrapolating the linear portion of the graph to hν-axis.

The variation of band gap of ZnS thin films synthesized in different molar ratios of $Zn(O_2CCH_3)_2$: thiourea is shown in Fig. 5.2(a). The films prepared in molar ratio 1:1 exhibit an optical band gap of 3.44 eV and as the thiourea content increased, it slightly decreased up to 3.41 eV. Other research groups have also reported this kind of variation with Zn^{+2}/S^{-2} ratio [26]. The values of band gap were slightly decreased due to the increase of crystallite size as the thiourea content increased within the thin films and hence; for high temperature synthesized sample, the measured value is around 3.48 eV and gradually decreased to ~ 3.23 eV with the decrease in synthesis temperature. By considering the variation in particle size, this result can be explained.

The band gap of semiconductor thin films varies inversely with the variation of particle dimensions as reported by various research groups. Here also, a probable increment in band gap was observed from UV–vis derived band gap values which are in complete agreement of variation in particle size from nano to micro scale as analyzed from FESEM studies. Quantum size effect is responsible for widening of band gap for the thin films having particles of nano-dimension and when the particle size remains no more comparable with the De-Broglie wavelength of the carriers, the band gap decreases.

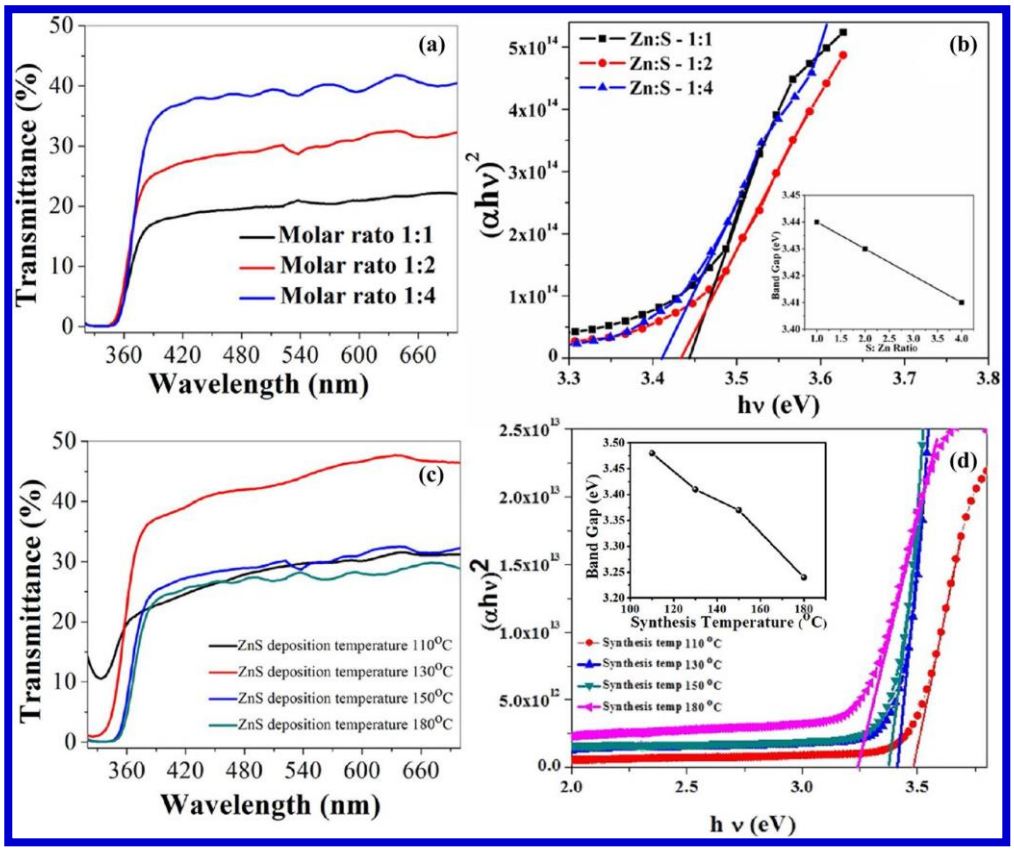

Fig. 5.2. ***(a,b)*** *Transmission spectra and variation of band gaps of ZnS thin films deposited in various molar ratios,* ***(c,d)*** *Transmission spectra and variation of band gaps of ZnS thin films deposited in various synthesis temperatures*

5.3.2.2. Cathodoluminescence study

In order to investigate the luminescence behavior directly, the films deposited on Si substrates were studied for cathodoluminescence response using the CL attachment of FESEM equipment (Gatan, Mono CL). The results are presented in Fig. 5.3. We can see that the constituent spherical particles of thin films are intensely illuminated when irradiated under electronic excitation thus indicating its effective application in display devices. The CL spectra of the samples synthesized in various temperatures are also presented in the same Fig. 5.3(c–f), it can be seen that all the CL peaks are very intense.

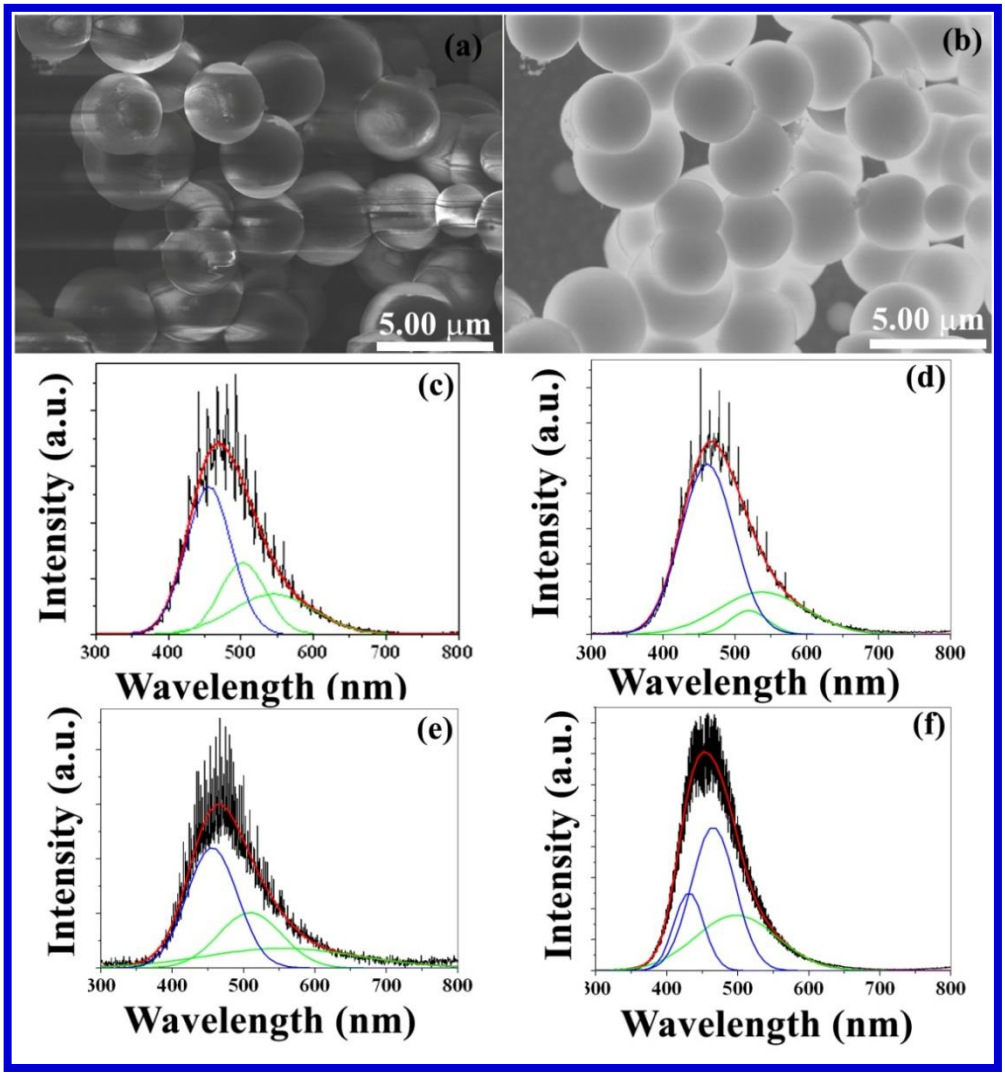

Fig. 5.3. ***(a)*** *FESEM and* ***(b)*** *corresponding CL image of ZnS thin film deposited in 180 °C. CL spectra of ZnS thin film deposited in* ***(c)*** *180 °C,* ***(d)*** *150 °C,* ***(e)*** *130 °C,* ***(f)*** *110 °C temperatures*

However, to determine the exact nature of cathodoluminescence, we deconvoluted the CL peaks. The deconvoluted CL spectrum of ZnS film grown at 110 °C shows three peaks, one at 430 nm showing near band edge emission and other two at 463 and 498 nm respectively. The last two peaks are at the range of blue and marginally at green ranges of visible spectra. The sample is therefore expected to exhibit bluish green visible emission. In Fig. 5.3(e), the deconvoluted CL spectrum of the ZnS film deposited in 130 °C show three constituent peaks as demonstrated in table 5.2. However, here the positions are at 462 nm, 518 nm and 539 nm

respectively. The last two peaks are purely within green range whereas the first one is in the blue range. Moreover, the blue and the green peaks have largest common area indicating cyan emission from these films. Again, the ZnS film deposited at 150 °C exhibits the CL spectrum which can be deconvoluted into three peaks, two at green range and one at blue range. The same trend was observed in case of the film deposited in 180 °C.

Table 5.2. *Deconvoluted CL peak positions of the ZnS film deposited in different temperatures.*

Temperature variation (ºC)	Deconvoluted peak position 1 (nm)	Deconvoluted peak position 2 (nm)	Deconvoluted peak position 3 (nm)
110	430	463	498
130	462	518	539
150	470	520	540
180	450	510	550

However, we can see that both the intensity and peak area of the peaks corresponding to green emission gradually increased as the synthesis temperature increased. The reason of increment of the contribution of green component of the emission with increase in synthesis temperature may be correlated with the change in particle dimension. Increase of synthesis temperature directly causes an increment in particle size and hence the red shift in the luminescence peak occurred. It is also worthy to be mentioned here that the count for intensity for the CL spectra presented in Fig. 5.3(f) reached a highest value of 23,000 which again confirms the efficiency of the synthesized films as a component of emission based display devices.

The chromaticity diagram is presented in Fig. 5.4. It can be clearly seen that the resultant emission locus is indicating that at least 2 points lie in cyan range which symbolize the thin films fabricated in 130 °C and 150 °C and whereas the same starts from a point lying in blue and ending in green colour. Such red shifts of emission peaks with increasing particle size are also reported for other thin films such as CdS NPs etc. [30,31].

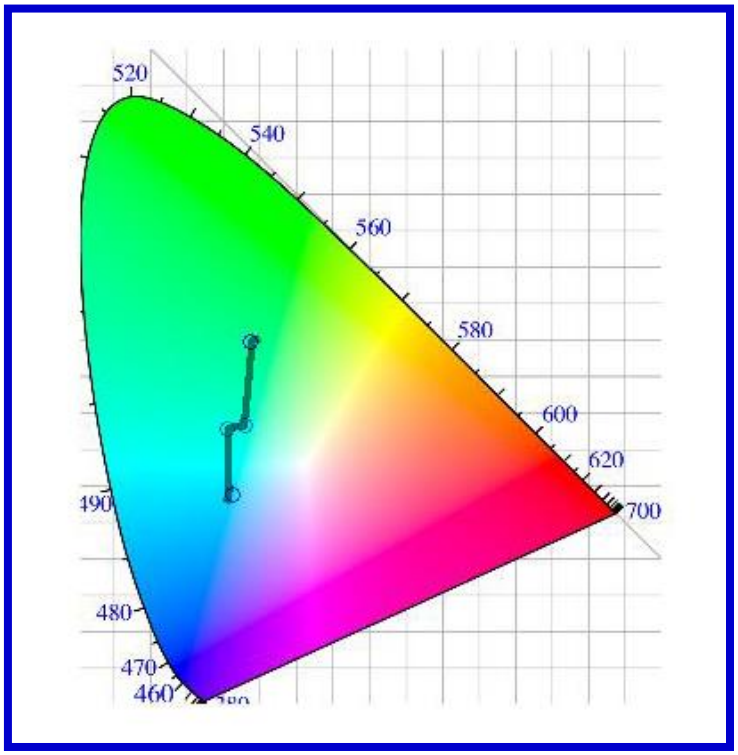

Fig. 5.4. *Chromaticity diagram of the samples*

UV photoresponse properties of the synthesized films were also studied and some result is shown in figure 5.5.

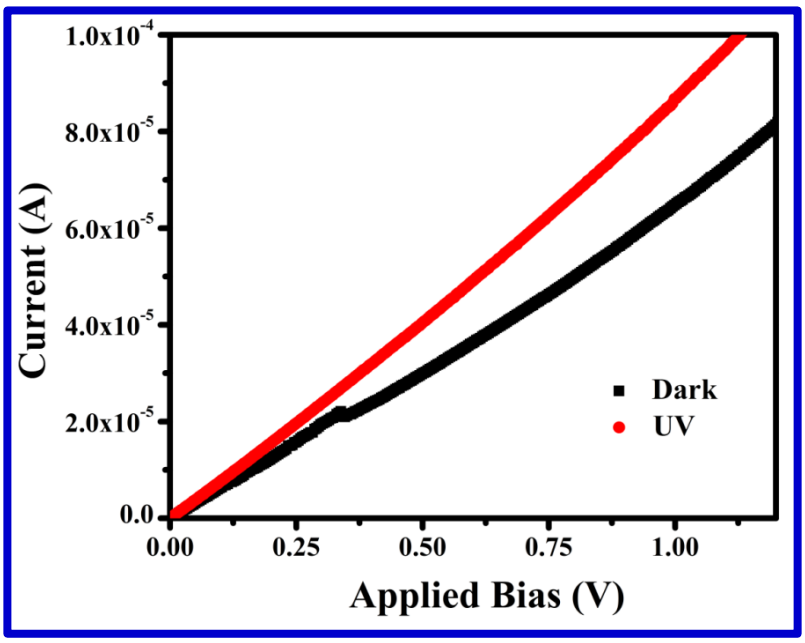

Fig. 5.5. *UV photoresponse study of ZnS film deposited on Si substrate at 180 °C.*

5.4. Conclusion

ZnS thin films were synthesized by hydrothermal method on seeded glass and silicon substrates prior to which the seeded substrates were prepared via RF magnetron sputtering technique. By varying the molar ratios of the chemicals present in the precursor solution and their pH values, the hydrothermal deposition parameters were optimized. The synthesis temperature played an important role in deposition of thin films which improved the crystallinity of the samples. The proper phase formation of the synthesized films was confirmed by XRD and HRTEM studies. By controlling the synthesis temperature, the average particle size of the thin films can be varied from nano to micro range as determined from the FESEM measurements. It was found that in the visible region, the samples have good transparency which was confirmed from the transmission spectra. UV-vis-NIR spectrophotometric measurement showed that with increase of particle dimensions, the optical band gap was found to decrease. The samples exhibited strong CL behavior irradiated under electronic excitation thus indicating its effective application in display devices.

5.5. References

[1] Y. He, T. Ouyang, G. Ouyang, J. Appl. Phys. **124**, 184302 (2018).

[2] V.I. Klimov, J. Phys. Chem. B **110**, 16827 (2006).

[3] I.H. Calderon, *II–VI Semiconductor Materials and their Applications*, 1st ed edn. (CRC Press, Boca Raton, 2018), pp. 113–170.

[4] R. Maity, K.K. Chattopadhyay, Nanotechnology **15**, 812 (2004).

[5] J. Lee, Thin Solid Films **45**, 170 (2004).

[6] P.J. Sebastian, Appl. Phys. Lett. **62**, 2956 (1993).

[7] F. Fang, J. Futter, A. Markwitz, J. Kennedy, Nanotechnology **20**, 245502 (2009).

[8] G. Kiriakidis, H. Ouacha, N. Katsarakis, Rev. Adv. Mater. Sci. **4**, 32 (2003).

[9] S. Santra, N.S. Das, B. Das, D. Banerjee, K.K. Chattopadhyay, Crystal Growth & Design **15**, 1518 (2015).

[10] G. Murugadoss, V. Ramasamy, Spectrochim. Acta Part A **93**, 290 (2012).

[11] J. Jubimol, M.S. Sreejith, C.S. Kartha, K.P. Vijayakumar, G. Louis, J. Lumin. **203**, 436 (2018).

[12] M. Luo, Y. Liu, J. Hu, J. Li, J. Liu, R.M. Richards, Appl. Catal. B **125**, 180 (2012).

[13] P.K. Ghosh, S.F. Ahmed, S. Jana, K.K. Chattopadhyay, Opt. Mater. **29**(12), 1584–1590 (2007).

[14] P.K. Ghosh, U.N. Maiti, S. Jana, K.K. Chattopadhyay, Appl. Surf. Sci. **253**, 1544 (2006).

[15] R.K. Chandrakar, R.N. Baghel, V.K. Chandra, B.P. Chandra, Superlattices Microstruct. **84**, 132 (2015).

[16] C.S. Pathak, D.D. Mishra, V. Agarwala, M.K. Mandal, Ceram. Int. **38**, 5497 (2012).

[17] P. Yang, M. Lū, D. Xu, D. Yuan, C. Song, S. Liu, X. Cheng, Opt. Mater. **24**, 497 (2003).

[18] T.H. Ngo, H.V. Bui, V.B. Pham, T.H. Tran, A.B. Ngac, N.N. Hoang, J. Lumin. **132**, 2135 (2012).

[19] T. Dedova, M. Krunks, O. Volobujeva, I. Oja, Phys. Status Solidi C **2**, 1161 (2005).

[20] P.K. Ghosh, M.K. Mitra, K.K. Chattopadhyay, Nanotechnology **16**, 107 (2004).

[21] K.T. Hillie, C. Curren, H.C. Swart, Appl. Surf. Sci. **177**, 73 (2001).

[22] G. Stuyven, P.D. Visschere, A. Hikavyy, K. Neyts, J. Crystal Growth **234**, 690 (2002).

[23] M. Vopsaroiu, M.J. Thwaites, G.V. Fernandez, S. Lepadatu, K. O'Grady,
J. Optoelectron. Adv. Mater. **7**, 2713 (2005).

[24] R. Nandi, S.S. Major, Appl. Surf. Sci. **399**, 305 (2017).

[25] H. Zhang, D. Yang, X. Ma, Mater. Lett. **61**, 3507 (2007).

[26] T.T.Q. Hoa, T.D. Canh, N.N. Long, J. Phys. **187**(1), 012081 (2009).

[27] T.L. Remadevi, A.C. Dhanya, Arch. Phys. Res. **2**, 128 (2011).

[28] K. Yamaguchi, T. Yoshida, D. Lincot, H. Minoura, J. Phys. Chem. B **107**, 387 (2003).

[29] T. Ren, Z. Lei, G. Luan, G. Jia, J. Zhang, R. Yu, C. Li, Thin Solid Films **513**, 99 (2006).

[30] N.R. Jana, S.C. Ray, Graphene-based carbon nanoparticles for bioimaging applications. Mater. Today **16**(10), 365–373 (2015).

[31] R. Saikia, P.K. Kalita, Int. J. Adv. Res. Sci. Eng. **5**, 493 (2016).

Chapter 6

Hierarchical nickel sulphide microstructures for controlled water disinfection and cold cathode emission

- Nickel sulphide microstructure growth has been explained using self catalysis mechanism.
- Photocatalytic degradation of phenol using Nickel sulphide has been studied for the first time under UV excitation.
- The role of stoichiometry of Nickel sulphide in indirect control of dye removal activity was investigated.

Abstract

Hierarchical nickel sulphide microtubes were prepared by cost effective sol-gel technique with tuning of morphology and applied for photo-induced hazardous dye segregation and cold electron emission. The synthesized samples were characterized for crystalline phase, morphology and composition via X-ray diffractometry, electron microscopy and energy dispersive X-ray studies respectively. The band gaps were estimated from UV–vis data. The samples were found to be effective as a dye degrading agent under UV irradiation. The pollutant removal efficiency of the nickel sulphide (NS) microstructures was found to be governed by dimension and compositional parameters jointly. The sample showing highest degradation efficiency was found to degrade phenol effectively. Scavenger test was carried out to identify the active radicals involved in the catalysis process. To ensure long term action of the catalyst sample, recyclability of the same was investigated thoroughly. The NS microstructures also showed field emission behavior which is reported for the first time. The growth of different shapes and hierarchical units of NS structures was correlated with stoichiometric alteration which may also be extended for synthesis of other nickel chalcogenides.

6.1. Introduction

With the fast growing machine based development in industrial areas, average human life has been facing increasing risk of pollutant contamination through consumable water. After increased usage of organic semiconductors [1,2] and organometallic compounds [3] in fabrication of energy storage devices [4,5], alternative energy sources [6] and electrochemical cells [7], several products containing organic residues are released in consumable water near the industrial sectors and eventually transported throughout the water bodies. Several organic residues also contain hazardous organic dyes like methylene blue, methyl orange, rhodamine

B, congo reds etc. which have raised severe health issues during last few decades [8]. Like several other cases where similar drawbacks are removed by incorporating advanced low dimensional materials in modern technology, inevitable water pollution occurring with organic industry can also be resolved by application of smart nanomaterials. Owing to the fact that reduced dimension can enhance exposable effective surface area and enable quantum confinement induced changes in optical and electrical properties [9], nanomaterials, especially semiconductor nanostructures are largely used in solar cells [10,11], electrochemical cells [12], sensors [13], light emitting diodes [14] and several other optoelectronic devices.

However, application of semiconductors in water disinfection technology is also not new. Several n-type semiconductor nanostructures like ZnO [15,16], TiO2 [17,18], CeO [19] are already famous for their photo induced dye degradation performance. Extensive works have already been executed on their photocatalytic activity in pure and modified [20–22] or doped [23–25] form. However, commercialization of photocatalysts for water disinfection purpose is rather not explored much except for TiO_2 [26,27] due to several shortcomings related to synthesis cost and difficult fabrication techniques of the catalysts. In some cases, classical photocatalysts were subjected to foreign materials attachment [28] and the internal e^-/h^+ pair separation becomes easier resulting in enhanced dye removal activities. However, this technique is again expensive and subject to extremely sophisticated experimental set up.

In our earlier works, we have focused on the efficiency in hazardous dye removal from consumable water by traditional n-type semiconductors like TiO_2 [29,30] and non-conventional p-type semiconductors like $CuBO_2$ [31], NiO [32], CuO [33–35] etc. From those studies and other published reports, it can be concluded that modifying photocatalyst dimension by means of internally introduced defects may lead to most efficient catalytic activity. There are several conventional techniques of introducing internal defects within a

pristine photocatalyst. Incorporation of foreign dopants [36] within a catalyst or applying intentional non-stoichiometry [37] is the most used one. These defect states, vacancies often act as trapping sites for the organic pollutant and hence lead to efficient cleaning performance. Additionally, variation of internal compositional non-stoichiometry sometime may also cause variation of microstructure, especially in case of compounds where transitional metal ions are involved. In some earlier studies, nickel sulphide showed promising photocatalytic hydrogen generation performance [38] while its elemental molar ratio were altered or incorporated with foreign components [39]. On the other hand, nickel sulphide exhibited remarkable catalytic activity in solar cells being combined with graphene [40]. Triggered by this idea, in this work, we have studied the photocatalytic activity of nickel sulphide microstructure by simply varying its compositional stoichiometry. Appropriate modulation of input precursor ratios caused effective variation in the structure of the building blocks which served as the unit of hierarchical NS microtubes and indirectly tuned the photocatalytic efficiency. Additionally, the samples synthesized here also showed prominent possibility of cold electron emission performance making the NS samples as 'truly multipurpose'. All the samples were characterized for their structural, morphological and optical properties. Photocatalytic performance of all the samples were investigated under UV irradiation which proved that NS microstructures are eligible to function as future efficient photocatalytic and cold cathode candidates and stoichiometric variation of the constituent elements can lead to enhancement of decay rate substantially. The sample emerged as the most efficient one to degrade Rhodamine B and the same could decompose phenol under UV irradiation with a decay rate of 1.02×10^{-2} min^{-1}.

6.2. Experimental details

6.2.1. Synthesis of nickel sulphide (NS) microtubes: NS microtubes were prepared using wet chemical technique [41]. In a typical experiment, 0.119 g of nickel

chloride hexahydrate ($NiCl_2.6H_2O$) and 1.66 g of Polyvinylpyrrolidone (PVP) were dissolved in 40 mL of ethylene glycol in a beaker. In another beaker, 2.6 mL of hydrazine monohydrate was diluted by 4 mL of ethylene glycol. This solution was added dropwise to 1st solution. The mixture was heated to 158 ℃ with stirring for 3 h. Afterwards, 0.114 g of thiourea dissolved in 16 mL of ethylene glycol was added to the mixture with stirring at 158 ℃ for another 7 h. Black precipitate (chain-like NiS tubes) were formed. Now, after being diluted with absolute ethanol, the solution was centrifuged at 4000 rpm for 30 min several times until its gel form was reduced. The product was then dried for 2 h in vacuum oven at 60 ℃. The obtained sample was labelled as N1S1 which symbolizes the expected atomic ratio of nickel and sulphur as 1:1. The same process was repeated to synthesize samples having atomic ratios 2:1, 3:1, 1:2 and 1:3 and labelled as N2S1, N3S1, N1S2 and N1S3 respectively.

6.2.2. Characterization

All the prepared samples were further characterized by X-ray diffractometer ((Bruker D8 Advanced) with Cu-Kα radiation (λ = 1.54 Å) in a 2θ range from 30°-70°). The morphological features were investigated using field emission scanning electron microscope (FESEM, Hitachi S-4800) and hollow nature of the microspheres was confirmed using transmission electron microscopy (HRTEM, JEOL JEM 2010). The chemical composition and stoichiometric ratio of the samples were studied using energy dispersive X-ray equipped with the FESEM setup. The transmittance spectra of the samples were obtained by a UV–vis-NIR spectrophotometer (Shimadzu UV-3600) and the same was obtained to find out the band gaps of the samples. The photocatalytic activity of the samples was measured using our laboratory made set-up under UV radiation of 254.6 nm wavelength. All the samples were further taken for photocatalytic activity studies in a standard photocatalysis set up. The same process was repeated for hazardous chemical reagent phenol with an exception of time evolution PL spectra was taken in place of UV spectra. Theoretical simulations showed that NS

microstructures can show moderate field emission performance depending upon their morphology. Some of the samples were also tested for electric field emission performance based on simulation results.

6.3. Results and Discussion

6.3.1. Structural studies

Structural information was obtained using XRD studies. The obtained spectra are presented in Fig. 6.1. Different phases of nickel sulphides were identified to be occurring due to variation of the compositional ratio. We can see in Fig. 6.1(a), the sample shows an inherent tendency of being sulphur rich. This is reflected by the peak occurring due to lattice plane (311), (440) of Ni_3S_4. The presence of NiS (002), (101), (102), (110), (200), (112) and (201) planes was also identified. The situation changed very little with increase in Ni precursor amount. Fig. 6.1(b) shows the XRD spectra of sample N2S1 which did not show any significant difference in lattice structure symbolizing the increase of Ni.

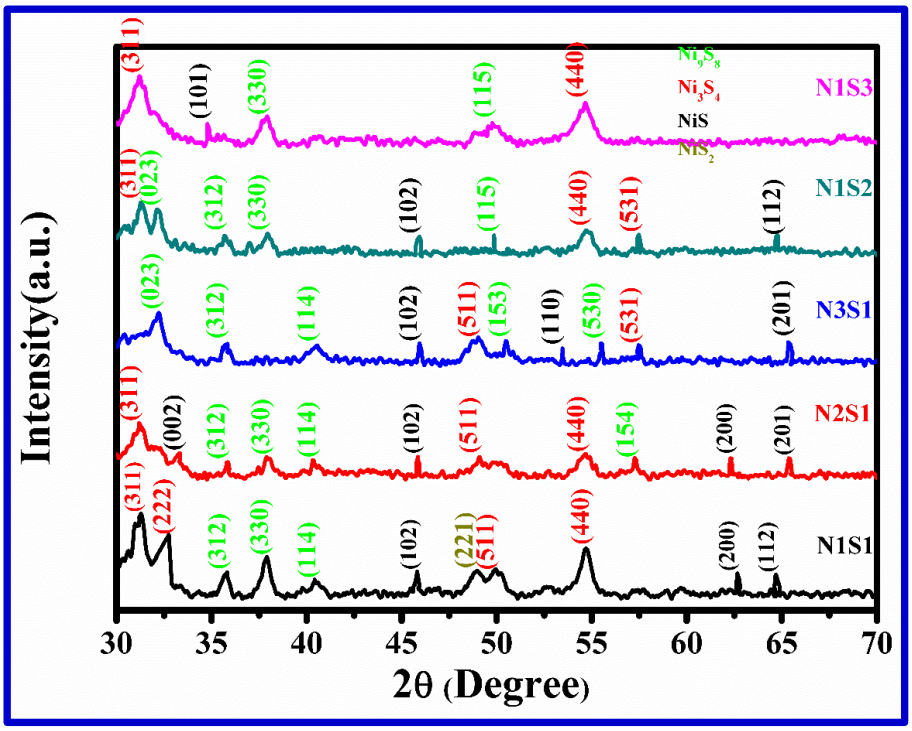

Fig. 6.1. *XRD spectra of sample (a) N1S1, (b) N2S1, (c) N3S1, (d) N1S2, (e) N1S3*

However, in case of sample N3S1, maximum numbers of peaks corresponding to Ni_9S_8 were observed in addition to previous peaks of Ni_3S_4. This was accounted for the significant increment in nominal input of Ni precursors in the reaction. The XRD spectra of sample N1S2 and N1S3 clearly shows that they are sulphur rich due to the increased amount of sulphur precursors in the reaction.

6.3.2. Morphological studies

6.3.2.1. FESEM study

The FESEM micrographs of the samples N1S1, N2S1 and N1S2 are presented in Fig. 6.2 and of N3S1, N1S3 in Fig. 6.3. All the samples show 3 step hierarchical morphologies. The most fundamental building blocks are particles/rod of nickel sulphide which eventually combined to form hollow spheres of the same, the hollow spheres of nickel sulphide together joined to form nickel sulphide microtubes. In sample N1S1 (shown in Fig. 6.2), some undistinguished particulate building blocks of nickel sulphide were observed. Sample N2S1 showed a combination of rod-like and particulate building blocks of hollow nickel sulphide microspheres.

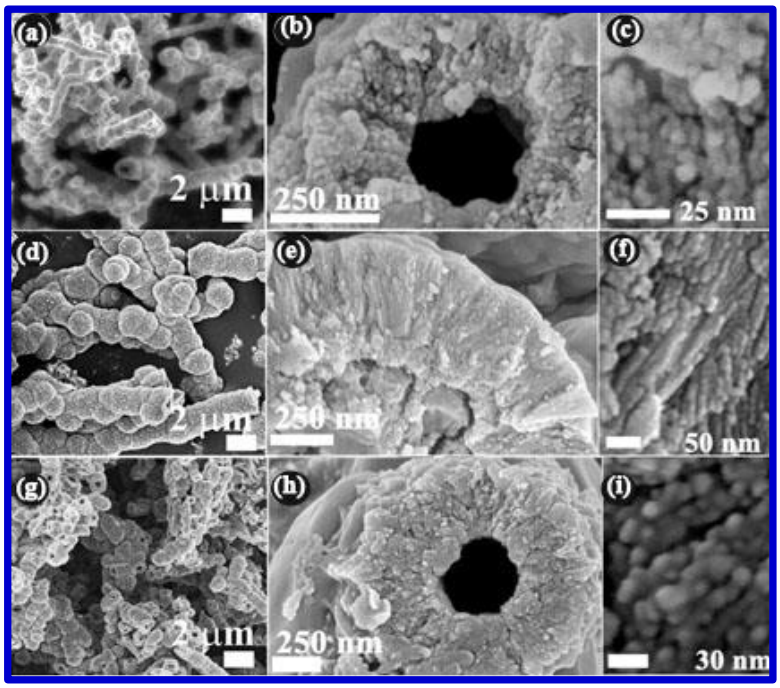

Fig. 6.2. *FESEM images of sample (a-c) N1S1, (d-f) N2S1, (g-i) N1S2*

The fundamental building units in case of sample N3S1 have fully been converted into nickel sulphide microrods. However, the building units of microspheres were observed to be irregular particles in case of samples N1S2 and N1S3.

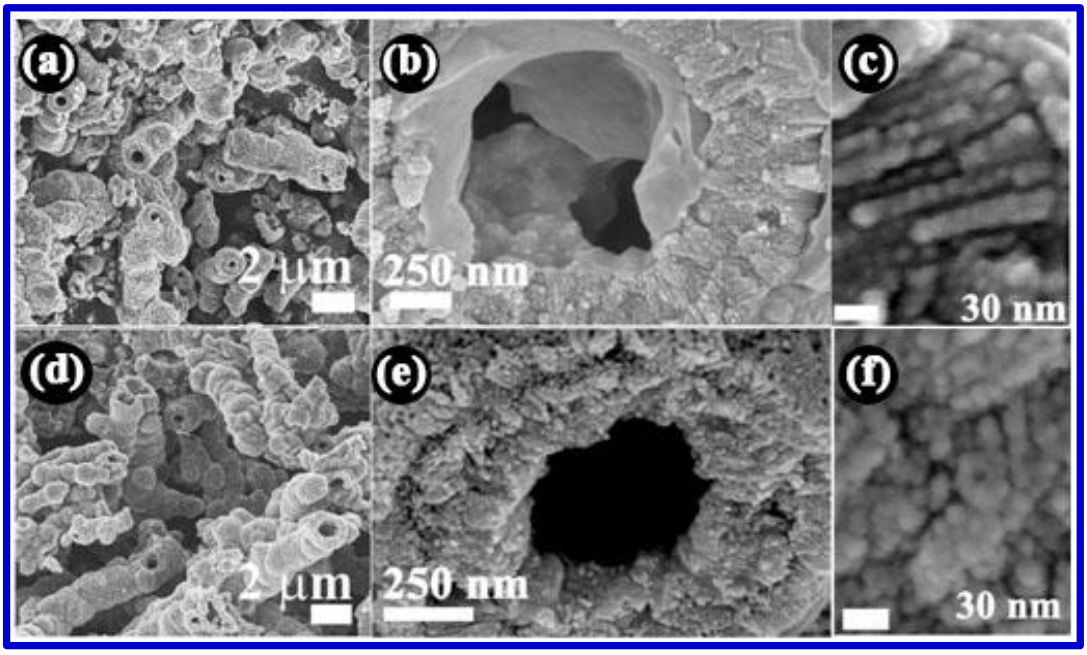

Fig. 6.3. *FESEM images of sample (a-c) N3S1 and (d-f) N1S3*

6.3.2.2. TEM study

To have an idea about the exact dimension of the microtube, wall thickness of the microsphere, transmission electron microscopic studies were carried out. The results are presented in Fig. 6.4. We can see in Fig. 6.4(a) that the fabricated final microstructures are hollow (microtube) in nature having length of few micrometers whereas Fig. 6.4(b) show that the hollow spheres of nickel sulphide have about 1.00 μm diameter and 80 nm wall thickness. The lattice images of the sphere wall is presented in Fig. 6.4(c) where we can observe that distinct lattice planes for (311) plane of Ni_3S_4 are visible whereas polycrystalline nature of the samples can be inferred from Fig. 6.4(d).

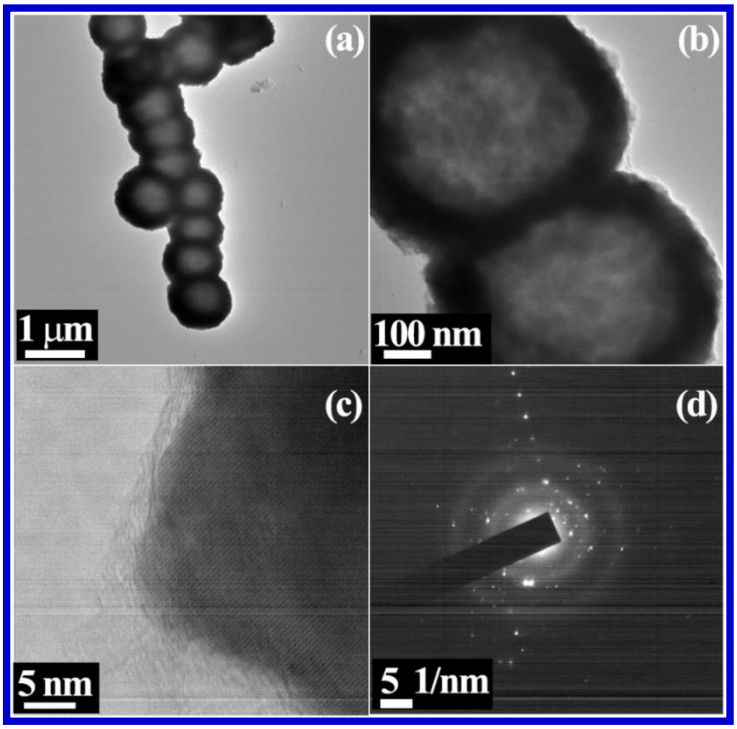

Fig. 6.4. *TEM micrograph of nickel sulphide (a) microtube, (b) microsphere, (c) lattice image of the microsphere wall and (d) corresponding SAED image of N1S1*

6.3.2.3. Probable mechanism of growth of nickel sulphide microstructure

The probable mechanism of this variation of morphology is demonstrated in Fig. 6.5. We know that nickel ions and nickel nanoparticles are often used as efficient seeds for growth of 1-dimensional nanostructures like CNT [42,43]. The technique of using precursor ratio variation for synthesis of nickel sulphide microstructure is based upon this unique feature of nickel nanoparticles. In our work, firstly it can be speculated that one Ni-ion and one S-ion eventually result in a particulate nickel sulphide having no distinguished geometrical shape. However, as the amount of nickel precursor increase beyond the ideal atomic ratio, the supply of nickel ion increases appreciably in the reaction medium. This additional nickel ions work as nucleation centres and thus growth of nickel sulphide with particular shape is enabled. As the supply of nickel ions is further increased in case of sample N3S1, the directional growth is more facilitated and nickel sulphide microrods with smoother surface are fabricated. In the next step, due to general magnetic feature of nickel in the medium, those fabricated nickel

sulphide rods are easily attached together to form the desired nickel sulphide microtubes. This mechanism cannot be expected in sulphur rich medium as obtained in case of synthesis of sample N1S2 and N1S3. In those cases, absence of any specific nucleation centre causes the growth of irregular shaped nickel sulphide microstructures which later combine together resulting in nickel sulphide microtubes. This possible mechanism of growth of hierarchical nickel sulphide microstructure also establishes the successful approach of self-catalysis technique in our work. This auto-catalytic growth technique enables good control over the shape of building blocks of target microstructure and offers easy tuning of application accordingly. As per our best understanding, the same technique can further be extended to the growth of other nickel containing microstructured functional materials.

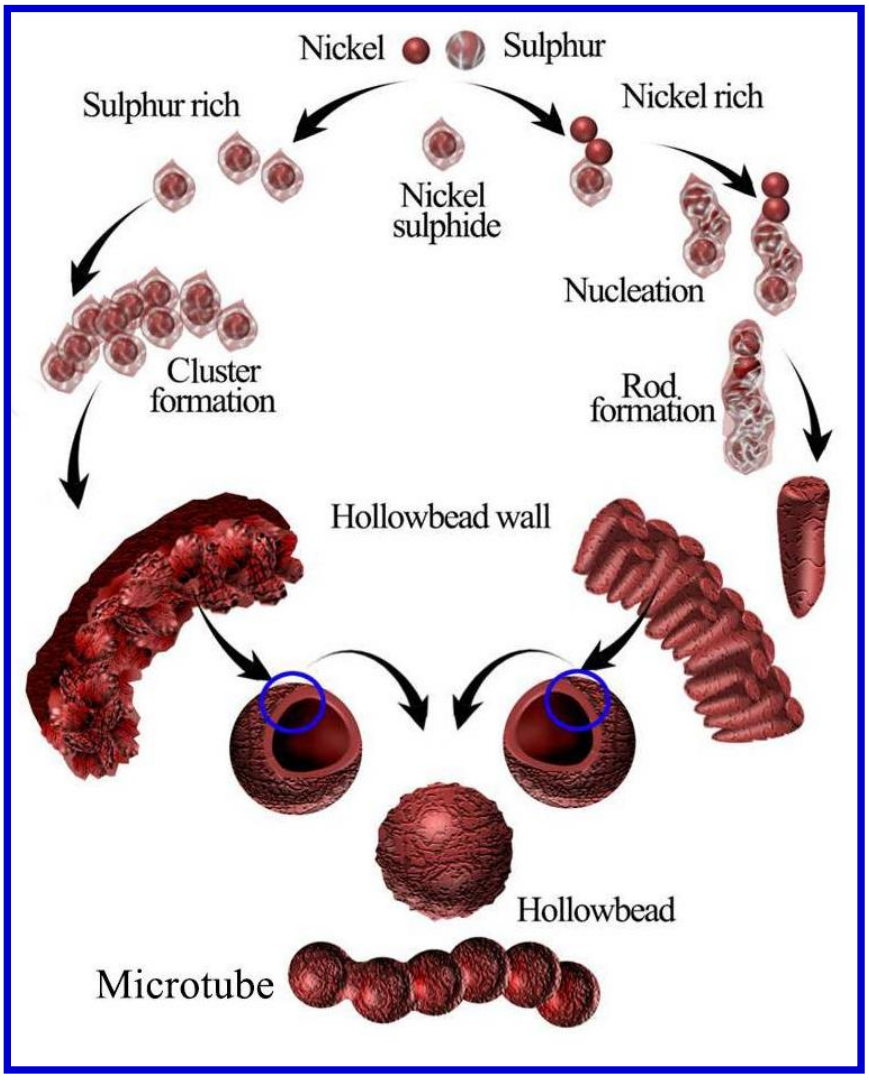

Fig. 6.5. *Schematic of possible growth mechanism of the samples*

6.3.3. Compositional studies

The samples were also characterized by EDX and the results are presented in Fig. 6.6. In the Fig. [6.6 (a–e)], we can see the presence of Ni and S in both EDX spectra and elemental mapping of the samples. The amounts of the constituent elements are quantitatively compared in Fig. 6.6(f). We can see that the elements are present in almost perfect atomic ratio in case of sample N1S1 and their inconsistency increases as the input of Ni or S increases in sample N1S3 or N3S1. However, the composition of the elements in the samples affected the structural feature up to a large extent and hence played an important role in the application i.e. photocatalytic activity of all the samples.

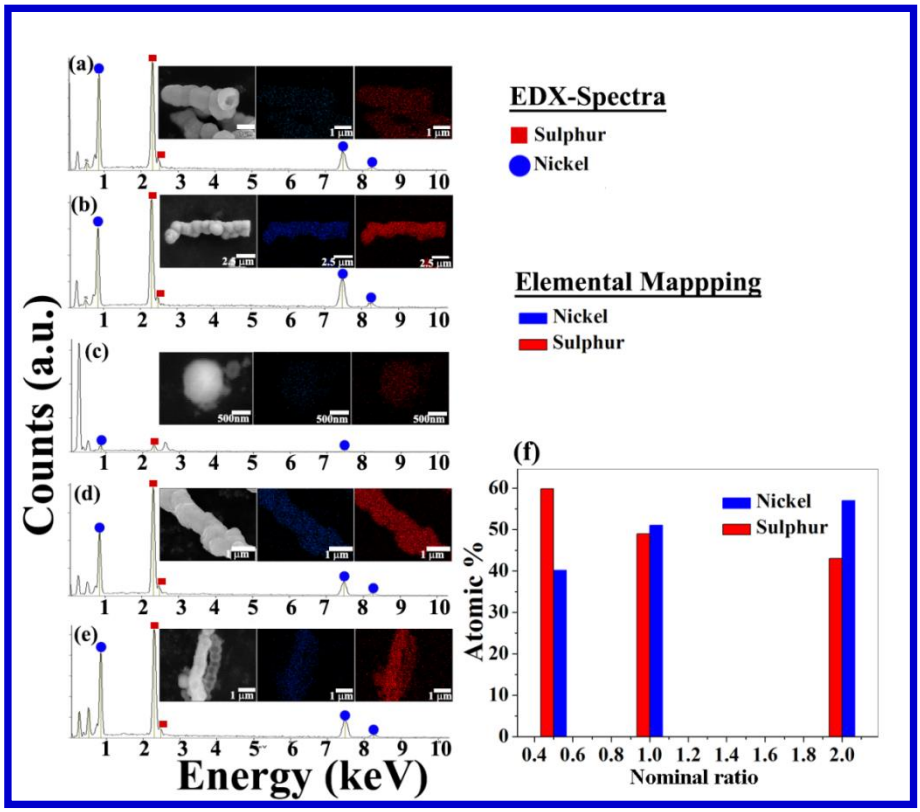

Fig. 6.6. *EDX spectra of sample (a) N1S1, (b) N2S1, (c) N3S1, (d) N1S2, (e) N1S3 and (f) variation of atomic % of Ni and S with amount of Ni:S ratio in precursors*

6.3.4. Optical studies

To determine the energy gap exhibited by the samples, UV–vis spectroscopic investigations

were carried out. The transmission spectra of the samples are presented in Fig. 6.7(a). The band gap was measured using the following equation

$$(\alpha h\nu)^{1/n} = A(h\nu - E_g) \quad (1)$$

where, A is a constant, E_g is the band gap energy of the material, and the exponent n depends on the type of the transition. The values of n for direct allowed, indirect allowed and direct forbidden transitions are n = 1/2, 2, and 3/2, respectively. To determine the possible transitions, $(\alpha h\nu)^{1/n}$ versus hν were plotted, and the corresponding band gaps were obtained by extrapolating the linear portion of the graph.

The obtained results are presented in Fig. 6.7(b). We can see that all the samples exhibit band gap in the UV region which agrees well with earlier reports [44].

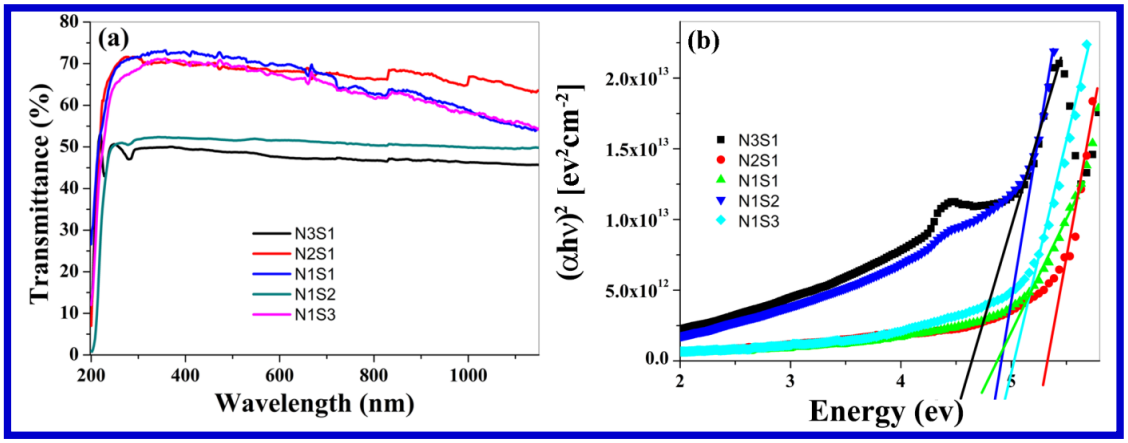

Fig. 6.7. *(a) Transmission spectra and (b) band gaps of the samples*

6.3.4.1. Photocatalytic activity studies

Based on the results obtained in UV–vis studies, all the samples were characterized to investigate their photocatalytic activities. A standard set up for investigation of photocatalytic activity was used which includes two 40 W UV (Philips) tubes capable of 254.6 nm (UVC) emission and a photocatalysis media placed at 15 cm distance. The catalysis media was composed of 40 mL 10^{-5} M RhB test solution and 0.03 g sample. Prior to actual catalytic performance investigation, photolysis of the dye was performed up to saturation and then, the

uniform dispersion of the sample in the dye solution was produced via adding the mentioned amount of the sample. The mixture was then kept under dark stirring for one hour to achieve the adsorption-desorption between the catalyst sample and the dye molecules. The dispersion was thereafter exposed to UV irradiation. The photocatalysis experiment was carried out under constant stirring for different time durations. After a pre-defined time interval, a certain portion of the degraded solution was collected. Those collected solutions were later subjected to absorption studies. The results are represented in Fig. 6.8 and Fig. 6.9.

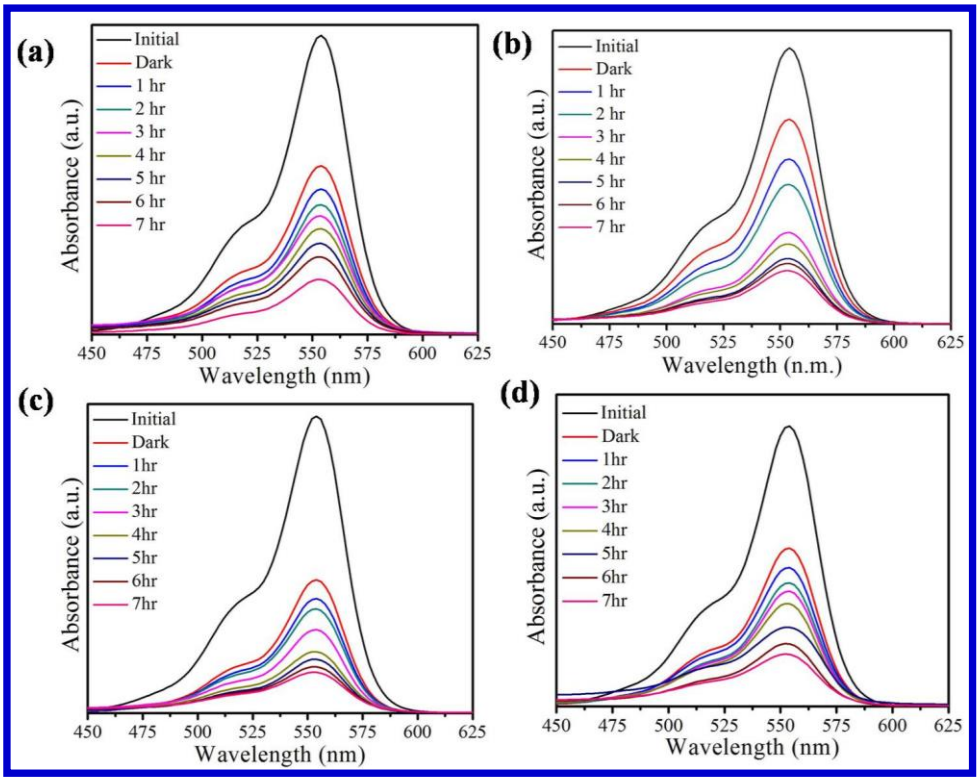

Fig. 6.8. *Photocatalytic activity of the samples (a) N1S1, (b) N2S1, (c) N1S2, (d) N1S3*

It is confirmed from the time evolved UV–vis absorbance spectra of the hazardous organic dye RhB that the catalyst sample degraded that pollutant appreciably almost within 7 h though a minor self-degradation by indirect activation of the dye molecule was also observed. The physical image presented in Fig. 6.9(b) also indicate the blank test of RhB degradation as

well as the time evolved degradation of that organic dye from test solution in presence of the best performing nickel sulphide catalyst.

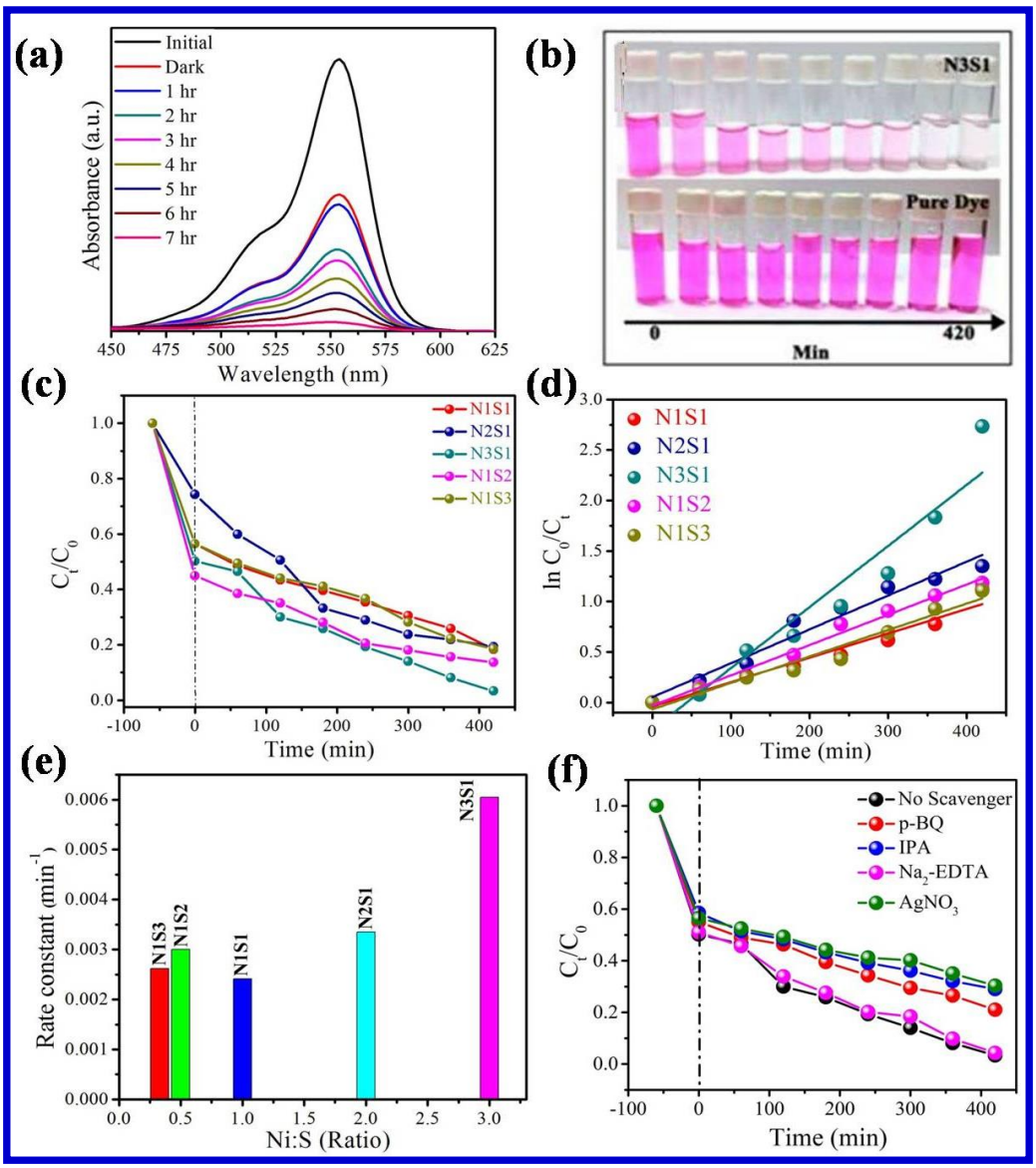

Fig. 6.9. *(a) Time evolved UV-Vis absorbance spectra of RhB in presence of photocatalyst N3S1, (b) digital image of degradation for N3S1 and pure dye, (c) Photocatalytic degradation profile of RhB in presence of the samples N1S1, N2S1, N3S1, N1S2 and N1S3, (d) ln(C_0/C_t) vs. time plot, (e) plot of the rate constant values with Ni:S ratio and (f) the scavenger test results*

Also, the degradation efficiency (η) of the as-synthesized samples can be calculated from C_t/C_0 *vs.* t plot (Fig. 6.9(c)) using the equation,

$$\eta = \frac{C_0 - C_t}{C_0} \times 100 \qquad (2)$$

The degradation percentage of the dye is ~ 37 % by direct UV photolysis for 7 h in the absence of the catalyst (Fig. 6.10) whereas its value become 81.57 %, 80.74 %, 96.72 %, 86.26 % and 81.35 % by using photocatalyst samples N1S1, N2S1, N3S1, N1S2 and N1S3 respectively.

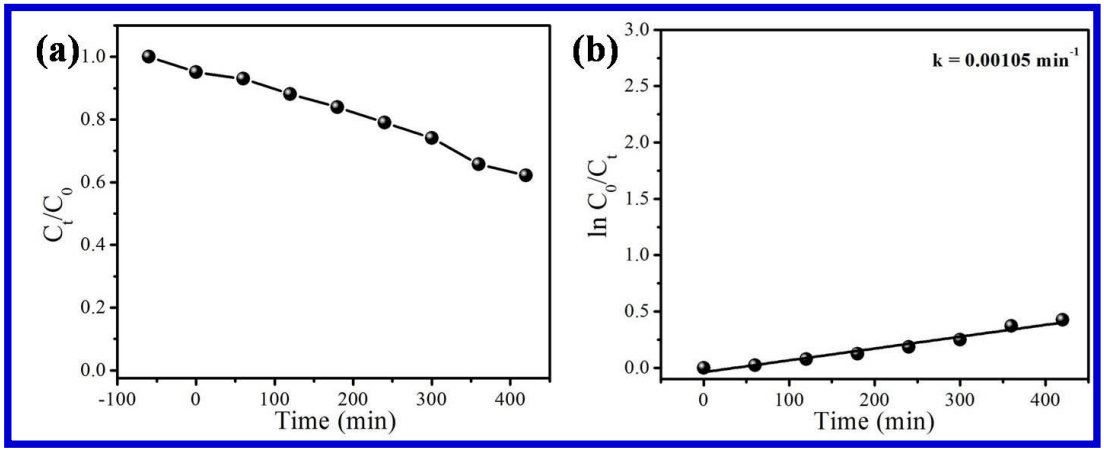

Fig. 6.10. *Photolysis of the dye RhB; (a) C_t/C_0 vs. time plot and (b) $ln(C_0/C_t)$ vs. time plot*

In addition to the absorption tests, the rate constants for RhB degradation with UV irradiation time were also determined using the Langmuir–Hinshelwood model for kinetics of photocatalytic reaction

$$r = \frac{-dc}{dt} = \frac{k_r k_a C}{1+k_a C} \quad (3)$$

where, k_r and k_a represent rate constant and adsorption constant respectively. Simplifying the above equation, we can write

$$ln\frac{C_0}{C_t} = k_r k_a t = kt \quad (4)$$

where, C_0 and C_t represent the concentration of the dyes at t = 0 and at any given time t and k is the rate constant. The photocatalytic activity of all the samples with respect to time i.e. $ln\frac{C_0}{C_t}\ vs.\ t$ plot is presented in Fig. 6.9(d) and the variation of rate constant with respect to ratio of nickel and sulphur are depicted in Fig. 6.9(e). We can clearly see that the

photocatalytic activity gradually enhanced with increase in nickel content in the synthesis medium. The same is reflected in the highest rate constant (0.00605 min^{-1}) exhibited by N3S1 sample.

Scavenger test was performed to identify the role of active radicals, electrons and holes in photocatalysis process. For this experiment, 0.01 mol/L p-benzoquinone, 0.01 mol/L IPA, 0.01 mol/L Na_2-EDTA and 0.01 mol/L $AgNO_3$ can be used as the scavengers for superoxide radicals ($\bullet O_2^-$), hydroxide radicals ($\bullet$ OH), holes (h_{VB}^+) and electrons (e_{CB}^-) respectively [45] and during the photocatalysis, the same were added to the active media. Fig. 6.9(f) shows the C_t/C_0 *vs.* time plot presenting the effect of scavenger additions to the reaction rate of N3S1 sample. Also, the respective degradation efficiency of the sample in the presence of different scavengers with UV irradiation is shown in Fig. 6.11.

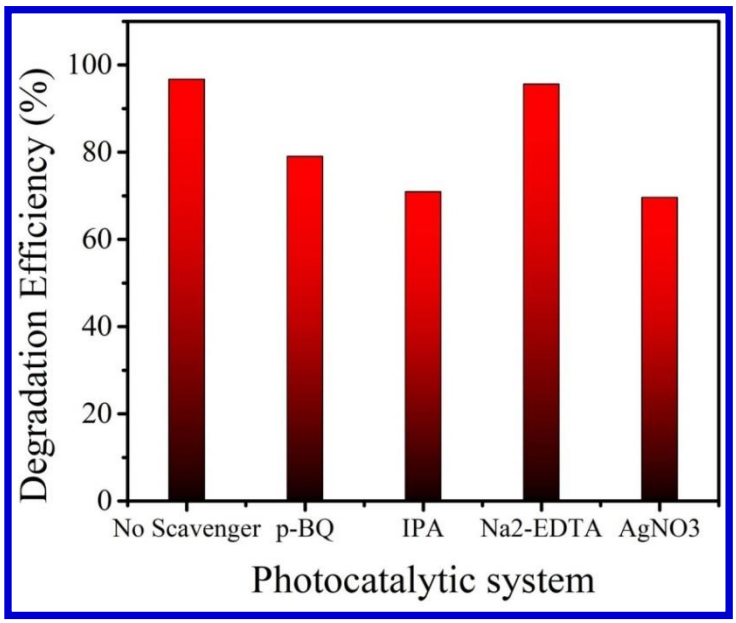

Fig. 6.11. *Degradation efficiency of N3S1 in the presence of different scavengers with UV irradiation*

It can be clearly observed that without any scavengers, N3S1 can degrade 96.72 % of Rhodamine B within 7 h. Whereas, in presence of the hole-capturing agent Na_2-EDTA, degradation percentage of the dye becomes 95.67 % within the same time. On the other hand, degradation percentage decreased to a high extent after addition of p-benzoquinone (79 %),

$AgNO_3$ (69.6 %) and IPA (70.9 %).This indicates that the superoxide radicals, photogenerated electrons and hydroxide radicals have a major contribution in catalysis process.

6.3.4.2. Plausible photocatalytic mechanism

The degradation of any hazardous organic dye in presence of catalyst samples is highly interconnected with the carrier transfer across the electronic bands of the catalyst (here nickel sulphide). To establish the well-known theory of catalysis by separation of photogenerated electron-hole pairs, the relative positions of conduction and valence bands must be considered. Using the empirical relation [5], the positions of the conduction and valence bands were determined theoretically

$$E_{CB} = \chi - E_e - 0.5E_g \quad (5)$$

where, E_{CB} represents the conduction band edge potential, χ is the geometric mean of the Mulliken's electronegativity exhibited by the constituent atoms. χ can be derived using the following equation

$$\chi = \left[\chi_A^a \times \chi_B^b \times \chi_C^c\right]^{\frac{1}{a+b+c}} \quad (6)$$

where, a, b, c represent the number of the atoms of element A, B and C respectively.

E_e is considered being ~ 4.5 eV which is the energy of the free electrons on hydrogen scale and E_g is the band gap of the system. The values of E_g and χ for nickel sulphide are 4.65 eV and 5.23 eV respectively.

Additionally, the position of the valence band (E_{VB}) can be evaluated from the equation as follows,

$$E_{VB} = E_{CB} + E_g \quad (7)$$

Now, the calculated values of E_{CB} and E_{VB} for NiS were determined to be -1.59 V and +3.05 V respectively versus normal hydrogen electrode (NHE). Using these obtained values, the degradation of hazardous organic dye in presence of samples N3S1 to N1S3 can be explained in terms of e^-/h^+ pair generation. When a light having same or higher energy than the band gap of nickel sulphide is incident upon the sample, the catalyst molecule absorbs photon and as a result, an electron-hole (e^-/h^+) pair is generated. However, the LUMO and HOMO positions of the RhB dye are -1.10 V and +1.14 V respectively (vs. NHE) [46]. So, the electrons from the conduction band and holes from the valence band of the catalyst molecule may directly interact to the dye molecule and actively participate in the photocatalytic dye degradation. Also, the standard redox potential of OH^- / • OH (+1.9 V vs. NHE [47]) was turned out to be less positive than the valence band position of nickel sulphide. So, the VB of NiS promotes the oxidation reaction of OH^- to • OH by supplying photogenerated holes. Whereas the position of O_2 / (• O_2^-) redox potential is at -0.33 V vs. NHE [48, 49] which is less negative and comparatively closer to the CB position of catalyst sample. Hence, the electron rich CB of NiS can trigger the reduction of the surface adsorbed O_2 to the superoxide radicals (• O_2^-). All of these active radical species along with electrons and holes further participate into actual decomposition of the organic RhB dye. Along with the catalyst, the dye also absorbs light and for this, the electron-hole pairs are generated in the HOMO and LUMO of the dye molecules. These electron and holes also take part in the degradation process. The entire photocatalytic degradation mechanism has been pictorially represented in a schematic as shown in Scheme 6.1.

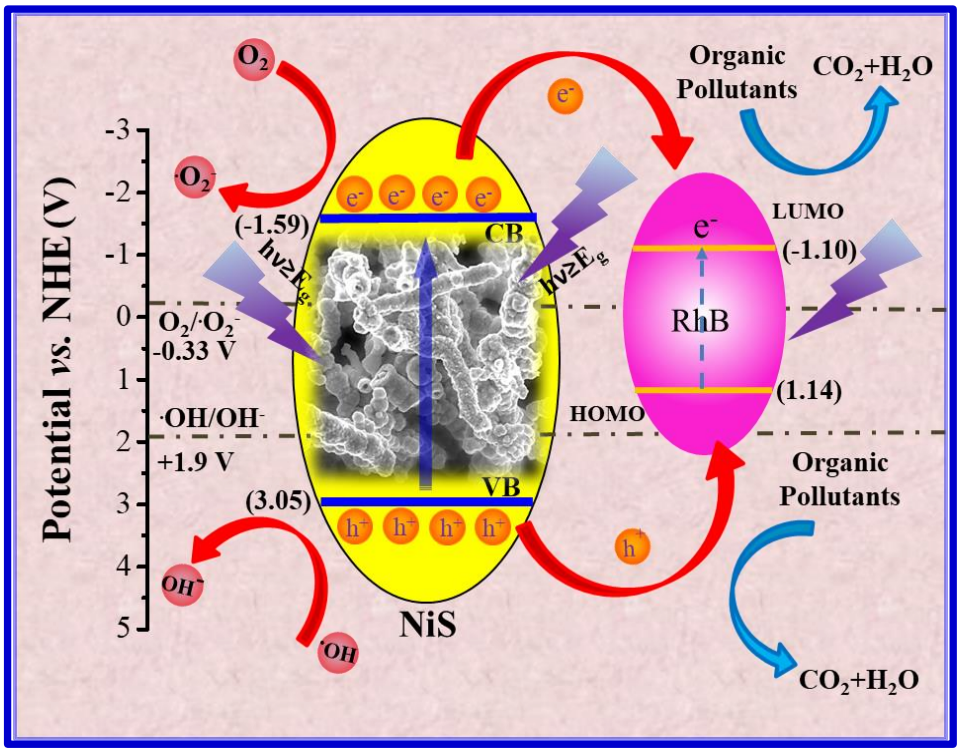

Scheme 6.1. *Probable photocatalytic mechanism of NiS microstructures*

A possible set of reaction steps to describe the degradation of RhB may be as follows,

Nickel sulphide → (hν) → $e^- + h^+$

RhB + hν → RhB* → $RhB^{+\cdot} + e^-$

$h^+ + H_2O \rightarrow HO\cdot + H^+$

$e^- + O_2 \rightarrow \cdot O_2^-$

$\cdot O_2^- + H^+ \rightarrow HOO\cdot$

$e^- + HOO\cdot + H^+ \rightarrow H_2O_2$

$H_2O_2 + e^- \rightarrow HO\cdot + OH^-$

$\cdot O_2^-/HO\cdot + RhB/RhB^{+\cdot}$ → intermediates → degradation product

However, the gradual enhancement of photocatalytic activity with nickel and sulphur ratio can directly be correlated with the morphological features of the samples. From the FESEM images of the samples, we observed that the fundamental building units varied with variation of amount of nickel or sulphur within the synthesis medium. The increase of sulphur content

in input precursor did not effectively influence the shape of building units of nickel sulphide microstructures. When the amount of sulphur was increased compared to the ideal ratio, the effect was not much reflected in the shape of the particles which formed the microspheres. But as the nickel content increased in case of sample N2S1, and further in N3S1, the building units were changed into smooth microrods instead of irregular microstructures. As a result, a considerable enhancement in the aspect ratio was obtained for the microrods and thus, the effective area of contact of the catalyst with the dye solution increased. The result was further reflected in the enhanced degradation rate of RhB from water by nickel rich NiS microstructures.

6.3.4.3. Stability test

To ensure the multiuse capabilities and stability of the cleaning agent, the photocatalytic reusability test was carried out under identical conditions [45]. The recyclability test result of the best performing catalyst sample up to three cycles is presented in Fig. 6.12(a). After completion of each cycle, the catalyst material was collected and dried to be used for the next cycle. It was observed that the degradation efficiency remained more than 87 % after 3 cycles. To check whether the sample could retain its phase and morphology after multiple use, the catalyst was subjected to XRD study and FESEM analysis after 3 photocatalytic cycles and the results are presented in Fig. 6.12(b, c).

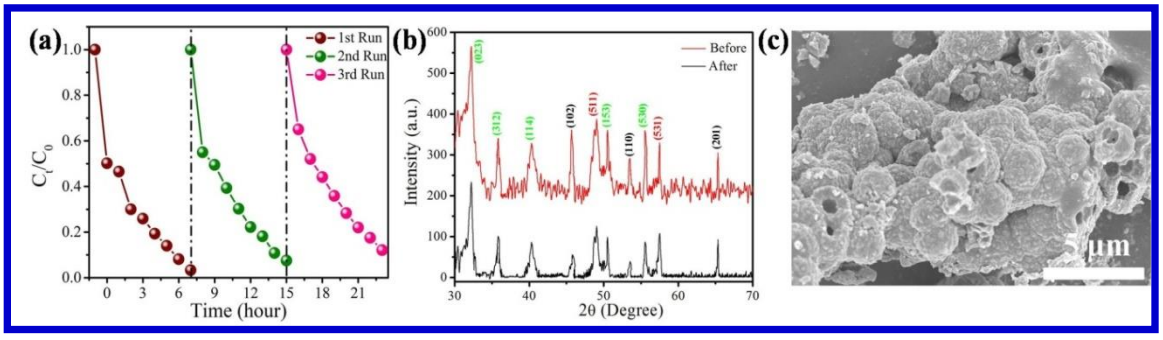

Fig. 6.12. *(a) Recyclability test for the degradation of RhB by the sample N3S1 up to 3rd cycle, (b) XRD pattern of the sample after and before catalysis and (c) FESEM image of the catalyst after catalysis*

This study confirmed that the sample could retain its phase purity and morphology even after prolonged UV irradiation and catalysis performance. These results ensure multiple uses of the Ni-rich catalysts as green cleaning agents.

6.3.4.4. Degradation of phenol

Based on the performance of the samples in degrading RhB, the activity of the most efficient sample in degrading phenol was also studied. For this purpose, 0.01 g of raw phenol was added in 500 mL of de-ionised water to make the stock solution. The reaction was carried out by dissolving 22 mg of NiS in 40 mL of stock solution and initially stirred in dark condition for 1 h. The solution was then exposed under UV irradiation and degradation of phenol was observed with time interval of 1 h for 5 h.

The self-degradation of phenol was tested under UV light irradiation for 5 h and the time evolved fluorescence absorbance spectra is presented in Fig. 6.13(a). However, the sample N3S1, appeared as the best photocatalyst, was further applied to execute degradation activity for phenol. From the time evolved fluorescence absorbance spectra of phenol (Fig. 6.13(b)), it can be concluded that within 5 h of UV-light irradiation, the sample N3S1 completely decomposed the targeted pollutant. The comparative F_t/F_0 vs. time plot is presented in Fig. 6.13(c). The degradation rate constant was also calculated from $\ln(F_0/F_t)$ *vs.* time plot (Fig. 6.13(d)), and the same was found to be 1.02×10^{-2} min^{-1} for the sample N3S1 as depicted in the inset of Fig. 6.13(d).

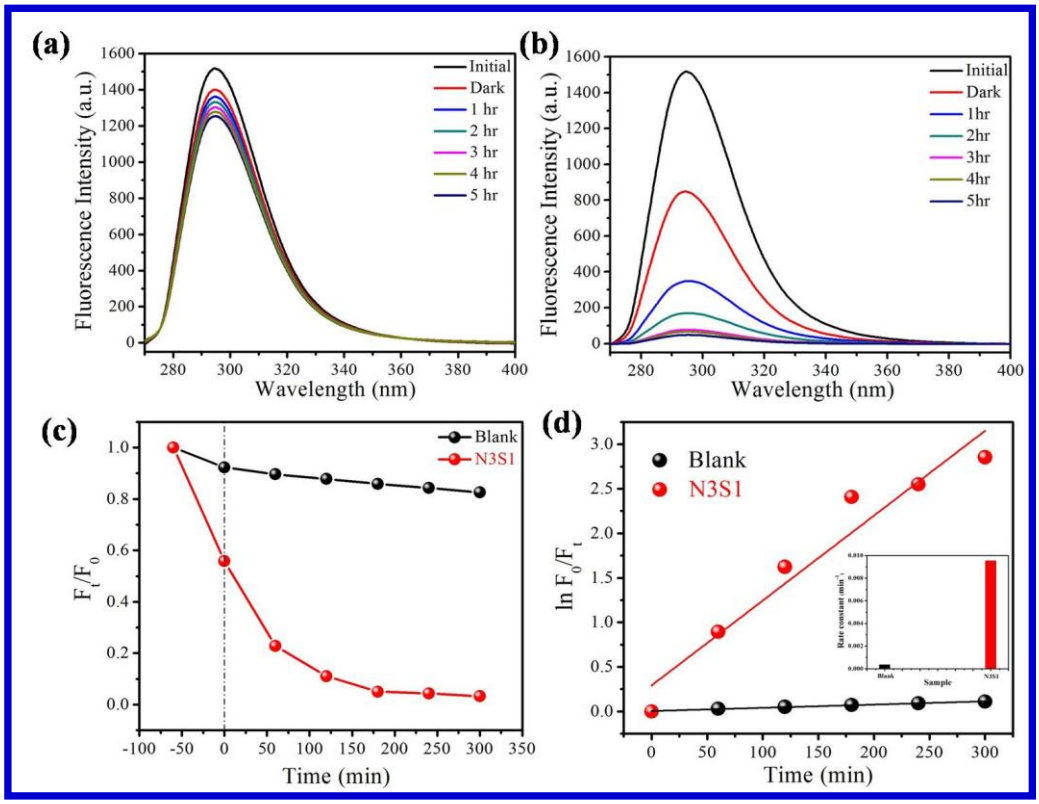

Fig. 6.13. *(a) Time-evolved PL spectra of phenol under UV light irradiation without catalyst, (b) Phenol degradation activity of the most efficient sample N3S1, (c) F_t/F_0 vs. time plot of pure phenol and N3S1 and (d) plot of $\ln(F_0/F_t)$ vs. UV irradiation time of the sample for degradation of phenol*

A comparison of photocatalytic activities of NiS microstructures with the same of other identical chalcogenide systems in degradation of RhB and Phenol have been presented in Tables 6.1 and 6.2 respectively. It can be clearly seen that NiS microstructures synthesized in this work can act efficiently as other similar catalyst under UV excitation. Moreover having a complex hierarchical morphology, this system can also be used for other applications like energy storage, photovoltaic and field emission purposes, and hence deserves to be a multipurpose advanced material.

Table 6.1. *Comparative data of photocatalysis performance of identical chalcogenide systems*

System	Dye used	Excitation type	Excitation Wavelength (nm)	Excitation Power (W)	Rate Constant (m^{-1})	Reference
Pure ZnS	Congo Red	UV	332	100	0.0028	[50]
ZnS:Co(3%)	Congo Red	UV	332	100	0.0049	[50]
Pure CuS NP	RhB	UV	-	12	0.0026	[51]
NiS NP	RhB	Visible	-	200	-	[52]
Pure CdS NWs	MO	UV	-	300	0.081	[53]
Pure SrS NP	MO	UV	-	300	0.004	[53]
NiS NP	RhB	UV	255	80	0.006	This work

Table 6.2. *Comparative data of phenol degradation performance of identical chalcogenide systems*

System	Dye used	Excitation Type	Excitation Wavelength (nm)	Excitation Power (W)	Phenol degradation after 120 min irradiation (in %)	Reference
Ag_2SZnS/TNF	Phenol	UV	286	100	87	[54]
ZnS(Ag_2S/TNF)	Phenol	UV	286	100	87	[54]
NiS NP	Phenol	UV	250	80	88.84	This work

6.3.5. ANSYS Simulation

Having observed the high surface roughness and inherent nanocrystallinity of the NS samples, we anticipate that the materials may exhibit electron emissions also under moderate

applied electric field. To check the suitability of such anticipation, at first, finite element based ANSYS MAXWELL simulations were carried out. NS samples were modelled using that software. The dimension and shapes of the microstructures were kept as per actual basis as obtained in morphological studies. The NS sample-collector distance was also maintained in few micrometers. A virtual external electric field was applied to the models and the corresponding simulated output field at their vicinity was plotted with appropriate colour code. The results are summarized in Fig. 6.14.

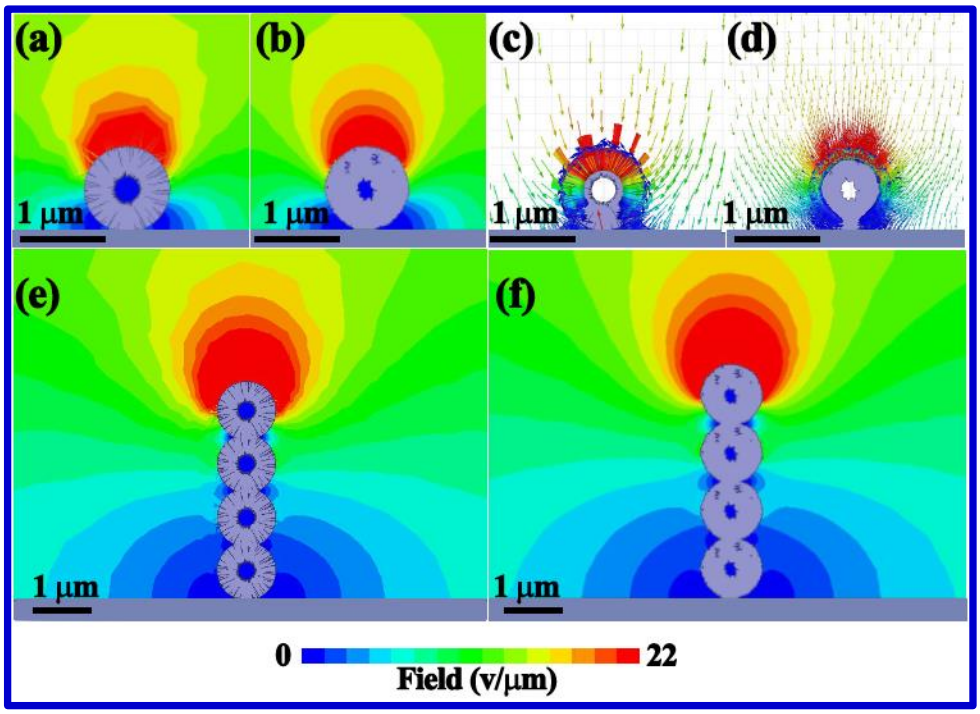

Fig. 6.14. *ANSYS simulation results of output field magnitude for nickel sulphide single (a) rod-made sphere (b) particulate sphere: Field vectors for single (c) rod-made sphere (d) particulate sphere and output field magnitude for micro tube with (e) rod-made sphere (f) particulate sphere*

It can be clearly seen that theoretical investigations predict that NS microstructures are exhibiting appreciable local field enhancement which may lead to electron emission if subjected to external electric field. However, slightly higher output field was simulated in case of particulate NS microstructures. The screening of output field due to large number of closely spaced individual nanorod may be responsible for comparatively lower simulated

field in case of nickel rich sample models. Encouraged by the above results, we have experimentally studied the electron emission which is discussed below.

6.3.6. Field emission studies

Based on simulation results, actual field emission studies were carried out in our laboratory made field emission set up. The field emission measurements were carried out within a closed vacuum chamber maintaining parameters like inter-electrode separation etc. identical as theoretical simulations. A provision for monitoring of electrical charging was associated with the closed chamber which was evacuated at about 1×10^{-6} Pa base vacuum with the help of a combination of rotary and diffusion pumps. Fig. 6.15 shows the J-E characteristics of the samples as observed experimentally. Identical to the theoretical prediction, the current density can be found to be slightly better in case of sample N1S2 which has particles as building blocks. Theoretically, the emission current density (J) and electric field (E) follows the well-known Fowler-Nordheim (F-N) equation

$$J = (a\beta^2 E^2/\phi)\exp\left[-b\phi^{3/2}/(\beta E)\right] \quad (8)$$

where, a = 1.54×10^{-6} A eV V^{-2} and b = 6.83×10^3 $eV^{-3/2}$ V μm^{-1} are Fowler-Nordheim (F-N) constants.

Here, ϕ and β are the work function and the field enhancement factor, respectively. This equation can be re-written as

$$\ln(J/E^2) = \ln(a\,\beta^2/\phi) - b\phi^{3/2}/(\beta E) \quad (9)$$

ϕ and β are related to each other by the equation

$$\beta = -b\phi^{3/2}/m \quad (10)$$

where, m is the slope obtained from F–N plot, i.e. a plot of $\ln(J/E^2)$ versus 1/E.

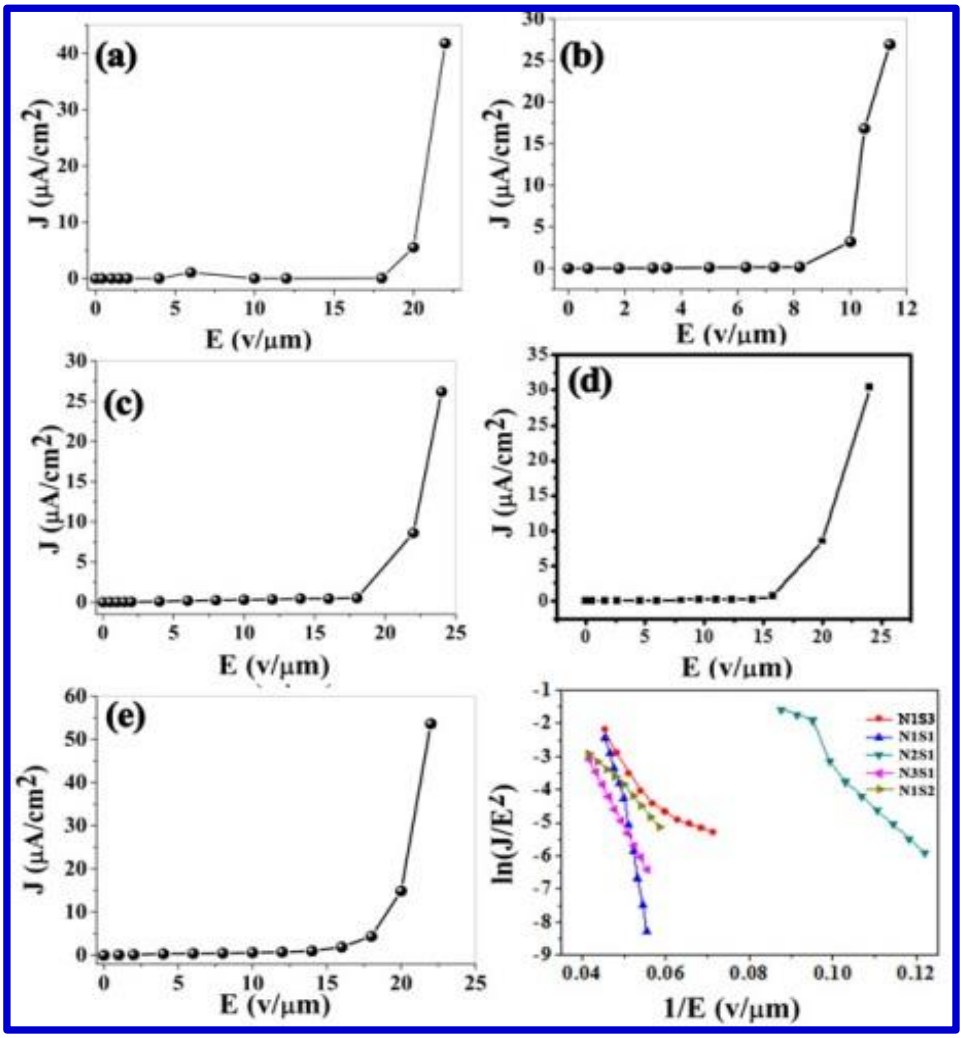

Fig. 6.15. *J-E curves for sample (a) N1S1, (b) N2S1, (c) N3S1, (d) N1S2, (e) N1S3; (f) corresponding F-N plots*

The negative slopes of the F-N plots ensured the cold emission nature of the results. The turn-on field was defined as the required electric field to achieve an emission current density 1 μA cm^{-2} and was noted from the J-E curves. The variation of turn-on field for different samples is presented in Fig. 6.16. It can be observed that the best field emission properties are executed by sulphur rich sample which is already indicated by ANSYS study.

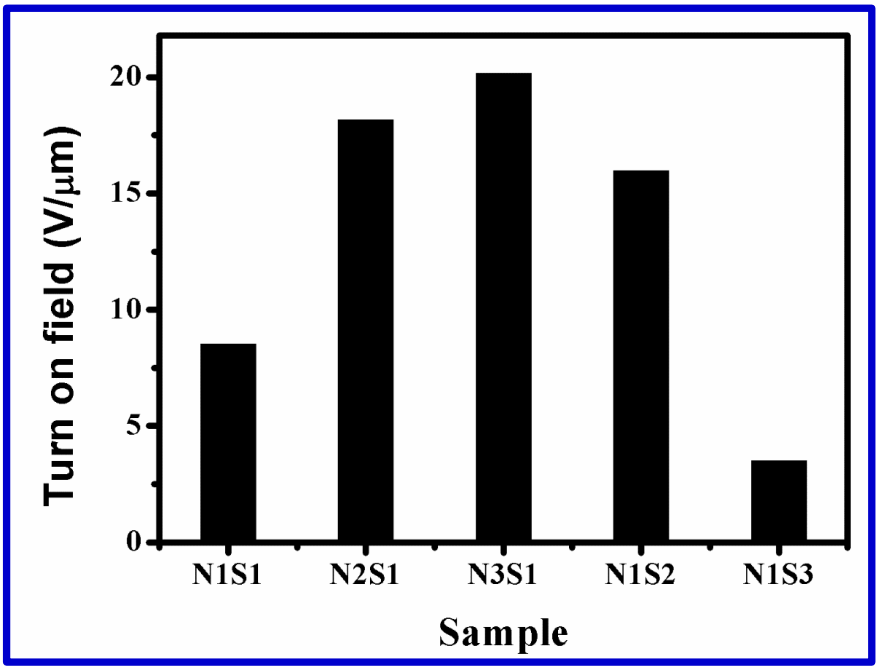

Fig. 6.16. *Turn-on fields for different samples*

The probable reason is also associated with sample morphology. With increase of rod-like building blocks in nickel rich samples, each rod is expected to behave like individual emitter which leads to higher screening effect. Whereas in sulphur rich samples, individual particles are not the effective emitters, rather the entire tube acts as the cold cathode, resulting in comparatively higher emission behaviours. Though it cannot be stated that the samples are competitively efficient cold cathodes as observed in carbon-based systems, the FE behaviour can further be enhanced with the boost of external functional groups and further modification of morphology. Moreover, additional efficiency in dye degradation establishes these morphology tuned nickel sulphide systems as potential future multifunctional material.

6.4. Conclusion

Application of nickel sulphide microstructures in UV driven water disinfection technology was reported for the first time. The compositional tuning of constituent elements was

employed to control the morphology of 3-step hierarchical microstructures and was explained in a novel auto-catalytic growth model which is extendable for other nickel compounds. The increase in nickel content within the samples was observed to govern the photocatalytic efficiency of the microstructures and was explained to be occurring due to the variation of aspect ratio. The active radicals responsible for photocatalysis process were investigated along with thorough study of its multiuse capability. Cold electron emission from nickel sulphide microstructures showed morphology dependent turn-on field and current density. This work therefore explores new application aspects of nickel sulphide microstructures which is easily tunable by simple variation of precursor ratio.

6.5. References

[1] Y. Yamashita, Sci. Technol. Adv. Mater. 10 (2016), 024313.

[2] M. Jakesova, D.H. Apaydin, M. Sytnyk, K. Oppelt, W. Heiss, N.S. Sariciftci, E. D. Glowacki, Adv. Funct. Mater. 26 (2016) 5248.

[3] G.J. Kubas, J. Organomet. Chem. 694 (2009) 2648.

[4] K. Gurunathan, A.V. Murugan, R. Marimuthu, U.P. Mulik, D.P. Amalnerkar, Mater. Chem. Phys. 61 (1999) 173.

[5] X. Wang, Y. Chen, O.G. Schmidt, C. Yan, Chem. Soc. Rev. 45 (2016) 1308.

[6] F. Khodadadian, M. Nasalevich, F. Kapteijn, A.I. Stankiewicz, R. Lakerveld, J. Gascon, Alternative Energy Sources for Green Chem., 2016, p. 227.

[7] K.Y. Lin, L.D. Bastatas, K.J. Suhr, M.D. Moore, B.J. Holliday, M.M. Jolandan, J. D. Slinker, ACS Appl. Mater. Interfaces 8 (2016) 16776.

[8] R. Pol, M. Guerrero, E.G. Lecina, A. Altube, E. Rossinyol, S. Garroni, M.D. Baro, J. Pons, J. Sort, E. Pellicer, Appl. Catal. B Environ. 181 (2016) 270.

[9] A. Ghorai, S. Bayan, N. Gogurla, A. Midya, S.K. Ray, ACS Appl. Mater. Interfaces 9 (2017) 558.

[10] C.K. Sumesh, Sol. Energy Mater. Sol. Cells 192 (2019) 16.

[11] R. Selvapriya, J. Mayandi, V. Ragavendran, V. Sasirekha, J. Vinodhini, J.M. Pearce, Ceram. Int. 45 (2019) 7268.

[12] A. Mohammad, K. Kapoor, S.M. Mobin, Chem. Sel. 1 (2016) 3483.

[13] J. Zhang, X. Liu, G. Neri, N. Pinna, Adv. Mater. 28 (2016) 795.

[14] J. Jayabharathi, S. Sivaraj, V. Thanikachalam, S. Panimozhi, J. Anudeebhana, J. Photochem. Photobiol. A: Chem. 389 (2020) 112229.

[15] P. Nandi, D. Das, Appl. Surf. Sci. 465 (2019) 546.

[16] C.J. Páez, J.A. Navío, M.C. Hidalgo, J. Photochem. Photobiol. A: Chem. 356 (2018) 112.

[17] R.S. Sabry, Y.K. Al-Haidarie, M.A. Kudhier, J. Solgel Sci. Technol. 78 (2016) 299.

[18] A. Hu, R. Liang, X. Zhang, S. Kurdi, D. Luong, H. Huang, P. Peng, E. Marzbanrad, K. D. Oakes, Y. Zhou, M.R. Servos, J. Photochem. Photobiol. A: Chem. 256 (2013) 7.

[19] D. Yin, F. Zhao, L. Zhang, X. Zhang, Y. Liu, T. Zhang, C. Wu, D. Chen, Z. Chen, RSC Adv. 6 (2016) 103795.

[20] W. Raza, S.M. Faisal, M. Owais, D. Bahnemann, M. Muneer, RSC Adv. 6 (2016) 78335.

[21] J.A. Rengifo-Herrera, M. Blanco, J. Wist, P. Florian, L.R. Pizzio, Appl. Catal. B: Environ. 189 (2016) 99.

[22] M. Nolan, A. Iwaszuk, A.K. Lucid, J.J. Carey, M. Fronzi, Adv. Mater. 28 (2016) 5425.

[23] W. Yu, J. Zhang, T. Peng, Appl. Catal. B: Environ. 181 (2016) 220.

[24] J.J. Zhuang, N. Xiang, X.Y. Lu, B. Xiang, Y. Xiong, R.G. Song, Mater. Technol. 31 (2016) 416.

[25] S. Mansingh, D.K. Padhi, K.M. Parida, Int. J. Hydrog. Energy 41 (2016) 14133.

[26] Y. Abdel-Maksoud, E. Imam, A. Ramadan, Catalysts 6 (2016) 138.

[27] S. Kanan, M.A. Moyet, R.B. Arthur, H.H. Patterson, Catal. Rev. 62 (2020) 1.

[28] D. Sarkar, C.K. Ghosh, S. Mukherjee, K.K. Chattopadhyay, ACS Appl. Mater. Interfaces 5 (2012) 331.

[29] R. Marks, T. Yang, P. Westerhoff, K. Doudrick, Water Res. 104 (2016) 11.

[30] C.L. Bianchi, B. Sacchi, C. Pirola, F. Demartin, G. Cerrato, S. Morandi, V. Capucci, Environ. Sci. Pollut. Res. 24 (2017) 12646.

[31] Y. Abdel-Maksoud, E. Imam, A. Ramadan, Catalysts 6 (2016) 138.

[32] E. Rokhsat, O. Akhavan, Appl. Surf. Sci. 371 (2016) 590.

[33] B. Fatima, S. Siddiqui, R. Ahmed, S.A. Chaudhry, Desalin. Water Treat. 164 (2019) 192.

[34] P. Bhattacharya, S. Swarnakar, S. Ghosh, S. Majumdar, S. Banerjee, J. Environ. Chem. Eng. 7 (2019) 102867.

[35] P.K. Raul, S. Senapati, A.K. Sahoo, I.M. Umlong, R.R. Devi, A.J. Thakur, V. Veer, RSC Adv. 4 (2014) 40580.

[36] D.Y. Sin, I.K. Park, H.J. Ahn, RSC Adv. 6 (2016) 58823.

[37] Y.Y. Lv, B.B. Zhang, X. Li, B. Pang, F. Zhang, D.J. Lin, J. Zhou, S.H. Yao, Y.B. Chen, S.T. Zhang, M. Lu, Z. Liu, Y. Chen, Y.F. Chen, Sci. Rep. 6 (2016) 26903.

[38] Z. Qin, Y. Chen, Z. Huang, J. Su, Z. Diao, L. Guo, J. Phys. Chem. C 120 (2016) 14581.

[39] D.V. Markovskaya, E.A. Kozlova, S.V. Cherepanova, P.A. Kolinko, E.Y. Gerasimov, V.N. Parmon, Chem Photo Chem 1 (2017) 1.

[40] X. Chen, F. Zhao, W. Liu, D. Sun, Y. Zuo, Z. Miao, P. Yang, J. Solid State Electrochem. 21 (2017) 2799.

[41] Y.H. Zhang, L. Guo, L. He, K. Liu, C. Chen, Q. Zhang, Z. Wu, Nanotechnology 18 (2007) 485609.

[42] D.K. Patel, H.B. Kim, S.D. Dutta, K. Ganguly, K.T. Lim, Materials 13 (2020) 1679.

[43] Y.M. Chen, Y. Zhu, Curr. Opin. Chem. Eng. 7 (2015) 32.

[44] A.A.A. El-Raady, A.M. Abo-Bakr, A.A. Ebnalwaled, Adv. Powder Technol. 28 (2017) 1079.

[45] B. Das, B. Das, N.S. Das, S. Pal, B.K. Das, S. Sarkar, K.K. Chattopadhyay, Appl. Surf. Sci. 515 (2020) 145958.

[46] P. Ruankham, C. Sae-kung, N. Mangkorntong, P. Mangkorntong, S. Choopun, J. Nat. Sci. 7 (2008) 177.

[47] X. Fu, W. Tang, L. Ji, S. Chen, Chem. Eng. J. 180 (2012) 170.

[48] H. Saito, Y. Nosaka, Green Chem. Lett. Rev. 41 (2012) 1591–1593.

[49] H.H. Yang, R.L. McCreery, J. Electrochem. Soc. 147 (2000) 3420–3428.

[50] H.R. Pouretedal, H. Beigy, M.H. Keshavarz, Environ. Technol. 31 (2010) 1183.

[51] D. Ayodhya, M. Venkatesham, A.S. Kumari, G.B. Reddy, D. Ramakrishna, G. Veerabhadram, J. Exp. Nanosci. 11 (2016) 418.

[52] A. Molla, M. Sahu, S. Hussain, Sci. Rep. 6 (2016) 1.

[53] Z. Khan, T.R. Chetia, M. Qureshi, Nanoscale 4 (2012) 3543.

[54] B. Barrocas, T.J. Entradas, C.D. Nunes, O.C. Monteiro, Appl. Catal. B: Environ. 218 (2017) 709.

Chapter 7

Chalcogenide beyond photovoltaics: Field emission from morphology tailored nanostructured molybdenum sulphide

Abstract

Molybdenum sulphide (MoS_2) nanoflakes were prepared by a facile room temperature wet chemical method and further modified with RF magnetron technique. Proper phase formation was confirmed by X-ray diffraction study whereas the morphological feature was investigated using field emission scanning electron microscopy. In an attempt to explore the potential of the chalcogenide beyond photovoltaic applications, the field emission performance of the nanostructure MoS_2 was investigated. Finite element based simulation was performed using ANSYS which was carried out to predict the feasibility of potential field emission behavior of the low dimensional MoS_2 flakes. Based on the results, the theoretical simulation was further extended to predict whether morphological modification can enhance the FE properties of the samples. Encouraged by the outcome of simulation based results, the samples were further treated by inert ion bombardment via sputtering technique. Both the pure and sputtered treated samples were subjected to FE studies. The turn-on field (electric field corresponding to 10 μA cm^{-2} current density) was obtained to be as low as 0.963 V $(\mu m)^{-1}$ with current density reaching up to 23.11 μA cm^{-2} for inter-electrode spacing of 2500 μm for the nanoflake samples. The emission current density enhanced remarkably after modification of sample morphology and reached up to 12 mA cm^{-2}.

7.1. Introduction

With remarkable development of industry based urban civilization during the last few decades, a huge requirement of uninterrupted energy supply has also increased. Traditional usage of fossil fuels for power harnessing cannot be a permanent solution to solve this demand. In this regard, several new technologies and advanced materials were developed to obtain consumable power from solar energy. Transition metal based ternary oxides [1], low

dimensional chalcogenides [2] and metal delafossites were identified as new age solar cell candidates. However, their applications are still under investigation compared to established effectiveness of silicon in this sector. Silicon based solar cells are still much popular due to their suitable power conversion ability [3], nontoxicity and availability. Besides, the most important feature of this material is its multipurpose applications. Therefore, newer materials for solar cell and any other advanced technology are required which possess easily tunable optical and electrical properties for multipurpose applications in order to be commercialized. Organometallic sulfides have been identified as a promising group in this regard [4,5]. Among this group, (MoS_2) has already shown remarkable power conversion efficiency [6-8]. The craze for this material is solely attributed to its physical properties. At room temperature, it possesses hexagonal crystal structure [9]. This material is under extensive research focus due to its interesting optoelectronic properties like high absorption coefficient [10], easily tunable band gap [11,12], long carrier diffusion lengths [13] and high carrier mobility [14]. Moreover, low temperature synthesis [15] routes have explored for this material which enables low production cost and better opportunity of fabrication of MoS_2 based composites without hampering the intrinsic properties of the counterparts. Owing to those features, MoS_2 is now being used in several extensions of photo induced applications like LEDs [16], photo detectors [17], field effect transistors [18] in addition to photovoltaic industry [19].

However, most of the applications based upon this material have been utilizing its photovoltaic character. Some other aspects, apart from the photovoltaic one, have not been investigated properly yet. From our previous experience, metal sulfides, transition metal based binary and ternary oxides etc. often show enhanced luminescence and field emission (FE) properties with wide range tuning by variation of synthesis and structural parameters [20]. This type of electron emission has tremendous applications in the area of field emission displays (FEDs), pressure sensors, field emission microscopy (e.g. FESEM), etc. It is

observed that low dimensional semiconductor nanostructures are in general promising electron emitters. Some well-known field emitting materials e.g. CNT [21], RGO nanocomposites [22], ZnO [23], graphene [24], LaB_6 [25], MoO_2 [26], etc. are well studied and has already been commercialized. However, almost each of them has limitations related to synthesis routes, stability, toxicity etc. To the best of our knowledge, very few attempts have so far been reported regarding the field emission behavior of MoS_2 nanostructures. Additionally, theoretical and experimental studies on the electronic band related properties of this novel sulphide are also contradictory to each other and are of wide range [27,28]. This work focuses the tuning of FE properties of MoS_2 in low dimension by cost effective chemical route and variation of shape/dimension of this novel material has been achieved by simple physical techniques which resulted into some encouraging outcomes.

The work function of this material was studied from available literature and was further used in calculation of various field emission parameters. The dependence of the field emission parameters upon the shape of MoS_2 emitters has also been studied through ANSYS MAXWELL simulation. The results obtained by this simulation based study were further correlated with experimental output. The field emission performance executed by this novel sulphide MoS_2 as presented in this work clearly indicates this as a future promising candidate for emission based display devices which further may be included into a photo excitable cold emission device.

7.2. Experimental details

7.2.1. Synthesis of MoS_2 nanoflakes

All the chemicals used in our synthesis were purchased from Merck (India) and treated without any further purification. MoS_2 nanostructures on carbon cloth were synthesized by facile hydrothermal method [29]. Firstly, the carbon cloth (CC) was cleaned in acetone, DI and ethanol sequentially for 15 min each by ultrasonication. Before deposition, the carbon

cloth was activated chemically with $KMnO_4$ so that the barriers can be overcomed that originate at the time of physical deposition. The solution was prepared by dissolving 42 mg of ammonium tetrathiomolybdate ($(NH_4)_2MoS_4$) in the mixture of 21 mL of N, N-Dimethylformamide (DMF) and de-ionized water in the ratio of 2:1 and stirred for 15 min. It was then transferred into a 40 mL stainless steel autoclave and the seeded CC mounted on a glass slide was inserted in the solution at an inclination of 45°. Then, the sealed autoclave was placed in an oven at 200 °C for 12 h. After the completion of hydrothermal reaction, the autoclave was allowed to cool down to room temperature naturally. The obtained dark film of CC was washed with acetone, ethanol and lastly with DI to remove the surface impurities. After drying in vacuum oven at 60 °C, the deposited substrate was annealed in furnace for 2 h at 350 °C in an atmosphere of H_2 (5%) mixed with N_2 (95%) at a heating rate of 1 °C min^{-1}. Finally, the black-colored CC was obtained which indicated the formation of MoS_2 nanostructures.

7.2.2. Characterization

The as-synthesized samples were subjected to several characterizations. The proper phase formation was investigated by X-ray diffractometer (Bruker D8 Advanced) with Cu-Kα radiation (λ=1.54 Å). The morphological analysis was carried out by field emission scanning electron microscopic studies (FESEM, Hitachi S-4800) and EDX was done to determine the composition of the elements. Finally, all the samples were investigated by our laboratory made high vacuum field emission set up to study the field emission properties and cold emission current density and other relevant FE parameters were obtained for all the samples. ANSYS Maxwell was further used to carry out finite element electrostatic simulations study and the effects of dimensional variation of the sample. The outcomes of this simulation based study were correlated with experimental results.

7.3. Results and Discussion

7.3.1. XRD Analysis

The phase of the as-prepared samples was confirmed from X-ray Diffraction with Cu-Kα radiation (λ=1.5406 Å), operating at 40 kV, 40 mA in 2θ range from 10-60^{o} at 0.2 sec/step. Figure 7.1 depicts the XRD profiles of the samples. The figure shows the presence of diffraction peaks corresponding to the planes (002), (101), (103) and (105) indexed at 2θ (degree) = 14.36, 33.64, 39.49 and 49.64 respectively [JCPDS no. 77-1716] which confirms the formation of highly crystalline hexagonal MoS_2 [30].

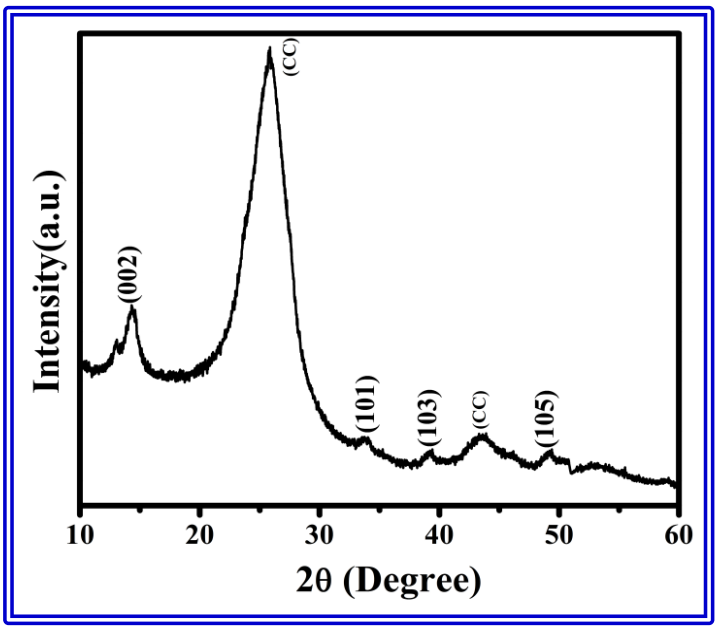

Fig. 7.1. *XRD spectra of MoS_2 nanoflakes grown on carbon cloth*

7.3.2. Morphological studies

Field Emission Scanning Electron Microscopy (FESEM) was employed to observe the morphologies of the as synthesized samples. It can be seen from Fig. 7.2 that MoS_2 nanoflakes have average dimension of ~ 150-200 nm with average length of ~ 5-6 µm.

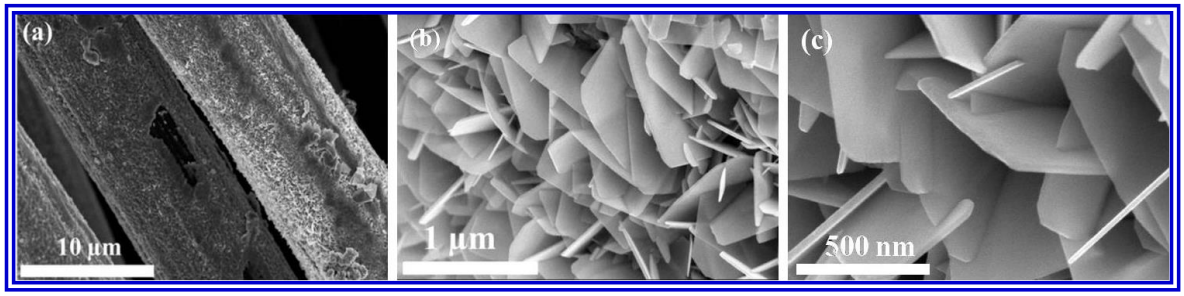

Fig. 7.2. *FESEM images of MoS_2 nanoflakes grown on carbon cloth before sputtering*

The flakes after sputtering treatment are shown in Fig. 7.3. It can be seen that the samples gradually dissociated in small particles after being sputter treated though the particulate structure finally showed a self-standing array-like feature with an overall shape of flake.

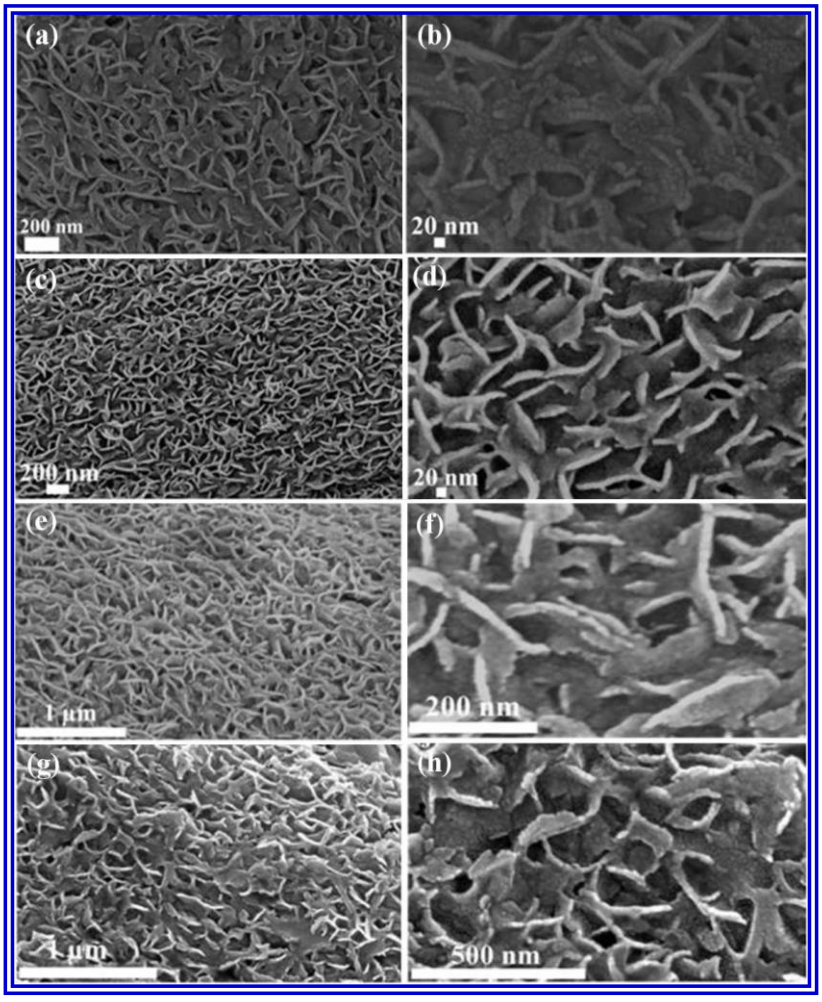

Fig. 7.3. *FESEM images of MoS_2 nanoflakes grown on carbon cloth after sputtering for (a,b) 30 sec, (c,d) 60 sec, (e,f) 90 sec, (g,h) 150 sec*

However, the samples treated by 150 s sputtering can be seen having higher degree of surface damage and more non-uniformly distributed array of MoS_2 particles. The particles in all duration of sputtering have an average dimension less than 10 nm.

7.3.3. Compositional analysis

Energy dispersive X-ray (EDX) analysis was performed for the two samples to check the stoichiometric balance of the constituent elements and the results are summarized in Table 7.1. The results showed that each sample contain main constituent elements Mo and S in almost accurate stoichiometric ratio. It was further confirmed from EDX studies that the stoichiometric balance of the constituent elements was not disturbed due to sputtering. The samples exhibited atomic ratio within a variation of 4-5%. Moreover, the elemental uniformity also remained unaltered after sputtering. This was accounted for etching process by inert argon ions.

Table 7.1. *Table for stoichiometric ratio of Mo and S on carbon cloth before and after sputtering*

Type of carbon cloth film	Atomic % of Mo	Atomic % of S
Non-sputtered	36.03	63.97
Sputtered	31.48	68.52

7.3.4. ANSYS Maxwell simulation

Finding high aspect ratio of the nanoflakes from morphological study, the potential field emission behavior of the samples was predicted. For this, ANSYS Maxwell simulation based studies were carried out. Both 3D and 2D models were employed in order to identify the output field distribution separately for array and single MoS_2 nanoflake emitter. All models

of the emitters (MoS_2 nanoflake) were designed in the software keeping the dimension, electrode separation as per actual basis. The dimensional control by growth time was designed and the predicted samples were subjected to virtual macroscopic field separately and the output field was plotted around the emitter array using colour mapping. The results are presented in Fig. 7.4. It can be seen that the samples showed better predicted output field with increasing deposition time. Higher aspect ratio associated with dimensional variation may be accounted for this output of simulation. However, from the simulated results, it was established that the samples grown for 12 h should be the best one for cold electron emission performance.

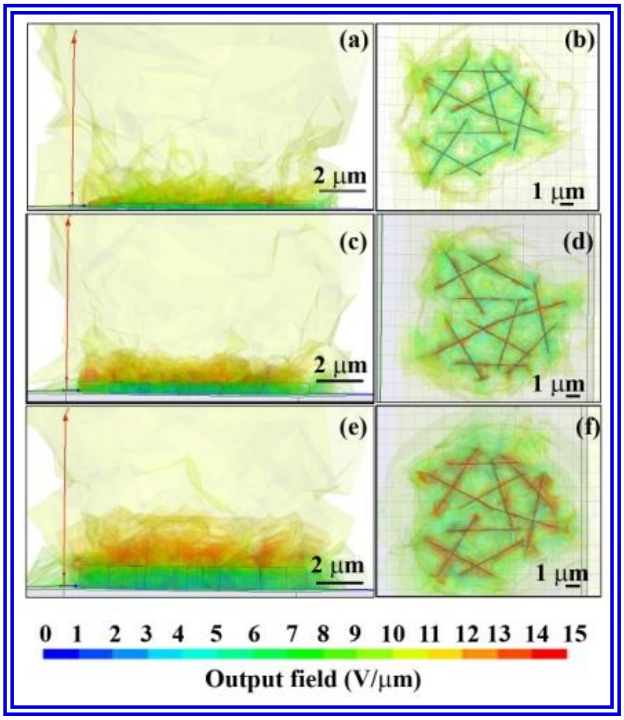

Fig. 7.4. *Simulated fields for (a) lower growth time, (b) corresponding top view, (c) medium growth time, (d) corresponding top view, (e) higher growth time and (f) corresponding top view*

Separate model for a single emitter was designed in ANSYS keeping the dimension and other details same as actual basis. Further the edges of that model was modified and transformed to an ion etched edge of the flake as obtained in the FESEM image of small duration sputter-

edged sample. Virtual field excitation was then applied and the output field distribution was plotted using appropriate colour code. The results are depicted in Fig. 7.5. It can be seen that the output field density increased considerably for the etched model. Especially, the particular points of etching showed predicted field enhancement. This theoretical simulation based results were considered as guiding factors for actual field emission studies as demonstrated in the next section.

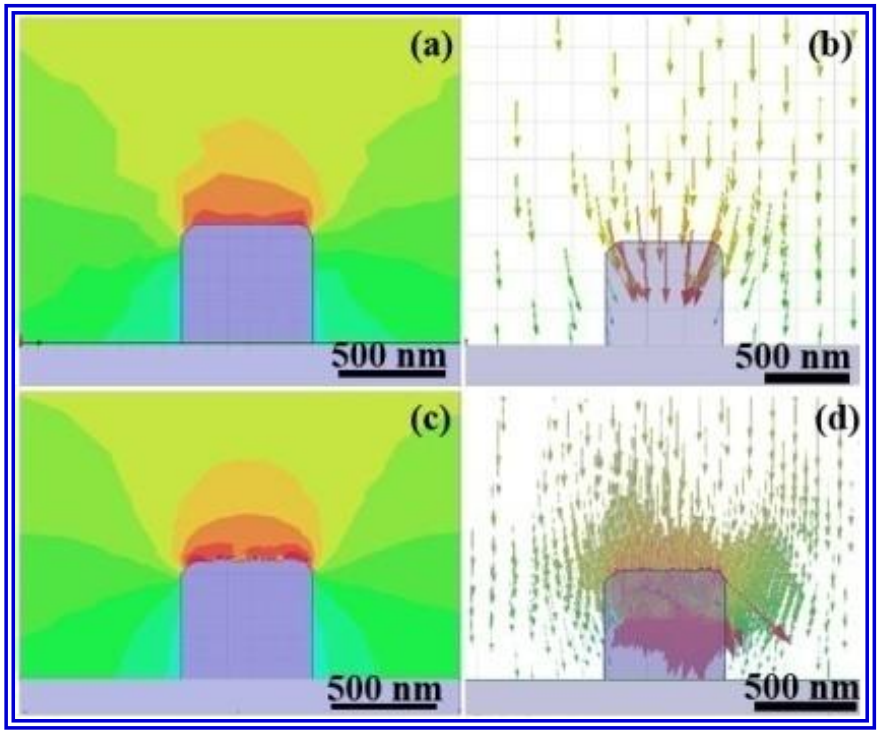

Fig. 7.5. *(a) Output simulated field magnitude and (b) field vector for pristine MoS_2 nanoflakes; (c) Output simulated field magnitude and (d) field vector for sputter etched MoS_2 nanoflakes*

7.3.5. Field emission study

Encouraged by simulation based results, field emission properties of the as-synthesized MoS_2 nanoflakes were performed in our homemade high vacuum field emission setup. The set up includes two electrodes consisting of a stainless steel platform which acts as the cathode and a stainless steel conical tip (1.5 mm dimension) which acts as the anode. The samples were mounted on a steel platform. The samples were placed at different inter-electrode distances

by a micrometer screw attached to the system. Furthermore, this entire diode system was placed in a transparent chamber which was evacuated up to $\sim 10^{-6}$ mbar base pressure using a combination of rotary and oil diffusion pump. The transparency of the chamber enabled us to ensure that no discharge from the surface of the sample took place while applying high electric field. Theoretically, the emission current I and the applied electric field E are related by the equation [31]

$$I = (Aa\beta^2 E^2/\phi)\exp[-b\phi^{3/2}/(\beta E)] \quad (1)$$

where, A is the emission area (= area of the anode tip = $(\pi/4)\times(1.5\ \text{mm})^2$); a, b are Fowler-Nordheim (F-N) constants having values a = 1.54×10^{-6} A eV V^{-2} and b = 6.83×10^3 $eV^{-3/2}$ $V\ (\mu m)^{-1}$, ϕ and β are the local work function and the field enhancement factor respectively.

E was calculated by dividing the externally applied input voltage V (in Volt) by the inter-electrode distance x (in μm).

Eqn. (1) can be rewritten as

$$\ln\left(\frac{J}{E^2}\right) = \ln(a\,\beta^2/\phi) - b\phi^{3/2}/(\beta E) \quad (2)$$

where, J = I/A is emission current density.

Hence, a plot of ln (J/E^2) vs. 1/E gives a straight line having slope (say m) = $-b\phi^{3/2}/\beta$ and intercept =$\ln(a\beta^2/\phi)$. So from the knowledge of this slope, one can figure out the field enhancement factor β using

$$\beta = -b\phi^{3/2}/m \quad (3)$$

Besides, the effective work function ϕ_{eff} i.e. work function reduced locally at the emission sites is obtained from the relation given below [32].

$$\phi_{eff} = \phi/\beta^{2/3} \quad (4)$$

7.3.5.1. Effect of electrode separation

The samples synthesized for 12 h was first investigated for FE performance under different electrode separations of 1500 μm, 2000 μm and 2500 μm. The obtained J vs. E curves is presented in Fig. 7.6. It can be seen that the sample showed highest emission current density at 2500 μm. This result can be associated with the number of emitters. As the electrode separation gradually increases, higher number of flaky emitters is included under the collector coverage leading to higher emission current density. Hence, the emission current density gradually increased upon increasing the inter-electrode separation. Hence, the further study of FE behavior was carried out with 2500 μm electrode separation.

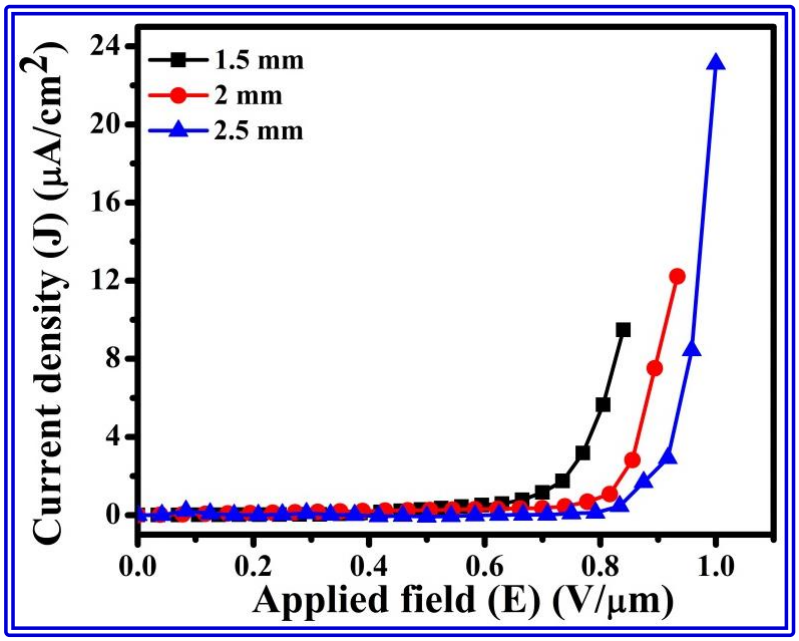

Fig. 7.6. *J vs E curves of MoS_2 nanoflakes on CC before sputtering at different inter-electrode distances*

7.3.5.2. Effect of emitter morphology

Figure 7.6 shows the J-E curves obtained from the experimentally observed current voltage data for MoS_2 nanoflakes for electrode separations 1500, 2000 and 2500 μm. After the samples were treated by sputtering method, a remarkable enhancement of FE properties was obtained as shown in Fig. 7.7(a). The emission current density enhanced up to 11.6 mA cm^{-2}

for the sample treated for 90 sec as compared to the untreated MoS_2 sample. However, further increasing the sputtering duration effectively decreased the emission current density down to ~ 1 mA cm^{-2}. Though this value is yet higher than the current density exhibited by the untreated sample but is inferior to other sputter treated samples.

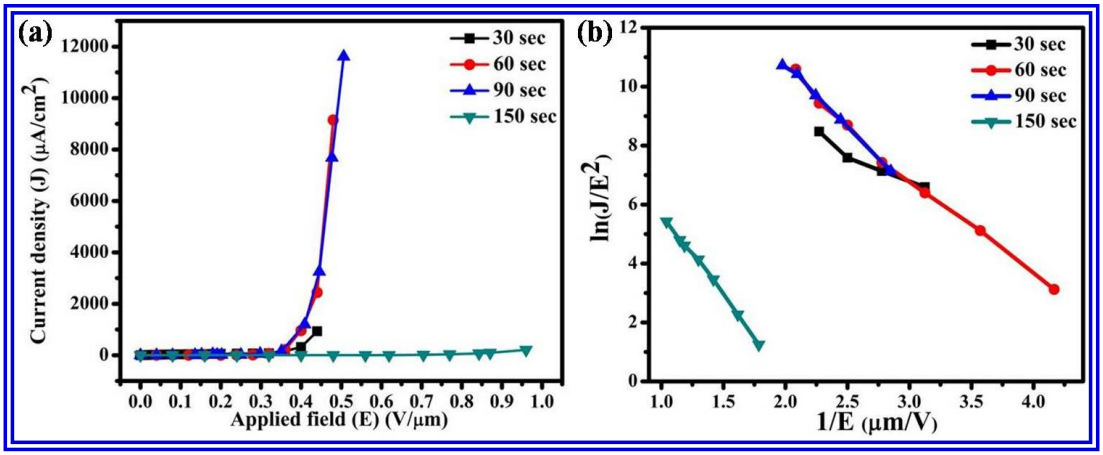

Fig. 7.7. ***(a)*** *J vs E curves of sputtered MoS_2 nanoflakes at different time durations,* ***(b)*** *corresponding F-N plots*

To understand the variation between the emission behavior of untreated and various sputter treated samples, the basic morphological changes occurring after sputtering must be analyzed. After sputtering, the previously solid and smooth MoS_2 flakes become granular. The roughness and granular feature increase as the sputtering duration increases gradually. Initially, in untreated condition, the MoS_2 layer emitted electrons only from the sharp edges with little contribution from the central parts. After sputtering, some porous nature was introduced within the flakes leading to enhanced number of electron emission centers. This was reflected in gradual enhancement of emission current densities after increment of sputtering duration. However, increasing the sputtering duration too much caused almost complete destruction of self-standing feature of the flakes and left the system in no better than a collection of discrete MoS_2 nanoparticles. This should give rise to screening effect and hence appreciably inferior electron emission occurred in case of the sample sputter treated for 150 s.

A graphical representation of the turn-on field of the samples vs. time duration of sputtering are presented in Fig. 7.8. Like the emission current densities, the samples showed similar enhancement of FE behavior in view of turn-on fields also. Turn-on field was defined as the field required for achieving emission current density of 200 μA cm^{-2}. As can be clearly observed from Fig. 7.8, sample treated for 90 s showed lowest turn on field which increased for 150 s treated sample but all treated samples exhibited higher turn on field than the untreated one. In fact the untreated sample could not emit 200 μA cm^{-2} current in our maximum possible range of external electric field. This result was also correlated with the morphological features of treated and untreated samples, which was responsible for different magnitude of emission current densities.

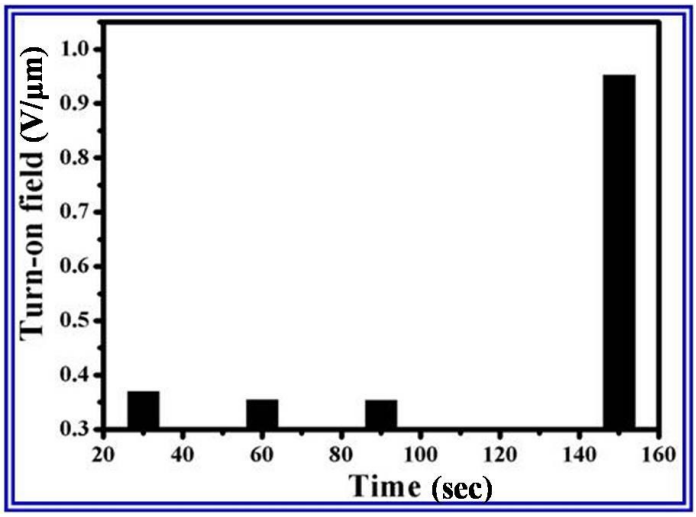

Fig. 7.8. *Graphical representation of turn-on field vs. time duration of sputtering*

The smallest turn-on field was obtained for sample treated with 90 s. Actually due to moderate sputtering duration, a large number of individual particulate emitters were present in that particular sample which in turn easily supplied required amount of emission current upon application of minimum external field. But further treatment with sputtering caused severe damage to the flaky emitters so that any individual solid emitter could hardly exist and thus, it required much higher field to achieve necessary emission current density. This is

reflected in slight increment of turn-on field. However, this turn-on field exhibited by the 150 sec sputtered sample is still larger than the untreated sample. Actually, in the untreated sample, the entire flake works as the emitter whereas in all the treated samples, particulate array in shape of a flake works as emitter. Higher aspect ratio in the latter caused lower turn-on field for each treated sample compared to the untreated one.

The FE behavior was further characterized by comparing the field enhancement factors exhibited by different samples. For this, first, F-N plots were drawn for the samples which are depicted in Fig. 7.7(b). The negative slopes of F-N plots ensured cold electron emission from all the samples. However, the values of field enhancement factors were determined using equation (3) and the results are comparatively presented in Fig. 7.9. It can be seen that field enhancement factors gradually decreased after sputtering treatment which can also be accounted for the morphological modification of the samples. As there exist higher number of emitters with higher sputtering time, formation of too many emission centers actually hinders the effect of each other and thus the field lines are repelled which is reflected in decrement of local field enhancement factor.

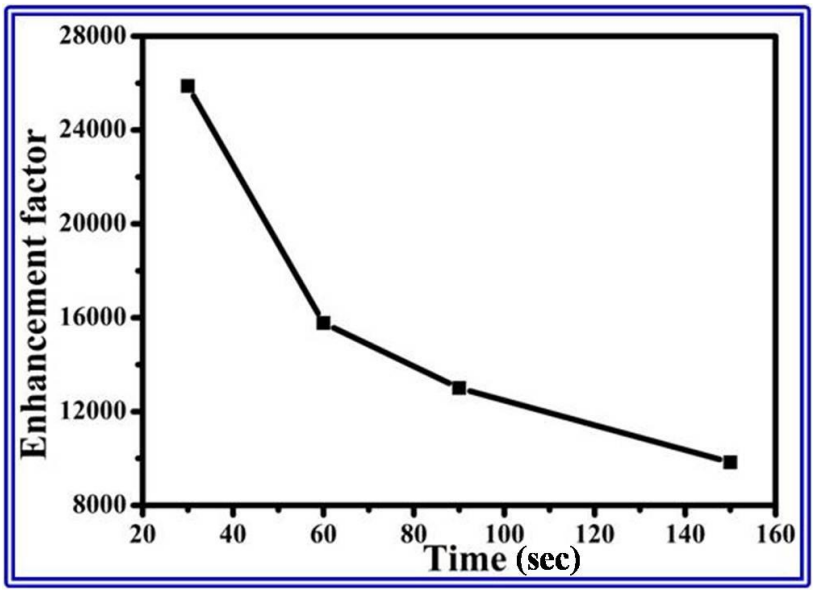

Fig. 7.9. *Plot of the field enhancement factor vs. time duration of sputtering*

A comparative presentation showing the FE performances of many identical systems is presented in Table 7.2 which showed that the sputter treated MoS_2 samples can serve as efficient cold cathodes in future flexible emission based devices.

Table 7.2. *Comparative study of FE performances of many identical systems*

Catalyst	Inter-electrode separation	Turn-on field required to draw a current density of 10 μA cm^{-2}	Enhancement factor	Reference
Layered MoS_2 sheets	500 μm	3.5 V/μm	~ 1138	[33]
MoS_2 nanoflowers	100-150 μm	4.5-5.5 V/μm	-	[34]
PLD MoS_2/ W-tip emitter	500 μm	-	~ 15,500 (low field region) ~ 47,000 (high field region)	[35]
PLD MoS_2/ Si planar emitter		2.8 V/μm	~ 1900	
MoS_2 nanoflakes on CC after 30 s sputtering	2500 μm	0.37 V/μm	~ 25875	This work
After 60 s sputtering		0.355 V/μm	~ 15770	
After 90 s sputtering		0.35 V/μm	~ 13000	
After 150 s sputtering		0.953 V/μm	~ 9830	

7.4. Conclusion

Field emission property of sputtered modified nanoflakes of MoS_2 has been reported for the first time. The samples were prepared by a very simple wet chemical approach. After proper characterizations by XRD, EDX, FESEM, the field emission property of these samples was investigated. The compositional and structural observations were explained as direct

consequences of synthesis techniques. Between the two types of samples, the nanoflakes treated by sputtering showed a considerable enhancement in field emission behavior with current density reaching few milli-ampere per square centimeter and a turn-on field of 0.95 V $(\mu m)^{-1}$, owing primarily to their rod like 1-D nanostructure. The dependence of the FE properties e.g. field enhancement factor, turn on field etc. upon the inter-electrode separation were also been studied. The work function ϕ (~ 4 eV) of the material has been considered as per reported values [33]. Furthermore, a theoretical analogy by ANSYS simulation has been provided to validate our experimental findings. Finally, the samples were etched by magnetron sputtering with varying duration to fabricate samples with different roughness and porosity. It was observed that an optimized value of sputtering time resulted into most efficient cold cathode with emission current density as high as ~ 12 mA cm^{-2} and turn-on field as low as 0.35 V $(\mu m)^{-1}$. This present work leads to a new path way for the potential application of MoS_2 to be used as an emission based display and other devices. It also provokes to further research on the FE properties of other related sulphide chalcogenides with different morphologies.

7.5. References

[1] J. Gao, C.L. Perkins, J.M. Luther, M.C. Hanna, H.Y. Chen, O.E. Semonin, A.J. Nozik, R.J. Ellingson, M.C. Beard, *Nano Lett.* 11 (2011) 3263-3266.

[2] E. Singh, K.S. Kim, G.Y. Yeom, H.S. Nalwa, *RSC Adv.* 7 (2017) 28234-28290.

[3] V. Sivakov, G. Andrä, A. Gawlik, A. Berger, J. Plentz, F. Falk, S. H. Christiansen, *Nano Lett.* 9 (2009) 1549-1554.

[4] P.J. Dean, A.D. Pitt, M.S. Skolnick, P.J. Wright, B. Cockayne, *J. Cryst. Growth* 59 (1982) 301-306.

[5] E. Cárdenas, A. Arato, E.P. Tijerina, T.K.D. Roy, G.A. Castillo, B. Krishnan, *Solar Energy Materials and Solar Cells* 93 (2009) 33-36.

[6] S. Kohnehpoushi, P. Nazari, B.A. Nejand, M. Eskandari, *Nanotechnol.* 29 (2018) 205201.

[7] G. Yue, J.Y. Lin, S.Y. Tai, Y. Xiao, J. Wu, *Electrochimica Acta* 85 (2012) 162-168.

[8] C. Yu, X. Meng, X. Song, S. Liang, Q. Dong, G. Wang, C. Hao, X. Yang, T. Ma, P.M. Ajayan, J. Qiu, *Carbon* 100 (2016) 474-483.

[9] D. Liu, X. Chen, D. Li, F. Wang, X. Luo, B. Yang, *J. Mol. Struc.* 980 (2010) 66-71.

[10] D.S. Tsai, K.K. Liu, D.H. Lien, M.L. Tsai, C.F. Kang, C.A. Lin, L.J. Li, J.H. He, *ACS Nano* 7 (2013) 3905-3911.

[11] T. Chu, H. Ilatikhameneh, G. Klimeck, R. Rahman, Z. Chen, *Nano Lett.* 15 (2015) 8000-8007.

[12] A. Ebnonnasir, B. Narayanan, S. Kodambaka, C.V. Ciobanu, *Appl. Phys. Lett.* 105 (2014) 031603.

[13] S. Alzahly, L.P. Yu, C.J. Shearer, C.T. Gibson, J.G. Shapter, *Materials* 11 (2018) 639.

[14] A. Capasso, F. Matteocci, L. Najafi, M. Prato, J. Buha, L. Cinà, V. Pellegrini, A.D. Carlo, F. Bonaccorso, *Adv. Energy Mater.* 6 (2016) 1600920.

[15] D. Wang, Z. Pan, Z. Wu, Z. Wang, Z. Liu, *J. Pow. Sour.* 264 (2014) 229-234.

[16] G.J. Choi, Q.V. Le, K.S. Choi, K.C. Kwon, H.W. Jang, J.S. Gwag, S.Y. Kim, *Adv. Mater.* 29 (2017) 1702598.

[17] W. Tang, C. Liu, L. Wang, X. Chen, M. Luo, W. Guo, S.W. Wang, W. Lu, *Appl. Phys. Lett.* 111 (2017) 153502.

[18] X. Zou, J. Wang, C.H. Chiu, Y. Wu, X. Xiao, C. Jiang, W.W. Wu, L. Mai, T. Chen, J. Li, J.C. Ho, L. Liao, *Adv. Mater.* 26 (2014) 6255-6261.

[19] S. Wi, H. Kim, M. Chen, H. Nam, L.J. Guo, E. Meyhofer, X. Liang, *ACS Nano* 8 (2014) 5270-5281.

[20] M. Zhang, T. Zhai, X. Wang, Y. Ma, J. Yao, *Cryst. Growth & Design* 10 (2010) 1201-1206.

[21] H. Murakami, M. Hirakawa, C. Tanaka, H. Yamakawa, *Appl. Phys. Lett.* 76 (2000) 1776-1778.

[22] A.K. Samantara, D.K. Mishra, S.R. Suryawanshi, M.A. More, R. Thapa, D.J. Late, B.K. Jena, C.S. Rout, *RSC Adv.* 5 (2015) 41887-41893.

[23] D. Banerjee, S.H. Jo, Z.F. Ren, *Adv. Mater.* 16 (2004) 2028-2032.

[24] Z.S. Wu, S. Pei, W. Ren, D. Tang, L. Gao, B. Liu, F. Li, C. Liu, H.M. Cheng, *Adv. Mater.* 21 (2009) 1756-1760.

[25] J.Q. Xu, Y.M. Zhao, Q.Y. Zhang, *J. Appl. Phys.* 104 (2008) 124306.

[26] F. Wang, B. Lu, *Physica B: Condensed Matter* 404 (2009) 1901-1904.

[27] D. Karmakar, R. Halder, N. Padma, G. Abraham, K. Vaibhav, M. Ghosh, M. Kaur, D. Bhattacharya, T.V.C. Rao, *J. Appl. Phys.* 117 (2015) 135701.

[28] A.M. Sánchez, K. Hummer, L. Wirtz, *Surf. Sci. Rep.* 70 (2015) 554-586.

[29] Y. Yan, B.Y. Xia, N. Li, Z. Xu, A. Fisher, X. Wang, *J. Mater. Chem. A* 3 (2015) 131-135.

[30] C. Feng, J. Ma, H. Li, R. Zeng, Z. Guo, H. Liu, *Mater. Res. Bull.* 44 (2009) 1811-1815.

[31] N. Besra, S. Pal, B.K. Das, K.K. Chattopadhyay, *Phys. Chem. Chem. Phys.* 19 (2017) 26708-26717.

[32] A. Jha, D. Banerjee, K.K. Chattopadhyay, *Appl. Surf. Sci.* 257 (2011) 1946-1951.

[33] R.V. Kashid, D.J. Late, S.S. Chou, Y.K. Huang, M. De, D.S. Joag, M.A. More, V.P. Dravid, *Small* 9 (2013) 2730-2734.

[34] Y.B. Li, Y. Bando, D. Golberg, *Appl. Phys. Lett.* 82 (2003) 1962-1964.

[35] D.J. Late, P.A. Shaikh, R. Khare, R.V. Kashid, M. Chaudhary, M.A. More, S.B. Ogale, *ACS Appl. Mater. Interfaces* 6 (2014) 15881-15888.

Chapter 8

Grand Conclusion and Scope for future work

8.1. Grand Conclusion

From the detailed investigation presented in the chapters 4-7 of the thesis, the points emerged as conclusions are described below:

1) Co incorporated Ni_3S_2 nanostructured composites were synthesized for the first time using cost effective and eco-friendly hydrothermal method on Ni foam substrates under different synthesis temperatures. Successful doping of Co, contributed by major portion of initial cobalt precursor was predicted from XRD spectra which was further confirmed from XPS study. To find out the basic morphology, all the samples were initially characterized with FESEM and all the samples show uniform rod like morphology grown over large area. The length of the rods varied from 3 μm – 10 μm and this increment of rod length was directly associated with increment of synthesis temperature. The rod diameter ~ 500 nm was reconfirmed using HRTEM. However, the pristine sample without Co incorporation showed that the particle size was around 30 nm and no morphology with enhanced aspect ratio was found. The absence of Co atoms as growth centres was identified as the major reason behind this general blunt morphology. All samples showed the presence of constituent elements (Ni, O, S and Co) in proper stoichiometric ratio. XPS analysis confirmed the existence of Co within Ni_3S_2 system. In addition to regular structural, morphological and compositional studies, the efficiency of the samples for HER was tested in acidic medium. It was observed that the samples synthesized with higher temperature shows most efficient catalysis performance for HER with overpotential 206 mV. The superior morphological features with high aspect ratio were identified as the key factor for such efficient HER catalytic performance.
2) ZnS thin films were synthesized by hydrothermal method on seeded glass and silicon substrates prior to which the seeded substrates were prepared via RF magnetron sputtering technique. By varying the molar ratios of the chemicals present in the precursor

solution and their pH values, the hydrothermal deposition parameters were optimized. The synthesis temperature played an important role in deposition of thin films which improved the crystallinity of the samples. The proper phase formation of the synthesized films was confirmed by XRD and HRTEM studies. The film obtained for molar ratio 1:2 showed best crystallinity and almost amorphous phase was obtained for the other two molar ratios, 1:1 and 1:4. Further, the thin films of this particular ratio deposited in various synthesis temperatures (110℃, 130℃, 150℃ and 180℃) on glass and Si substrates also indicated proper phase formation. HRTEM studies confirmed the nanocrystalline nature of the film synthesized at lower temperatures. By controlling the synthesis temperature, the average particle size of the thin films can be varied from nano to micro range as determined from the FESEM measurements. EDX study confirmed that the samples exhibit nearly stoichiometric composition of Zn and S. It was found that in the visible region, the samples have good transparency which was confirmed from the transmission spectra. UV-vis-NIR spectrophotometric measurement showed that with increase of particle dimensions, the optical band gap was found to decrease. The samples exhibited strong CL behavior irradiated under electronic excitation thus indicating its effective application in display devices.

3) Hierarchical nickel sulphide microtubes by varying the ratios of nickel and sulphur precursors in the solution, were prepared by cost effective sol-gel technique with tuning of morphology and applied for photo-induced hazardous dye segregation and cold electron emission. The synthesized samples were characterized for crystalline phase, morphology and composition via X-ray diffractometry, electron microscopy and energy dispersive X-ray studies respectively. Application of nickel sulphide microstructures in UV driven water disinfection technology was reported for the first time. The increase in nickel content within the samples was observed to govern the photocatalytic efficiency of

the microstructures and was explained to be occurring due to the variation of aspect ratio. The sample showing highest degradation efficiency was found to degrade phenol effectively. Cold electron emission from nickel sulphide microstructures, reported for the first time showed morphology dependent turn-on field and current density. The growth of different shapes and hierarchical units of NS structures was correlated with stoichiometric alteration which may also be extended for synthesis of other nickel chalcogenides.

4) Molybdenum sulphide (MoS_2) nanoflakes were prepared by a facile room temperature wet chemical method and further modified with RF magnetron technique. X-ray diffraction studies confirmed the proper phase formation whereas the morphological features were investigated using FESEM. The field emission performance of the nanostructure was studied to explore the potential of the chalcogenide beyond photovoltaic applications. Furthermore, a theoretical analogy by ANSYS simulation has been provided to validate our experimental findings. Finally, the samples were etched by magnetron sputtering with varying duration to fabricate samples with different roughness and porosity. It was observed that an optimized value of sputtering time resulted into most efficient cold cathode with emission current density as high as ~12 mA cm^{-2} and turn-on field as low as 0.35 V $(\mu m)^{-1}$. This present work leads to a new path way for the potential application of MoS_2 nanostructures to be used as an emission based display and other devices. It also provokes to further research on the FE properties of other related sulphide chalcogenides with different morphologies.

8.2. Scope for future work

The future scope of the research will be concentrated on the following things:

1) We will focus on the synthesis of nanostructures of other transition metal sulphides as well as different nanocomposite materials by solvothermal method.

2) Application of branched chalcogenides nanostructures for electrochemical water splitting emerged as a most successful technological achievement in this thesis, the same nanostructures could be synthesized on flexible substrates and their cold electron emission performance may be investigated.
3) Attachment of foreign booster candidates like novel metal nanoparticles on the surface of catalyst nanostructures may result in even better and faster catalytic response from them. This may be attempted with nickel sulphide nanostructures to enhance the photocatalytic activities of the same.
4) As we have already succeeded to combine two important applications of field emission and photocatalytic dye removal in the same material system (nickel sulphide), the same approach may be implied to other chalcogenide systems involving Mo and Zn. This may open up the possibilities of 'environment friendly' technical development by nanostructured materials in future.